AN INVESTIGATION INTO FATIGUE CRACK PROPAGATION IN STIFFENED AND UNSTIFFENED 350WT STEEL SHIP PLATING SUBJECTED TO VARIABLE AMPLITUDE LOADING

by

Brian Ka Chun Yuen

Submitted
in partial fulfillment of the requirements
for the degree of

DOCTOR OF PHILOSOPHY

Major Subject: Civil Engineering

at

DALHOUSIE UNIVERSITY

Halifax, Nova Scotia September, 2006

Your file Votre référence
ISBN: 978-0-494-27654-9
Our file Notre référence
ISBN: 978-0-494-27654-9

DALHOUSIE UNIVERSITY

To comply with the Canadian Privacy Act the National Library of Canada has requested that the following pages be removed from this copy of the thesis:

Preliminary Pages
- Examiners Signature Page
- Dalhousie Library Copyright Agreement

Appendices
- Copyright Releases (if applicable)

Table of Contents

List of Tables

Page

List of Figures

Page

Abstract

In engineering, fatigue is defined as the decrease in strength of a material under repeated load cycles, ultimately leading to fracture. It is an issue for the design of bridges, cranes, transmission towers, ships and airplanes. The objective of this thesis was to investigate the fatigue behaviour of stiffened and unstiffened 350WT Category 5 steel plates when subjected to a number of fatigue scenarios that are commonly experienced in the life of ship plating. 350WT steel is a typical material used in Canadian bridges, offshore structures and the hulls of the City class frigates. The fatigue scenarios considered in this thesis included constant amplitude loading, multiple overloading, compressive underloading with crack surface roughness, fatigue of a brittle material and welded stiffened plates. As a result of the present research, the accuracy of two well-known fatigue models, that is, the Zheng and Hirt model and the Wheeler model, were improved. This has been shown to provide a better fatigue prediction in the threshold region and under multiple tensile overloading. A systematic study of crack surface roughness and compressive underloading, which in the past had not been given as much attention as tensile overloading, was developed. The present results showed that there appears to be some merit to the "prying" effect of the crack surface asperities, comparable to the well-known crack closure concept. By testing polymethyl methacrylate (PMMA), evidence was provided for the lack of load interaction effects in brittle materials. In other words, it was discovered that the load interaction effects are largely the result of plastic deformation. This has implications on the fatigue behaviour of steel under certain embrittling conditions. Finally, a procedure was established to predict the fatigue crack growth rates of welded stiffened steel plates using the finite element method, which involved the simulation of the residual stresses followed by a fracture mechanics analysis. The procedure was shown to offer an adequate alternative to experimental testing in predicting the fatigue behaviour of welded stiffened structures. To summarize, it is believed that fatigue life prediction of ship plating would be improved based on the results of the present research.

List of Abbreviations and Symbols

A	Cross-sectional area of stringer
A_e	Effective cross-sectional area of stiffener
a	Crack length
da/dN	Fatigue crack growth rate
Δa	Crack extension (Chapter 2); Normalized crack growth between overload application (Chapter 7)
a_c	Critical crack length
a_d	Delay retardation crack length
a_f	Final recorded valid crack length
a_i	Initial crack size (Chapter 2); Current crack length (Chapters 3 and 7)
a_{lim}	Crack length at which the average stress in the uncracked ligament of a middle tension specimen is 80% of the yield strength of the material
a_o	Crack length at which the first overload was applied
a_{OL}	Crack length at which an overload is applied
$a_{OL,lim}$	Crack length at which an overload that is applied would have its total retardation crack length ended at a_{lim}
a_r	Total retardation crack length

B	Specimen thickness; Material constant in the Zheng and Hirt model, $B = \frac{1}{2\pi\sigma_{ff}^2}$ (Chapters 3 and 6)
$B_{Predicted}$	Value of the material constant B in the Zheng and Hirt model predicted by the model
$B_{Reanalyzed}$	Value of the material constant B in the Zheng and Hirt model obtained by reanalysis of test data
b	Reinforcement spacing
CAL	Constant amplitude loading
CNBC	Canadian Neutron Beam Centre
CSA	Canadian Standards Association
CVN	Charpy V-notch
$[C]$	Stiffness matrix
C_{11}, C_{12}, C_{44}	Components of the stiffness matrix
C	Curve fitting parameter for the Paris model; Closed contour in defining the J-integral (Chapter 2); Stress intensity modification factor (Chapter 5); Heat capacity (Chapter 10)
C_b	Stress intensity modification factor for broken stiffener
$C_{\min}$	Minimum value of stress intensity modification factor
c	Specific heat
DRDC	Defence Research & Development Canada
d	Spacing between diffracting planes of atoms
d/a	Normalized asperity location
d_o	Reference spacing of atomic planes in unstrained condition

d_f	Spacing of atomic planes in strained condition
EDM	Electrical discharge machining
ENDURE	Fracture mechanics and fatigue module for NISA
E	Modulus of elasticity; Modulus of elasticity for sheet (Chapter 5)
E_{kin}	Kinetic energy
E_s	Modulus of elasticity for stiffener
EL	Elongation at fracture
FE	Finite element
F	Work performed by external force (Chapter 2); Maximum force in stiffener (Chapter 5)
F_{tyf}	Tensile yield strength for stiffener
F_{tys}	Tensile yield strength for sheet
f_L	Friction limit for the 2-D gap/friction element in NISA
f_n	Normal compressive force in the 2-D gap/friction element in NISA
f_t	Shear force in the 2-D gap/friction element in NISA
G	Strain energy release rate
G_c	Critical strain energy release rate
G_I	Mode I strain energy release rate
G_{Ic}	Plane strain, mode I critical strain energy release rate
G_{1c}	Plane stress, mode I critical strain energy release rate
g_0	Initial gap width for the 2-D gap/friction element in NISA

HAZ	Heat-affected zone
HEAT	Heat transfer module for NISA
H	Work hardening parameter
h	Convective heat transfer (film) coefficient
J	J-integral
ΔJ	J-integral range
ΔJ_n	Normalized J-integral range
K_n	Stiffness in the normal direction of the 2-D gap/friction element in NISA when the element is closed
K_t	Stiffness in the tangential direction of the 2-D gap/friction element in NISA when the element is closed
K	Stress intensity factor
K_c	Critical stress intensity factor or Fracture toughness
K_d	Maximum stress intensity factor at the current crack length $a_i = a_{OL} + a_d$
K_I	Mode I stress intensity factor
K_{max}, K_{min}	Maximum and minimum applied stress intensity factor of a given fatigue cycle
$K_{max,eff}$, $K_{min,eff}$	Effective maximum and minimum applied stress intensity factor of a given fatigue cycle
K_{OL}	Overload stress intensity factor
K_r	Maximum stress intensity factor at the current crack length, $a_i = a_{OL} + a_r$
K_{res}	Residual stress intensity factor
ΔK	Stress intensity factor range

$\overline{\Delta K}$	Equivalent stress intensity factor range in the Walker model
ΔK_{ac}	Accelerated stress intensity factor range in the modified Wheeler model
ΔK_{eff}	Effective stress intensity factor range
ΔK_i	Stress intensity factor range at the current crack length, a_i
ΔK_{OL}	Overload stress intensity factor range
ΔK_{th}	Threshold stress intensity factor range or Fatigue crack growth threshold
k	Thermal conductivity
L	Specimen length; Stiffener load concentration factor (Chapter 5)
MIG	Metal inert gas
m	Shaping exponent in the Wheeler model
m_{mod}	Shaping exponent in the modified Wheeler model
m_{org}	Shaping exponent in the original Wheeler model
NDT	Nil-ductility temperature
NISA	Numerical Integrated elements for System Analysis (commercial finite element code)
NKTP	Element type number for NISA
NRU	National Research Universal
NSERC	Natural Science and Engineering Research Council of Canada
N_a	Accelerated cycles
N_{CAL}	Number of elapsed cycles, corresponding to N_{OL} or N_{UL}, in a constant amplitude fatigue test

N_d	Delay cycles
N_{exp}	Number of cycles to propagate the crack from a_o to a_f observed in experiments
N_{mod}	Number of cycles to propagate the crack from a_o to a_f predicted by the modified Wheeler model
N_{OL}	Number of elapsed cycles measured between the overload and the last recorded crack length in an overload fatigue test
N_{org}	Number of cycles to propagate the crack from a_o to a_f predicted by the original Wheeler model
N_{UL}	Number of elapsed cycles measured between the underload and the last recorded crack length in an underload fatigue test
n	Curve fitting parameter for the Paris model; Component of the unit outward normal vector to the closed contour in defining the *J*-integral (Chapter 2); An integer (Chapter 5)
n_{OL}	Total number of overloads applied
OL	Overload
OL	Magnitude of a tensile overload
OLR	Overload ratio
PMMA	Polymethyl methacrylate
ΔP	Load range of a given fatigue cycle
P_{max}, P_{min}	Maximum and minimum load applied during a given fatigue cycle under constant amplitude loading
P_{OL}, P_{UL}	Maximum and minimum load applied during a tensile overload and compressive underload
P_s	Load carried by stiffened plate in front of crack tip
P_u	Load carried by unstiffened plate in front of crack tip

p	Attachment spacing (rivet pitch)
Q	Scattering vector
Q	Shear force in the most highly loaded fasteners
dQ/dT	Change in energy per unit change in temperature
q	Heat flux; Convective heat flux
R^2	Coefficient of determination for regression analysis
R	Stress ratio of a given fatigue cycle; Crack resistance (force) (Chapters 2 and 5)
R_a	Normalized accelerated cycles
R_d	Normalized delay cycles
R_{eff}	Effective stress ratio
RA	Reduction in area at fracture
r, θ	Polar coordinates with origin at the crack tip
r_d	Size of the effective delay zone
$r_{d,d}$	Size of the effective delay zone produced at the current crack length, $a_i = a_{OL} + a_d$
$r_{d,i}$	Size of the effective delay zone produced at the current crack length, a_i
$r_{d,OL}$	Size of the effective delay zone produced by an overload at a_{OL}
r_p	Size of the effective plastic zone
$r_{p,i}$	Size of the effective plastic zone produced at the current crack length, a_i
$r_{p,lim}$	Size of the effective plastic zone produced at a_{lim}

$r_{p,OL,lim}$	Size of the effective plastic zone produced by an overload at $a_{OL,lim}$
$r_{p,OL}$	Size of the effective plastic zone produced by an overload at a_{OL}
$r_{p,r}$	Size of the effective plastic zone produced at the current crack length, $a_i = a_{OL} + a_r$
S_n	Stiffness in the normal direction of the 2-D gap/friction element in NISA when the element is open
S_t	Stiffness in the tangential direction of the 2-D gap/friction element in NISA when the element is open
S	Stress on the panel
ds	An element of the closed contour in defining the J-integral
T	Pseudo-time
T	Temperature; Traction perpendicular to the closed contour in defining the J-integral (Chapter 2)
dT / dn	Temperature gradient
ΔT	Change in temperature
T_s	Temperature of the plate
T_{shift}	Shift in the nil-ductility temperature
T_∞	Temperature of the surrounding
t	Sheet thickness
UL	Underload
U	Strain energy
UL	Magnitude of a compressive underload
ULR	Underload ratio

u	Displacement component in defining the J-integral
v	Crack speed
v_s	Speed of sound in a material
W	Specimen width; Energy for crack formation (Chapter 2); Strain energy density in defining the J-integral (Chapter 2)
w, w'	Curve fitting parameters in the original and rewritten Walker model
x	Distance along bottom of finite element model
x/a	Normalized distance ahead of crack tip
Y	Geometric parameter
Y_s	Geometric parameter for a stiffened plate
Y_u	Geometric parameter for an unstiffened plate
y	Distance from the inner surface of the sheet to the centroid of a stringer
α	Effective plastic zone size constant; Coefficient of thermal expansion (Chapter 10)
β	Effective delay zone size constant; Hardening control parameter (Chapter 10)
ε	Strain
ε_f	Fracture ductility in the Zheng and Hirt model
$\dot{\varepsilon}$	Strain rate
$\{\varepsilon\}$	Strain vector
ϕ_D	Delay parameter in the modified Wheeler model
ϕ_I	Overload interaction parameter in the modified Wheeler model

$\phi_{min,i}$	Minimum value of the retardation parameter in the Wheeler model calculated from previous overloads at the current crack length, a_i
ϕ_R	Retardation parameter in the Wheeler model
γ	Stiffener efficiency factor
λ	Wavelength of neutron beam
μ	Coefficient of friction for the 2-D gap/friction element in NISA
μ	Coefficient of crack surface friction; Relative stiffness parameter (Chapter 5)
ν	Poisson ratio
θ	Angle of diffracted neutron beam (Chapters 5 and 10); Crack inclination angle (Chapter 8)
ρ	Specific density (Chapter 5); Radius of gyration of stringer (Chapter 5); Density (Chapter 10)
σ	Stress; Far-field applied stress; Far-field stress in a stiffener (Chapter 5)
$\Delta\sigma$	Stress range of a given fatigue cycle
σ_a	Stress amplitude of a given fatigue cycle
σ_c	Residual strength; Residual strength of a plain sheet (Chapter 5)
σ_{cs}	Residual strength in a stiffened panel; Residual strength of a stringer
σ_{cu}	Residual strength in an unstiffened panel
σ_f	Fracture strength in the Zheng and Hirt model
σ_{ff}	Critical fracture stress in the Zheng and Hirt model

σ_m	Mean stress of a given fatigue cycle
$\sigma_{\max}$, $\sigma_{\min}$	Maximum and minimum far-field applied stresses of a given fatigue cycle
σ_{op}	Crack opening stress of a given fatigue cycle
σ_{res}	Residual stress
$\sigma_{R,x}$, $\sigma_{R,y}$	Transverse and longitudinal residual stress
σ_s	Residual strength of a stiffened panel
σ_t	Total stress in a stiffener
σ_{ult}	Ultimate strength
σ_x, σ_y, σ_z	Stress in the transverse, longitudinal and normal directions
σ_{yld}	Yield strength
$\{\sigma\}$	Stress vector

Acknowledgements

I wish to express my appreciation to my supervisor, Dr. Farid Taheri, for his encouragement, guidance and support throughout the course of this study. I also wish to thank the members of my thesis supervisory committee, Dr. Jane Thorburn and Dr. Michael Gharghouri, and Dr. David Stredulinsky of Defence Research & Development Canada – Atlantic for their help and advice. The financial supports of Natural Science and Engineering Research Council of Canada and Defence Research & Development Canada – Atlantic are also gratefully acknowledged.

Special thanks are extended to Dr. David Stredulinsky and Mr. John Porter of the Halifax Dockyard for making available the steel plating required to perform the experimental investigation. Appreciation is extended to the Civil Engineering Department's technicians, Mr. Mark MacDonald and Mr. Blair Nickerson, and my colleagues, Phil Rushton, Richard Lewis, Khalid Shahin and Zhang Zheng, for their assistance in the fatigue testing at Dalhousie University. I am also grateful for the help in the neutron diffraction experiment from Dr. Michael Gharghouri, Dr. John Root, Dr. Ron Rogge and Mr. John Fox at the Canadian Neutron Beam Centre.

Finally, I would like to thank my mom, Bill Chow and the rest of my family for their support and patience throughout the course of this study.

Chapter 1 Introduction

1.1 Historical Perspective

In engineering, fatigue is defined as the decrease in strength of a material under repeated cycles of stress or strain. The cause of this loss in strength is due to the formation and propagation of micro-cracks at the stress concentrations of a member. At these stress concentrations, damage is accumulated since the localized cyclic stresses are much greater the average stress over the entire cross section. Fracture, which is the complete breakage of a structure, can then occur below the design stress if the crack is allowed to grow to a critical size under the repeated loading.

The discovery of fatigue occurred during the industrial revolution in the 1800's, which brought an increase in the use of metals in construction to take advantage of their strength and ductility. Throughout this period of time, fatigue was found to be responsible for the collapse of bridges and pressure vessels explosions on an almost daily basis, which happened suddenly and unexpectedly at stresses below their design strength, resulting in extensive property damage and loss of life.

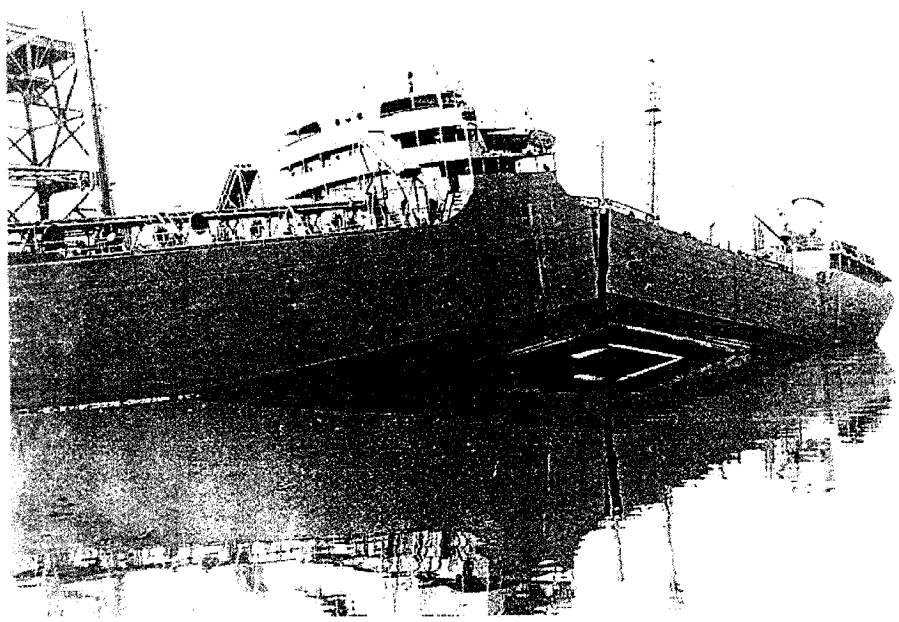

Figure 1-1 Fracture of the USS Schenectady at Pier in San Diego [1]

However, extensive research into this mode of failure was not undertaken until WWII, when, of the 2,500 Liberty cargo ships built by the United States, 145 broke in two and almost 700 experienced serious failures. These ships featured all-welded hulls, which were built much faster than the traditional rivet construction. These failures often occurred suddenly under conditions of low stresses, as shown in Figure 1-1 by the fracture of USS Schenectady while docked in the harbour. Numerous subsequent investigations revealed that the majority of fractures in the Liberty ships started at square hatch corners, where cracking was promoted by stress concentration due to the sharp geometry, poor welding practices and the use of low-toughness steel.

1.2 Motivation of Research

The cost of fracture is greater today as structures are more complex and are designed to carry higher loads. Nowadays, fatigue is a design issue for bridges, cranes, transmission towers, ships and airplanes which are under repeated loading in the form of traffic, impact, wave or wind loads. Due to the increased understanding of fatigue, it has since been included in various structural design codes. However, most of these approaches are based on the assumption that the applied stress range is constant, which neglects the load interaction effects in random loading that can either increase or decrease the fatigue life.

Defence Research & Development Canada (DRDC) – Atlantic has been assessing the probable behaviour of fatigue cracks in ship structure for a number of years. There are several fatigue crack propagation models available, each taking different approaches to model fatigue loading and the associated propagation. Selection of the most suitable model for the assessment of ship fatigue crack propagation is still challenging and at times, quite complex. This is due to the fact that ships are subjected to semi-random loading. During the past number of years, the suitability of several fatigue crack growth models for crack propagation in ship plating when subjected to constant amplitude and random loading was systematically investigated [2-6]. These previous investigations indicated a need to further study the parameters of a constant amplitude fatigue model and the influence of multiple tensile overloading and crack surface roughness. Therefore, the motivation for the present research was to continue the work of the previous

investigations to tackle the above issues and to initiate investigation on the fatigue of welded stiffened ship plating.

The main objective of the present work is the investigation into some of the load interaction effects in stiffened and unstiffened 350WT steel ship plating subjected to variable amplitude loading. The investigation included a number of fatigue scenarios that are commonly experienced in the life of ship plating. Specifically, the following issues and tasks were both experimentally and computationally investigated and accomplished in this thesis: 1) modification was proposed to a constant amplitude fatigue model; 2) modifications were proposed to a fatigue retardation model; 3) the "prying" effect of crack surface roughness during compressive underloading was computationally evaluated; 4) the fatigue behaviour of the steel when its ductility is reduced was experimentally simulated; and 5) the fatigue behaviour of welded stiffened steel plates was examined. The following sections provide a brief summary and motivation of each task.

1.2.1 Proposed Modification to a Constant Amplitude Fatigue Model

Many fatigue crack growth models, such as the well known Paris model [7], include empirical parameters that have no physical basis. Such models are material dependent which require calibrations from the fatigue testing of each different material. Fatigue testing is expensive and time-consuming; therefore it is desirable to employ fatigue models that have some physical significance by using known material properties from less lengthy tests. One such attempt is the Zheng and Hirt model [8], which does not require several fatigue tests to establish the empirical parameters required by most models. It relies on the tensile properties and the threshold value, thus making it a cost effective fatigue crack propagation methodology. The Zheng and Hirt model is moderately successful in predicting fatigue crack growth rates and a modification made to the model is presented in Chapter 6, which was shown to improve its accuracy.

1.2.2 Proposed Modifications to a Fatigue Retardation Model

The Wheeler retardation model [9] is one of the simplest and most widely employed [2-6, 10-22] models to quantify the fatigue crack growth retardation after a single overload, and it offers the most potential for modifications and improvements. The model is based on the interaction of the overload plastic zone and the current plastic zone. However, its simple formulation falls short of accounting for the initial crack growth acceleration, delay retardation, overload interaction and net section yielding effect. Therefore, a number of modifications to the Wheeler model were proposed in the present work to improve its accuracy in predicting fatigue crack growth, and retardation, including multiple overloading situations. In the present work, both single and multiple overloading fatigue tests were performed on 350WT steel specimens and the fatigue life predictions by the original and the modified Wheeler model were then compared in Chapter 7.

1.2.3 Investigation into the "Prying" Effect due to Crack Surface Roughness

In the investigation by Rushton [2], it was hypothesized that when a compressive underload is applied, instead of the crack tip asperities being flattened as the crack closes, the crack tip might instead be "pried" open as some of the more rigid asperities on the opposite mismatched crack surfaces make contact. This "prying" effect could possibly enhance the tensile plastic zone at the crack tip, reduce crack closure and cause additional fatigue crack growth acceleration following the compressive underload. In order to investigate this possibility, a parametric study by the finite element method was performed in the present work on centre-cracked steel plates to examine the effects of crack inclination angle, compressive underload, crack surface roughness and friction on the J-integral following the underload. It was assumed that the J-integral could be regarded as the driving force behind fatigue crack growth. The finite element models incorporated contact elements between the crack surfaces to simulate the "prying" and frictional forces at the crack tip. The model development and the results of this investigation are presented in Chapter 8.

1.2.4 Simulation of Reduced Ductility in Steel using PMMA

It is well-known in steel that due to load interaction effects, the fatigue crack growth is retarded after an application of tensile overload and is accelerated to a lesser degree after a compressive underload. This phenomenon is attributed to the formation of a relatively large zone of residual compressive or tensile stress in front of the crack tip after the application of the overload or underload respectively. Since the amount of crack growth retardation and acceleration is influenced by the amount of crack tip plastic deformation, it is then conceivable that the reduction in the ductility of steel caused by low temperature, high strain rate, high constraint and/or welding would decrease the overload and underload effects as well. In order to investigate this possibility, overloading and underloading fatigue tests were performed on centre-cracked polymethyl methacrylate (PMMA) specimens in the present work. PMMA is a semi-brittle glassy polymer which shows little reduction in area and elongation at fracture. In the present work, the effects of loading frequency, tensile overload and compressive underload on the fatigue crack propagation of PMMA were examined in Chapter 9.

1.2.5 Fatigue of Welded Stiffened Steel Plates

Typical stiffened sheet structures are metal sheets reinforced by stiffeners and are widely used in aircraft, ships and chemical industry structures for their light weight and high strength and stiffness. They are mostly found in the airframes, fuselages and wings of aircraft and the deck and side plating on a ship where the amount of fatigue loading is the greatest. Much research has been performed in the past to address fatigue crack growth in aircraft, with the studies made on aluminum panels that have either riveted or adhesive bonded stiffeners. On the other hand, relatively few studies [23-29] have been conducted on welded stiffeners that are often found in ship structures. The welding of the stiffeners induces complex residual stresses in the structure that are caused by the heating and cooling effects of welding. In general, the fatigue behaviour of welded stiffeners is not well understood and test data of welded stiffeners are limited. Nonetheless, the distribution of these residual stresses is recognized to have considerable influence on the fatigue crack growth rates of welded stiffened panel. However, experimental techniques for the determination of residual stresses have their disadvantages. Therefore, the

motivation of the present research was to investigate whether a finite element approach could provide an adequate alternative for evaluating the residual stresses and their influence on the fatigue of welded stiffened steel plates.

In the present investigation, the fatigue behaviour of welded stiffened centre-cracked 350WT steel plates was studied. The residual stress fields near the fatigue crack tips in the steel plates were derived using the neutron diffraction method, which is a versatile and nondestructive technique [30-50]. The residual stress intensity factors produced by the measured residual stress fields were then calculated using the Green's function in order to determine the effective stress intensity factors. The residual stress fields were also simulated by the finite element method, which consisted of heat transfer analysis followed by nonlinear static analysis. Following the residual stress simulation, the effective stress intensity factors were computed from fracture mechanics analysis. Finally, the fatigue crack growth rates of the stiffened plates were predicted using the effective stress intensity factors from both methods and compared to the experimental results from fatigue testing in Chapter 10.

1.3 Organization of Thesis

The remainder of this thesis is organized into 10 chapters. Chapters 2 to 5 provide the background information on the topics of fracture mechanics, fatigue, brittle fracture in steel and stiffened sheet structures, respectively. Chapters 6 to 10 present the experimental and numerical procedure, results and discussion of the above work. Chapter 11 contains the summary and conclusions drawn from the present work and recommendations for future research based on the present results.

Chapter 2 Fracture Mechanics

Fatigue and fracture are closely related in that fatigue is the accumulation of damage in a structure that leads to crack growth and eventually fracture if the crack is allowed to reach a critical size. Therefore the same parameters that control fracture also govern fatigue. Figure 2-1 shows the three general modes of loading that can cause crack growth. Mode I is the opening mode where the applied load is perpendicular to the crack surfaces. It is the most common mode of cracking and is the focus of the present investigation. There are also the sliding and tearing modes (mode II and III) caused by in-plane and out-of-plane shear respectively that are usually mixed with mode I loading in actual structures.

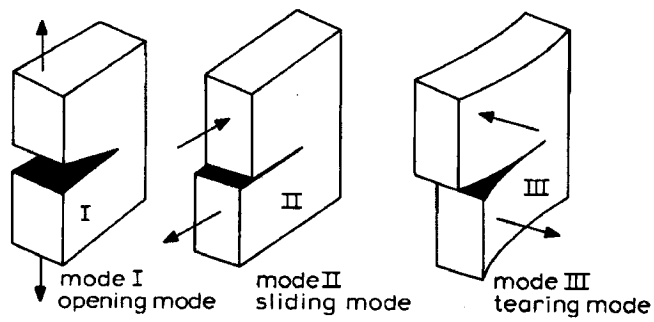

Figure 2-1 The three modes of cracking [51]

2.1 Strain Energy Release Rate

In 1920, Griffith [52] proposed an energy criterion for fracture based on the energy conservation law which can be stated as: crack growth can occur if the energy required to form an additional crack of size *da* can just be delivered by the system. The energy delivered by the system comes in forms of the release of the strain energy in the system and the work done by the external load on the system. The strain energy of a deformed body can be determined as the area under its load-displacement curve as shown in Figure 2-2. For a plate of unit thickness the Griffith energy criterion can be written in terms of the strain energy and the external work as:

$$\frac{d}{da}(U-F+W)=0 \text{ or } \frac{d}{da}(F-U)=\frac{dW}{da}, \tag{2-1}$$

where U is the strain energy contained in the plate, F is the work performed by the external force and W is the energy for crack formation. The "strain energy release rate" or the "crack extension force" is then defined as $G = d(F-U)/da$, and the crack resistance (force) $R = dW/da$. In other words, the strain energy release rate is the strain energy in the material which is available for producing crack extension. Also, although G and R are at times called forces, it should be noted that they are energy measurements and have the unit of energy per unit crack extension and per unit thickness. Griffith's theory states that fracture occurs when the strain energy release rate reaches the critical strain energy release rate, G_c, due to an unfavorable combination of load magnitude and crack size on the body. The value G_c depends on the specimen thickness but is a material constant under plane strain condition.

For mode I loading on a cracked plate, in which the load is perpendicular to the crack surfaces, the strain energy release rate can be shown to be equal to:

$$G_I = \frac{\pi\sigma^2 a}{E}, \tag{2-2}$$

where G_I is the mode I strain energy release rate, σ is the far-field applied stress, a is the length of an edge crack or half the length of a central crack, and E is the modulus of elasticity of the plate. The equations for the other loading modes (sliding mode and tearing mode) are similar and the total energy release rate in combined mode cracking is obtained by adding the energies from the different modes.

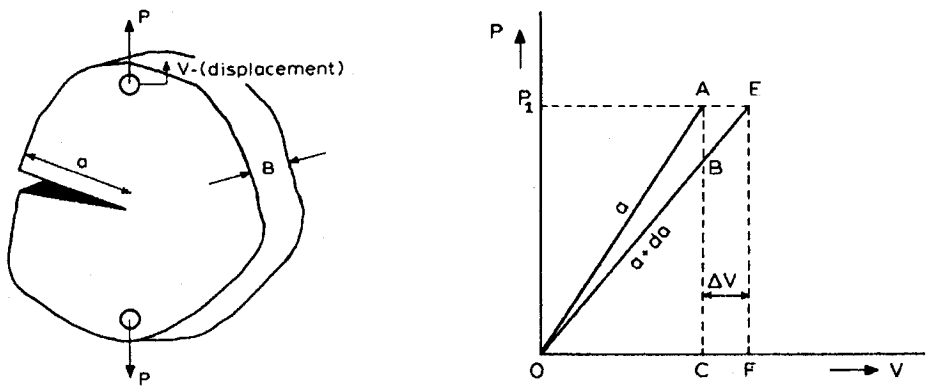

Figure 2-2 Loading on a cracked plate and the resulting load-displacement diagram [51]

2.2 Stress Intensity Factor

Although the fracture criterion is based on energy equilibrium, a stress-based fracture parameter called the stress intensity factor, K, is more commonly used in experimental and numerical analysis. The stress intensity factor is a measure of the severity of the crack in terms of the far-field applied stress, crack size, and specimen geometry. In other words, the crack tip stresses are proportional to the stress intensity factor, as shown in Equations 2-3 that are derived from the Westergaard [53] complex stress function. For two-dimensional mode I loading:

$$\begin{aligned}
\sigma_x &= \frac{K_I}{\sqrt{2\pi r}}\cos\frac{\theta}{2}\left[1-\sin\frac{\theta}{2}\sin\frac{3\theta}{2}\right]+\ldots \\
\sigma_y &= \frac{K_I}{\sqrt{2\pi r}}\cos\frac{\theta}{2}\left[1+\sin\frac{\theta}{2}\sin\frac{3\theta}{2}\right]+\ldots \\
\tau_{xy} &= \frac{K_I}{\sqrt{2\pi r}}\cos\frac{\theta}{2}\sin\frac{\theta}{2}\sin\frac{3\theta}{2}+\ldots \\
\sigma_z &= 0 \quad (\text{plane stress}) \\
\sigma_z &= \nu(\sigma_x+\sigma_y) \quad (\text{plane strain})
\end{aligned} \qquad (2\text{-}3)$$

In Equations 2-3, K_I denotes the mode I stress intensity factor, ν is the Poisson ratio, r and θ are the polar coordinates and the stresses are defined in Figure 2-3. K_I is turn given by the following:

$$K_I = Y\sigma\sqrt{\pi a}, \qquad (2\text{-}4)$$

where Y is a dimensionless geometric parameter that depends on factors such as the crack length to the specimen width ratio and the specimen length to width ratio. The values for Y for the most common crack geometry are available in various design handbooks. For an infinitely wide panel, Y is equal to 1.

Similar to the strain energy release rate, the fracture condition in terms of the stress intensity factor can be written as $K = K_c$, where K_c is the critical stress intensity factor. K_c is also a material constant under plane strain condition and it can be shown that G and K are related by the following equations:

$$G_I = \frac{K_I^{\,2}}{E} \quad (\text{plane stress})$$
$$G_I = (1-\nu^2)\frac{K_I^{\,2}}{E} \quad (\text{plane strain}) \tag{2-5}$$

Both G_c and K_c are measures of fracture toughness of a material and it can be seen that the stress criterion for fracture is the same as the energy criterion discussed in the previous section.

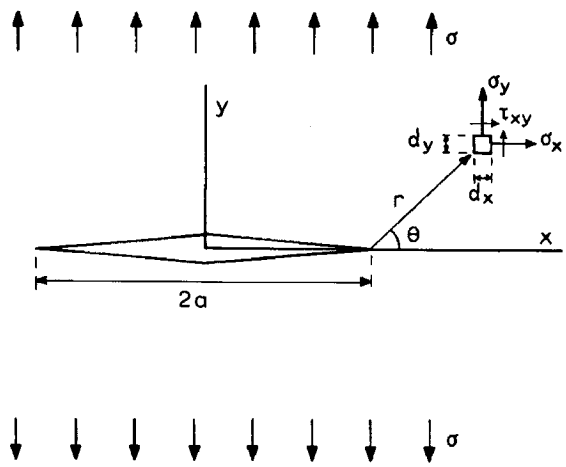

Figure 2-3 State of stress at crack tip [51]

2.3 J-Integral

For nonlinear elastic and elastic-plastic materials, the strain energy release rate in the energy criterion is replaced by the nonlinear energy release rate, *J*. In 1968, Rice [54] showed that *J* can be calculated from a path independent contour integral around the tip of a crack as:

$$J = \int_C \left(Wn - T\frac{\partial u}{\partial x} \right) ds, \tag{2-6}$$

where *C* is a closed contour as illustrated by Figure 2-4, *W* is the strain energy density, *T* is the traction perpendicular to *C*, *n* is the component of the unit outward normal vector to *C*, *u* is the displacement component and *ds* is an element of *C*. For a linear elastic material, the *J*-integral is equivalent to the strain energy release rate, *G*. It should be noted that the finite element method is well suited for calculating the *J*-integral by

providing the stress, strain and displacement values required in evaluating Equation 2-6. The value of the *J*-integral can then be substituted into Equation 2-5 in place of *G* to obtain an equivalent stress intensity factor.

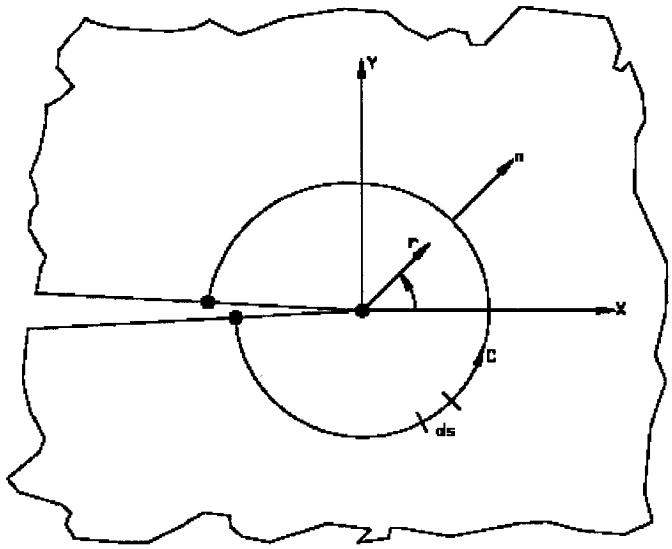

Figure 2-4 Definition of the *J*-integral [55]

2.4 Crack Resistance

It is stated in the last sections that fracture can occur when the strain energy release rate is equal to the critical value required for crack growth. For a truly brittle material like glass, this value is the energy required to form the new crack surfaces. This means the crack resistance is independent of crack length; R = constant G_c.

The situation in a ductile material like a metal is different. In addition to surface energy, in metals, plastic deformation occurs in front of the crack due to high stress concentration and during crack extension, energy is expended by the formation of a new plastic zone at the tip of the advanced crack. Experimentally, it appears that this plastic energy is approximately the same for every crack increment for plane strain cracks or when the material toughness is low. When the toughness is high, the R increases more steeply. This means under plane strain R is represented by a straight horizontal line $R = G_{Ic}$ when it is plotted against crack length. This is shown in Figure 2-5 where G_{Ic} is the critical strain release rate for the case of mode I loading and plane strain condition.

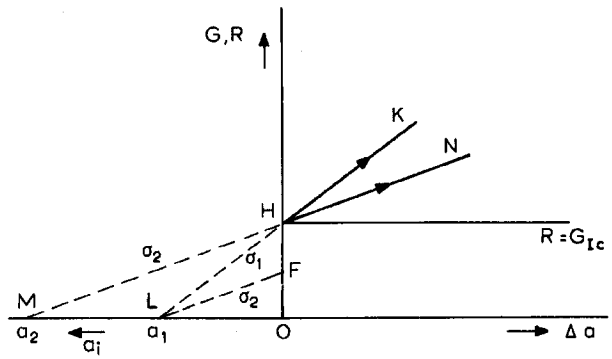

Figure 2-5 *R* curve under plane strain [51]

Figure 2-5 is a universal representation of the fracture criterion. The crack extension Δa is plotted on the right and the initial crack size a_i is on the left. Energy is plotted on the vertical axis. For plane strain condition, R is constant and is plotted as a straight horizontal line $R = G_{Ic}$. This curve represents the energy required for fracture and is referred to as an R curve. According to Equation 2-2, for a particular stress, σ, the energy release rate G is directly proportional to the crack size a. Thus G is represented by a straight line with a slope that is proportional to σ^2. These are shown in Figure 2-5 as lines LF and MHN at a stress of σ_2 and line LHK at a stress of σ_1, where $\sigma_1 > \sigma_2$. Note that line LHK has a steeper slope as a result of greater stress.

The fracture criterion can then be interpreted from the graph as follows: By loading the crack a_1 from zero stress to σ_2, its G value increases from O to F. Fracture does not occur since $F < G_{Ic}$. Further increase of the stress to σ_1 raises G to the point H. Fracture then occurs as $G = G_{Ic}$ and remains greater than G_{Ic} as the crack grows. For larger initial crack size, at a_2, G_{Ic} is reached (and thus fracture occurs) at a lower stress of σ_2. Note that LF and MHK are parallel since they are at the same stress.

It should be noted that G is a straight line only for an infinite plate containing a crack. For any other loading conditions or specimen geometry, G could either increase or decrease during crack growth. For example, at the onset of crack extension, G values are the same in the cracked plate under either load controlled or displacement controlled loading. However, during crack growth the stress drops under displacement controlled

loading, resulting in a decreasing G curve that curves downwards. Furthermore, for a cracked finite panel, the finite width correction can be applied to G giving a G curve that curves upward instead of being straight. For a small crack, the width correction can be neglected and the G curve is approximately straight. For longer cracks the curvature becomes larger and larger. The implication of the shape of the G curve on crack arrest is presented in Chapter 5.

The R curve for plane strain condition has been discussed. In reality, the fracture of thin structures such as ship plates occurs between plane strain and plane stress condition. In the case of plane stress, the crack resistance has been shown by experiments to vary with the amount of crack growth. Thin plates under plane stress show a steep, rising R curve as shown in Figure 2-6. The R curve starts at zero since the energy required for crack initiation by growth and coalescence of microvoids is presumably small in comparison with the plastic energy for crack growth in a ductile material. This means crack growth can occur at any stress different from zero. However, in reality, crack growth does not occur until G reaches a value of B in Figure 2-6 because of an important point about the energy criterion: The energy criterion is a necessary condition for crack growth, but not a sufficient condition. Crack growth does not occur until the stresses and strains at the crack tip are high enough such that the material is ready to separate.

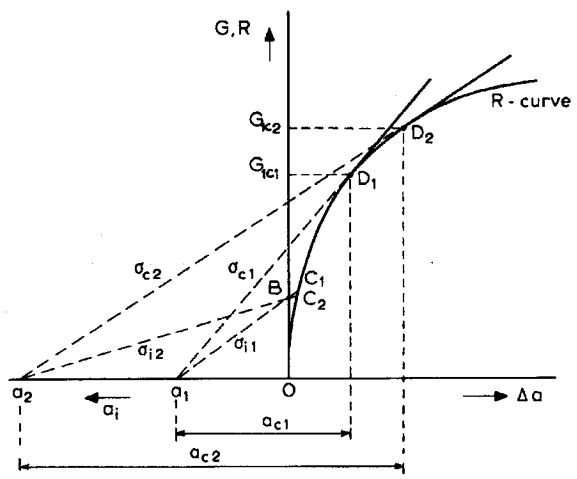

Figure 2-6 R curve under plane stress [51]

According to Figure 2-6, a crack of initial size a_1 reaches a G value of B at a stress of σ_{i1}. At this point the crack is suddenly extended until G reaches C_1. Further crack growth does not occur after the sudden crack extension at stress σ_{i1} since further crack growth would result in $G < R$. This first discrete crack extension is called pop-in because it is a sudden metastable crack extension, which is often associated with an audible click. Further increase in stress is required for further crack growth along the R curve until $G = G_{1c1}$ at $\Delta a = D_1$. At point D_1, G remains larger than R as Δa increases. Thus final fracture occurs at D_1. At this point the G curve is tangent to the R curve. The criterion for fracture under plane stress can then be written as:

$$\frac{\partial G}{\partial a} = \frac{\partial R}{\partial a}; \quad G = R. \tag{2-7}$$

In summary there is a constant critical strain energy release rate G_{Ic} under plane strain condition. Rapid fracture occurs when this value is reached. In contrast, the critical strain energy release rate under plane stress condition, G_{1c}, depends upon crack size and its value increases with crack size. This can be seen in Figure 2-6 where an initial crack size of a_2 fails at a higher $G = G_{1c2}$. In addition, under plane stress condition, there is a period of slow crack growth before the rapid fracture that occurs at $G = G_{1c}$. It should be emphasized that this period of crack growth occurs as the applied stress approaches the fracture stress and should not be confused with crack growth during normal service loading that is caused by, for example, fatigue or stress corrosion.

2.5 Residual Strength

The strength of a material is the highest when no flaws are present in the material. However, due to stress concentration, the presence of crack in a material decreases its strength. The strength of a cracked material is called its residual strength, σ_c, and it decreases progressively with increasing crack size. Fracture can occur if the residual strength of the material is exceeded. Therefore a structure that is initially safe under normal service load may be susceptible to fracture in the long run as cracks may initiate and grow in the structure to the size that makes the residual strength of the material less

than the normal service load. Such a crack is said to have reached a critical size and the structure should be repaired or replaced before the crack becomes critical.

A residual strength diagram is a plot of the residual strength of a material against the crack length. The critical crack size for a certain service load can then be determined from this diagram. Knowing the fracture toughness of a material, K_c, its residual strength diagram can be obtained from Equation 2-4, namely $\sigma_c = K_c/\sqrt{\pi a}$ with $Y = 1$ for simplicity. This has been done for three metals as shown in Figure 2-7. Clearly the material with the highest fracture toughness has the highest residual strength.

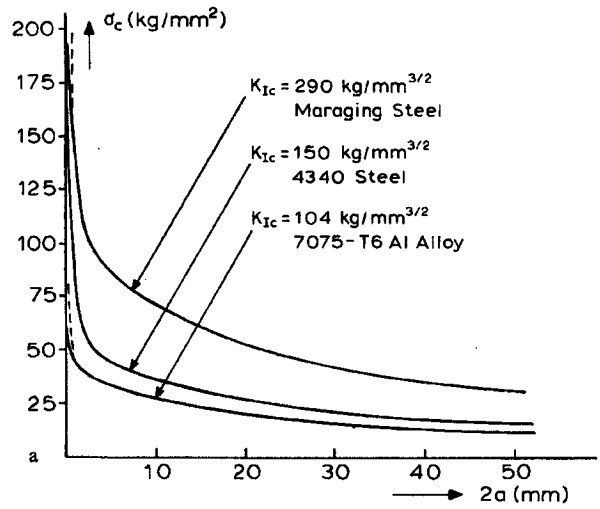

Figure 2-7 Residual strength diagram of three metals [51]

Although the residual strength diagram in Figure 2-7 is simple to construct, it suffers from two deficiencies. First, the residual strength of a material should approach the ultimate fracture strength of the material as the crack length, *a*, approaches zero, and not to infinity as suggested by the equation. Second, for a finite width panel, the residual strength should approach zero as the crack length approaches the width of the panel, *W*. To better represent the realistic behaviour, Feddersen [56] has proposed a technique that is based on displaying test data. The technique calls for drawing a straight line from the point $\sigma_c = \sigma_{yld}$, the yield strength of the material, tangent to a point on the curve based on the equation. Another tangent line is drawn from the point $2a = W$ to the curve. It

turns out that the tangent lines intersect the curve at $\sigma_c = 2/3\sigma_{yld}$ and $2a = W/3$ as shown in Figure 2-8. The residual strength diagram for an unstiffened panel can be constructed in this manner and provides a basis for the stiffened residual strength diagram.

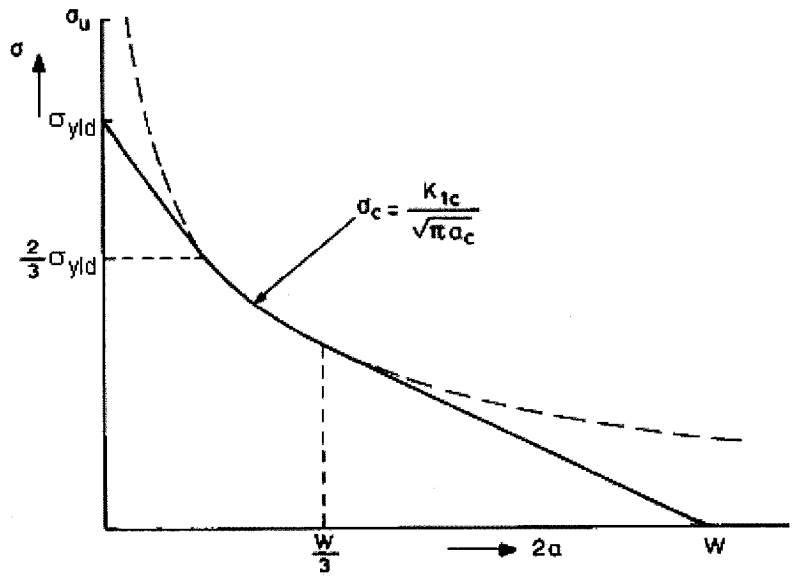

Figure 2-8 Method of Feddersen for constructing residual strength diagram [51]

2.6 Crack Tip Plastic Zone

When a cracked body is being loaded, Equations 2-3 predicts the stresses at the tip of a sharp crack to be infinitely large based on the theory of elasticity. Realistically, the crack tip becomes blunted upon loading. In addition, for a ductile material like steel, since the theoretical crack tip stresses exceed the yield strength of the material, a zone of plastically deformed material is formed ahead of the crack tip as shown in Figure 2-9. By substituting the yield strength into Equations 2-3 and then further accounting for the reduced load carrying capacity at the crack tip, Irwin's [57] estimated the size of this plastic zone is obtained as:

$$r_p = 2r_{o\sigma} = \frac{1}{\pi}\left(\frac{K}{\sigma_{yld}}\right)^2, \tag{2-8}$$

where K is the applied stress intensity factor and σ_{yld} is the yield strength of the material.

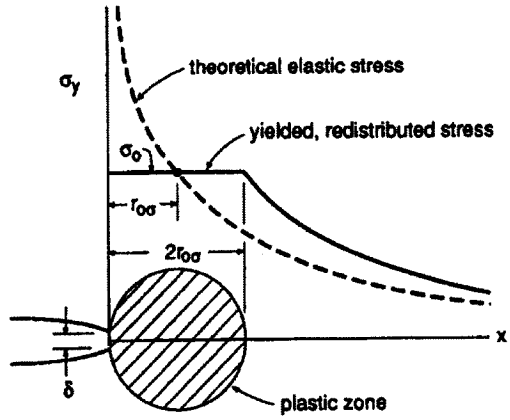

Figure 2-9 Stress distribution at the crack tip under tensile loading [58]

If the load applied to the cracked body is tensile, then the total elastic and plastic strain within the plastic zone becomes larger than the elastic strain of the surrounding material. During unloading, the surrounding elastic material acts like a spring that clamps the residual strain within the plastic zone and exerts compressive forces on the zone as shown in Figure 2-10. As a result, reversed yielding occurs and a zone of compressive residual stress ahead of the crack tip is created after unloading from tensile applied stress.

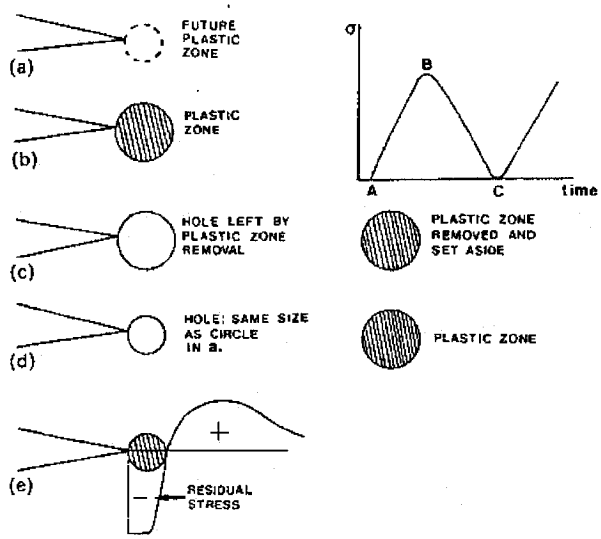

Figure 2-10 Residual stress at crack tip: (a) Load at A; (b) Load at B; (c) Load at B; plastic zone removed; (d) Load at C; plastic zone still out; (e) Load at C; plastic zone back in [59]

Similarly, a zone of tensile residual stress forms ahead of the crack tip after the cracked body is unloaded from a compressive applied stress. However, since the crack closes under compressive applied stress, the deformation at the crack tip has a more limited range, compared to the case of tensile applied stress. As a result, the stress concentration at the crack tip from a compressive applied stress is less severe. Therefore, the tensile plastic zone following compressive applied stress is less extensive than the compressive plastic zone following tensile applied stress.

Finally, the plastic zone can also be referred to as the load interaction zone since the residual stress interferes with the applied stress to the crack tip. The interference of the residual stress with the applied stress is known to have a significant effect on the fatigue crack growth rates of the structure in variable amplitude loading as will be discussed in the next chapter.

Chapter 3 Fatigue

3.1 Fatigue Loading

Fatigue crack growth in a structure is caused by repeated cycles of loading where the stress intensity factor of the crack remains below the fracture toughness of the material or the net section stress does not exceed the fracture strength of the material until the point of failure. Basically, the type of fatigue loading can be classified as either being constant amplitude or variable amplitude.

3.1.1 Constant Amplitude Loading

Constant amplitude loading is the simplest form of fatigue loading, consisting of the cycling between some constant maximum and minimum stress levels, $\sigma_{\max}$ and $\sigma_{\min}$. Other parameters, shown in Figure 3-1, that can be used to specify constant amplitude loading includes the mean stress ($\sigma_m = (\sigma_{max} + \sigma_{min})/2$), stress amplitude ($\sigma_a = (\sigma_{\max} - \sigma_{\min})/2$), stress range ($\Delta\sigma = \sigma_{max} - \sigma_{min}$) and stress ratio ($R = \sigma_{min}/\sigma_{max}$). Although constant amplitude loading is simple to describe, its occurrence in engineering structures is uncommon and is limited mainly to rotating machinery and piping components.

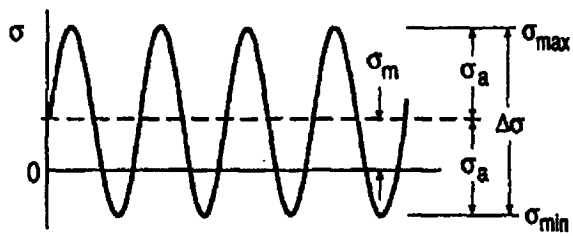

Figure 3-1 Constant amplitude loading [58]

3.1.2 Variable Amplitude Loading

Variable amplitude loading, which consists of load cycles of different stress amplitudes that can either be repeated, semi-random or completely random as shown in Figure 3-2, is the predominant type of fatigue loading on a structure. For example, the

fatigue loading on ships and offshore structures can be considered semi-random in nature as severe loading in their load-time histories appears in clusters (storms) rather than being completely randomly distributed. The different stress amplitudes in a variable amplitude loading spectrum produce different sizes of plastic zone ahead of the crack tip, which can introduce load interaction effects that cause the fatigue crack growth rates to deviate from the constant amplitude loading values.

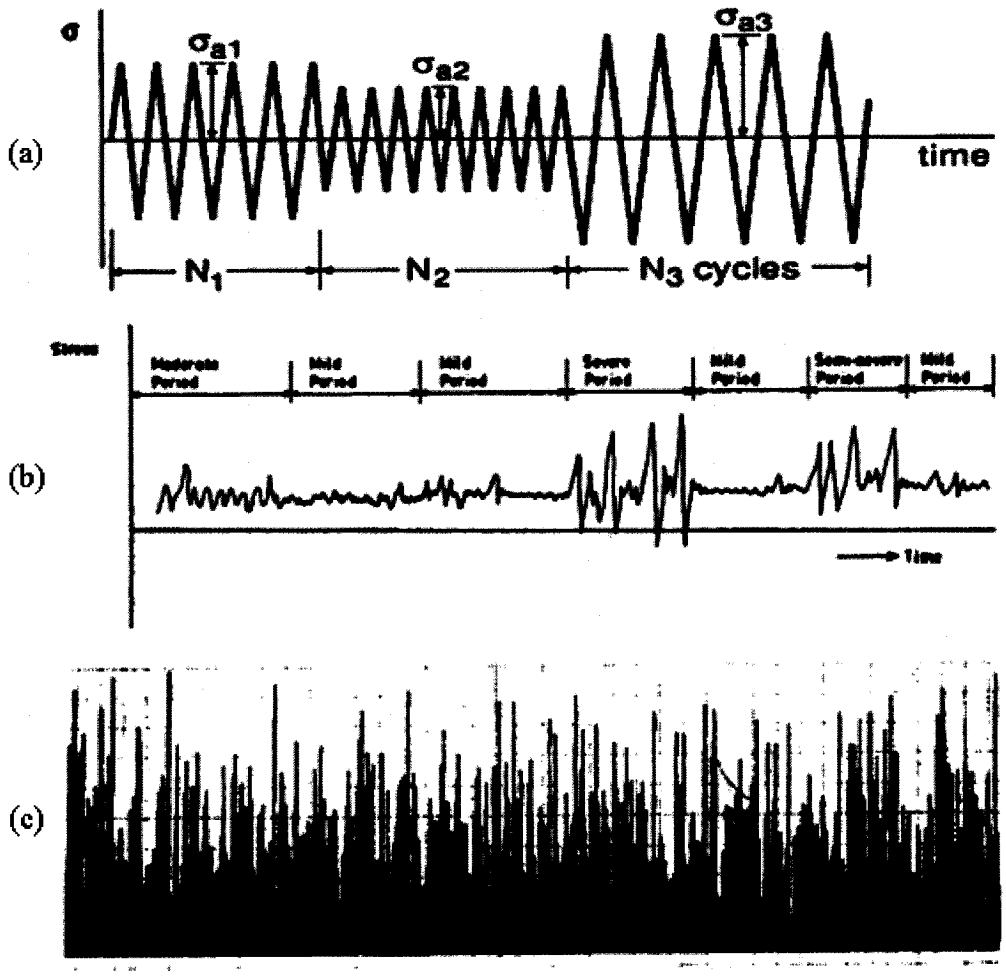

Figure 3-2 Variable amplitude fatigue loading: (a) Repeated [58]; (b) Semi-random [51]; and (c) Completely random [1]

3.2 Load Interaction Effects

Since the amplitudes of the load cycles are random in variable amplitude loading, it gives rise to load cycles that have significantly higher maximum load, P_{OL}, or lower

minimum load, P_{UL}, than the subsequent cycles, as shown in Figure 3-3. The type of peak load is generally classified as either a tensile overload (OL) if P_{OL} is tensile, or conversely a compressive underload (UL) if P_{UL} is compressive. In addition, the overload and underload are usually specified by their corresponding overload ratio (OLR) and the underload ratio (ULR). In the present work, OLR and ULR are defined as $OLR = OL/\Delta P$ and $ULR = UL/\Delta P$ respectively, where ΔP is the range of the subsequent load cycles as shown in Figure 3-3. In general, these peak loads in variable amplitude loading produce the so-called load interaction effects that affect fatigue crack growth rates following the peak loads by altering the residual stress state in front of the crack tip, the degree of crack closure and the amount of crack tip tunneling, blunting, branching and strain hardening in the subsequent fatigue cycles.

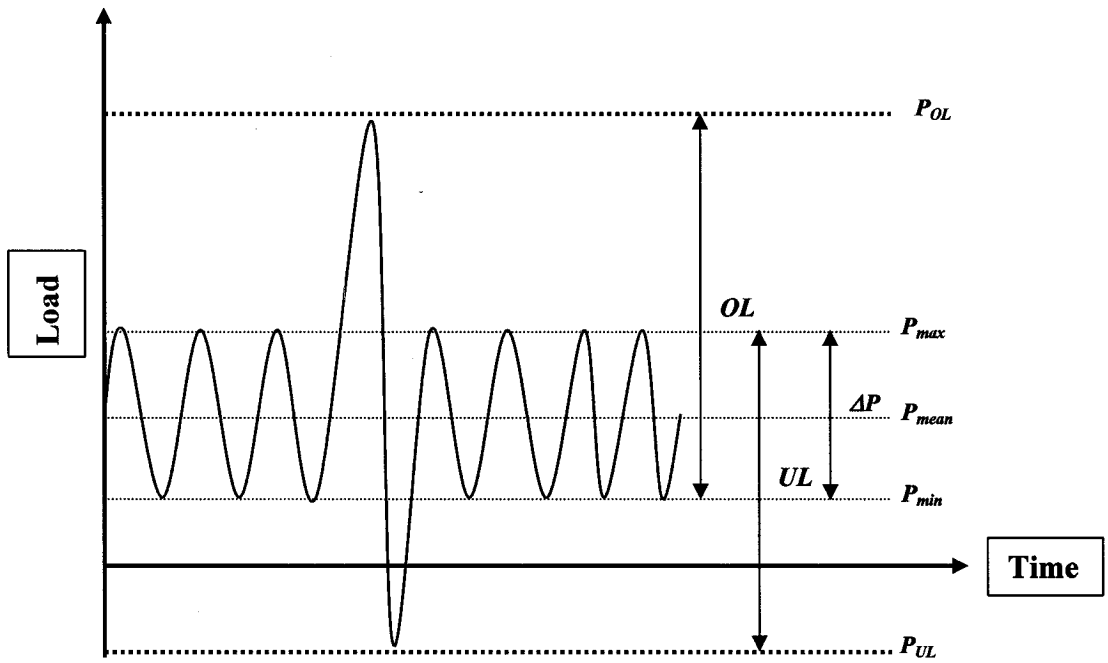

Figure 3-3 Schematic representation of overload and underload terms [2]

3.2.1 Crack Closure

The crack closure concept was proposed by Elber [60] to account for the effects of load interaction as well as stress ratio and to estimate the fatigue crack growth rates under variable amplitude loading. Crack closure may result from a number of causes

including those induced by: (a) compressive residual stresses at the crack tip, (b) rough fracture surfaces, (c) oxide debris on crack surfaces and (d) phase transformations, as illustrated in Figure 3-4.

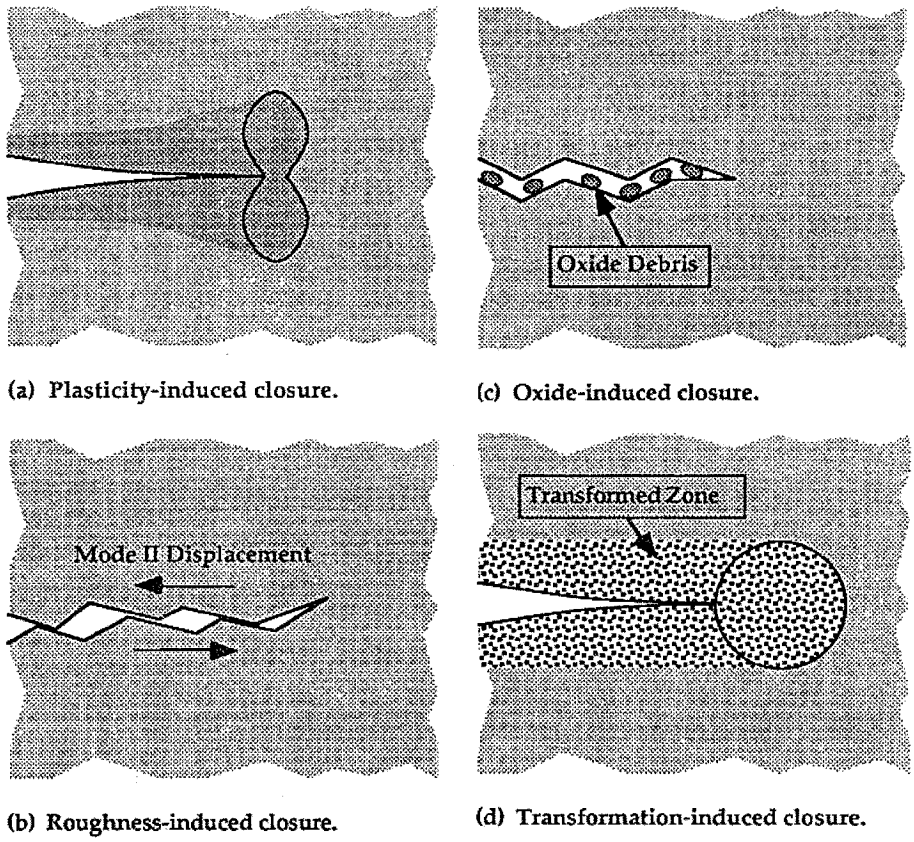

Figure 3-4 Schematic illustration of roughness-induced crack closure [61]

Crack closure refers to the fact that during the initial part of a fatigue cycle, the crack tip is found to remain closed while the crack behind the tip region is already open. As the crack cannot propagate while it is closed at the crack tip, the crack closure phenomenon reduces the load amplitude that is actually experienced by the crack tip and leaves the initial part of the fatigue cycle ineffective in propagating the crack. Thus, only a portion of a fatigue cycle is responsible for the extension of fatigue cracks as a result of crack closure. The stress at which the crack becomes fully opened is commonly called the crack opening stress, σ_{op}. The crack opening stress is found to decrease with increasing stress ratio, R, of the fatigue cycle and with increasing crack growth rates.

Furthermore, the crack opening stress level can be altered by the load interaction effects caused by the peak loads in variable amplitude loading to cause deviations in the fatigue crack growth rates as described in the next two sections.

One of the most studied crack closure mechanisms, the roughness-induced crack closure, was first identified by Walker and Beevers [62]. In many materials, the crack surface is not flat as the crack advance is influenced by crystallographic slip or encounters with microstructural barriers and the crack follows the weakest path in the material to propagate, resulting in a serrated or zig-zag fracture path as schematically shown in Figure 3-4 (b) and illustrated by the typical crack profile in Figure 3-5. Roughness-induced crack closure is attributed to this deflection of crack path as the asperities (roughness) on opposite crack faces come into early contact and interlock, resulting in compressive residual stress that reduce the crack-tip driving force.

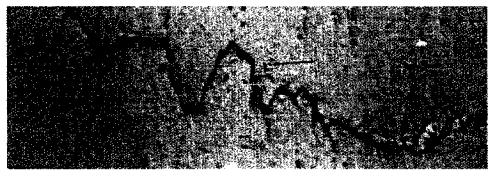

Figure 3-5 Typical fatigue crack profile [63]

Roughness-induced crack closure plays a particularly important role in crack growth process at the initial stages of crack growth when the stress intensity factor range and the crack growth rate is low and predominantly in plain strain condition, where the crack surface is very rough and the plastic zone size is negligible. However, as the crack grows, the roughness will decrease and the crack closure mechanism will be dominated by the compressive plastic zone at the crack tip (plasticity-induced crack closure).

Crack surface roughness is found to significantly alter both fracture loads and the direction of crack propagation. In addition, the rougher crack surface resulted in the higher crack opening point. A number of studies have shown that roughness-induced crack closure level is increased with increasing the degree and the variation of the angle of crack path deflection and increasing the asperity height and density [64-74]. Furthermore, asperities nearest to the crack tip were found to have the largest contributions to crack closure while the influence of crack surface roughness is smaller as

the distance from the crack tip increased [65, 70, 75-76]. Finally, although studies on the contribution of crack surface friction have been limited, it was found that part of the input energy to the crack was consumed in resisting the friction along the crack contact surfaces. In other words, friction tended to shield the crack tip from applied load, and thus retarded the development of plasticity, increased crack closure and decreased the crack tip stress intensity factor [72, 77-82].

3.2.2 Tensile Overload

According to Equation 2-8, the size of the crack tip plastic zone is a function of the applied stress intensity factor, or applied stress. Thus, in the event of a tensile overload, a more extensive and larger zone of compressive residual stress is created ahead of the crack tip. As the crack advances through the zone in the subsequent fatigue cycles, the compressive residual stress causes an increased degree of crack closure and crack opening load level, contributing to the well-known and most significant load interaction effects of fatigue crack growth retardation in the subsequent fatigue cycles following a tensile overload. In addition, the magnitude and duration of the retardation effects generally increase with increasing overload ratio as the size of the crack tip plastic zone is directly related to the stress level. In fact, crack growth is shown to be arrested at sufficiently large overloads. Finally, the amount of retardation is often quantified in terms of the delay cycles, N_d, which is the additional number of loading cycles a specimen can endure due to overload retardation compared to the fatigue life of the specimen under constant amplitude loading only.

Figure 3-6 plots a typical crack growth rate curve showing retardation following a single tensile overload. For a number of materials, it has been observed that an initial acceleration of the fatigue crack growth rate occurs immediately after an overload. The occurrence of the initial acceleration is postulated to be due to the blunting of the initially sharp crack plastically, which leaves the crack open for a distance behind the tip and thereby reducing the degree of crack closure and increasing the portion of the stress intensity factor that is effective at the crack tip. After the initial acceleration, the crack growth rate decelerates to a minimum value at some point ahead of the overload application, a_d, at which point the rate gradually returns to its steady state value at a_r as

the crack propagates through the region of residual compressive stress. This phenomenon is also known as "delay retardation" [10, 83-85].

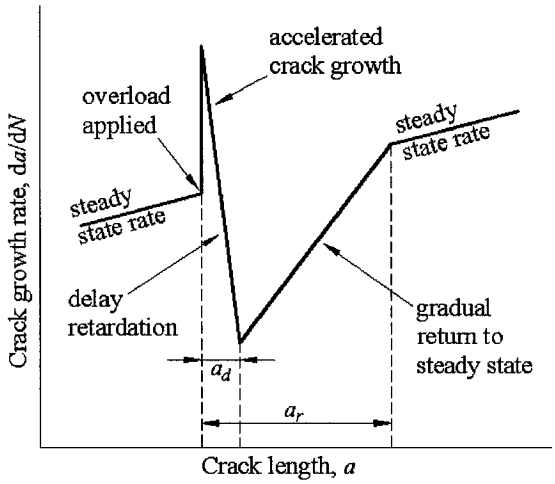

Figure 3-6 Schematic crack growth rate curve showing delayed retardation following tensile overload

In the case when multiple tensile overloads are applied, the overloads may interact with each other to either enhance or reduce to overall crack growth retardation if they occur close to each other. Such overload interaction is dependent on the relative magnitude and the spacing between the overloads [11, 76, 86-89], or the frequency of the overload application [90-94]. In other words, the overall crack growth retardation may be maximized by applying overloads at certain distances apart or at certain frequencies. On the other hand, due to the aforementioned initial crack growth acceleration immediately following an overload, overloads that are applied too closely or too frequently can lead to decreased overall crack growth retardation or even crack growth acceleration.

Finally, as will be described in Chapter 7, it was observed in the present work that crack growth retardation is reduced in the latter stage of the fatigue life. In other words, the crack growth rates return to the steady state values following a tensile overload sooner than expected when the net section stress of the specimen approaches the yield strength of the material.

3.2.3 Compressive Underload

As one might expect, a compressive underload in the loading spectrum produces the opposite effect to a tensile overload in which the fatigue crack growth is accelerated rather than retarded in the subsequent fatigue cycles following the underload. However, the crack growth acceleration phenomenon is much less pronounced and does not last as long as that of crack growth retardation. As a result, much less emphasis has been placed on the effect of compressive underloads. Nonetheless, non-conservative estimates of fatigue lifetimes may be produced by inappropriately overlooking the compressive underloads in fatigue data.

A compressive underload creates a zone of tensile residual stress ahead of the crack tip and flattens the crack tip asperities as the crack closes under the compressive stress. As a result, the contribution from crack closure is reduced and the effectiveness of the stress intensity factor at the crack tip is increased [76, 83, 95-106]. The crack growth rates in the subsequent fatigue cycles immediately following the underload are then accelerated and the rates gradually return to the steady-state level as the crack grows and crack surface roughness again develops until the influence of the underload is eliminated. In addition, the amount of crack growth acceleration generally increases with the underload ratio and with more frequent application of the underload. Finally, a compressive underload tends to erase some of the retardation caused by a tensile overload. Specifically, an underload immediately following an overload is found to reduce the amount of subsequent fatigue crack growth retardation. However, an underload immediately preceding an overload causes less reduction in the retardation effect.

In the investigation by Rushton [2], it was hypothesized that when a compressive underload is applied, instead of the crack tip asperities being flattened as the crack closes, the crack tip might instead be "pried" open as some of the more rigid asperities on the opposite mismatched crack surfaces make contact, as illustrated in Figure 3-7. This "prying" effect could possibly enhance the tensile plastic zone at the crack tip, reduce crack closure and cause additional fatigue crack growth acceleration following the compressive underload. In order to investigate this possibility, a parametric study by the finite element method was performed in the present work on centre-cracked steel plates

to examine the effects of crack inclination angle, compressive underload, crack surface roughness and friction on the *J*-integral following the underload. It was assumed that the *J*-integral could be regarded as the driving force behind fatigue crack growth. The finite element models incorporated contact elements between the crack surfaces to simulate the "prying" and frictional forces at the crack tip. The model development and the results of this investigation are presented in Chapter 8.

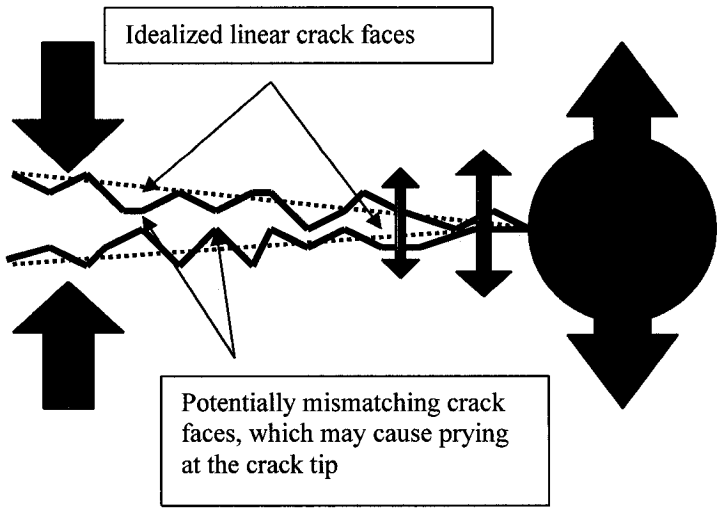

Figure 3-7 Schematic representation of potential crack tip prying under compressive underloads due to mismatched crack faces [2]

3.3 Fatigue Rate Curve

In order to study the fatigue behaviour of a material, testing should be done in an environment closely approximating the service conditions. The fatigue data can then be presented as a fatigue rate curve, which is a plot of the crack growth rate, da/dN, against the stress intensity factor range, ΔK, corresponding to the crack growth rate at the time. It should be noted that this curve has the advantage of being independent of the specimen geometry. This means that the crack growth rate of different specimens can be obtained from the same curve by calculating the stress intensity factor range associated with each specimen's geometry. Figure 3-8 shows a typical fatigue rate curve for a specimen under constant amplitude loading. The curve can be divided into three regions.

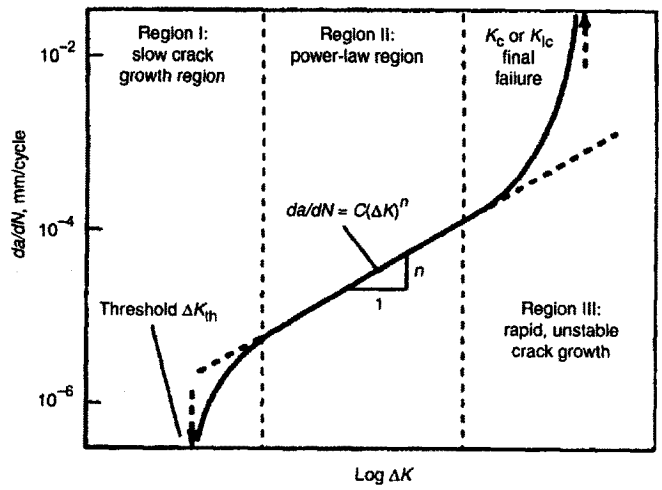

Figure 3-8 Typical shape of a fatigue rate curve [107]

Region I is the slow crack growth region representing the early growth and development of a fatigue crack. The most significant feature in this region is the threshold stress intensity factor range, ΔK_{th}, where no crack growth occurs if the applied stress intensity factor range is below this value. Region II represents a stable crack growth region that is characterized by a linear relationship between crack growth rate and stress intensity factor range on a log-log graph. In other words, the relationship can be described by a power law. Finally Region III corresponds to rapid and unstable fatigue crack growth as the maximum applied stress intensity factor, $K_{\max}$, approaches the fracture toughness, K_c, of the material. The study of fatigue in Region III is not as significant since most of the fatigue life is consumed in Region I and II.

3.4 Fatigue Models

Many models are available to describe the fatigue behaviour of a material under both constant and variable amplitude loading. However, due to the empirical nature of many of these fatigue models, a model that works for a particular fatigue scenario might not be suitable for another situation. Therefore, the preferred fatigue models are the ones that have the fewest empirical parameters in their formulations. Nonetheless, the stress intensity factor range, ΔK, and the stress ratio, R, of the fatigue loading are found to be the principle factors governing the crack growth rates. For the material employed in the

present work, 350WT steel, the following four fatigue models were used to describe its fatigue behaviour in the present work.

3.4.1 Paris Model

The Paris model [7] is one of the simplest and the most commonly used fatigue models for constant amplitude loading. The model, given by Equation 3-1, is essentially a power function that describes Region II of the fatigue rate curve with two curve fitting parameters, C and n:

$$\frac{da}{dN} = C(\Delta K)^n, \tag{3-1}$$

where C is the intercept and n is the slope of the fatigue rate curve in Region II. The drawback of this model is that the two parameters have no physical significance other than being the values that best fit the fatigue data. Furthermore, the values of the two parameters are dependent on the stress ratio of the fatigue loading. For a number of materials, such as 350WT steel, the fatigue crack growth rate is found to increase with the stress ratio. Therefore, one should ensure that the parameters are applicable to the stress ratio of the current situation when using the Paris model.

3.4.2 Walker Model

In 1970, Walker [108] proposed a new parameter, $\overline{\Delta K}$, to account for aforementioned the stress ratio effect experienced by many materials in a fatigue situation. The parameter $\overline{\Delta K}$ represents the equivalent stress intensity factor range at $R = 0$ that causes the same fatigue crack growth rate at all other stress ratios. It is defined as a function of the maximum applied stress intensity factor, K_{max}, the stress ratio, R, and a curve fitting parameter, w:

$$\overline{\Delta K} = K_{max}(1-R)^w. \tag{3-2}$$

From the relationships defined in Section 3.1.1, K_{max} can be written as:

$$K_{max} = \frac{\Delta K}{(1-R)}. \tag{3-3}$$

Thus Equation 3-2 becomes:

$$\overline{\Delta K} = \frac{\Delta K}{(1-R)^{1-w}}, \tag{3-4}$$

Finally, Walker substituted $\overline{\Delta K}$ in place of ΔK in the Paris model to arrive at the following equation:

$$\frac{da}{dN} = C\left(\overline{\Delta K}\right)^n = C\left[\frac{\Delta K}{(1-R)^{1-w}}\right]^n. \tag{3-5}$$

The Walker model can also be written as:

$$\frac{da}{dN} = C(1-R)^{w'}(\Delta K)^n, \tag{3-6}$$

where $w' = n(w-1)$.

It can be seen that the Walker model assumes that the fatigue rate curves at all stress ratios have the same slope n and the stress ratio effect is represented by the shift the in the intercept C by the function $(1-R)^{w'}$. Thus, the curve fitting parameter, w', in the intercept shifting function can be obtained from the plot of C versus $(1-R)$. To summarize, the Walker model is a modification of the Paris model that accounts for the stress ratio effect in constant amplitude loading at the expense of introducing a third curve fitting parameter. However, it should be noted that the intercept shifting function in the Walker model is arbitrarily defined. Therefore, it may not be capable of adequately describing the stress ratio effect in every material.

3.4.3 Zheng and Hirt Model

The Zheng and Hirt model [8] is a constant amplitude loading fatigue model for metals. It is itself a modification of the static fracture model proposed by Lal and Weiss [109], which assumes that the crack growth per loading cycle is equal to the distance in which the maximum normal stress, σ, is greater than the critical fracture stress σ_{ff} of the metal, as shown in Figure 3-9. From this assumption, the following equation can be derived from linear elastic fracture mechanics:

$$\frac{da}{dN} = B\Delta K_{eff}^2 = \frac{1}{2\pi\sigma_{ff}^2}(\Delta K - \Delta K_{th})^2, \tag{3-7}$$

where $B = \frac{1}{2\pi\sigma_{ff}^2}$, $\Delta K_{eff} = \Delta K - \Delta K_{th}$, da/dN is the crack growth per cycle, ΔK is the applied stress intensity factor range and ΔK_{th} is the fatigue crack growth threshold. The critical fracture stress σ_{ff} is in turn taken as the theoretical strength of metallic materials:

$$\sigma_{ff} = \sqrt{E\sigma_f \varepsilon_f}, \tag{3-8}$$

where E is the modulus of elasticity and σ_f and ε_f are the material's fracture strength and fracture ductility, respectively. The fracture strength and fracture ductility are given in [110] as:

$$\sigma_f = \sigma_{ult}(1 + RA), \tag{3-9}$$

$$\varepsilon_f = -\ln(1 - RA), \tag{3-10}$$

where σ_{ult} is the ultimate strength and RA is the reduction in area at fracture in a tension test.

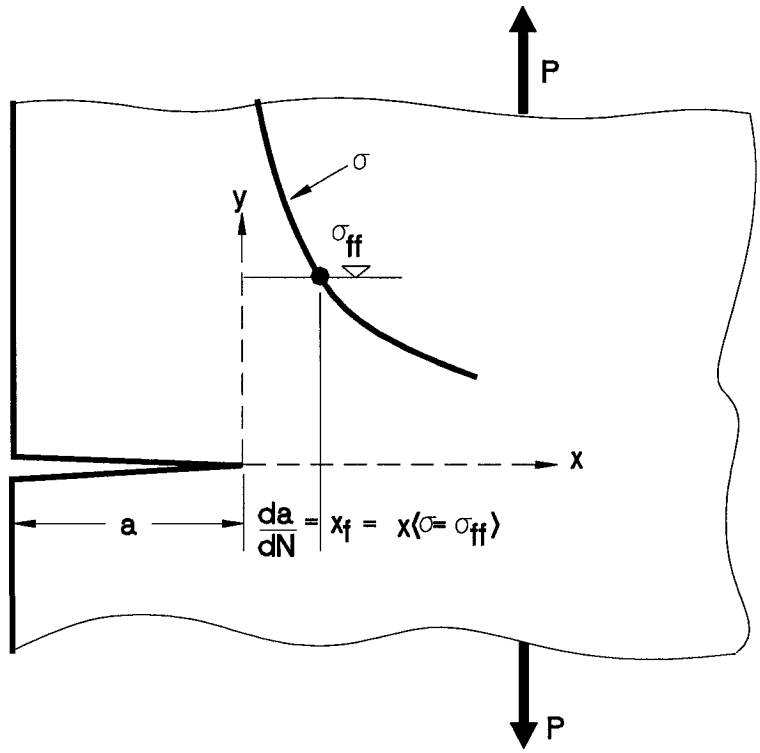

Figure 3-9 Schematic illustration of the assumption of the amount of incremental fatigue crack propagation [8]

The Zheng and Hirt model is capable of describing both regions I and II, but its drawback is that the value of the threshold stress intensity factor range for a particular stress ratio must be accurately known [5-6]. Furthermore, in the model the fracture strength of the material is calculated in Equation 3-9 from the ultimate stress of the material. However, it is questionable whether the ultimate stress, defined as the maximum nominal stress attained in a conventional tension test, can be related to the stress at fracture. Instead, the fracture strength of the material should be obtained from the measured true stress at fracture in a tension test, calculated from the final fracture load and the final fracture area. It is therefore postulated that using such a measured fracture strength of the material should provide a better predicted value of B in Equation 3-7.

In order to verify the above hypothesis, an experimental investigation was performed on 350WT steel. The investigation consisted of performing tension tests to obtain the tensile properties of the steel, a constant amplitude loading fatigue test to provide baseline fatigue data, a fatigue crack growth threshold test to determine the threshold value and a reanalysis of the baseline fatigue data to compare the predicted values of B from using Equation 3-9 and from the measured true fracture strength of the steel. The fatigue testing procedure and the results of the tests are presented in Chapter 6.

3.4.4 Wheeler Model

The Wheeler model [9] is one of the simplest models to calculate the fatigue crack growth retardation following a single tensile overload by introducing a retardation parameter, ϕ_R, which can be multiplied to any constant amplitude fatigue model. In here, it is applied to the Paris equation:

$$da/dN = \phi_R \cdot \left[C(\Delta K)^n\right], \tag{3-11}$$

With reference to Figure 3-10, the retardation parameter can be defined as:

$$\phi_R = \begin{cases} \left[\dfrac{r_{p,i}}{a_{OL} + r_{p,OL} - a_i}\right]^m & \text{, when } \; a_i + r_{p,i} < a_{OL} + r_{p,OL} \\ 1 & \text{, when } \; a_{OL} + r_{p,OL} \le a_i + r_{p,i} \end{cases}, \tag{3-12}$$

where a_{OL} is the crack length at which the overload is applied, a_i is the current crack length, $r_{p,OL}$ is the size of the plastic zone produced by the overload at a_{OL}, $r_{p,i}$ is the size of the plastic zone produced at the current crack length a_i, and m is the curve fitting parameter for the Wheeler model termed the shaping exponent. The size of the plastic zones can be estimated by Irwin's equation (Equation 2-8) or by the procedure described in Section 7.2.1.

The Wheeler model states that while the crack is advancing through the overload effective plastic zone, crack growth retardation occurs as long as the current effective plastic zone lies completely within the overload effective plastic zone. In addition, according to its formulation, the crack growth rate is at its minimum immediately after the overload application and gradually returns to its steady state value as the current effective plastic zone reaches the boundary of the overload effective plastic zone. Thus, the Wheeler model is not adequate for materials that experience crack growth acceleration and delay retardation immediately after an overload as described in Section 3.2.2. Furthermore, the model makes no attempts to account for the overload interaction when multiple overloads are applied. In the present work, a few modifications, described in Chapter 7, were proposed to the Wheeler model to address these effects.

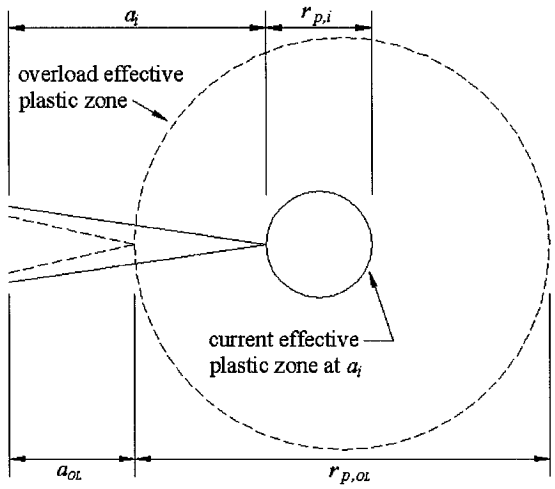

(a)

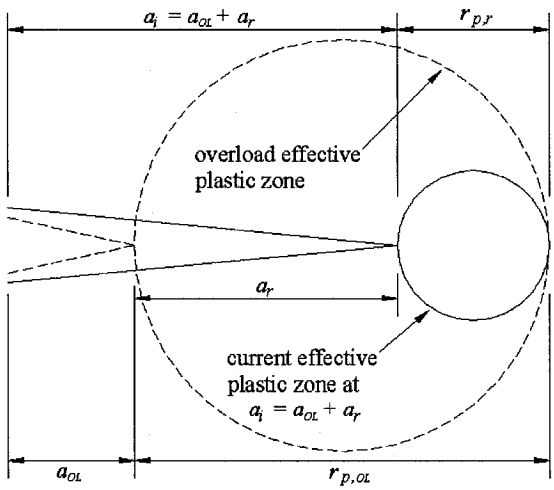

(b)

Figure 3-10 Illustration of the terms defining the retardation parameter

Chapter 4 Brittle Fracture in Steel

The cause of fracture is the presence of microcracks in a structure that have grown to a critical size, usually by the process of fatigue or stress corrosion. Fracture is the final event which is caused by two mechanisms: rupture and cleavage. Depending on the brittleness of the material, one mechanism of fracture will dominate. Steel, a normally ductile material, can be made to behave in a brittle manner by subjecting it to low temperature, high strain rate, high constraint and welding. Under these circumstances the likelihood of brittle fracture increases.

4.1 Fracture Mechanisms

Both fracture mechanisms, rupture and cleavage, are extremely fast processes, with rupture running as fast as 500 m/s and cleavage at 1600 m/s. Rupture, which is a result of plastic deformation, is the prominent fracture mechanism in ductile materials, while cleavage is the most brittle form of fracture which does not require plastic deformation. Since most building materials have some degree of ductility, the majority of service fractures occur by rupture. Yet most service fractures are brittle from the engineering point of view since the amount of plastic deformation is small and is confined to the wake and the tip of the crack.

4.1.1 Rupture

In ductile engineering metals, fatigue cracks propagate by the repeated blunting and resharpening of the crack tip due to plastic deformation in the form of slip of atomic planes as shown in Figure 4-1. During the loading phase of a tensile load, the crack opens and extends in length due to the slipping of the material at the crack tip along a favourable slip plane in the direction of maximum shear stress. During unloading the elastic material imposes compressive stresses on the plastically deformed region surrounding the crack tip, which will close and resharpen the crack tip.

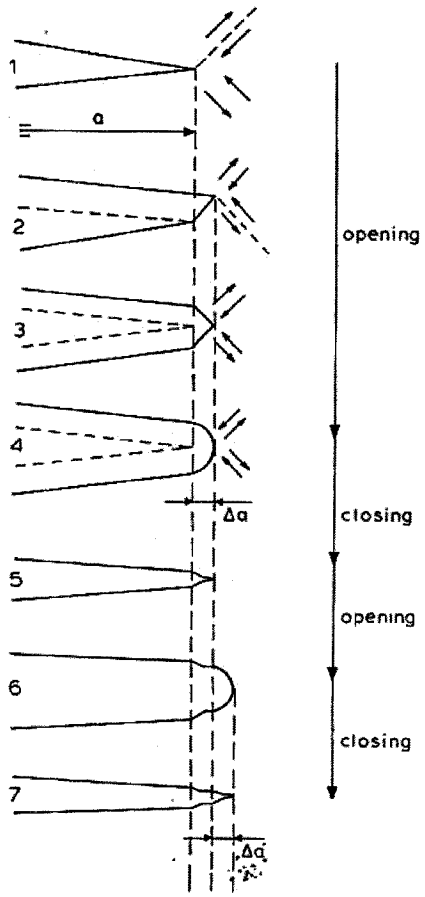

Figure 4-1 Slippage model for fatigue crack propagation [51]

All engineering materials contain large amounts of second phase particles that are often very brittle. These particles can only undergo a small amount of plastic deformation. This means voids are formed surrounding these particles. Rupture occurs when these voids join up to fracture the structure. This process is shown in Figure 4-2.

Since the plastic deformation (yielding) occurs in the direction of maximum shear stress, the rupture surface is often singly or doubly slanted. This is especially true under plane stress condition, where the plane of maximum shear stress is oriented 45° to the loading direction. In addition, the rupture surface is irregular and diffuses light, so that the fracture looks dull grey to the naked eye. Figures 4-3 show both an illustration of a slant rupture surface and an actual rupture surface of a 350WT steel plate. The figure shows yielding along the fracture surface, especially on the edge of the specimen.

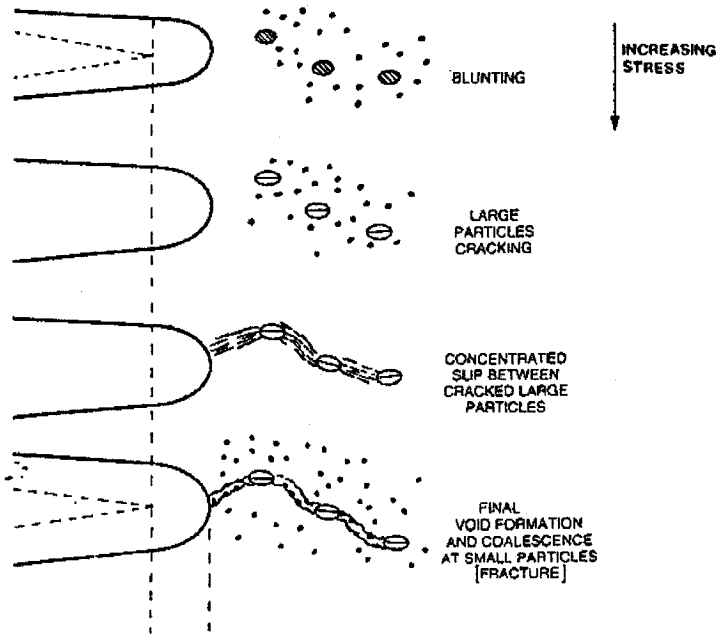

Figure 4-2 Four stages of rupture [59]

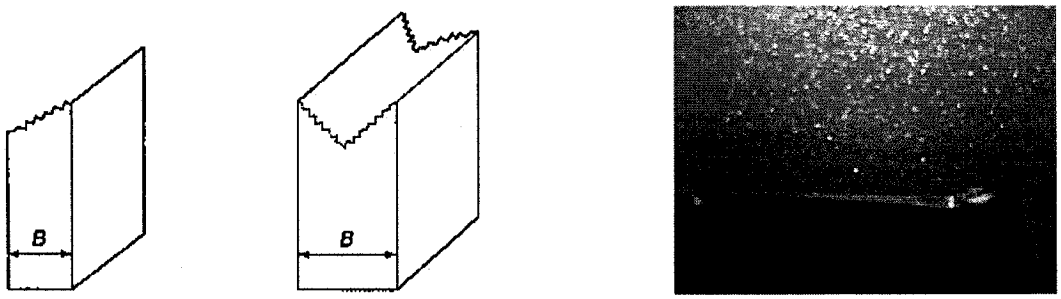

Figure 4-3 Rupture surface: (a) Illustration [1]; (b) 350WT steel

4.1.2 Cleavage

In highly brittle materials, fatigue cracks propagate by the same mechanism as fracture, namely cleavage. Cleavage is simply a direct separation due to a breaking of atomic bonds. As a result, fatigue cracks grow along planes of maximum tensile stresses and the fracture surface is flat and highly reflective, giving the cleavage fracture a bright shiny appearance as shown in Figure 4-4(b) for a polymethyl methacrylate (PMMA) plate. The lack of plastic deformation along the fracture surface is evident in PMMA as compared to steel in Figure 4-3(b). In the absence of plastic deformation, the energy involved during cleavage is extremely small when compared to the energy of deformation

necessary for rupture. The energy required for cleavage crack propagation is negligible. Cleavage fracture is thus able to run faster than rupture. For this reason, cleavage is the less desirable form of fracture mechanism.

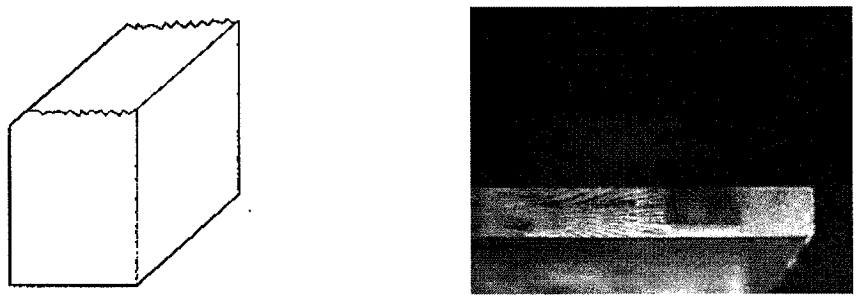

(a) (b)

Figure 4-4 Cleavage surface: (a) Illustration [1]; (b) PMMA

4.2 Conditions Promoting Brittleness in Steel

Steel exhibits a well-known ductile-brittle transition behaviour that is function of temperature, strain rate and constraint. In general, under the conditions of low temperature, high strain rate and high constraint, the yield strength of steel is increased, the amount of plastic deformation is reduced and the fracture toughness is lowered, which decreases the fracture stress and the critical crack size. Figure 4-5 shows the stress-strain curves of an 18Cr-18Mn-0.7N austenitic steel at various temperatures. It can be seen that the yield strength is increased and the percentage of elongation is reduced significantly at low temperature. In addition, welding introduces several embrittlement mechanisms in the heat-affected zone surrounding the weldment. Under these conditions, cleavage is a more likely fracture mechanism. Since the amount of plastic deformation ahead of the crack tip (plastic zone) is small, the theory of linear elastic fracture mechanics is more applicable under these conditions.

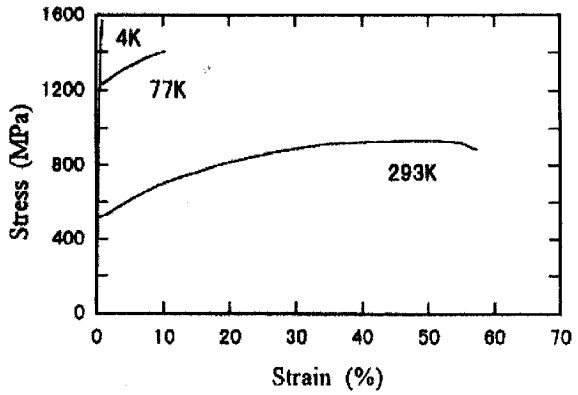

Figure 4-5 Stress-strain curves of 18Cr-18Mn-0.7N steel at various temperatures [111]

4.2.1 Low Temperature

Ductility is defined as the ability of a material to undergo large plastic deformation without fracture. Since plastic deformation requires energy, the more ductile the material is, the more energy is absorbed before fracture. In general, at low temperatures materials become harder and more brittle, whereas when the temperature rises they become softer and more ductile. This is true for steel, which shows increasing yield strength and decreasing fracture toughness with decreasing temperature. In addition, shiny and faceted fracture surfaces have been observed in low-temperature fracture of many steels, indicating a cleavage fracture [111].

One way to describe the ductility of a material is to measure its "notch toughness", which is defined as the ability of a material to absorb energy in the presence of a sharp notch. One of the most widely used test specimens to measure notch toughness is the Charpy V-notch (CVN) specimen [112]. The specimen can be subjected to different rates of loading, at various temperatures. The results for impact and slow-bend test of standard CVN specimens for a low-strength structural steel are shown in Figure 4-6.

In the figure, the absorbed energy, lateral expansion or contraction at the root of the notch and the percent of shear (slant) on the fracture surface are plotted against the test temperature. It should be noted that the higher these values are, the more ductile the steel is at that temperature. The figure shows that below a certain temperature, the steel is completely brittle, while there is increasing ductility above that temperature. This temperature is called the nil-ductility temperature (NDT), which is defined as "the

temperature above which cleavage fracture can be initiated only after appreciable plastic flow at the base of a notch, and below which cleavage fracture will be initiated with little evidence of notch ductility" [113]. In other words, below the NDT, the fracture mechanism is cleavage and above the NDT the likelihood of rupture increases.

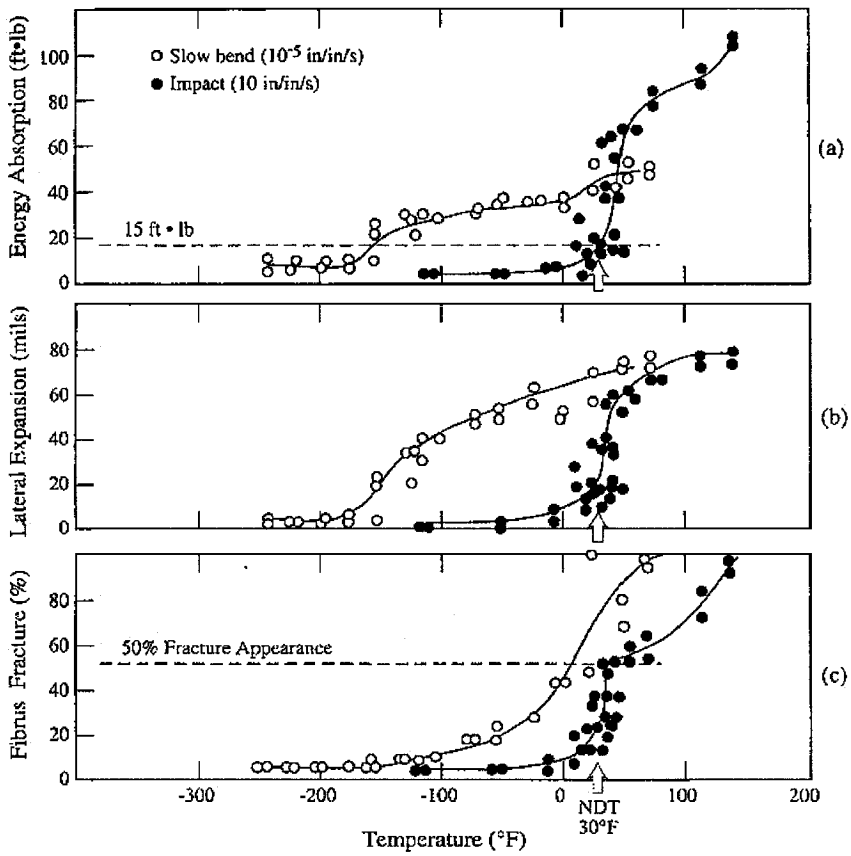

Figure 4-6 Charpy V-notch energy absorption, lateral expansion, and fibrous fracture for impact and slow-bend test of standard CVN specimens for a low-strength structural steel [114]

In design, the NDT is often specified by the amount of energy absorbed in a CVN test. For example, as shown in Figure 4-6, the NDT of the structural steel for impact loading is 30°F if the cutoff energy absorption is 15ft·lb. The NDT of a material is a function of both the loading rate and the state of stress at the root of the notch, as is evident in Figure 4-6 by the fact that the NDT of the structural steel for slow-bending

loading is much lower than it is for impact loading at the same cutoff energy absorption of 15ft·lb.

Various investigators have found that low temperature is beneficial at lower crack growth rates (or stress intensity factor range) while it is detrimental at higher crack growth rate [115-119]. This is illustrated in Figure 4-7, which shows that the fatigue crack growth rate of Fe-2.4Si is in general lower at low temperature (123 K, 173 K and 233 K) than at room temperature (296 K) at low stress intensity factor range while crack growth rate is higher at low temperature than at room temperature at high stress intensity factor range. However, the figure also shows that too low of a temperature (123 K, 173 K) would increase the fatigue crack growth rates compared to the moderately low temperature (233 K) as the material becomes more brittle. Finally, the fatigue crack initiation resistance (or threshold stress intensity factor range) increases when the temperature is decreased until the ductile-brittle transition occurs in the crack initiation mechanism [117, 120].

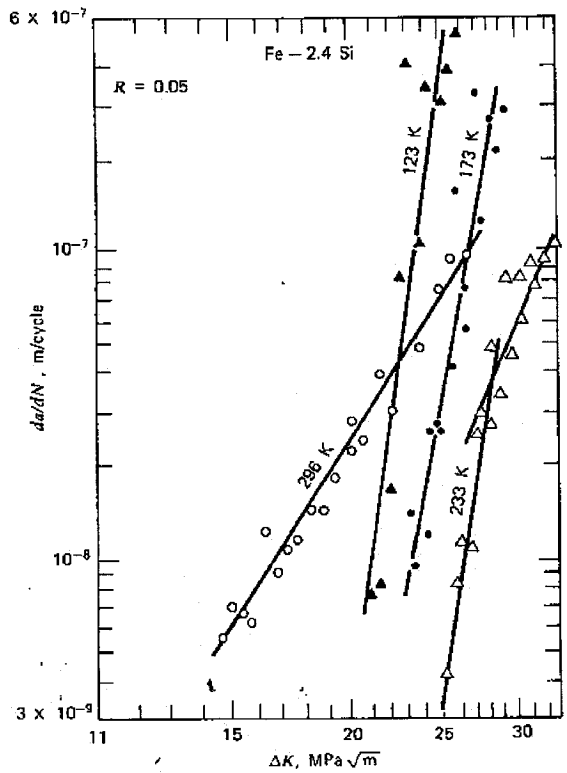

Figure 4-7 Fatigue crack growth rate versus ΔK in Fe-2.4Si at room and low temperatures [115]

In general, the environmental effects on fatigue at low temperature are diminished since the reaction kinetics are slower. Thus, low temperature is beneficial to fatigue in steel as long as slippage is the dominant fatigue mechanism. However, as the temperature approaches the NDT, the onset of cleavage cracking leads to acceleration in fatigue crack growth rate. This can be seen by the increase in the value n in the Paris equation for various steels with decreasing testing temperature as shown in Figure 4-8. The typical values of n for metals are 2-4 while the values for brittle materials such as ceramics are in the range of 15-50.

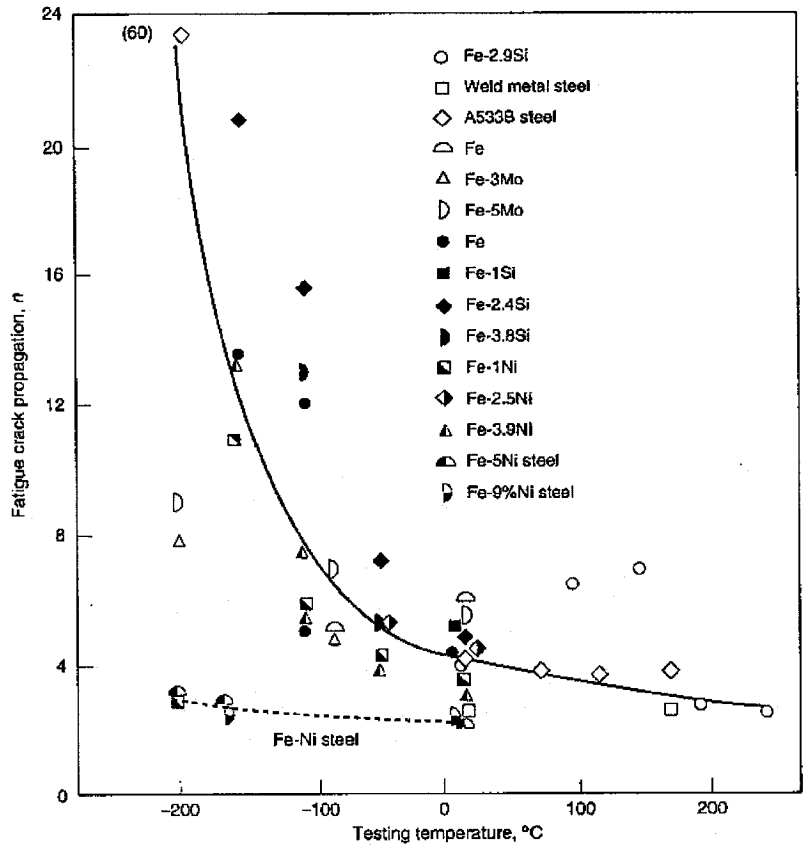

Figure 4-8 Influence of testing temperature on fatigue crack propagation exponent for iron-base alloys [1]

4.2.2 High Strain Rate

High strain rate, usually in the form of impact loading, has the same effect on steel as low temperature; that is increasing the yield strength and decreasing the fracture

toughness of steel [121-122]. In fact, "in low carbon steels, an increase in the strain rate by several orders of magnitude will increase the stress at which yield occurs by 100 or 200%" [114]. Therefore, under high strain rate, steel behaves in a brittle manner as the amount of plastic deformation is reduced and also the size of the critical crack is smaller as the fracture toughness is lowered. In addition, under conditions of high strain rate the nil-ductility temperature (NDT) is raised as discussed in the previous section and seen in Figure 4-6. This shift in NDT is dependent on the strain rate, $\dot{\varepsilon}$, and the yield strength of the steel, σ_{yld}, as shown in Figure 4-9. The figure indicates that the higher the strain rate and the lower the yield strength, the higher the NDT shift, T_{shift}. Based on observations from A36, ABS-C and A572 Grade 50 steels, this relationship is given by [114]:

$$T_{shift} = (150 - \sigma_{yld})(\dot{\varepsilon})^{0.17}, \tag{4-1}$$

where T_{shift} is in °F, σ_{yld} is in ksi and $\dot{\varepsilon}$ is in s^{-1}.

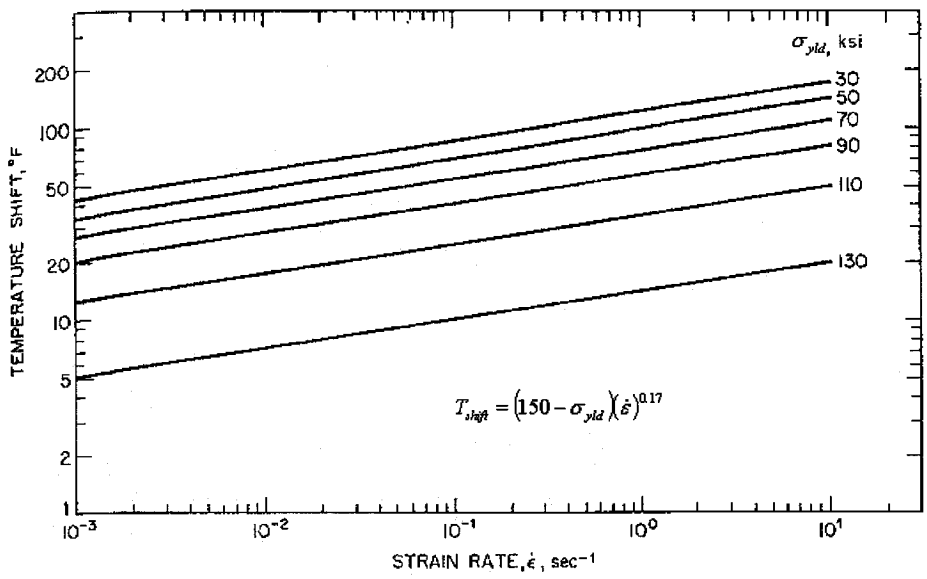

Figure 4-9 Shift in transition temperature for various steels and strain rates [114]

To illustrate the effect of high strain rate on the fatigue strength (number of cycles to failure) of steel, experiments by Shul'ginov and Matveyev showed that "under the conditions of repeated impact loading and low temperature the fatigue strength of welded joints of low-alloy steels is lower than that under sinusoidal loading and room

temperature" [123]. In addition, they observed a reduction in the fatigue strength of the base metal under the same conditions, but only in the presence of a stress concentrator. "For specimens without stress concentrators even a little increase in the fatigue strength is observed" [123]. Some of their results are shown in Figure 4-10, which illustrates that at the same stress ratio, the specimens under impact loading have lower fatigue strength than specimens under sinusoidal loading at both low and room temperatures. Furthermore, Yang *et al.* [124] found that cyclic deformation at high strain rates causes heavier fatigue damage and results in lower fatigue life.

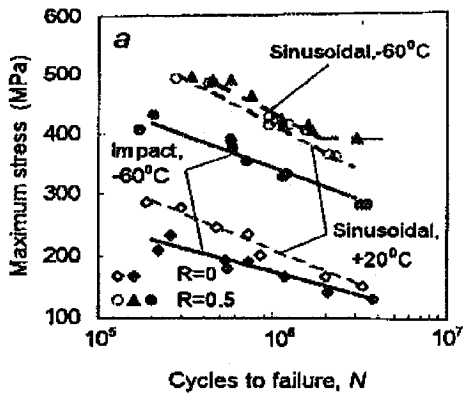

Figure 4-10 Fatigue curves for butt joints of low-alloy steels udner impact loading and sinusoidal loading [123]

Lastly, in addition to impact loading, the strain rate at the tip of a fast growing crack is also very high. This explains the detrimental effect of low temperature at high crack growth rate that is discussed in the previous section as the high strain rate at the crack tip raises the NDT and increases the likelihood of fatigue crack propagating by cleavage.

4.2.3 High Constraint

Constraint can be defined as the amount of material surrounding the crack tip, which is usually controlled by the thickness of the structure. As the structure is being loaded in tension, the material contracts in the thickness direction because of the Poisson's effect, especially at the tip of a crack, since this area is the most highly stressed. In the case of a very thin structure, contraction can take place freely, while in a

very thick structure, contraction is restricted by surrounding elastic material as shown in Figure 4-11. In the case of free contraction, the through thickness stress is essentially zero and the condition is called plane stress. In the case of restricted contraction, the surrounding elastic material exerts tensile stress, σ_z, on the material surrounding the crack tip while the through thickness contraction (strain) is essentially zero. This condition is called plane strain.

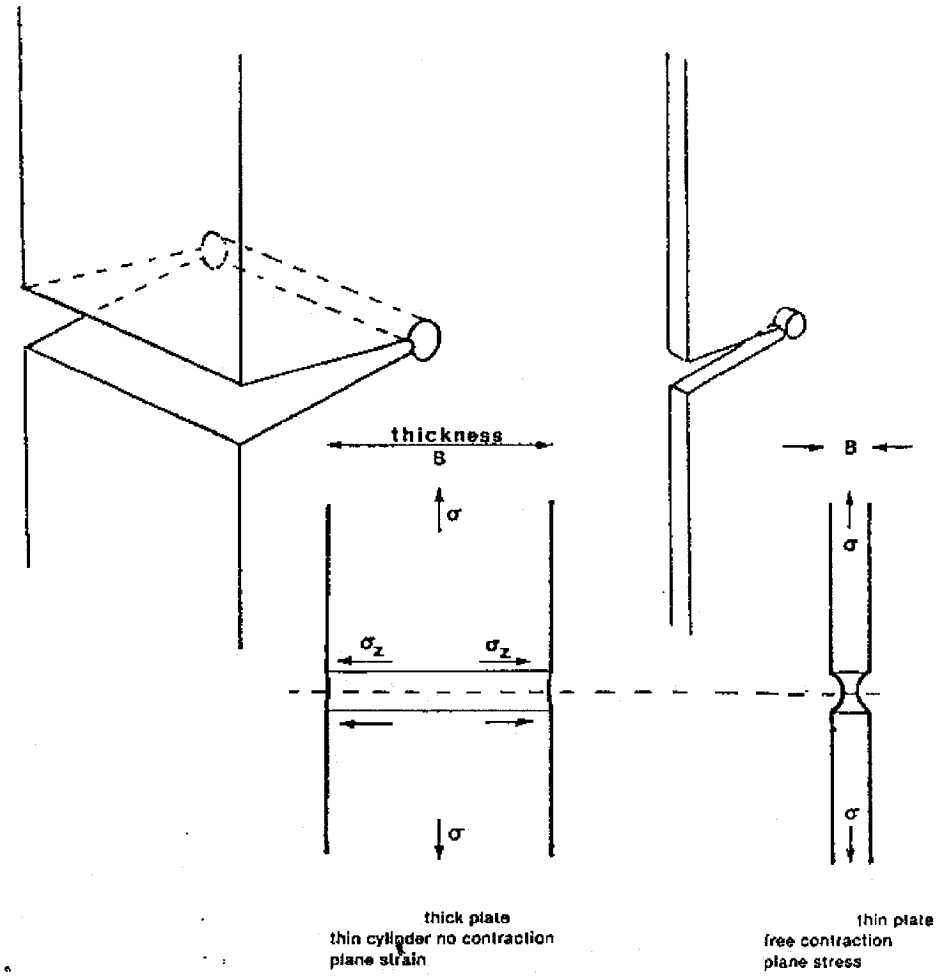

Figure 4-11 Contraint of large thickness and free contraction of small thickness [59]

The presence of the through thickness stress σ_z in plane strain creates a triaxial state of stress ahead of the crack tip. For steel having a Poisson's ratio of 0.33, $\sigma_z = 0.33(\sigma_x + \sigma_y) = 0.66\sigma_y$, where σ_y is the average cross-section stress in the loading direction. Using Tresca yield criterion, where yielding requires that the difference

between the largest and smallest principle stress is equal to the yield strength of the material, σ_{yld}, the plastic deformation ahead of the crack tip under plane strain condition requires a stress of $\sigma_y - \sigma_z = \sigma_{yld}$, or $\sigma_y = 3\sigma_{yld}$. In contrast, without the through thickness stress (plane stress), plastic deformation requires a stress of only σ_{yld}.

The stress distribution ahead of the crack tip for both plane stress and plane strain conditions are shown in Figure 4-12. It can be seen that the extent of plastic deformation, shown as r_p in the figure, is smaller in plane strain than in plane stress. In fact, for steel, r_p in plane strain is approximately one-third of the value in plane stress. Thus high constraint increases the degree of brittleness in a material and promotes cleavage fracture.

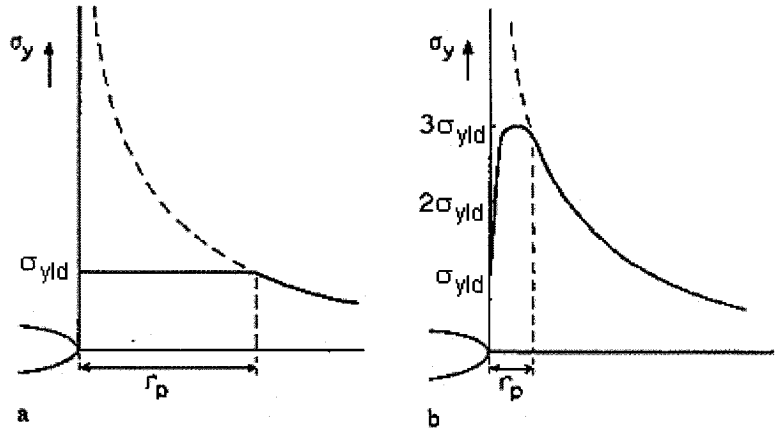

Figure 4-12 Approximate stress distribution in plane stress and plane strain: (a) Plane stress; (b) Plane strain [51]

In addition to having less plastic deformation, the plane strain state of stress ahead of the crack tip is also more severe than plane stress, with the tensile stress under plane strain being three times the value under plane stress as shown in Figure 4-12. It is then expected that the plane strain fracture toughness be less than the plane stress fracture toughness since the more severe state of stress will more easily lead to cracking and fracture. This is indeed the case as shown in Figure 4-13 by the results of a number fracture toughness tests on different thicknesses of high-strength steel specimens.

Constraint also has a small but systematic effect on fatigue crack propagation. As constraint increases, the fatigue mechanism changes from slippage to cleavage, which

leads to higher fatigue crack growth rate. Figure 4-14, which shows the influence of sheet thickness on fatigue crack propagation in 2024-T3 aluminum alloy sheet, suggests this is true.

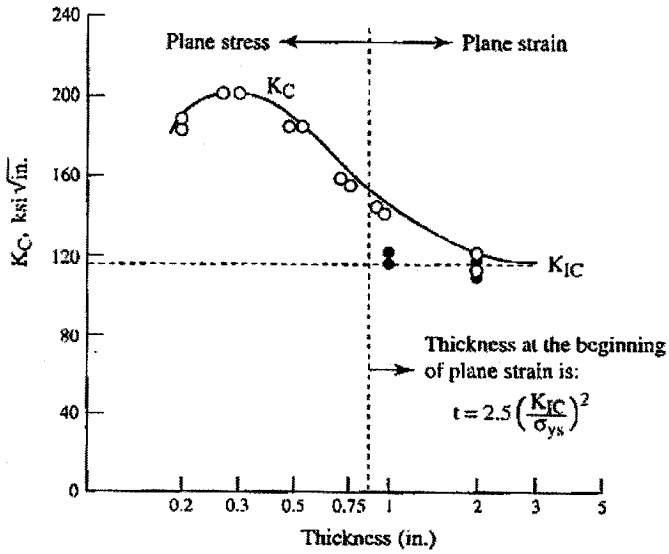

Figure 4-13 Effect of thickness on fracture toughness [114]

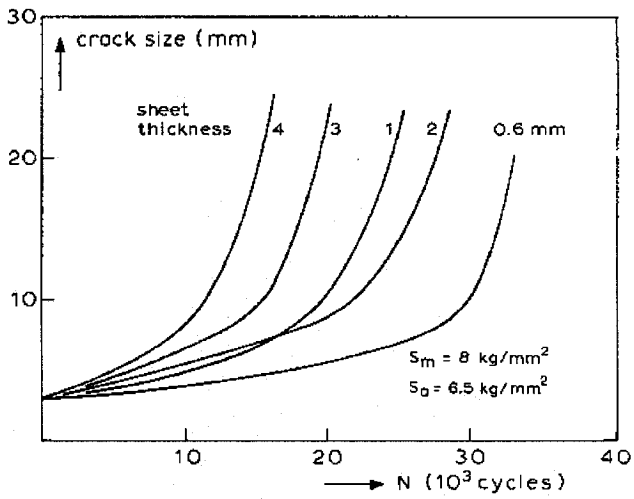

Figure 4-14 The influence of sheet thickness on fatigue crack propagation in 2024-T3 aluminum alloy sheet [51]

4.2.4 Welding

Welded construction has the advantage of allowing the designer to freely "place the material in almost any place that he wishes and create continuous structures of almost

any size" [113]. However among its disadvantages are the creation of residual stresses, distortion, stress concentrations and weld discontinuities (crack initiation sites) in the structure. In addition, the changes in microstructure in the heat-affected zone surrounding the weldment raise the nil-ductility temperature (NDT) and introduce several embrittlement mechanisms to the base metal. Furthermore, welded construction increases the rigidity of the structure, which has the same effects as high constraint as discussed in the previous section.

The heat-affected zone (HAZ) is "the portion of the base metal which has not been melted but whose mechanical properties or microstructure have been altered by the heat of the welding" [113]. This zone experiences the highest temperatures and the largest variations in temperature gradient and cooling rate. As a result, this region has coarser microstructure and exhibits lower fracture toughness. The NDT of this zone may go up as a result of heat cycles during the welding process. An illustration of the HAZ surrounding a butt weld is shown Figure 4-15.

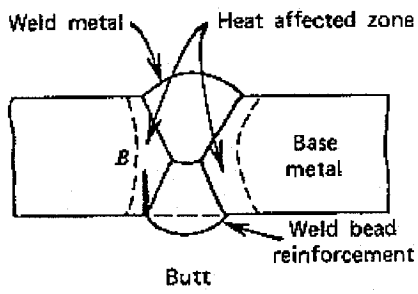

Figure 4-15 Weldment nomenclature and fatigue crack initiation sites [115]

Despite their small sizes, the HAZ has been the initiation site of a number of catastrophic brittle fractures of engineering structures, including pressure vessels, storage tanks and bridges. In steel, a number of mechanisms are responsible for the brittleness in the HAZ; they are: hydrogen embrittlement, strain aging and temper embrittlement. Hydrogen embrittlement is caused by hydrogen that is dissolved into the liquid weld pool and retained as the weld cools quickly. Hydrogen embrittlement causes cracking in the weld metal and the HAZ, resulting in reduced ductility and fracture toughness. Strain aging is the increase in yield and tensile strength and decrease in toughness caused by the thermal and strain cycles that accompany the welding process. Finally, temper

embrittlement is simply the loss in toughness of alloy steels when exposed to temperatures in the range of 325 to 575 °C.

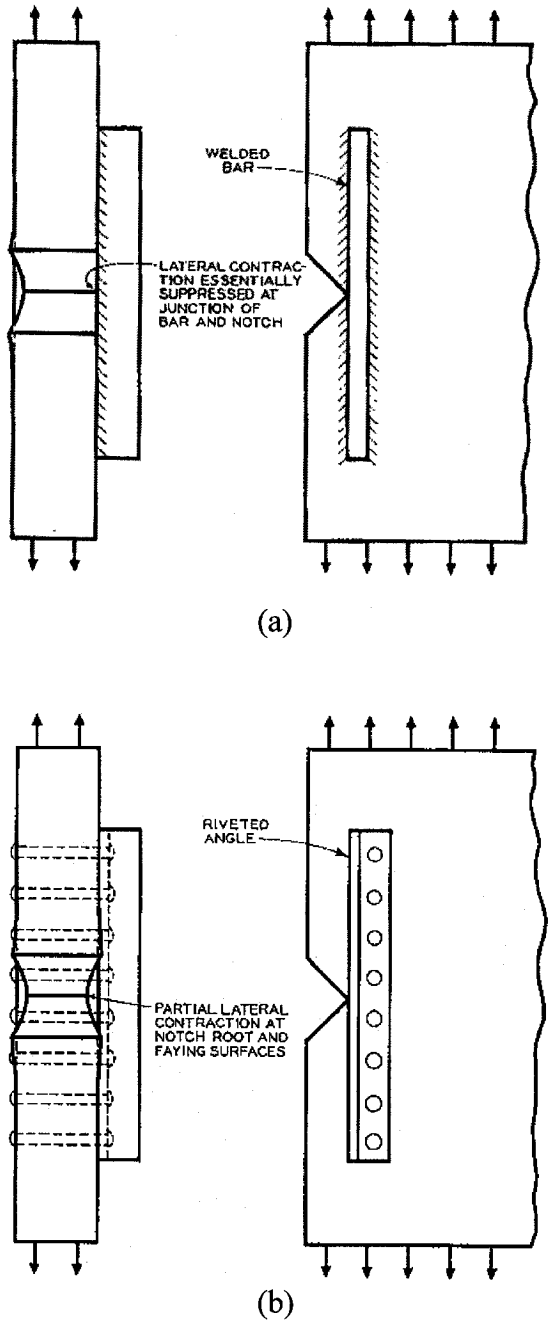

Figure 4-16 (a) Notched plate with welded bar; (b) Notched plate with riveted angle [113]

As indicated before, welded construction increases the rigidity of the structure and introduces high constraint effects. Consider the notched plate with welded bar in Figure 4-16(a). The lateral contraction at the tip of the crack is suppressed since the welded bar is joined to the plate to form a single piece of metal. This has the same effect as having the contraction restricted in a thick plate, which is discussed in the previous section. On the other hand, for the notched plate with riveted angle shown in Figure 4-16(b), "an appreciable degree of lateral contraction is still possible because the faying surfaces can separate to some extent" [113]. In this case the lateral constraint is less severe. Therefore in areas of a structure prone to cracking, riveted construction should be employed to provide some degree of flexibility to those areas.

4.3 Prevention of Brittle Fracture

Conventional design based on the static strength of the material is inadequate to prevent brittle fracture as made evident by numerous sudden failures of engineering structures at low operating stress throughout history. Today, brittle fracture can be satisfactorily prevented by following a few guidelines. First, the designer must determine the lowest operating temperature of the structure to ensure it is above the nil-ductility temperature (NDT) of the material. The structure can be conservatively assumed to be under impact loading so that the NDT of the material is the highest possible. At the lowest operating temperature, the material must have certain fracture toughness as calculated by fracture mechanics. The common way to establish the fracture toughness is by the Charpy V-notch (CVN) impact test since the CVN notch toughness is related to the fracture toughness of the material. The Canadian Standards Association (CSA) has established five categories of notch tough steel. Within each category, the steel must absorb a specified amount of energy in a CVN test at a specified test temperature. CSA Category 5 is reserved for user-specified energy and temperature requirements. For example, the 350WT Category 5 steel that is used in the hulls of the City class frigates, as well as Canadian bridges, offshore structures and pressure vessels, has a minimum CVN notch toughness of 40 J at a temperature of $-40°C$ [2-6]. In addition, the designer must avoid conditions of high constraint at areas of high stress concentration and possible crack initiation sites. This usually requires some creativity as shown below by the

redesign of the hatch corner in the Liberty ship. Lastly, the designer must ensure the welding process does not raise the NDT of the material and that the weld is virtually free of defects.

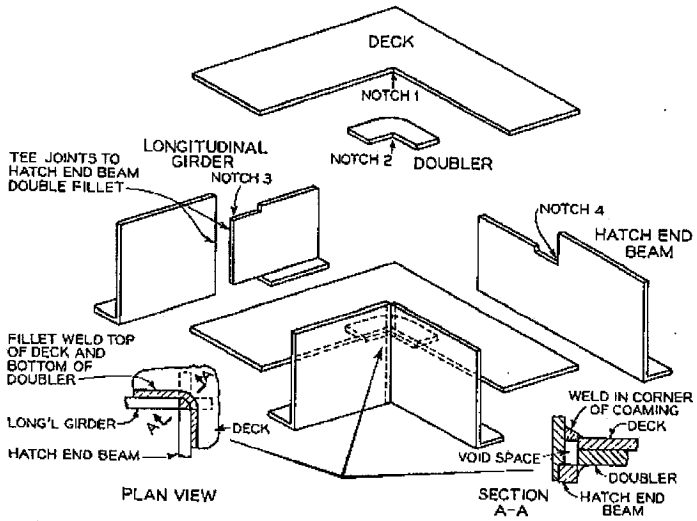

(a)

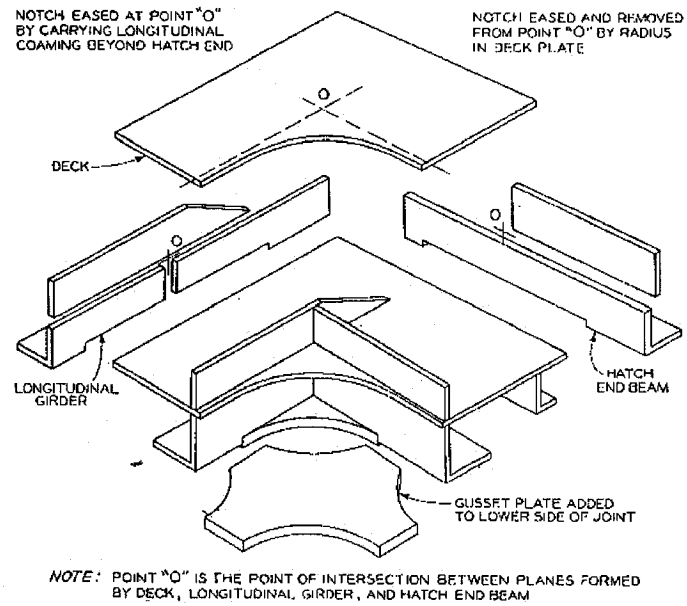

(b)

Figure 4-17 Hatch corner assembly and exploded views for: (a) Liberty ship; (b) Victory ship [113]

Numerous investigations revealed that the majority of fracture in the Liberty ships started at the square hatch corners. Figure 4-17(a) is a schematic of a typical hatch corner, which shows that the high stress concentration at the square corner is compounded by a triaxial state of stress at the intersection of the deck, longitudinal girder, doubler and hatch end beam. This created a restriction of plastic flow and caused the steel to act in a brittle manner. Figure 4-17(b) shows a redesign of the hatch corner used in the Victory ships. The improvements consisted of rounding and strengthening of the hatch corner, locating the intersection of the girder and the beam away from the corner and adding riveted crack arresters in various locations. Although the Victory ships are built from the same material as the Liberty ships, the redesign of the hatch corners led to immediate reductions in the incidence of failures.

4.4 Effects of Overload and Underload on the Fatigue Behaviour of Steel and PMMA

It is well-known in steel that due to load interaction effects, the fatigue crack growth is retarded after an application of tensile overload and is accelerated to a lesser degree after a compressive underload as described in Chapter 3. This phenomenon is attributed to the formation of a relatively large zone of residual compressive or tensile stress in front of the crack tip after the application of the overload or underload respectively. Since the amount of crack growth retardation and acceleration is influenced by the amount of crack tip plastic deformation, it is then conceivable that the reduction in the ductility of steel caused by low temperature, high strain rate, high constraint and/or welding would decrease the overload and underload effects as well. For example, Gan and Guo [117] studied the influence of the overload retardation at low temperature (as low as $-80°C$) on fatigue crack growth of steel 16Mn and discovered that the lower the temperature is, the weaker the retardation effect. They also noted that at low temperature, a high overload "can accelerate the propagation rate of the fatigue crack and even results in a sudden brittle fracture" [117]. In addition, Le Pautremat and Vallet [118] performed fatigue-overload tests on E355 grade RAD steel welded joints at both $20°C$ and $-50°C$. For that particular grade of steel, they found that there is no difference in the amount of crack growth retardation in the base metal between the two

test temperatures and that the heat-affected zone behaves more poorly in overload than the base metal. However, they remarked that retardation is "generally reduced with temperature, which is explained by the latter's effect on the size of the plastic region and its influence on closure phenomena" [118]. Furthermore, Shuter and Geary [125] reported that the amount of fatigue crack growth retardation occurring in 50D steel after a single tensile overload decreases with an increase in specimen thickness.

In order to simulate the reduced ductility of steel when under the above embrittling conditions, overloading and underloading fatigue tests were performed on centre-cracked polymethyl methacrylate (PMMA) specimens in the present work. PMMA is a semi-brittle glassy polymer which shows little reduction in area and elongation at fracture. The fatigue behaviour of PMMA has been characterized by both the stress intensity factor [126] and the strain energy release rate [127]. Pitoniak *et al.* [128] reported that the retardation effect caused by tensile overload in PMMA is dependent on the baseline constant amplitude load level and the magnitude and number of overloads. In other words, the higher the baseline load level, the greater the number of overloads is required to cause retardation. On the other hand, the work by Shiraishi and Soyama [129] showed that a single overload causes crack acceleration in PMMA during overloading and retardation after removing it, with the maximum retardation occurring immediately after the overload. Furthermore, due to the brittleness of PMMA, the crack acceleration is very high and the retardation effect is small compare to metals. Some of their results are plotted in Figure 4-18, which shows a jump in crack length (a) and a decrease in crack growth rate (da/dN) after the overload (OL). In the present work, the effects of loading frequency, tensile overload and compressive underload on the fatigue crack propagation of PMMA were examined. The experimental procedure and results are presented in Chapter 9.

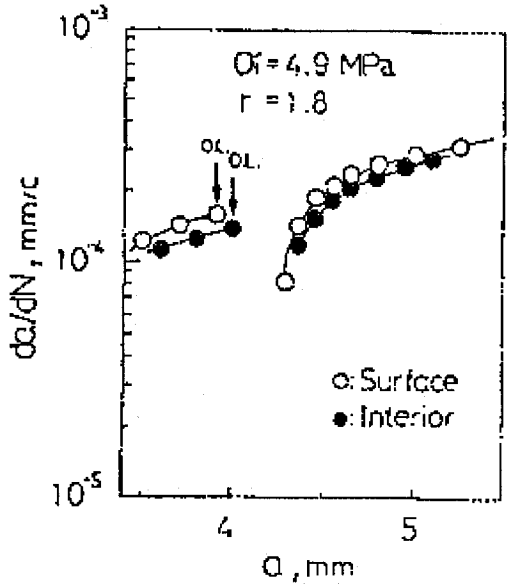

Figure 4-18 Retardation in the fatigue crack propagation after a single peak overload for PMMA [129]

Chapter 5 Stiffened Sheet Structures

Stiffened sheet structures are metal sheets reinforced by stringers that can be bonded or welded to the sheets, connected to them by fasteners such as rivets or bolts, as schematically shown in Figure 5-1, or machined as an integral part of the panels. They are widely used in aircraft, ship and chemical industry structures for their light weight and high strength and stiffness. They are mostly found in the airframes, fuselages and wings of aircraft and the deck and side plating on a ship where the amount of fatigue loading is the greatest.

From a static loading point of view, stiffened structures provide higher buckling strength and flexural stiffness. In terms of fracture mechanics, the stringers (or stiffeners) provide a secondary structure for the load to bypass a cracked panel. The crack tip stress intensity factor is therefore lowered in the vicinity of an intact stringer so that the growth of a crack towards a stringer is slowed down or even arrested. For this reason, a stringer is sometimes called a crack arrester. Because of its crack arresting capability, a stiffened structure can sustain cracks safely until it is repaired or its economic service life has expired. Such structure is said to have high damage tolerance and it can represent major cost savings as the inspection interval of the structure for cracks can be longer.

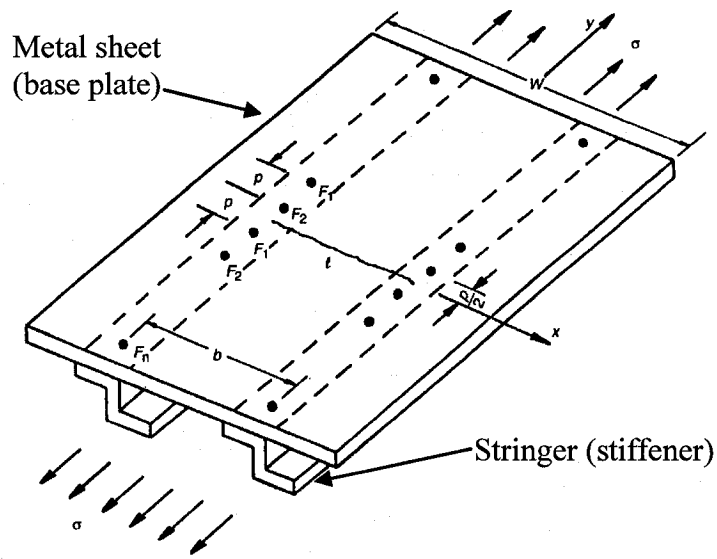

Figure 5-1 Through-the-thickness crack in a skin-stiffened panel [107]

5.1 Dynamics and Crack Arrest

In Chapter 2, the concepts of strain energy release rate, stress intensity factor, crack resistance, and residual strength are introduced under static conditions. However both crack propagation and fracture are dynamic processes where the crack can grow at a high speed. This introduces dynamic effects to the problem due to the inertia forces, rate-dependent material behaviour, and reflected stress waves. Thus the stress intensity factor in the dynamic case is different from the static case. The kinetic energy of the crack also enters into the energy criterion for fracture. Under the right conditions, crack growth or fracture can be stopped. This phenomenon is called crack arrest. For this to happen, the speed of the crack must be reduced to zero. This means the kinetic energy has to be dissipated. In this section, the theory behind dynamic fracture and crack arrest is presented using concept of R curve discussed in Chapter 2.

5.1.1 Crack Speed and Kinetic Energy

Whenever the strain energy release rate G is greater the crack resistance R, there is a surplus of release energy, $G-R$, that can be converted into kinetic energy, E_{kin}. Since kinetic energy is proportional to the square of speed, the surplus energy also governs the speed at which the crack will propagate through the material.

Consider the situation depicted in Figure 5-2. It shows the plane strain R curve and a cracked body that had been loaded to fracture. As the crack grows at fracture stress, G remains larger than R and an increasing amount of surplus energy is available to be converted to kinetic energy as indicated by the shaded area in the figure. This explains why final fracture is rapid process with the crack growing across the width of body at a high speed.

If the surplus energy (shaded area in Figure 5-2) is equated to the familiar formula for kinetic energy, $E_{kin} = \frac{1}{2}mv^2$, then the crack speed can be expressed as follows:

$$v = 0.38 v_s \left(1 - \frac{a_c}{a}\right), \tag{5-1}$$

where v is the crack speed, $v_s = \sqrt{E/\rho}$ is the speed of sound in the material with E and ρ being the modulus of elasticity and the specific density of the material respectively, and

a_c is the critical crack length. Equation 5-1 predicts how the crack growth rate increases from zero at the start of fracture at $a = a_c$, to a limiting velocity of 0.38 v_s, when the crack size is large. However measured crack velocities in different materials are well below the theoretical values predicted by Equation 5-1. Reported propagation rates of ductile cracks are even lower. This is due to a number of assumptions made in Figure 5-2, which are discussed below.

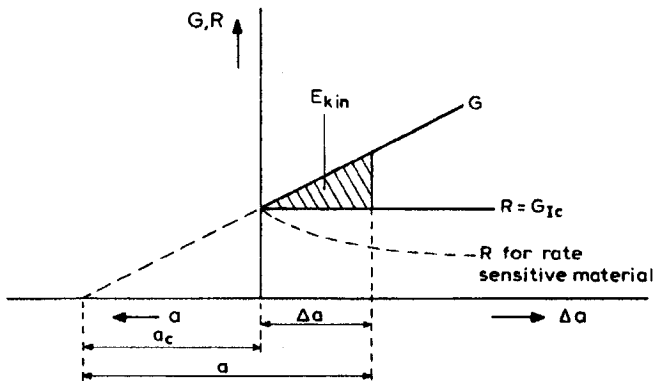

Figure 5-2 Representation of kinetic energy [51]

The case depicted in Figure 5-2 is simplified in a number of ways to facilitate the above discussion. First, the *R* curve is shown to be a horizontal line. In reality true plane strain condition is rare and in many cases *R* is a rising function. For a rate sensitive material the *R* curve may be decaying, as shown in dash in Figure 5-2, since the material behaves in a more brittle manner at higher crack speed. As mentioned before, brittle materials do not require plastic energy for crack growth and thus have lower crack resistance. However, an increasing crack resistance may also be observed for some materials.

Second, in reality the stress distributions in the static and dynamic cases are different, due to the introduction of time dependent parameters. Therefore the strain energy release rate is dependent upon crack speed and the *G* curve is not a straight line as shown. Recent work on more realistic crack problems has shown that the dynamic stress intensity factor, and therefore the dynamic strain energy release rate, decreases with increasing crack velocity. The dynamic stress intensity factor becomes zero when the crack velocity reaches the surface wave velocity. Therefore in real structures, the *G* and

R curves may rise and fall as the crack grows depending on the geometry and material properties. Crack arrest may result when these curves are crossed. The subject of crack arrest is present in the next section.

5.1.2 Crack Arrest Principles

In Figure 5-2 the G curve is depicted as a straight line such that when the fracture stress is reached, G remains greater than R as the crack grows until final failure. However, under certain loading conditions or specimen geometry, such as loading a plate with fixed ends or with stiffeners, G decreases with crack length so that crack growth may be arrested. The decrease in G may also be a result of the dynamic effects and an example of a decreasing G curve is shown in Figure 5-3.

In Figure 5-3, R is assumed to be constant and G begins to decrease at B. At C, the condition that $G = R$ is again satisfied. However crack arrest does not occur even though $G < R$ from this point onward since the speed of the crack is not equal to zero as the kinetic energy is equal to area ABC. The crack slows down after C as the kinetic energy is consumed for further crack growth. Crack arrest (crack speed equals zero) finally occurs at E when all the kinetic energy is consumed, such that area CDE = ABC. From the figure, one can see that the value of G at arrest is lower than G_{Ic}. This lower value is called the arrest toughness. It can also be seen from Figure 5-4 that this value depends on the initial crack size, as crack a_{c1} and a_{c2} has different arrest toughness values of G_A and G_B respectively.

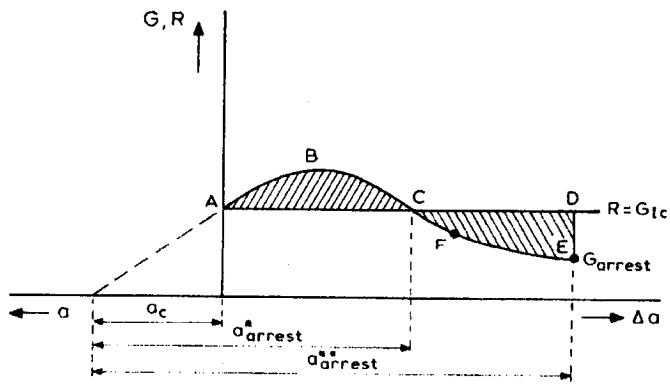

Figure 5-3 Crack arrest due to decreasing G [51]

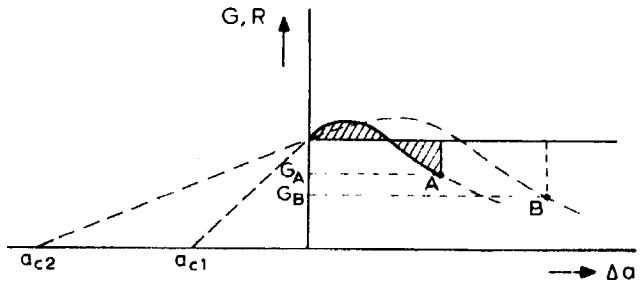

Figure 5-4 Effect of crack size on G_{arrest} [51]

The above discussion on crack arrest illustrates the case when G drops below R. Alternatively crack arrest can occur when R rises above G as depicted in Figure 5-5. R can increase in a number of ways. Due to the growing crack, the plastic zone at the crack tip increases in size and the through-thickness restraint becomes less. When the plastic zone becomes of a size of the order of the plate thickness, plane stress may develop. As mentioned before, this causes a steep rise in R, such that it may become larger than G.

Temperature rise in the plastic zone resulting from the high rates of deformation can also cause an increase in R. A rise in temperature means that energy is dissipated as heat. This heat energy is supplied from the strain energy release and can be regard as an added crack resistance. The heat generation will depend upon crack speed and the resulting temperature rise will depend upon specimen geometry.

Lastly R can be increased by the insertion of strips of material with a higher toughness. This situation is depicted in Figures 5-6. A high toughness strip is welded to the base material and it is shown as a sudden jump in value in the R curve. One can see in Figure 5-6(a) that the kinetic energy can easily be absorbed by the high toughness strip provided that it is wide enough. However the strip is not effective if the crack is too far away from the strip as shown in Figure 5-6(b).

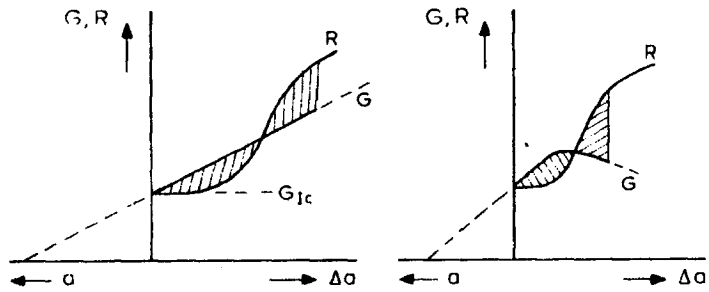

Figure 5-5 Arrest due to rising *R* [51]

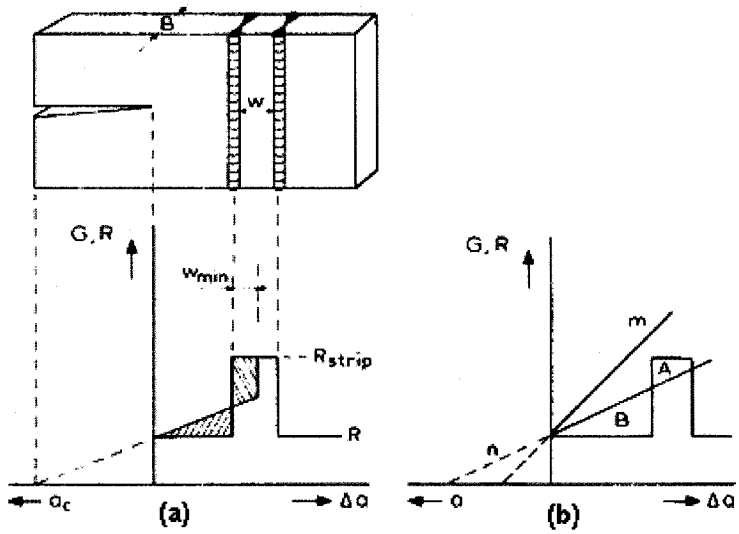

Figure 5-6 Welded crack-arrest insert: (a) Arrest; (b) Arrest not achieved [51]

The above is a simplified discussion on crack arrest which is sufficient for the purpose of this review. The problem, however, is complicated by the following facts. First, it is unlikely that the kinetic energy can always be used for crack propagation, particularly in the case of very long cracks for which much of the kinetic energy is contained in a region far behind the crack tip. It has been concluded that there is a maximum effective crack length beyond which the crack behaves as if it has a constant size. Also, if G drops below G_c, the stresses at the crack tip are also below critical, such that crack growth should be expected to stop even if sufficient kinetic energy is available. This is another example illustrating that the energy condition is a necessary condition for crack growth, but it is not necessarily a sufficient condition.

5.2 Design Factors for Stiffened Structures

This section introduces several factors that can be used to design stiffened structures. They are the stress intensity modification factor, stiffener efficiency factor and the stiffener and fastener load concentration factors. For simple geometry, their values can be found in various design handbooks. For more complicated arrangements, an analytical or numerical method has to be used. At the end of this section, a method for estimating the load concentration factors with the stress intensity modification factor is presented.

5.2.1 Stress Intensity Modification Factor

Since the stress intensity factor, K, of a stiffened cracked panel is lower than its corresponding unstiffened panel, one way to access the effectiveness of a stiffener is to consider its stress intensity modification factor, C, which is defined as the ratio of the stress intensity factor for the stiffened panel to the stress intensity factor for the plain sheet (without stiffener). Poe [130] has compiled the C factors for various stiffener configurations in his work and presented them as design graphs. Figure 5-7 is one of the examples, which plot the C factor against crack length for a one-bay crack in the middle of a bay between two stiffeners. Poe considered the C factor as a function of attachment spacing (rivet pitch), p, reinforcement spacing, b, and a relative stiffness parameter, μ, which is defined as:

$$\mu = \left[1 + \frac{b \cdot t}{A_e} \cdot \frac{E}{E_s}\right]^{-1}, \tag{5-2}$$

where t is the sheet thickness, A_e is the effective cross-sectional area of the stiffener, and E and E_s are the modulus of elasticity for the sheet and the stiffener, respectively.

For the stiffeners shown in Figure 5-1, only a part of them (the area that is close to the skin) makes a contribution to reducing the crack tip stress intensity factor. An estimate for A_e is given as:

$$A_e = A\left[1 + \left(\frac{y}{\rho}\right)^2\right]^{-1}, \tag{5-3}$$

where A is the cross-sectional area of the stringer, y is the distance from the inner surface of the sheet to the centroid of the stringer, and ρ is the radius of gyration of the stringer.

For a flat strap, A_e is approximately equal to the actual size of the strap. If the strap is not made of the same material as the sheet, then A_e is modified as:

$$A_e = A \cdot F_{tyf} / F_{tys} , \tag{5-4}$$

where F_{tyf} and F_{tys} are the tensile yield strength for the stiffener and the sheet respectively.

In the case of an integral or a welded stiffener, the curves in Figure 5-7 are still applicable by considering very close reinforcement spacing.

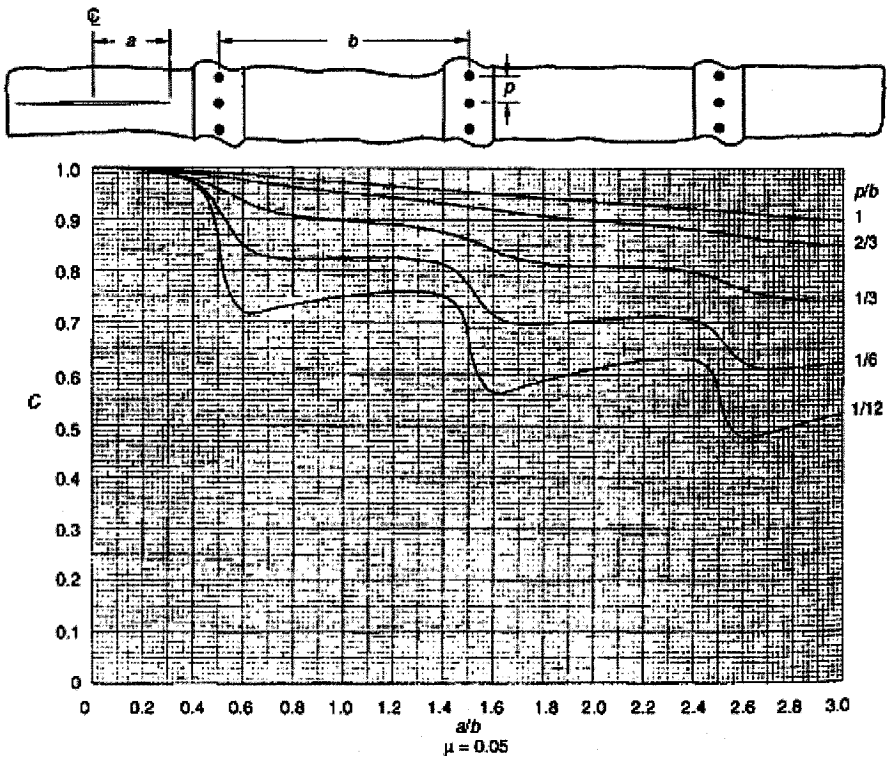

Figure 5-7 Stress intensity modification factors for a one-bay crack centred between two stiffeners [130]

As seen from Figure 5-7, reduction in C increases as relative spacing of the attachment decreases. This is because the smaller the attachment spacing, the more effective load transfer is to the reinforcement. However, it turns out that the ratio of

stiffener modulus to sheet modulus is a more important factor for improving reinforcement efficiency, and thus a higher μ value will result in a greater reduction in K. Incorporating the C factor, the general stress intensity factor in a stiffened structure can be written as:

$$K = CY\sigma\sqrt{\pi a}\,. \tag{5-5}$$

The strain energy release rate and the residual strength of a stiffened structure can be obtained similarly.

5.2.2 Stiffener Efficiency Factor

The stiffener efficiency factor, γ, is closely related to C as a description of a stiffener's effectiveness. γ is defined as the ratio of the residual strength of a stiffened panel, σ_s, to that of a plain sheet, σ_c:

$$\gamma = \frac{\sigma_s}{\sigma_c}\,. \tag{5-6}$$

The value of γ for any type of reinforcement can be determined from its C factor curve such as shown in Figure 5-7. The stiffener is most effective where the value of C is at its minimum, $C_{\min}$. That is, the $C_{\min}$ is the value for the point at the bottom of the valley in the C versus a/b curve. The residual strength at this point is thus equal to $\sigma_s = \sigma_c / C_{\min}$, such that $\gamma = 1/C_{\min}$. Figure 5-8 presents several γ versus μ curves that are reduced from Poe's work. It shows again that the effectiveness of a stiffener increases with its relative stiffness parameter.

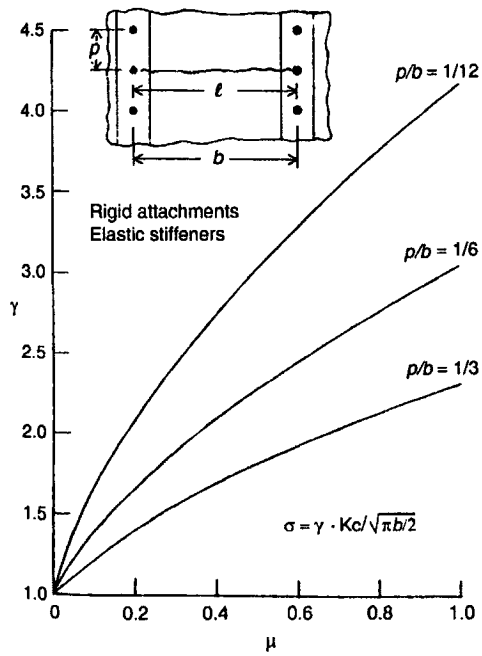

Figure 5-8 Stiffener efficiency factor for a one-bay crack [107]

5.2.3 Load Concentration Factor

The crack tip stress intensity factor in a stiffened panel is lowered as part of the load is transferred to the stiffener. In the case of a riveted or bolted stiffener, this load is transmitted through the fasteners connecting the panel and the stiffener. As the crack grows closer to the stiffener, the stiffener becomes more highly loaded and the shear stress in the fasteners increases. The maximum force in a stiffener occurs between the crack and the rivet on either side nearest the crack. The force F at this location in the stiffener is:

$$F = S \cdot L \cdot A \cdot E_s / E, \tag{5-7}$$

where S is the stress on the panel, L is the stiffener load concentration factor, and A, E_s and E are defined as before. L can be defined as the ratio of the maximum local stress to the far-field applied stress on the stiffener.

A high load concentration can cause yielding or breakage in the stiffener. This has detrimental effects on the crack tip stress intensity factor. The most highly loaded fasteners are always the pair that is nearest to the crack tip as most of the load transfer activity actually takes place there. Their shear forces Q increase from essentially zero

when the crack length is zero to a significant value as the crack grows towards the stiffener until the first pair of fasteners yields and subsequently breaks. Failure of the other fasteners will then follow in a process referred to as fastener unzipping. The failure of the stiffener and fasteners has significant effect on the efficiency of the reinforcement and is discussed in more details in Section 5.5.

Poe [130] has presented the values of L and Q in his work as shown in Figures 5-9 and 5-10. The stiffener configuration is again for a one-bay crack in the middle of a bay between two stiffeners. In this stiffener configuration, L and Q behave differently under the influence of p, b, and μ. Similar to the C factor, L decreases as μ increases. But unlike the C factor, L increases as p/b decreases. The situation in Q is more complicated. In this case Q increases as μ increases. At low μ, Q increases with decrease in p/b. However, the opposite is true at high μ. The values of L and Q can be used to plot the residual strength of the stiffener and the fasteners together with the residual strength of the panel. This is done in Section 5.5.

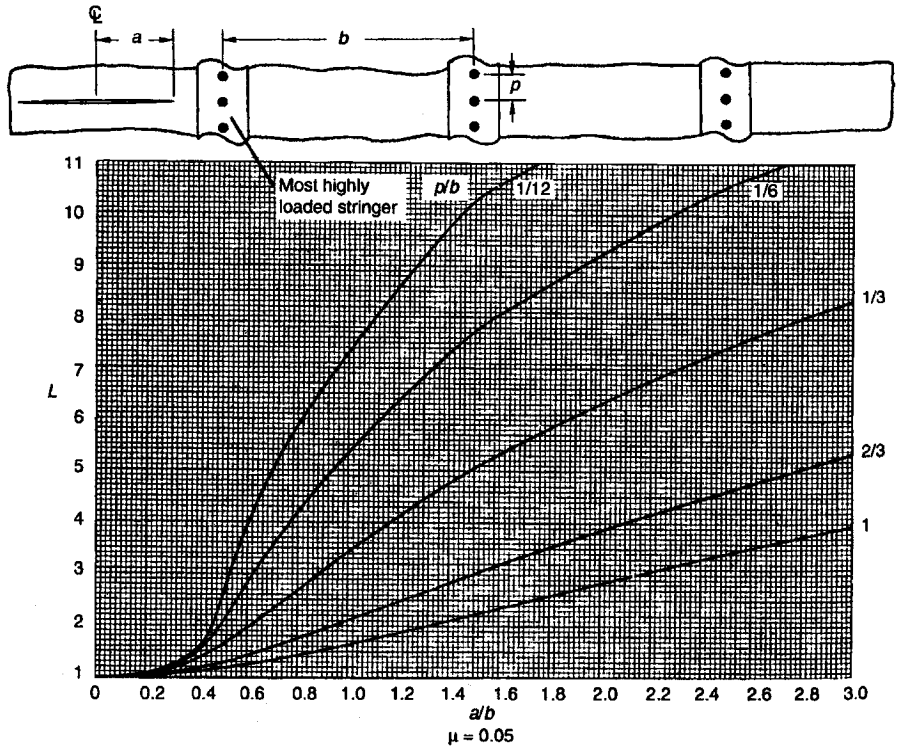

Figure 5-9 Stiffener load concentration factor in most highly loaded stiffener [130]

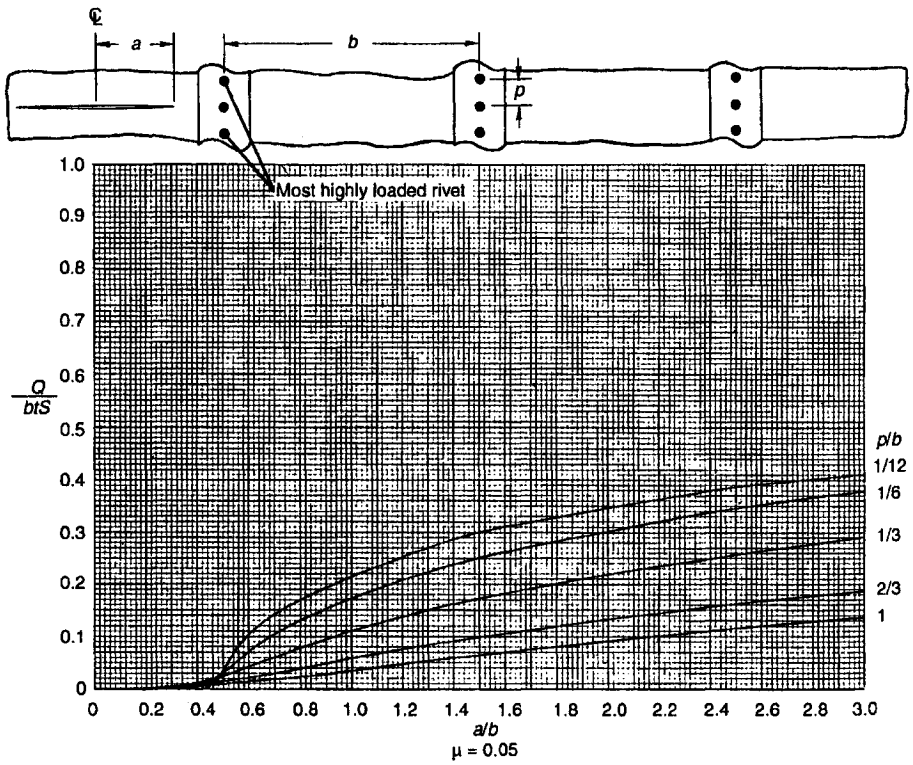

Figure 5-10 Rivet forces in most highly loaded rivets [130]

5.2.4 Method of Estimation

In most design handbooks, only the values of the C factor are provided while for design both the L and Q values are necessary. Still, good estimates of L and Q can be obtained from the C factor. The following method is presented in [59]. In an unstiffened plate, the load carried by the plate in front of the crack tip is:

$$P = \int \sigma_y t \, dr . \tag{5-8}$$

From Equations 2-3 and 2-4, for mode I loading:

$$\sigma_y = \frac{K}{\sqrt{2\pi r}} = \frac{Y\sigma\sqrt{\pi a}}{\sqrt{2\pi r}} . \tag{5-9}$$

To obtain the load transferred to the stiffener, it is assumed to be sufficient to integrate Equation 5-8 over a distance of $r = a$ in front of the crack tip:

$$\begin{aligned} P &= \int_{r=0}^{r=a} \frac{tY\sigma\sqrt{\pi a}}{\sqrt{2\pi r}} dr = tY\sigma\sqrt{a/2}\int_0^a r^{-1/2}\, dr \\ &= \sqrt{2}Y\sigma at. \end{aligned} \tag{5-10}$$

Thus the additional load carried by the stiffener is P_u (unstiffened) minus P_s (stiffened) and the additional stiffener stress is $(P_u - P_s)/A$. The total stress in the stiffener is $\sigma_t = \sigma + (P_u - P_s)/A$, where σ_t is the total stress and σ is the far-field stress in the stiffener. The stiffener-load-concentration factor $L = \sigma_t/\sigma$ becomes, with Equation 5-10:

$$L = 1 + \frac{at\sqrt{2}(Y_u - Y_s)}{A} = 1 + \frac{at\sqrt{2}(1-C)}{AY_u}, \tag{5-11}$$

where Y_s and Y_u are the geometric parameters for the stiffened and unstiffened plate. The values of C and Y_u can be obtained in most design handbooks.

To estimate Q, assume that the entire load is transferred by the closest three fasteners above and below the crack. Together the three fasteners transfer the total load which is $(\sigma_t - \sigma)A$. Typically, the fastener closest to the crack transfer most of the load. Assuming a load distribution of 60%, 30%, and 10% to the three fasteners, then the highest fastener shear load would be:

$$Q = 0.6(L-1)\sigma A. \tag{5-12}$$

Thus the fasteners must be made strong enough to carry this. It turns out that the actual fastener load on the average is only in the order of 60-70% of the value in Equation 5-12 due to plastic deformation in the fastener hole.

5.3 R Curve of Stiffened Panel

The R curve and crack arrest concepts presented in the previous sections can be readily combined with the C factor to illustrate the crack arrest situation in a stiffened structure. Crack arrest occurs in a stiffened structure mainly due to a decreasing strain energy release rate G (or stress intensity factor) that falls below the crack resistance R as the crack approaches a stiffener.

Consider a simple case depicted in Figure 5-11, which consists of a strip bolted to a cracked plate at points A and B. In the presence of the strip, the crack surfaces cannot move apart freely as the crack approaches the strip. This acts as if the ends of the plate are fixed. As mentioned before, G decreases with crack length under fixed end condition. However this condition in the vicinity of the strip is only approximately true, such that if

the crack grows past the influence of the strip, G increases again as shown in Figure 5-11. The figure also shows that the largest reduction in G occurs if the crack tip is slightly beyond AB. The R curve is shown for plane strain condition for simplicity. In the absence of the strip, the G curve is straight and the applied stress to produce the G curve shown in the figure would have been high enough to cause fracture. However, since G is related to K by Equation 2-5, the C factor discussed in the previous section can be used to construct the G curve of a stiffened structure. From Equations 2-5 and 5-5, one obtains $G = C^2 \pi \sigma^2 a / E$. Thus the G curve of a stiffened structure is not a straight line but has a shape as shown in Figure 5-11 since the C factor varies with crack length. In addition, in the presence of the strip, G drops below R and crack arrest occurs when the kinetic energy of the crack is equal to zero.

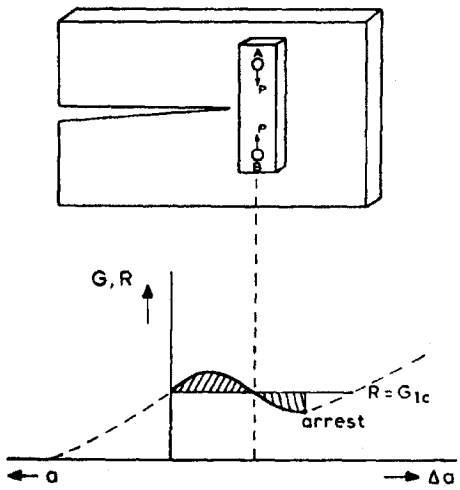

Figure 5-11 Bolted arrest strips [51]

Figure 5-12 depicts a more realistic representation of the energy state of a stiffened panel. In this figure the crack has extended to the centre line of the stringer and the R curve is shown to be steeply rising. Slow crack growth will commence at the stress σ_i. In the absence of the stringer, the G curve would be a straight line as indicated in dashed. Thus, at the stress of σ_{cu}, failure would take place with slow crack growth to B in an unstiffened panel. However, in a stiffened panel, the stress σ_{cu} will only cause

slow crack growth to point C. The stress must be further raised to σ_{cs} (with simultaneous slow crack growth to D), before final failure takes place. At this point G remains larger than R as the crack grows. On the other hand, it should be noted that if kinetic energy is taken into consideration, fracture could occur at a lower stress than σ_{cs}.

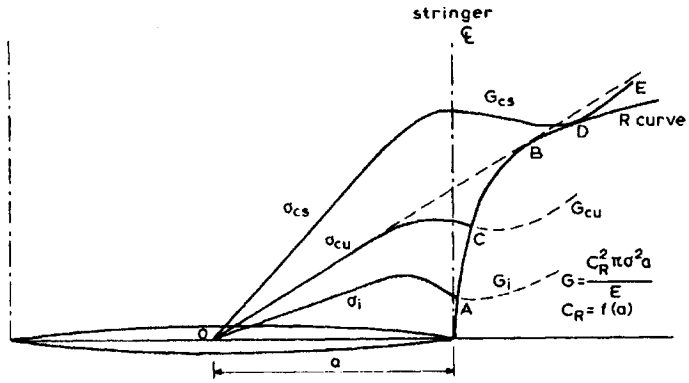

Figure 5-12 *R* curve concept for stiffened panel (crack extending to stringer) [51]

For the case of a short crack in a stiffened panel, the situation is more complicated, as depicted in Figure 5-13. As the crack is far away from the stringer, the G curve is straight until it reaches the vicinity of the stringer. Slow Stable crack growth starts at the stress σ_i and is arrested almost immediately at A. Since the part OA of the curve G_i is still straight, slow growth commences at the same stress σ_i as in the unstiffened panel.

At the stress σ_{cu}, unstable crack growth occurs, since the line G_{cu} is tangent to the R curve at point B. Since the part OB of the curve is also straight, σ_{cu} is the fracture stress in the unstiffened panel. However, fracture does not occur in the stiffened panel as the unstable crack growth is arrested at C, where the G curve drops below the R curve under the influence of the stringer.

As the applied stress increases, more slow crack growth follows until fracture occurs at the stress σ_{cs}, where G remains larger than R after point E. Again, any contribution of kinetic energy and any rate effect on R is disregarded in the discussion, which could result in a lower fracture stress in the stiffened panel than depicted. In

addition, in reality the *R* curve for a stiffened and unstiffened panel need not, and should not, be the same. Also stringer failure and fastener failure have not been incorporated into the foregoing figures. These issues are addressed in Section 5.5.

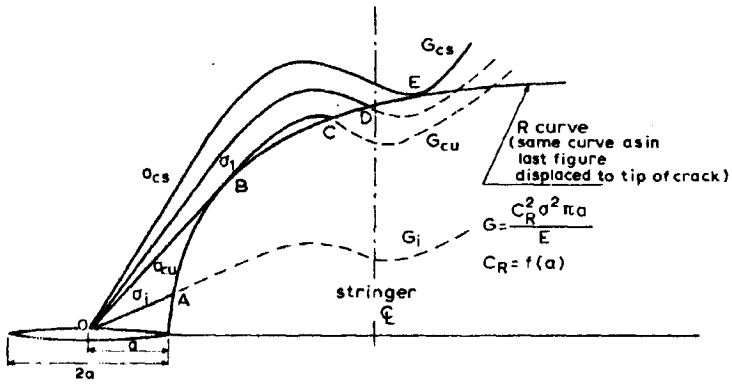

Figure 5-13 *R* curve concept for stiffened panel (short crack) [51]

5.4 Residual Strength of Stiffened Panel

The residual strength diagram provides a convenient means of determining the fracture stress of a stiffened structure. The calculation of the residual strength of a cracked stiffened panel is based on the residual strength properties of an unstiffened case by incorporating the *C* factor. From Equation 5-5, one obtains the residual strength of a stiffened structure as $\sigma_c = K_c / CY\sqrt{\pi a}$.

The residual strength of both a stiffened and unstiffened panel is plotted against crack length in Figure 5-14. The residual strength of the stiffened panel has the same basic shape as the *C* factor curve. When the crack is small and remote from the stringer, the influence of the stringer is small and the residual strength of the stiffened case is the same as that of the unstiffened case. However, as the crack grows in length, there is a continuous decrease in residual strength of the unstiffened panel while the residual strength increases as the crack approaches the stringer. The difference in residual strength between the two cases is the greatest at a point slightly beyond the centre line of the stringer. After that point the residual strength of stiffened panel starts to decrease.

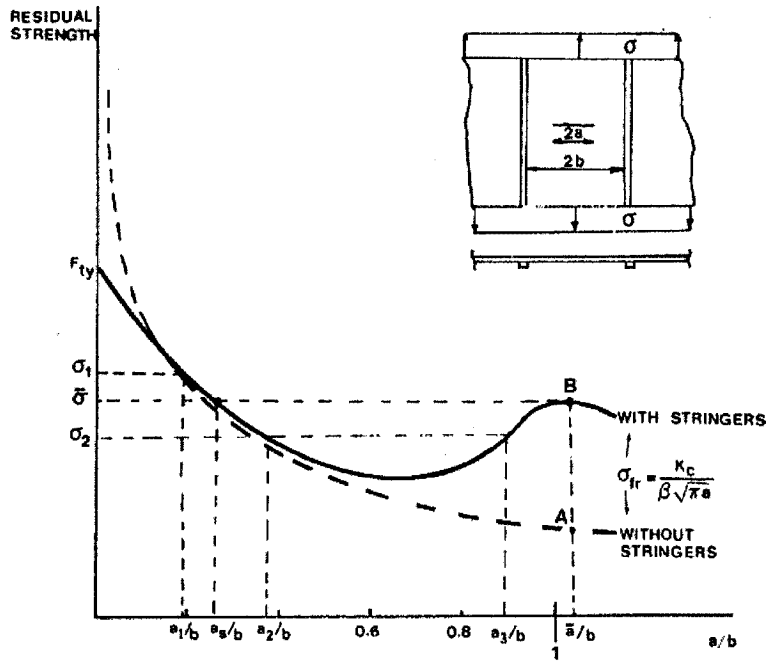

Figure 5-14 Residual strength diagram of stiffened panel [59]

Consider a crack of size a_2 in the stiffened panel. If a stress of σ_2 is applied to the panel, unstable crack growth will commence, as the residual strength is lower than σ_2 as the crack grows in length. However when the crack grows to a length of a_3, the residual strength is again equal to σ_2 and the residual strength increases above σ_2 afterwards. In order for fracture to continue, the applied stress must be increased. Thus, under constant applied stress of σ_2, the crack is arrested by the stringer at a crack length of a_3.

Based on the same reasoning, it can be seen that the stringer is able to arrest any crack with a length between a_s and $\bar{a}$, where the residual strength of the panel is less than $\bar{\sigma}$, which is the maximum value of residual strength that can be provided by the stringer. For a crack size less than a_s (a_1 for example), the residual strength, or fracture stress, is higher than $\bar{\sigma}$ such that crack arrest is not possible if the fracture stress is reached and maintained. It can be concluded from the residual diagram that stiffened structures can sustain larger damage. Whereas, at an applied stress of $\bar{\sigma}$, the unstiffened

panel would fail with a crack size of approximately a_s, the stiffened panel can tolerate a larger crack size up to $\bar{a}$.

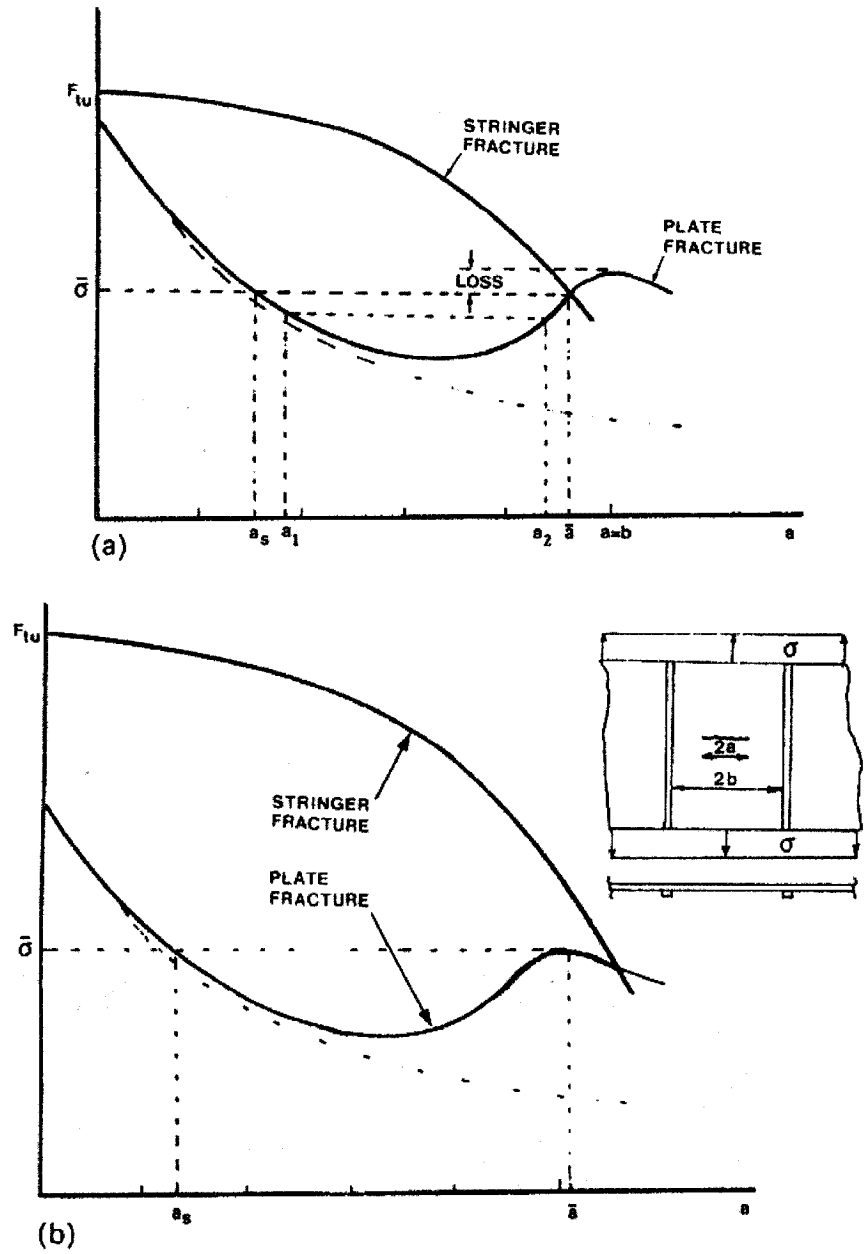

Figure 5-15 Effect of stringer on residual strength diagram: (a) Stringer critical; (b) Plate critical [59]

The foregoing discussion has ignored the residual strength of the stiffener and the fasteners. However, if the stress concentration in the stiffener and fasteners is sufficiently high to cause yielding and failure, then their residual strengths have to be

taken into consideration. The detrimental effects of stiffener and fasteners failure have on the fracture characteristics of the stiffened panel are discussed in more details in Section 5.5. For now the residual strength of the stringer shown in Figure 5-14 is plotted together with residual strength of the stiffened panel in Figure 5-15(a). The residual strength of the stringer, σ_{cs}, can be determined by its load concentration factor, L, and its tensile strength, σ_t, that is $\sigma_{cs} = \sigma_t / L$. The residual strength of the fastener can be calculated similarly using its own load concentration factor.

In Figure 5-15(a), a crack of size a_1 can be arrested at a_2. At this point, further increase in stress to $\bar{\sigma}$ leads to stringer fracture at crack size $\bar{a}$. The stringer then becomes ineffective and total fracture of the panel occurs. Thus, due to stringer fracture, the crack arrest stress is lower than the maximum possible value, which at the peak of the residual strength curve of the panel. This is an undesirable situation, as part of the stringer's crack arrest ability is not realized. One way to improve this situation is to select a stringer material with a higher tensile strength as shown in Figure 5-15(b). In this case fracture of the panel occurs before the stringer fails.

5.5 Crack Arrest Parameters in Stiffened Structures

In Section 5.2, several factors have been identified as having significant effects on the stiffener's efficiency. They are the attachment spacing, reinforcement spacing, and the relative stiffness parameter. In addition, the failure of the stiffener and the fasteners affect the overall effectiveness of a stiffened structure and are discussed in this section. Furthermore, the dynamic aspect of fracture in stiffened structure, which has been largely ignored up to this point, is addressed in this section. Finally, the fracture behaviour of integral and welded stiffeners, which differs from that of riveted and bolted stiffeners, is briefly presented in this section.

5.5.1 Dynamic Effects

Throughout this chapter the contribution of the kinetic energy as a crack driving force has been ignored. This can be justified by test data on stiffened panels showing that the contribution of kinetic energy as a crack driver is small. There are two reasons for this. The most important one is that when the crack passes the intact stringer, a large

amount of plastic deformation energy is absorbed by the stringer, so that the apparent energy required for crack advance is much larger than the skin crack resistance *R*. This is shown in Figure 5-16. This deformation energy is far greater than the kinetic energy even for large amounts of crack growth. A second reason is that the *R* curve for a stiffened panel steeply rises. As the kinetic energy is represented by the area between the *G* curve and the *R* curve the kinetic energy tends to be small. This also implies that the growth rate of the unstable crack is relatively slow in a stiffened panel.

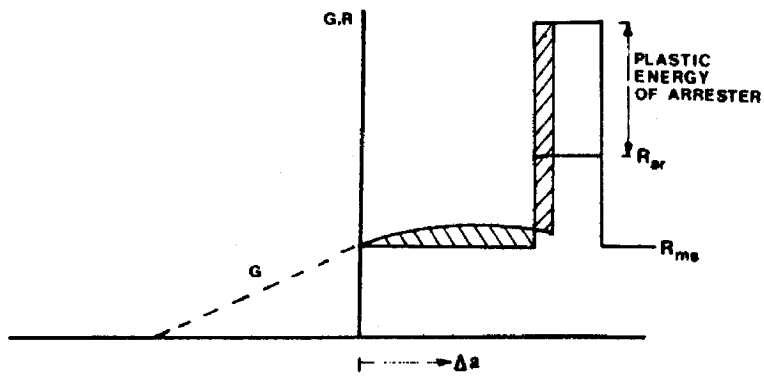

Figure 5-16 Stiffener plastic deformation [59]

5.5.2 Integral and Welded Stiffeners

Although this chapter is mainly focused on mechanically fastened stiffeners, the materials presented are also suitable for integral and welded stiffeners by considering very close fastener spacing. However, there are two fundamental differences in crack arrest behaviour between integral and welded stiffeners and mechanically fastened stiffeners. First, in case of a fatigue crack, crack arrest in mechanically fastened stiffeners can be achieved when the crack runs into a fastener hole. In case of integral or welded stiffeners, this option is not possible. In fact, there is no real crack arrest, but only a reduction of crack growth rate. Despite having no arrest in fatigue cracking, the overall crack propagation is slower in integral or welded stiffener. Second, in mechanically fastened stiffener, the skin crack grows under the stiffener so that the stiffener can remain intact. For integral or welded stiffener, the crack advances by growing into the stiffener and thereby severing it. The stiffener then loses its efficiency [131]. In general, the crack arrest capabilities for integral or welded stiffeners are not

well understood and test data of this type are limited. A more detailed discussion on welded stiffeners can be found in Section 5.6.

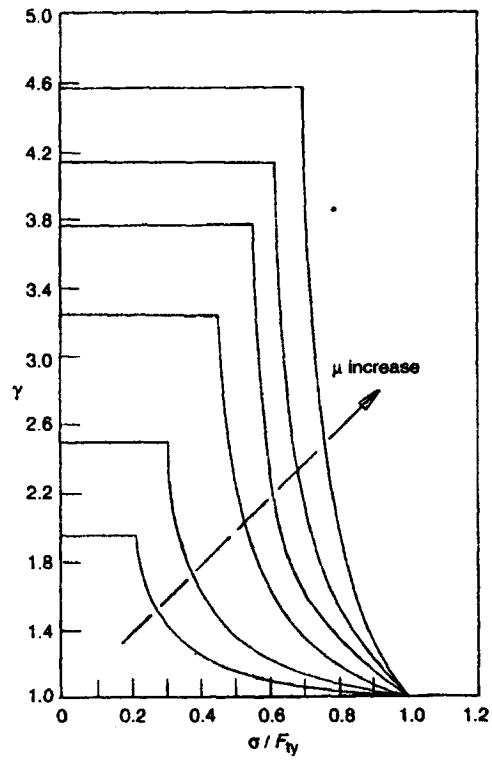

Figure 5-17 Effects of applied stress levels on the stiffener efficiency [107]

5.5.3 Stiffener Yielding

The efficiency of a stiffener drops once it starts to yield. This is particularly evident for stiffener having a small cross-sectional area. Figure 5-17 is a plot of the stiffener efficiency γ for various values of relative stiffness μ against the applied stress for a one bay crack. In the figure, F_{ty} is the yield strength of the stiffener. For a stiffener having a large μ, it can be seen that until the stiffener begins to yield, the yield strength does not play a role. The efficiency is constant, up to an applied stress that is close to the stiffener's yield strength ($\sigma \rightarrow F_{ty}$). After that point, there is a rapid drop in efficiency down to 1.0 at the stiffener's yield strength. However, for a stiffener having a small cross-section area (small μ), the drop in efficiency starts much earlier at a lower ratio of

applied stress to yield strength. Thus, when the effects of yielding are included, the difference in stiffener efficiency between the different sizes is very significant.

5.5.4 Stiffener Failure

Due to high stress concentration at the crack tip, the stiffener may break if its tensile strength is exceeded. In that case, not only is the stiffener no longer effective, the loads carried by the stiffener is also fed back into the cracked sheet, causing the stress intensity factor at the crack tip to suddenly increase.

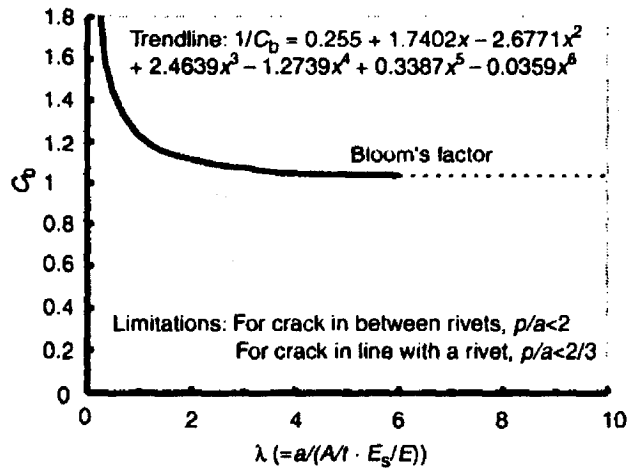

Figure 5-18 Effect of broken stiffener on stress intensity factor [107]

Consider the case of a two-bay crack with a centre broken stiffener shown in Figure 5-19. The stiffener efficiency factor of the intact edge stiffener γ is plotted against the relative stiffness parameter μ. γ is obtained by superposition of two separate cases, the case without a centre stiffener and the case involved with a broken stiffener alone. The stress intensity modification factor for the broken stiffener, C_b, is shown in Figure 5-18. Figure 5-19 shows that γ increases with μ up to a point. Since the load carried by the stiffener increases as a function of μ, the feed back load by the broken stiffener into the sheet increases also. At some point the stress intensity factor increase by the feed back load becomes greater than the reduction provided by the intact stiffeners, and their efficiencies decrease. Figure 5-18 also shows that a small stiffener can be just as

effective as a large stiffener in case of having a broken central stiffener. This could mean a saving of materials in stiffener design.

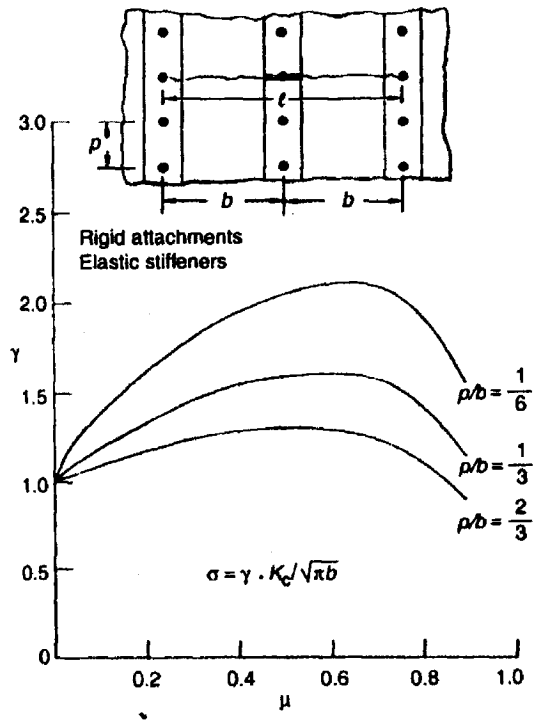

Figure 5-19 Stiffener efficiency factor for a two-bay crack with a centre broken stiffener [107]

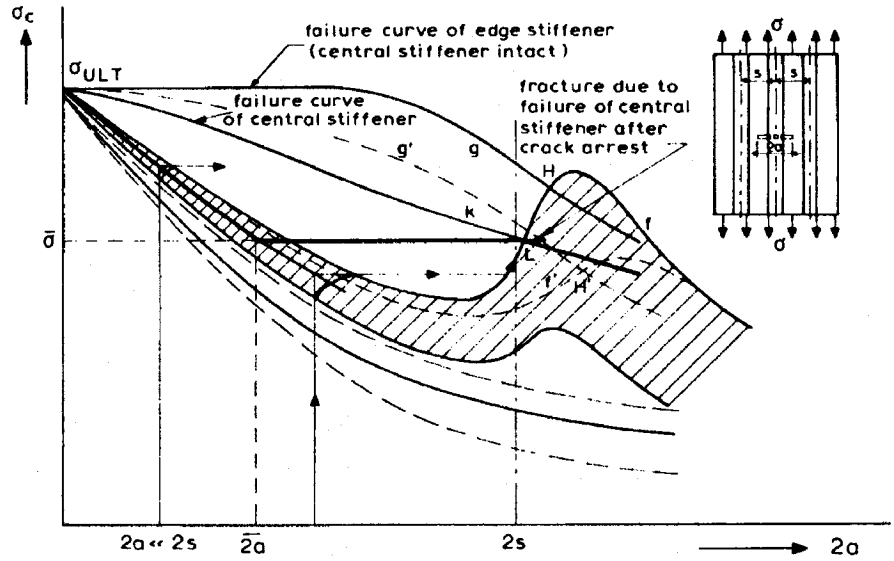

Figure 5-20 Residual strength diagram for a panel with three stringers and a central crack [51]

Now consider the residual strength diagram of the same situation shown in Figure 5-20. In this figure the failure curves of the skin, edge stiffener, and central stiffener are shown as curves f, g, and k respectively, if the central stiffener remains intact. The maximum crack arrest capability of the panel is then at L with a crack arrest stress of $\overline{\sigma}$. If the central stiffener is broken, then the skin and the edge stiffeners must carry extra load from the failed stiffener. Thus their failure curves f and g are lowered to f' and g', shown as dashed lines in Figure 5-20. The crack arrest stress is then reduced to the intersection of f' and g' at H'.

5.5.5 Fastener Failure

Similar to the stiffener, the fasteners that transfer the load from the skin to the stiffener experience increasing stress as the crack tip approaches. If the fastener loads become too high, fastener failure may take place by shear. When this occurs, the fastener is no longer effective in transmitting loads, causing the stress to increase in the skin and decrease in the stiffener. The residual diagram for this situation is depicted in the Figure 5-21. In this figure the residual strength of the fastener is included, which can be calculated from its shear strength and its load concentration factor. In the course of crack arrest, the shear strength of the fastener is exceeded at the intersection of curve f and h. Fastener failure causes the stress to rise in the skin and reduce in the stringer and their corresponding failure curve is lowered to f' and raised to g' respectively. The point of crack arrest is then lowered from H to H'.

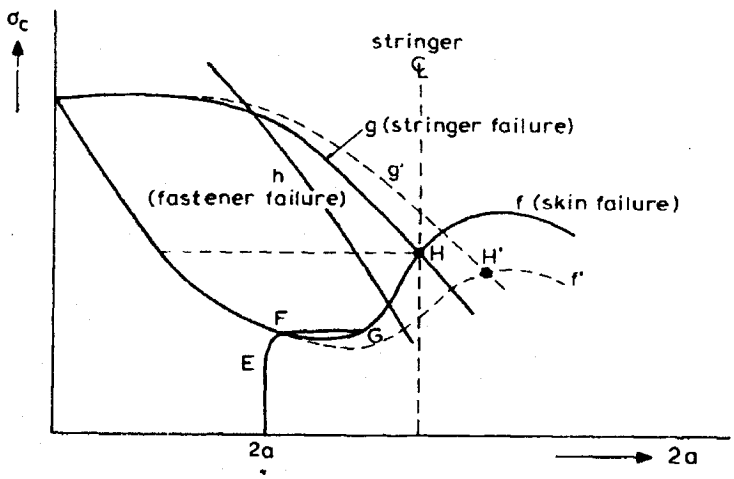

Figure 5-21 Criterion for fastener failure [51]

5.6 Welded Stiffeners

Much research has been performed in the past to address fatigue crack growth in aircraft, with the studies made on aluminum panels that have either riveted or adhesively bonded stiffeners. On the other hand, relatively few studies [23-29] have been conducted on welded stiffeners that are often found in ship structures. In case of welded stiffeners, there is no real crack arrest, but only a reduction of crack growth rate. In addition, the crack can grow into the stiffener and thereby severing it. The stiffener then loses its efficiency and its load is shed to the remaining net section of the base plate, causing a jump in the stress intensity factor. Furthermore, this type of stiffeners induces complex residual stresses in the structure that are caused by the heating and cooling effects of welding. The welded sites are also prone to containing regions of poor microstructure and defects. They are therefore frequently a source where fatigue cracks initiate. In general, the fatigue behaviour of welded stiffeners is not well understood and test data of this type are scarce. Nonetheless, the distribution of these residual stresses is recognized to have considerable influence on the fatigue crack growth rates of welded stiffened panel.

5.6.1 Residual Stresses in Welded Structures

In a welded stiffened plate, the heat generated during the welding of the stiffener causes thermal expansion in the weld and the base plate, in the vicinity of the weld. As the weld cools and contracts, the contraction is resisted by the surrounding base metal. As a result, in general, tensile residual stresses are found near stiffeners and weld lines as schematically shown in Figure 5-22(a), which in turn are equilibrated by compressive residual stresses between stiffeners. In addition, the distribution and the magnitude of the tensile residual stresses depend on welding sequence, weldment geometry and welding process and can be equal to or exceed the yield strength of the base plate material. On the other hand, the magnitude of the compressive residual stresses increases as the spacing between the stiffeners decreases. Furthermore, the thermal expansion and contraction may also cause distortion of the fabricated component as demonstrated by the exaggerated schematic example in Figure 5-22(b). Several remedial approaches can be

used to minimize these effects, including proper fit-up, proper sequencing and positioning of welds and preheating and postheating of the welded assembly [107].

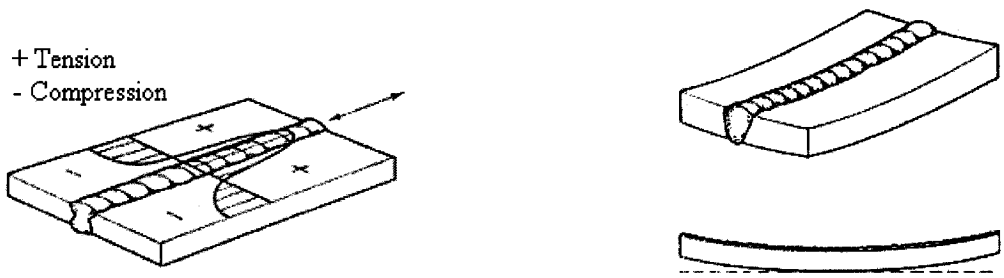

Figure 5-22 (a) Longitudinal residual stress; (b) Exaggerated distortion in the longitudinal direction for a butt-welded plate [114]

It is recognized that the fatigue life of welded structures is significantly affected by the welding residual stresses [23-29, 36-37, 132-136]. Nussbaumer [23, 25] studied the propagation of long fatigue cracks in multi-cellular box beams. He concluded that the compressive residual stresses between welded stiffeners caused variability in observed fatigue crack growth rates. In addition, the high tensile residual stresses at the intersection of the stiffener and panel reduced the amount of crack closure. Dexter *et al.* [26-29] further observed that the compressive residual stresses between the welded stiffeners significantly retarded the fatigue crack growth rates in the panel with the restraining effects of the stiffeners playing a minor role. In general, the compressive residual stresses between the welded stiffeners increase the amount of crack closure and retard the fatigue crack growth rates in the base plate. In fact, the compressive residual stresses are perhaps even more effective in retarding the fatigue crack growth rates than the restraining effects of the stiffeners. On the other hand, the tensile residual stresses near the stiffeners tend to accelerate the crack growth rates by reducing the amount of crack closure and thus allowing the fatigue loading to be more effective in propagating the crack.

Fatigue crack growth through a residual stress field can be described in terms of the effective stress intensity factor range, ΔK_{eff}, and the effective stress ratio, R_{eff}. As a fatigue crack propagates through a residual stress field, the residual stresses acting on the

crack faces produce residual stress intensity factors, K_{res}. By the principle of superposition, the residual stress intensity factor is added to the applied stress intensity factor produced by the fatigue loading; that is, the effective maximum and minimum applied stress intensity factor is taken as, respectively, $K_{max,eff} = K_{max} + K_{res}$ and $K_{min,eff} = K_{min} - K_{res}$. Assuming that the part of the fatigue cycle during which the crack is closed at its crack tip (*i.e.*, $K \le 0$) makes no contribution to crack growth, the fatigue crack growth rate within a residual stress field is governed by both the effective stress intensity factor range and the effective stress ratio given by the following equations:

$$\left.\begin{aligned} \Delta K_{eff} &= K_{max,eff} - K_{min,eff} = K_{max} - K_{min} = \Delta K \\ R_{eff} &= \frac{K_{min,eff}}{K_{max,eff}} = \frac{K_{min} - K_{res}}{K_{max} + K_{res}} \end{aligned}\right\} \text{when } K_{min,eff} > 0, \qquad (5\text{-}13)$$

$$\left.\begin{aligned} \Delta K_{eff} &= K_{max,eff} - K_{min,eff} = K_{max} + K_{res} \\ R_{eff} &= \frac{K_{min,eff}}{K_{max,eff}} = 0 \end{aligned}\right\} \text{when } K_{min,eff} \le 0. \qquad (5\text{-}14)$$

It is well known that the crack growth rate is significantly affected by the stress ratio; that is, in the same stress intensity factor range, the higher the stress ratio, the higher the crack growth rate. Thus, it can be seen from the above equations that the crack growth acceleration within a tensile residual stress field ($K_{res} > 0$) is determined by the increase in R_{eff} while ΔK_{eff} remains at ΔK. On the other hand, the crack growth retardation within a compressive residual stress field ($K_{res} < 0$) is attributed to both the decrease in R_{eff} and the potential reduction in ΔK_{eff}.

From the above discussion, it can be seen that residual stress plays an important role in the fatigue behaviour of welded structures. One approach to calculate the residual stress intensity factor is by finite element analysis. The general procedure for simulating the residual stress field using the finite element method is described in the next section while the detailed description of the finite element model in the present work can be found in Chapter 10. However, if the residual stress distribution on the crack faces is known, the residual stress intensity factor can be derived using the so-called Green's functions. For example, the left hand side of Figure 5-23 shows the Green's function for

calculating the stress intensity factor caused by a pair of splitting forces F acting on the crack surfaces. For a stress field σ acting on the crack surfaces, the splitting forces can be written as σdx as shown in the right hand side of Figure 5-23. The residual stress intensity factor can then be obtained by integrating the Green's function over the length of the crack *a*, which results in the following equation:

$$K_{res} = \sqrt{\pi a}\frac{2}{\pi}\int_0^a \frac{\sigma_{res}(x)}{\sqrt{a^2 - x^2}}dx, \tag{5-15}$$

where $\sigma_{res}(x)$ is the distribution of the residual stress acting on the crack surfaces. In the present work, both the finite element method and the Green's function were used to calculate the residual stress intensity factor of welded stiffened steel plates in order to predict the fatigue crack growth rates and the results are presented in Chapter 10.

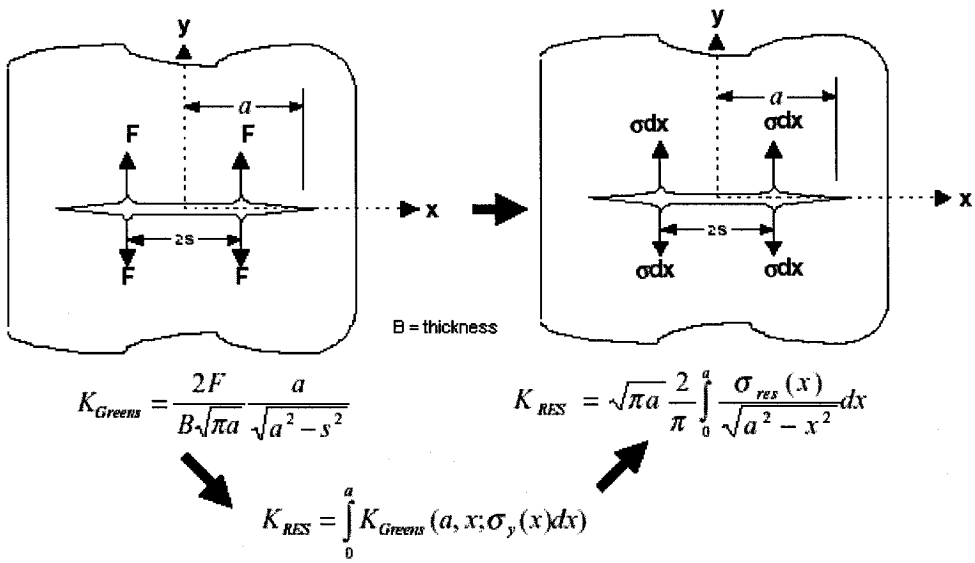

Figure 5-23 Use of Green's function to develop the stress intensity factor due to the residual stress field [137]

5.6.2 Measurement and Simulation of Residual Stresses

The most common experimental techniques for the determination of residual stresses in welded structures are the hole drilling, X-ray diffraction and neutron diffraction. The hole drilling is a destructive technique that involves the drilling of a hole at the centre of a strain gauge rosette attached to the specimen's surface to relieve the residual strains. The residual stress field is then deduced from the recorded strain

relaxation. However, only near surface stresses up to 2 mm depth can be evaluated using this technique and the results have lower accuracy and more scatter than the other two techniques.

The X-ray diffraction method uses X-rays to determine the spacing of the lattice planes in a polycrystalline material. In this method, the crystal lattice effectively acts as a very small strain gauge. Strain is determined by the change in angular position of the diffracted X-rays. However, as in the case of hole drilling, only very near surface residual stresses can be measured as the penetration depth of X-rays is a few tens of micrometers at most.

The neutron diffraction method is a relatively new technique, which in principle is similar to the X-ray diffraction method. However, neutrons have a significant advantage over X-rays in the form of a much larger penetration depth that neutrons can obtain, which makes them capable of making through-thickness measurements of up to 50 mm in steel and 140 mm in aluminum. Thus, it is the only method which permits the determination of all residual stress tensor components for thicker components. On the other hand, the technique is only available at laboratories with high-flux nuclear reactors or accelerator-induced neutron sources.

In addition to experimental measurements, residual stresses in welded structures have also been effectively simulated by finite element analysis [38-40, 45-50]. One such approach, adopted in the present work, is an uncoupled thermal and thermo-mechanical analysis, in which a heat transfer analysis was performed first to calculate the temperature history during welding and subsequent cooling of the weldment. The transient temperature outputs from this analysis are saved, which are then used as thermal loads in the subsequent thermo-mechanical analysis. In the thermo-mechanical analysis, the thermal loading causes thermal expansion and volumetric change in the model and the resulting residual stresses are calculated.

To summarize, each of the experimental techniques for the determination of residual stresses has its disadvantage; that is, hole drilling is semi-destructive, the penetration of X-ray is poor and neutron diffraction requires expensive equipments. Therefore, the motivation of the present research was to investigate whether a finite

element approach could provide an adequate alternative for evaluating the residual stresses and their influence on the fatigue of welded stiffened steel plates.

5.6.3 Principle of Neutron Diffraction

Neutron diffraction is a versatile and nondestructive technique used in research areas such as materials science and engineering, magnetism and superconductivity, surfaces and interfaces, molecular structures and dynamics and biomaterials. The method can provide residual stress measurements ranging from the surface to well inside a specimen.

When an incident neutron beam, of wavelength λ, strikes a specimen (Figure 5-24), the beam will be scattered in all directions by the atoms in the material that lies within the beam's path. Some of these scattered waves mutually reinforce one another if they are in phase, producing a so-called diffracted beam. This is made possible if the path length difference between the scattered waves is an integral number of the wavelengths, $n\lambda$ [138]. This necessary condition for the formation of a diffracted beam is described by Bragg's law, which relates the angle of the diffracted neutron beam, θ, to the spacing between the diffracting planes of atoms, d, and the wavelength, λ:

$$n\lambda = 2d\sin\theta . \tag{5-16}$$

According to Bragg's law, a change in the distance between the planes of atoms results in a change in the angle of the diffracted beam, from which strain measurements, ε, can be calculated:

$$\varepsilon = \frac{d_f - d_o}{d_o}, \tag{5-17}$$

where d_o is the reference spacing of the atomic planes in the unstrained condition and d_f is the corresponding spacing in the strained condition. Thus, the neutron diffraction method for strain measurement is a two step process that involves first scanning of a reference, unstrained specimen and then of the deformed specimen.

The stresses, $\{\sigma\}$, are then calculated from the strain measurements, $\{\varepsilon\}$, by the theory of elasticity:

$$\{\sigma\} = [C]\{\varepsilon\}, \tag{5-18}$$

where [*C*] is the stiffness matrix of the material. It should be noted that the normal to the diffracting planes, and hence the component of the strain measurement, is in the direction of the scattering vector, Q, which bisects the incident and diffracted beams.

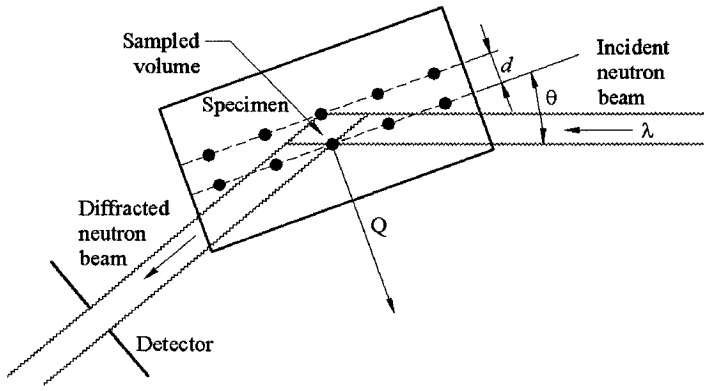

Figure 5-24 Principle of neutron diffraction

In the present work, the fatigue behaviour of welded stiffened centre-cracked 350WT steel plates was studied. Using the neutron diffraction method, the residual stress fields near the fatigue crack tips in the steel plates were derived. The residual stress intensity factors produced by the measured residual stress fields were then calculated using the Green's function in order to determine the effective stress intensity factors. The residual stress fields were also simulated by the finite element method, which consisted of heat transfer analysis followed by nonlinear static analysis. Following the residual stress simulation, the effective stress intensity factors were computed from fracture mechanics analysis. Finally, the fatigue crack growth rates of the stiffened plates were predicted using the effective stress intensity factors from both methods and compared to the experimental results from fatigue testing. The details of this investigation are presented in Chapter 10.

Chapter 6 Proposed Modification to a Constant Amplitude Fatigue Model

6.1 Introduction

Many fatigue crack growth models, such as the well known Paris model [7], include empirical parameters that have no physical basis. Such models are material dependent which require calibrations from the fatigue testing of each different material. Fatigue testing is expensive and time-consuming; therefore it is desirable to employ fatigue models that have some physical significance by using known material properties from less lengthy tests. One such attempt is the Zheng and Hirt model [8], which does not require several fatigue testing to establish the empirical parameters required by most models. It relies on the tensile properties and the threshold value, thus making it a cost effective fatigue crack propagation methodology. The Zheng and Hirt model is moderately successful in predicting fatigue crack growth rates and this chapter presents a modification made to the model in order to improve its accuracy.

6.2 Background

6.2.1 Description of Zheng and Hirt Model

The Zheng and Hirt model is a constant amplitude loading fatigue model for metals. It is itself a modification of the static fracture model proposed by Lal and Weiss [109], which assumes that the crack growth per loading cycle is equal to the distance in which the maximum normal stress, σ, is greater than the critical fracture stress σ_{ff} of the metal, as shown in Figure 6-1. From this assumption, the following equation can be derived from linear elastic fracture mechanics:

$$\frac{da}{dN} = B\Delta K_{eff}^2 = \frac{1}{2\pi\sigma_{ff}^2}(\Delta K - \Delta K_{th})^2, \tag{6-1}$$

where $B = \frac{1}{2\pi\sigma_{ff}^2}$, $\Delta K_{eff} = \Delta K - \Delta K_{th}$, da/dN is the crack growth per cycle, ΔK is the applied stress intensity factor range and ΔK_{th} is the fatigue crack growth threshold. The critical fracture stress σ_{ff} is in turn taken as the theoretical strength of metallic materials:

$$\sigma_{ff} = \sqrt{E\sigma_f \varepsilon_f}\,, \tag{6-2}$$

where E is the modulus of elasticity and σ_f and ε_f are the material's fracture strength and fracture ductility, respectively. The fracture strength and fracture ductility are given in [105] as:

$$\sigma_f = \sigma_{ult}(1 + RA), \tag{6-3}$$

$$\varepsilon_f = -\ln(1 - RA), \tag{6-4}$$

where σ_{ult} is the ultimate stress and RA is the reduction in area at fracture in a tension test.

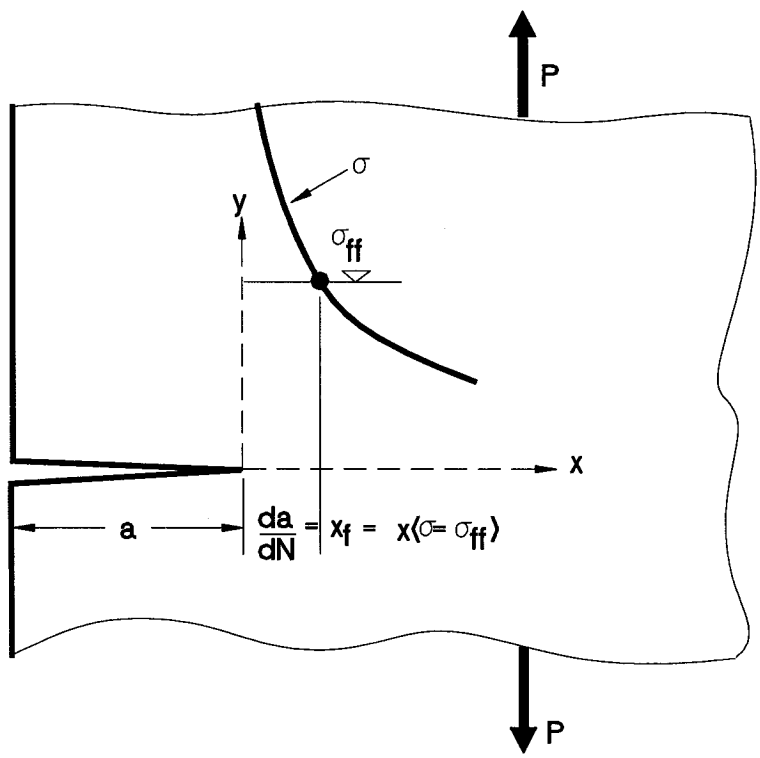

Figure 6-1 Schematic illustration of the assumption of the amount of incremental fatigue crack propagation (Reproduced from [8])

6.2.2 Reanalysis of Existing Test Data

A reanalysis of fatigue crack propagation test data for various steels was done in [8] to compare the predicted values of B from tensile properties and the reanalyzed values. The reanalysis involved taking the logarithmic transformation of Equation 6-1 to obtain:

$$\log\frac{da}{dN} = \log B + 2\log(\Delta K - \Delta K_{th}), \tag{6-5}$$

which represents a straight line with slope 2 when $\log(da/dN)$ is plotted against $\log(\Delta K - \Delta K_{th})$. The values of B and ΔK_{th} were obtained by trial and error such that the slope is approximately 2 in a linear regression analysis. The results of the reanalysis are shown in Table 6-1. It can be seen that Equation 6-1 over predicted the value of B in most cases. The ratio of the predicted value of B to the reanalyzed value of B ranged from 0.07 to 4.30.

6.2.3 Proposed Modification to the Model

In the Zheng and Hirt model the fracture strength of the material is calculated in Equation 6-3 from the ultimate stress of the material. However, it is questionable whether the ultimate stress, defined as the maximum nominal stress attained in a conventional tension test, can be related to the stress at fracture. Instead, the fracture strength of the material should be obtained from the measured true stress at fracture in a tension test, calculated from the final fracture load and the final fracture area. It is therefore postulated that using such a measured fracture strength of the material should provide a better predicted value of B in Equation 6-1.

In order to verify the above hypothesis, an experimental investigation was performed on a sample of steel. The investigation consisted of performing tension tests to obtain the tensile properties of the steel, a constant amplitude loading fatigue test to provide baseline fatigue data, a fatigue crack growth threshold test to determine the threshold value and a reanalysis of the baseline fatigue data to compare the predicted values of B from using Equation 6-3 and from the measured true fracture strength of the steel. The following sections describe the fatigue testing procedure and discuss the results of the tests.

Table 6-1 Reanalyzed results for various steels (Reproduced from [8])

	Material	σ_{ult} (MPa)	σ_{yld} (MPa)	RA (%)	Stress Ratio R	B (10^{-10} MPa^{-2}) Reanalyzed	B (10^{-10} MPa^{-2}) Predicted	ΔK_{th} (MPa m$^{1/2}$)	$B_{Predicted}/B_{Reanalyzed}$
Martensite Steels	18Ni(900)	1769	1679	31.0	0.05-0.2	8.67	9.29	11.15	1.07
	18Ni(1100)	1587	1493	35.6	0.05-0.2	8.37	8.50	7.76	1.02
	4340(200)	2324	1325	17.2	0.05-0.2	197	15.5	19.90	0.08
	4340(500)	1714	1521	26.3	0.05-0.2	13.7	13.6	14.05	0.99
	H-11	1958	1424	31.8	0.05-0.2	137	9.10	19.86	0.07
	D6AC	1618	1499	36.5	0.1-0.3	4.53	7.73	6.78	1.71
	12Ni-5Cr-3Mo	1290	1269	64.0	0-0.7	2.72	3.70	2.73	1.36
	H-130	1015	936	70.0	0-0.7	3.14	3.70	2.24	1.18
	10Ni-Cr-Mo-Co	1434	1310	72.0	0-0.7	2.11	2.47	8.53	1.17
	9Ni-4Co-0.25C	1338	1257	61.0	-0.1-0.25	41.0	3.87	27.86	0.09
	10Ni-8Co-Mo	951	917	69.0		3.06	4.11	4.65	1.34
	30CrMnSiNi2	1676	1387	45.0	0.2	7.42	5.59	2.26	0.75
Pearlite-ferrite Steels	A357A	569	405	73.0	0-0.7	5.38	5.99	10.17	1.11
	A302B	604	384	67.0	0-0.7	4.27	6.93	11.37	1.62
	A36	514	247	68.0	0-0.7	3.59	7.84	10.06	2.18
	ABS-C	432	268	66.0	0-0.7	3.21	9.98	9.62	3.11
	SAE0030	494	302	46.0	0	7.54	17.4	17.60	2.31
					-1	5.95	17.4	20.01	2.92
	SAE1020	412	261	58.0	0	14.8	13.7	24.71	0.93
					-1	16.8	13.7	21.00	0.82
	A572	535	370		0	5.95	8.92	20.01	1.50
					-1	9.09	8.92	20.88	0.98
Quenched-tempered Steels	4340(1000)	1205	1120	38.8	0.05-0.2	9.03	9.46	13.28	1.05
	4340(1400)	665	431	53.3	0.05-0.2	16.4	9.97	21.00	0.61
	AISI403(Heat637)	769	641	56.5		2.61	7.65	6.45	2.93
	AISI403(Heat933)	748	611	53.1		4.23	8.92	8.31	2.11
	AISI403(Heat484)	817	678	48.5		2.23	9.60	7.43	4.30
	5Ni-Cr-Mo-V	1043	974	68.0	0.1	2.30	3.87	5.79	1.68
	SAE4140(720)	1468	1372	55.0	0	1.25	4.25	-4.48	3.40
					-1	1.43	4.25	-1.20	2.97
	SAE4140(970)	1146	1098	59.0	0	1.32	4.72	5.79	3.58
					-1	2.95	4.72	9.40	1.60
	SAE4140(1230)	720	617	63.0	0	2.07	6.63	13.23	3.20
					-1	2.66	6.63	11.59	2.49

6.3 *Experimental Procedure*

6.3.1 Overview

The experimental fatigue crack propagation testing consisted of subjecting centre-cracked specimens of 350WT steel to a constant amplitude loading test and a fatigue

crack growth threshold test. All fatigue crack growth tests were conducted in accordance with ASTM Standard E647, *Standard Test Method for Measurement of Fatigue Crack growth Rates* [139]. The test method covers the determination of fatigue crack growth rates from fatigue testing, including discussions on special requirements for various specimen configurations and recommended techniques from calculating the fatigue crack growth rates.

6.3.2 Test Material

The 350WT Category 5 steel used in the present investigation was provided by Defence Research & Development Canada – Atlantic. This type of steel is both weldable and notch tough at low temperature with a minimum required yield strength of 350 MPa and a Charpy V-Notch toughness of at least 40 J at $-40°C$. It is a typical material used in the hull of City class frigate as well as Canadian bridges, pressure vessels and offshore structures. The chemical composition of the steel is presented in Table 6-2.

Table 6-2 Chemical composition of 350WT steel [6]

Specimen, %	Element	350WT, %
0.075	Carbon	0.22 max
0.034	Chromium	...
0.016	Cobalt	...
0.010	Copper	...
1.250	Manganese	0.80 - 1.50
0.006	Molybenum	...
0.300	Niobium	...
0.008	Nickel	...
0.009	Phosphorus	0.03 max
0.230	Silicon	0.15 - 0.40
0.052	Vanadium	...
0.004	Sulphur	0.03 max

A total of three tension tests (ASTM E8M [140]) were performed on the steel to calculate the parameters in the Zheng and Hirt fatigue model and the average results are

shown in Table 6-3. It can be seen that the measured true fracture strength (870 MPa) is slightly higher than the fracture strength (836 MPa) calculated from Equation 6-3. It should be noted that the measured true fracture strength had been corrected by the Bridgeman correction factor [58].

Table 6-3 Material properties of 350WT steel

Material Property	Value
Yield Strength, σ_{yld}	365 MPa
Ultimate Strength, σ_{ult}	496 MPa
Reduction in Area, RA	68%
Modulus of Elasticity, E	200 GPa
Poisson's Ratio, ν	0.3[1]
Fracture Strength, σ_f	870[2]/836[3] MPa
Fracture Ductility, ε_f	1.15[4]

[1] From [6]

[2] Determined experimentally

[3] Equation 6-3

[4] Equation 6-4

6.3.3 Test Specimen

The 350WT steel test specimens used in the fatigue tests were middle tension rectangular specimens with a centre-crack. ASTM E647 provides recommended dimensions and equations for calculating the stress intensity factor for such a specimen. The test specimen layout and dimensions are shown in Figure 6-2. The specimens were cut lengthwise in the rolling direction of the steel such that the fatigue cracks would grow perpendicular to the rolling direction. Seven grip holes of approximately 11 mm (7/16 in) diameter were drilled at each ends of each specimen to accommodate the grips of the test fixture. A small hole of 3.2 mm (1/8 in) diameter was drilled at the centre of the specimen to allow a starter notch to be machined from each side of the hole. The starter notch for each specimen was done at the Halifax Dockyard machine shop by the electrical discharge machining (EDM) process, resulting in a notch width of 0.254 mm (0.010 in). The specimen's surface was then polished to provide a clear image of the

crack tip when observed under a microscope. In summary, the overall specimen dimensions were approximately 300 mm long x 100 mm wide x 5 mm thick, with a starter notch length (2a) of approximately 20 mm.

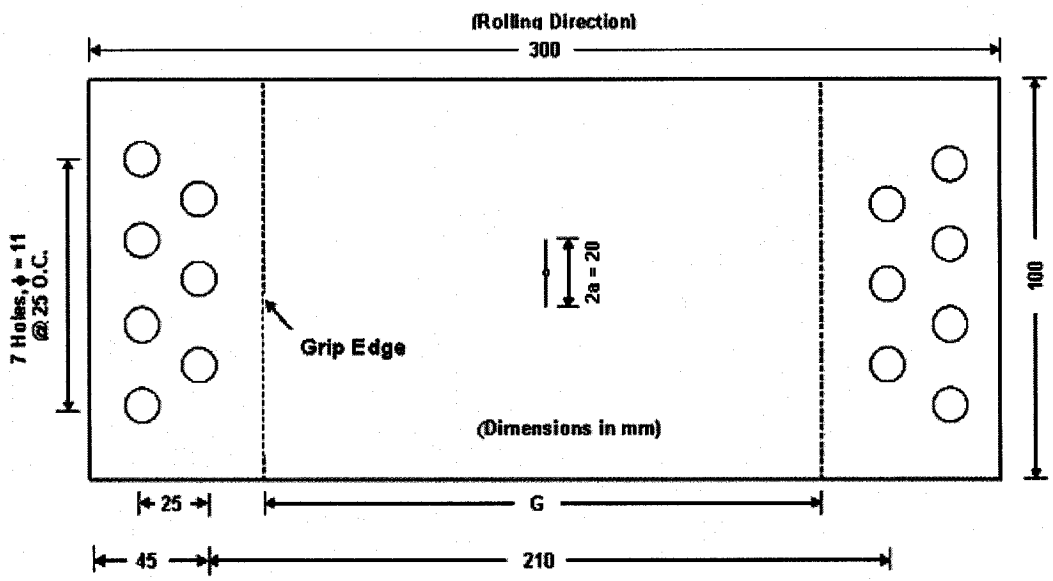

Figure 6-2 Specimen layout and dimensions [6]

6.3.4 Test Apparatus

An Instron model 8501 (Canton, MA) servo-hydraulic universal testing machine was used to perform the fatigue testing. The machine employed an Instron digital control panel (model 8500^{+}) and a load cell with a capacity of $\pm$ 100 kN and 200 kN under dynamic and static loading conditions, respectively. Each of the test specimen was mounted to the machine by the way of grips and fixtures, which were screwed into the load cell at the top and the actuator at the bottom of the load frame. A traveling microscope consisting of a microscope at 10X magnification attached on top of two micrometers with a resolution of 0.01 mm each was used to measure incremental fatigue crack growth. Finally, a fibre optic light was used to illuminate the specimen surface. The completely assembled experimental setup is shown in Figure 6-3.

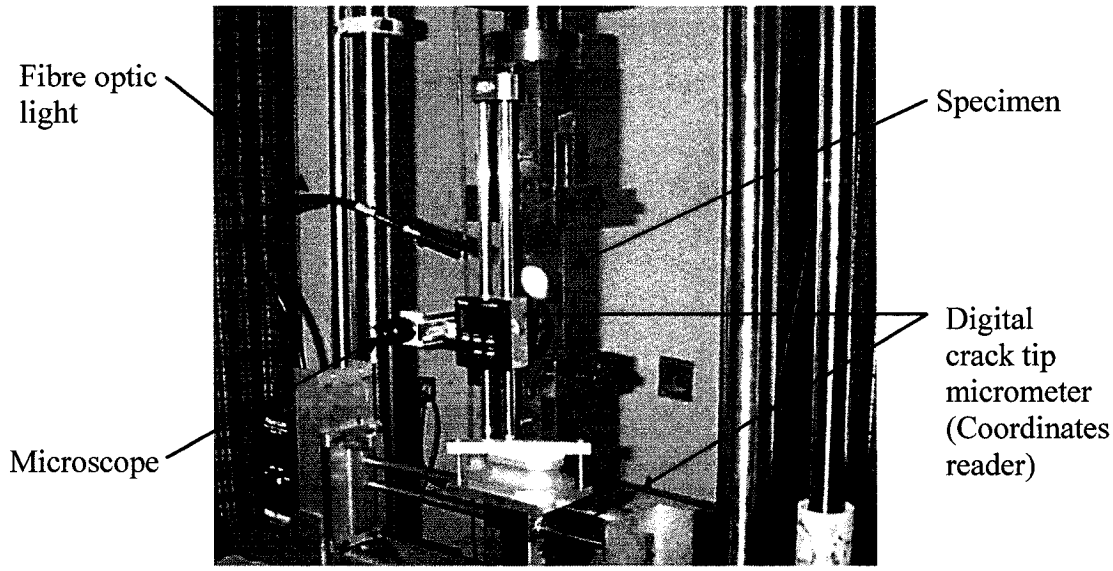

Figure 6-3 Completely assembled test setup

6.3.5 Test Procedure

All fatigue tests were performed in accordance with ASTM E647 under load control, with the fatigue loading on the specimens comprised of axial tension in a sinusoidal wave form at room temperature in air. In all cases, the baseline constant amplitude loading consisted of cycles at maximum load, $P_{max,CAL}$, of 60 kN and stress ratio R of 0.1 at a load frequency of 20 Hz. Each specimen were precracked to a minimum length of 1.0 mm from both sides of the starter notch as required by ASTM E647 to remove the effect of the blunt starter notch and provide a sharpened fatigue crack of adequate size and straightness before valid crack length data could be recorded. The crack length was then measured periodically with the help of the traveling microscope until fracture. The crack length data was calculated by the average of the left and right cracks and then reduced to fatigue crack growth rate data by both the secant and the incremental methods as recommended by ASTM E647.

6.4 Experimental Results and Discussion

6.4.1 Constant Amplitude Loading Test Results

The constant amplitude loading test involved testing a specimen at the baseline constant amplitude loading described above until failure. The results are presented by

plotting the crack growth rate (ΔK) against the corresponding stress intensity factor range (da/dN), or fatigue rate curve, in Figure 6-4. The Paris equation for this specimen was given by:

$$da/dN = \begin{cases} 1.66\times10^{-13}(\Delta K)^{4.06} & \text{, when} \quad \Delta K < 26.5 \text{ MPa}\cdot\text{m}^{1/2} \\ 4.45\times10^{-12}(\Delta K)^{3.06} & \text{, when} \quad \Delta K \geq 26.5 \text{ MPa}\cdot\text{m}^{1/2} \end{cases}, \tag{6-6}$$

where da/dN is in m/cycle and ΔK is in MPa $\text{m}^{1/2}$.

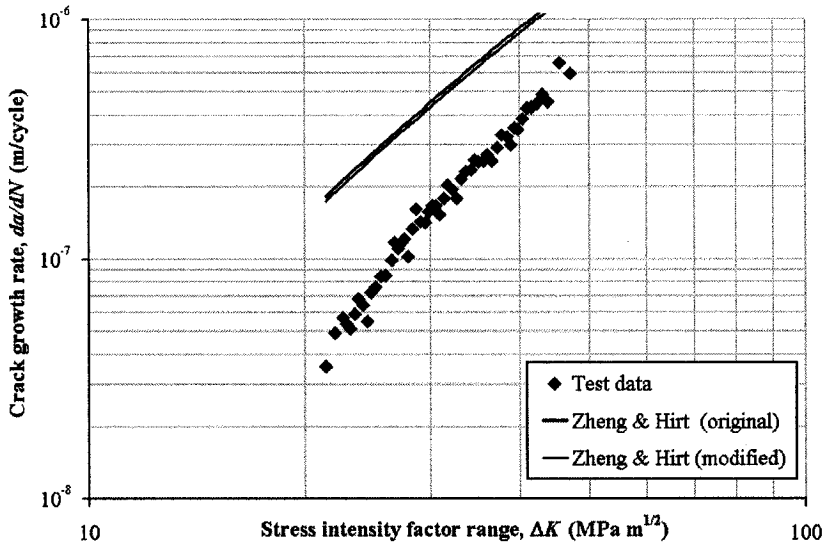

Figure 6-4 Fatigue rate curves from constant amplitude loading test and from Zheng and Hirt prediction

6.4.2 Fatigue Crack Growth Threshold Test Results

The fatigue crack growth threshold test involved testing a specimen at constant amplitude loading but reducing the maximum load by 10% in successive steps while keeping the stress ratio at 0.1 until fatigue crack growth rates between 10^{-9} to 10^{-10} m/cycle were achieved. The operational fatigue crack growth threshold, ΔK_{th}, as defined in the ASTM E647, was then obtained by linearly extrapolating the fatigue crack growth data to a fatigue crack growth rate of 10^{-10} m/cycle on a log-log graph as shown in Figure 6-5. A value of ΔK_{th} = 6.55 MPa $\text{m}^{1/2}$ was obtained in the present study, which is similar to 5.56 MPa $\text{m}^{1/2}$ reported in [2].

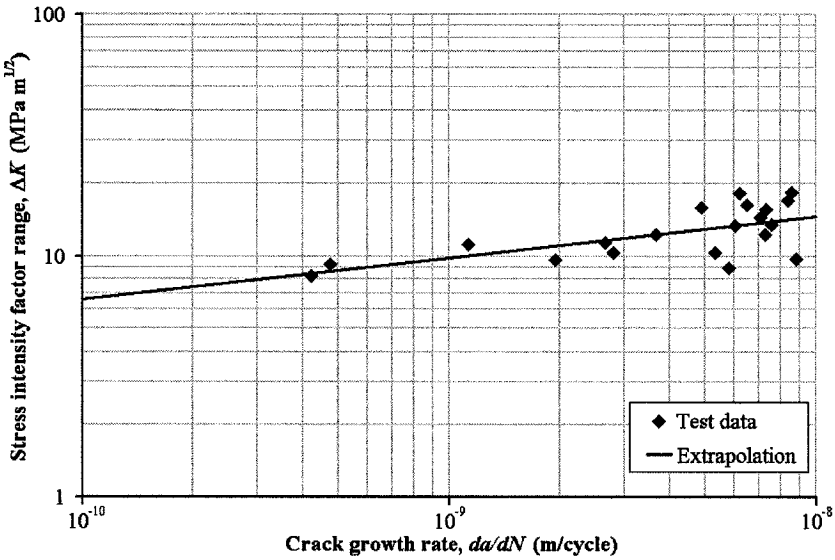

Figure 6-5 Fatigue crack growth threshold test results and extrapolation

6.4.3 Fatigue Crack Growth Prediction by the Modified Zheng and Hirt Model

From the above testing, the tensile properties and the fatigue crack growth threshold were obtained for the 350WT steel. The modified Zheng and Hirt model for the steel, using the measure fracture strength, was then given by Equation 6-7:

$$\frac{da}{dN} = 7.91\times10^{-10}(\Delta K - 6.55)^2, \tag{6-7}$$

where da/dN is in m/cycle and ΔK is in MPa $m^{1/2}$. The equation is plotted along with the constant amplitude loading test data in Figure 6-4. It can be seen that the model over predicted the fatigue crack growth rates of the specimen and thus would give a conservative estimate of its fatigue life.

A reanalysis similar to that done in [8] was performed to obtain the best-fit values of B and ΔK_{th} to the test data. After taking the square root of Equation 6-1, it becomes:

$$\sqrt{\frac{da}{dN}} = \sqrt{B}\Delta K - \sqrt{B}\Delta K_{th}, \tag{6-8}$$

which represents a straight line with slope $\sqrt{B}$ when $\sqrt{da/dN}$ versus ΔK is plotted. Thus a linear regression analysis would give the best-fit values of B and ΔK_{th} to the test data. Such an analysis yielded the following equation:

$$\frac{da}{dN} = 5.12\times10^{-10}(\Delta K - 12.65)^2. \tag{6-9}$$

It can be seen that the ratio of the predicted value of B from tensile properties to the reanalyzed value of B was 1.26, which was within the range calculated from the data in [8]. Note that if Equation 6-3 was used to calculate the fracture strength of the steel instead, the predicted value of B would be 8.23×10^{-10}, which over predicts the fatigue crack growth rates slightly more, as shown in Figure 6-4. Therefore, although both methods of calculating the fracture strength of the steel resulted in over predicting its fatigue crack growth rates, using the measured fracture strength was shown to provide a better prediction than using Equation 6-3 to calculate the fracture strength.

Finally, based on the present results, it is proposed that a different definition of the critical fracture stress σ_{ff} from the conventional tensile properties of the material, or perhaps the development of a new experimental technique for determining such critical fracture stress, might further improve the accuracy of the predicted value of B.

6.5 Conclusions

The Zheng and Hirt constant amplitude fatigue model describes the fatigue behaviour of metals based on the tensile properties, thus eliminating the need for extensive fatigue crack propagation tests as required by other fatigue models. The model uses the fracture strength of the material based on a relationship. A modification was proposed to the model, using the measured fracture strength of the metal instead of the calculated strength. Standard tension tests were performed to determine the tensile properties, in particular the true stress at fracture of 350WT category 5 steel. In addition, fatigue crack growth threshold tests were performed to determine the necessary model parameter. Finally, constant amplitude loading fatigue tests were performed on the steel to evaluate the modifications to the model. Based on the analysis of tests results, it is concluded that the proposed modified Zheng and Hirt model using the measured fracture strength of the metal provides a better estimate of its fatigue crack propagation rates.

Chapter 7 Proposed Modifications to a Fatigue Retardation Model

7.1 Introduction

A fatigue induced crack acts as a severe stress raiser in a structure, forming a zone of plastic deformation and residual stresses ahead of the crack tip. This zone can also be called a load interaction zone since the residual stresses within the zone interfere with the applied stresses to the crack and thereby affecting its fatigue crack growth rates. A well known load interaction effect is the retardation of the fatigue crack growth rates following the application of single or multiple tensile overloads within constant amplitude fatigue loading. This occurs due to the presence of a larger zone of compressive residual stresses ahead of the crack tip produced by the overloads, resulting in crack tip blunting, crack closure and increased level of crack opening stress in the subsequent fatigue cycles.

Figure 7-1 shows a typical crack growth rate curve showing retardation following a single tensile overload. For a number of materials, it has been observed that an initial acceleration of the fatigue crack growth rate occurs immediately after an overload. The crack growth rate then decelerates to a minimum value at some point ahead of the overload application, at which point the rate gradually returns to its steady state value. The phenomenon is also known as the "delay retardation" [10, 83-85]. In addition, when multiple tensile overloads are closely applied, they may interact with each other to either enhance or reduce to overall crack growth retardation. Such overload interaction is dependent on the relative magnitude and the spacing between the overloads [11, 76, 86-89], or the frequency of the overload application [90-94]. In other words, the overall crack growth retardation may be maximized by applying overloads at certain distances apart or at certain frequencies. At the same time, due to the aforementioned initial crack growth acceleration immediately following an overload, overloads that are applied too closely or too frequently can lead to decreased overall crack growth retardation or even crack growth acceleration. Furthermore, it was observed in the experimental portion of the present work that crack growth retardation is reduced in the latter stage of the fatigue

life when the net section stress of the specimen approaches the yield strength of the material.

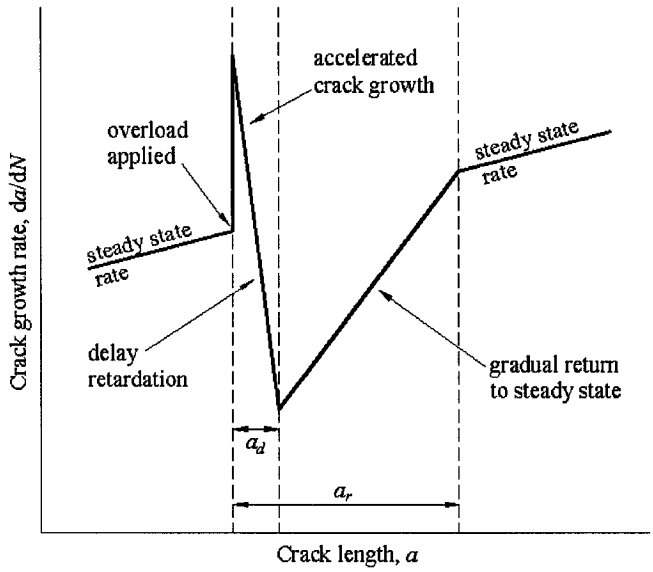

Figure 7-1 Schematic crack growth rate curve showing delayed retardation following a tensile overload

Several researchers have proposed various models to describe the overload retardation phenomenon. Generally, these retardation models may be classified into two main categories: (i) crack tip plasticity models and (ii) crack closure models. The crack tip plasticity models are based on the assumption that crack growth retardation occurs due to the large plastic zone developed during overloading. The residual compressive stresses formed in this zone will in turn reduce the magnitude of the tensile stresses during the next fatigue cycle and tend to delay the crack growth. A number of retardation models belong to this category.

The Wheeler model [9] predicts the retardation in the crack growth rate following an overload by modifying the constant amplitude growth rate. The modification is done by an experimentally determined retardation parameter, which is a function of the ratio of the current plastic zone size to the plastic zone size created by the overload. A number of modifications [10, 12-13] have been proposed to the model to account for the delay retardation phenomenon. In addition, the Wheeler model was found to provide

satisfactory prediction of the overload retardation for 350WT steel [2-6], which is the material used in the present investigation.

The Willenborg model [5-6, 11, 141-143], on the other hand, does not incorporate any empirical parameters but uses the material yield strength to evaluate the plastic zone size. The amount of retardation is determined as a function of the stress intensity factor necessary to cancel the effect of the overload plastic zone. The model computes an effective stress intensity factor that is being reduced by the compressive residual stress. However, the Willenborg model was found to produce unreliable results when used in predicting the overload retardation for 350WT steel [5-6].

The Multi-Parameter Yield Zone model [144-145], proposed by Johnson, is a modification to the Willenborg model. The model is able to account for the crack growth retardation, acceleration and underload effects, but requires four load interaction parameters. The parameters are selected from the simple overload test observations and produce the best fit of the predicted to the experimental test results through these simple tests.

The EXPOL model [146], proposed by Nicholas *et al.*, is similar to both the Wheeler and Willenborg models from both the theoretical and capability perspectives. The model reduces the applied stress intensity factor to an effective stress intensity factor by an exponential function, which bears two parameters that should be experimentally determined. In addition, the model accounts for the initial crack growth acceleration immediately following an overload by simply adding an experimentally observed crack jump following the overload.

The Kim and Shim model [147] is a purely empirical model that is similar to the Wheeler model. The model also introduces a retardation coefficient, which is simply defined as the ratio of the experimentally determined retarded crack growth rate to the constant amplitude crack growth rate. The model is able to simulate the delay retardation, but requires knowledge of several parameters, namely: the delay and complete retardation durations, and the minimum crack growth rate during retardation. These parameters are evaluated through pertinent experiments.

The Pavlou model [148] is another retardation based model that uses a retardation factor to modify the constant amplitude crack growth rate. The model takes into account

the influence of the degree of material strain hardening within the overload plastic zone on the fatigue crack growth rate. This is accomplished by defining the retardation factor as a function of the changing yield strength due to strain hardening within the overload plastic zone. Similar to the Wheeler and Willenborg models, it appears that the Pavlou model does not simulate delay retardation.

Finally, Lang and Marci [89, 102] proposed that the load interaction effects are governed by the residual compressive stresses accounted for by the crack propagation stress intensity factor. The crack propagation stress intensity factor is used to compute an effective stress intensity factor. This must be determined and monitored either experimentally, by the crack propagation load measurement method, or by the finite element method [149]. The model has been used for prediction in both single and multiple overloading cases, as well as for overloading followed by unloading and underloading.

The second main category of retardation models, that is, the crack closure models, is based on Elber's experimental observation [60]. It was observed that a partial closure of the crack faces would occur during a portion of a fatigue load cycle as a result of the tensile plastic deformation left in the wake of a fatigue crack. Since crack propagation can only occur during the time for which the crack is fully open, the formation of crack closure reduces the range of the applied stress that is effective for crack propagation. In addition, the magnitude of the stress required for the crack to be fully open (*i.e.* the crack opening stress), depends on the preceding load history. For example, as a crack propagates through an overload plastic zone, the residual stresses in the zone increase the load required to open the crack and cause crack growth retardation. Thus, the use of the crack closure models required the crack opening stress to be determined throughout the load history. This is accomplished either by direct experimental measurements [103, 150-151] or by finite element computations [152-154]. However, the major drawback to using such crack closure models is that the experimental measurement of the crack opening stress under variable amplitude loading is very difficult and the magnitude and precision would be a function of the measurement techniques used. In the same vein, the finite element analysis for computing the crack opening stress is often complicated and relatively time consuming.

The CORPUS model proposed by de Koning [155] uses an approximate description of the crack closure behaviour to predict the crack growth acceleration and retardation observed experimentally under variable amplitude loading. In the model, the crack opening stress is computed from experimentally determined functions. Material memory rules are formulated to account for the plastic zone interaction in variable amplitude loading case. The crack opening function in the CORPUS model was later modified by Skorupa *et al.* [156] to simulate the delay retardation.

In the Strip Yield model proposed by Newman [97, 157-161], the crack tip plastic zone and the region of residual plastic deformation is subdivided into one-dimensional rigid perfectly plastic elements. The deformation state of these elements is monitored cycle-by-cycle and compared with the elastic displacements of the crack flanks. Contact stresses arise on the crack surfaces in order to meet the compatibility between the elastic crack flanks and the plastically deformed elements. The crack opening stress is taken at the point when the contact stresses become zero. In addition, the model uses a plastic constraint factor to account for the three-dimensional effects at the crack tip. However, the effect of the stress history on the magnitude of the constraint factor is not clear and is the subject of on-going research [162-164]. Nonetheless, the Strip Yield model appears to be able to simulate the delay retardation and the initial crack growth acceleration immediately following an overload and account for the material's memory. The model is however more computationally involved than the previously discussed models.

In addition to the two main categories of retardation models, a number of models have been developed recently based on the fatigue damage accumulation and the crack tip strain energy release rate [98, 165-166]. However, these models are more theoretical and complex in nature than the previously discussed models and require more experimental validation.

To summarize, it is concluded that the Wheeler retardation model [9] is one of the simplest and most widely employed models [2-22] to quantify the fatigue crack growth retardation after a single overload, and it offers the most potential for modifications and improvements. The model is based on the interaction of the overload plastic zone and the current plastic zone. However, its simple formulation falls short of accounting for the aforementioned initial crack growth acceleration, delay retardation, overload interaction

and net section yielding effect. Therefore, a number of modifications to the Wheeler model were proposed in the present work to improve its accuracy in predicting fatigue crack growth, and retardation, including multiple overloading situations. In the present work, both single and multiple overloading fatigue tests were performed on 350WT steel specimens and the fatigue life predictions by the original and the modified Wheeler model were then compared.

7.2 Development of the Modified Wheeler Model

7.2.1 Description of the Original Wheeler Model

The original Wheeler model is a simple model that calculates the fatigue crack growth retardation following a single tensile overload by introducing a retardation parameter, ϕ_R, which can be multiplied to any constant amplitude fatigue model. In here, it is applied to the Paris equation:

$$da/dN = \phi_R \cdot \left[C(\Delta K)^n\right], \tag{7-1}$$

With reference to Figures 7-2, the retardation parameter can be defined as [18]:

$$\phi_R = \begin{cases} \left[\dfrac{r_{p,i}}{a_{OL} + r_{p,OL} - a_i}\right]^{m_{org}} & \text{, when } \; a_i + r_{p,i} < a_{OL} + r_{p,OL} \\ 1 & \text{, when } \; a_{OL} + r_{p,OL} \le a_i + r_{p,i} \end{cases}, \tag{7-2}$$

where a_{OL} is the crack length at which the overload is applied, a_i is the current crack length, $r_{p,OL}$ is the size of the plastic zone produced by the overload at a_{OL}, $r_{p,i}$ is the size of the plastic zone produced at the current crack length a_i, and m_{org} is the curve fitting parameter for the original Wheeler model termed the shaping exponent.

However, Sheu *et al.* and Song *et al.* [18, 21] observed that crack growth retardation actually takes place within an effective plastic zone. They estimated the size to be:

$$r_p = \alpha\left(\frac{K}{\sigma_{yld}}\right)^2, \tag{7-3}$$

where K is the applied stress intensity factor, σ_{yld} is the yield strength of the material and α is the effective plastic zone size constant, which can be established experimentally by noting the total retardation crack length (a_r in Figures 7-1 and 7-2(b)), which is the distance over which the retarded crack propagates before the constant amplitude crack growth rate resumes [18]. Figure 7-3 shows the Wheeler model prediction of a typical single overloading fatigue test conducted in the present work.

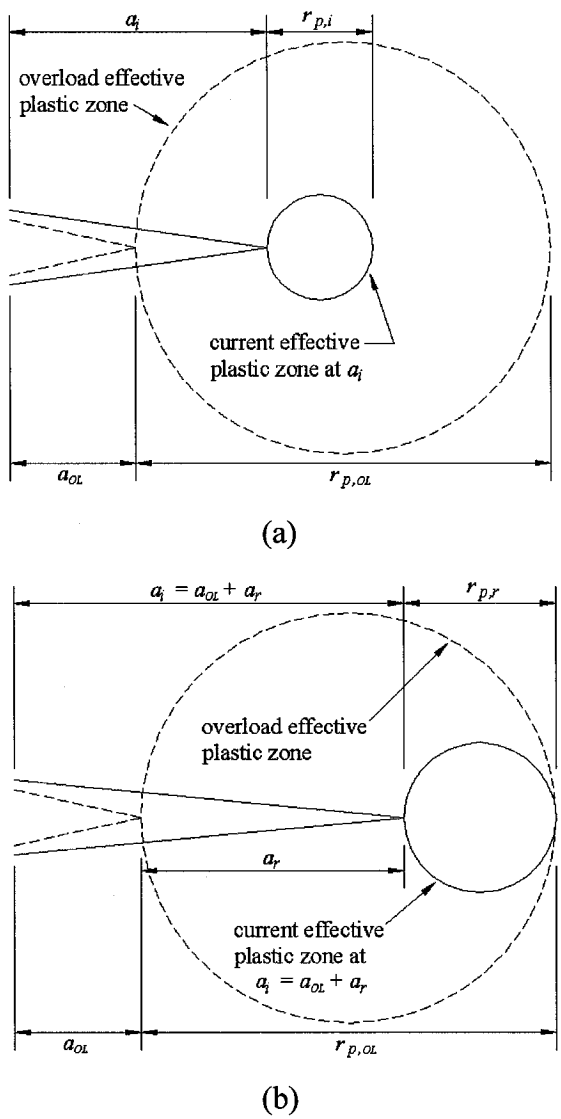

Figure 7-2 Illustration of the terms defining the retardation parameter

According to Sheu *et al.* [18], and in reference to Figures 7-2, the overload applied at the crack length a_{OL} causes an overload plastic zone size, $r_{p,OL}$, and the crack growth retardation occurs. During the subsequent crack extension, the current plastic zone advances with the crack. The retardation ceases when the crack propagates further to the crack size $a_i = a_{OL} + a_r$ (Figure 7-2(b)). At this moment the crack tip plastic zone size is denoted as $r_{p,r}$. Referring to Figure 7-2(b), the relationship of a_r to plastic zone size is expressed as follows:

$$a_r = r_{p,OL} - r_{p,r} = \alpha\left[\left(\frac{K_{OL}}{\sigma_{yld}}\right)^2 - \left(\frac{K_r}{\sigma_{yld}}\right)^2\right], \tag{7-4}$$

where K_{OL} is the overload stress intensity factor and K_r is the maximum stress intensity factor at $a_i = a_{OL} + a_r$. Once the value of a_r is determined from the experimental data, the constant α in Equation 7-4 is obtained.

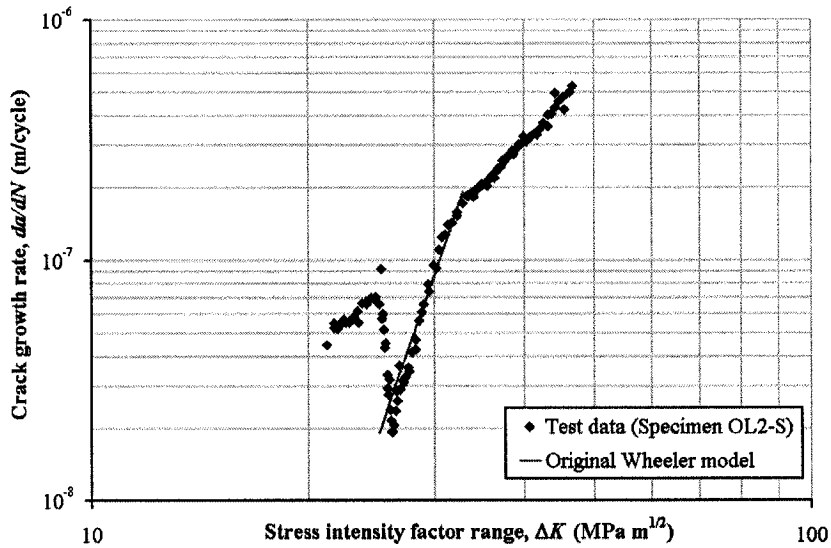

Figure 7-3 Fatigue rate curve of Specimen OL2-S and the Wheeler model prediction

The Wheeler model states that while the crack is advancing through the overload effective plastic zone, crack growth retardation occurs as long as the current effective plastic zone lies completely within the overload effective plastic zone. In addition, according to its formulation, the crack growth rate is at its minimum immediately after

the overload application and gradually returns to its steady state value as the current effective plastic zone reaches the boundary of the overload effective plastic zone. Thus, the Wheeler model is not adequate for materials that experience crack growth acceleration and delay retardation immediately after an overload, as can be seen in Figure 7-3. Furthermore, the model makes no attempts to account for the overload interaction when multiple overloads are applied. The following describes a few modifications to the Wheeler model to address these effects.

7.2.2 Proposed Modifications to the Wheeler Model

In the proposed modified Wheeler model, two additional parameters are incorporated and an accelerated stress intensity factor range is defined to account for the delay retardation, the overload interaction and the crack growth acceleration, respectively. Furthermore, a set of parameters are formulated in the modified model to account for the net section yielding effect observed in the present fatigue testing.

Similar to the original Wheeler model, the modified model can be written, in conjunction with the Paris equation, as:

$$da/dN = \phi_R \cdot \phi_D \cdot \phi_I \cdot \left[C(\Delta K_{ac})^n\right], \tag{7-5}$$

where ϕ_D is the delay parameter, ϕ_I is the overload interaction parameter and ΔK_{ac} is the accelerated stress intensity factor range. The formulations and the rationale for each of these additional parameters are presented below.

7.2.2.1 Delay Retardation, ϕ_D

For the materials that experience delay retardation and crack growth acceleration after an overload, it is postulated that a tensile overload causes blunting of the initially sharp crack plastically, causing the crack open and lowering the crack opening stress for a distance following the overload [83].

In order to simulate this delay retardation phenomenon in the modified Wheeler model, fatigue loading is assumed to produce a zone of delay retardation and crack growth acceleration, or effective delay zone, r_d, in addition to and similar to the effective plastic zone. Furthermore, the size of the effective delay zone can be assumed to be calculated in the same manner as the effective plastic zone (Equation 7-3):

$$r_d = \beta\left(\frac{K}{\sigma_{yld}}\right)^2, \tag{7-6}$$

where β is the effective delay zone size constant which can be similarly established experimentally by noting the delay retardation crack length (a_d in Figures 7-1 and 7-4(b)) following the overload. In other words, the delay retardation crack length is where the crack growth rate reaches its local minimum value.

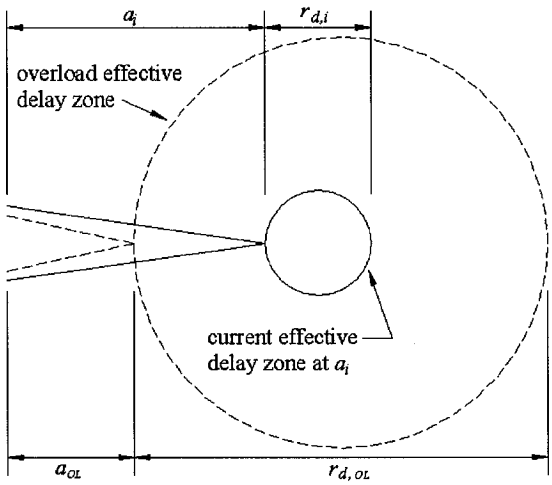

(a)

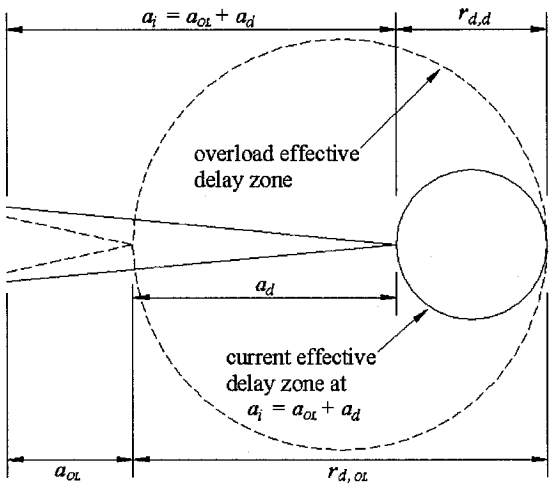

(b)

Figure 7-4 Illustration of the terms defining the delay parameter

Referring to Figure 7-4(a), the overload applied at the crack length a_{OL} develops an overload effective delay zone size, $r_{d,OL}$, resulting into the delay crack growth retardation. During the subsequent crack extension, the current effective delay zone advances with the crack. The delay retardation ceases when the crack propagates further to the crack size $a_i = a_{OL} + a_d$ (Figure 7-4(b)). At this moment the crack tip effective delay zone size is denoted as $r_{d,d}$. Referring to Figure 7-4(b), the relationship of a_d to effective delay zone size is expressed as follows:

$$a_d = r_{d,OL} - r_{d,d} = \beta\left[\left(\frac{K_{OL}}{\sigma_{yld}}\right)^2 - \left(\frac{K_d}{\sigma_{yld}}\right)^2\right], \tag{7-7}$$

where K_{OL} is the overload stress intensity factor and K_d is the maximum stress intensity factor at $a = a_{OL} + a_d$. Once the value of a_d is determined from the experimental data, the constant β in Equation 7-7 is obtained.

In order to achieve the delay retardation within the effective delay zone, the delay parameter, ϕ_D, should be a decreasing function within the zone to counteract the increasing Wheeler retardation parameter, ϕ_R. One possibility, employed in the proposed modified model, is to define ϕ_D as:

$$\phi_D = \begin{cases} \left[\dfrac{a_{OL} + r_{d,OL} - a_i}{r_{d,i}}\right]^{m_{mod}} & \text{, when } \; a_i + r_{d,i} < a_{OL} + r_{d,OL} \\ 1 & \text{, when } \; a_{OL} + r_{d,OL} \le a_i + r_{d,i} \end{cases}, \tag{7-8}$$

where $r_{d,OL}$ is the size of the overload effective delay zone, $r_{d,i}$ is the size of the current effective delay zone and m_{mod} is the shaping exponent for the modified model.

According to the above definition, the delay parameter is at its maximum immediately following the overload, and then decreases to unity at the point of minimum crack growth rate. The Wheeler model's prediction was shown in Figure 7-3; after the incorporation of the above delay parameter, the prediction will be as illustrated in Figure 7-5. Comparison of Figures 7-3 and 7-5 illustrates how ϕ_D, which accommodates the delay retardation, affects the predictions of the Wheeler model.

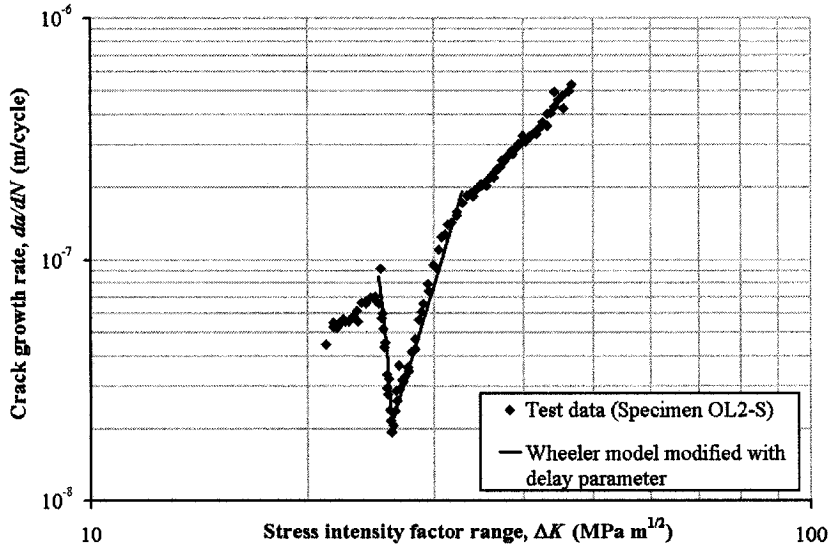

Figure 7-5 Fatigue rate curve of Specimen OL2-S and the Wheeler model prediction modified with the delay parameter

7.2.2.2 *Initial Crack Growth Acceleration, ΔK_{ac}*

During the application of the tensile overload, the crack grows at a rate that is theoretically equal to the rate corresponding to the overload stress intensity factor range. The crack growth rate then gradually decreases to a minimum value at the end of the delay retardation crack length, a_d. Therefore, it is reasonable to assume that, effectively, the stress intensity factor range within a_d decreases from the overload stress intensity range value to the steady state value.

With the above assumption in mind, the accelerated stress intensity factor range, ΔK_{ac}, is defined in the modified Wheeler model as:

$$\Delta K_{ac} = \begin{cases} \Delta K_i + (\Delta K_{OL} - \Delta K_i) \cdot \left[1 - \dfrac{r_{d,i}}{a_{OL} + r_{d,OL} - a_i} \right]^{m_{mod}} & \text{, when } a_i + r_{d,i} < a_{OL} + r_{d,OL} \\ \Delta K_i & \text{, when } a_{OL} + r_{d,OL} \le a_i + r_{d,i} \end{cases} \quad (7\text{-}9)$$

where ΔK_{OL} is the overload stress intensity factor range and ΔK_i is the current stress intensity factor range (at the currently monitored crack length).

According to the above definition of the accelerated stress intensity factor range, the effect of the overload stress intensity factor range on crack growth acceleration is at its maximum immediately following the overload and decreases to zero at the end of the

delay retardation crack length. The accelerated stress intensity factor range was incorporated into the prediction in Figure 7-5 and the results are plotted in Figure 7-6. By comparing Figure 7-6 to Figure 7-5, one could see how ΔK_{ac} affects the model's prediction by simulating the initial crack growth acceleration immediately following the overload.

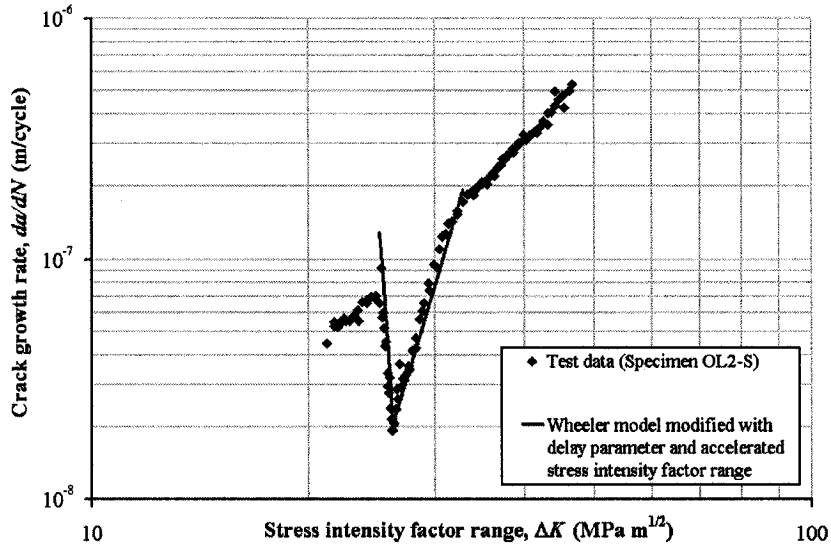

Figure 7-6 Fatigue rate curve of Specimen OL2-S and the Wheeler model prediction modified with the delay parameter and the accelerated stress intensity factor range

7.2.2.3 Overload Interaction, ϕ_I

As stated, the overload interaction is not accounted for in the original Wheeler model. In the proposed model, the interaction can be considered to occur when an overload is applied while the crack is within the previous overload effective plastic zones. In this case, the subsequent crack growth would be under the influence of both the new and the previous overload effective plastic zones. In the crack closure model by de Koning [155], the load sequence effect is accounted for by determining the crack opening stress of both the current and previous load cycles. The effective stress range of the current cycle is then assumed to be the minimum value calculated from these crack opening stresses.

In the modified Wheeler model, the overload interaction parameter, ϕ_I, is therefore assumed to have a similar minimizing effect on the current crack growth rate.

At the same time, the influence of the previous overloads should diminish, and the current overload influence should dominate as the crack grows across the new overload effective plastic zone and away from the previous zones. In order to satisfy these two objectives, the overload interaction parameter is defined in the modified Wheeler model as:

$$\phi_I = \begin{cases} 1-(1-\phi_{min,i})\cdot\left[1-\dfrac{r_{p,i}}{a_{OL}+r_{p,OL}-a_i}\cdot\dfrac{a_{OL}+r_{d,OL}-a_i}{r_{d,i}}\right]^{m_{mod}} & \text{, when } a_i+r_{d,i} < a_{OL}+r_{d,OL} \\ 1-(1-\phi_{min,i})\cdot\left[1-\dfrac{r_{p,i}}{a_{OL}+r_{p,OL}-a_i}\right]^{m_{mod}} & \text{, when } \begin{matrix} a_{OL}+r_{d,OL} \le a_i+r_{d,i} \\ a_i+r_{p,i} < a_{OL}+r_{p,OL} \end{matrix}, \\ 1 & \text{, when } a_{OL}+r_{p,OL} \le a_i+r_{p,i} \end{cases} \tag{7-10}$$

where $\phi_{min,i}$ is the minimum value of the retardation parameter ϕ_R, which is calculated from the previous overloads at the current crack length.

According to the above formulation, over the course of the crack growth, the average value of $\phi_{min,i}$, and thus the overload interaction parameter, decreases and crack growth retardation increases as the spacing between the overloads decreases for the same overload load magnitudes. This is because the number of the overloads from which the minimum retardation parameter is extracted further increases. Figure 7-7(a) shows the prediction of a typical multiple overloading fatigue test carried out in the present work, without the overload interaction parameter incorporated, while Figure 7-7(b) shows the prediction of the same fatigue test with the overload interaction parameter incorporated. By comparing Figure 7-7(a) to Figure 7-7(b), it can be seen how ϕ_I modifies the original model's predictions by accounting for the overload interaction and lowering the predicted crack growth rates due to the influence of previous overloads.

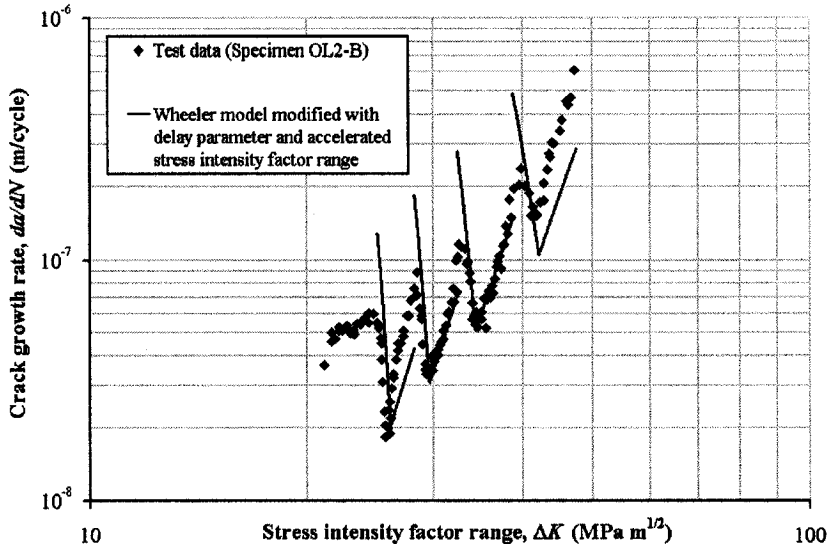

(a)

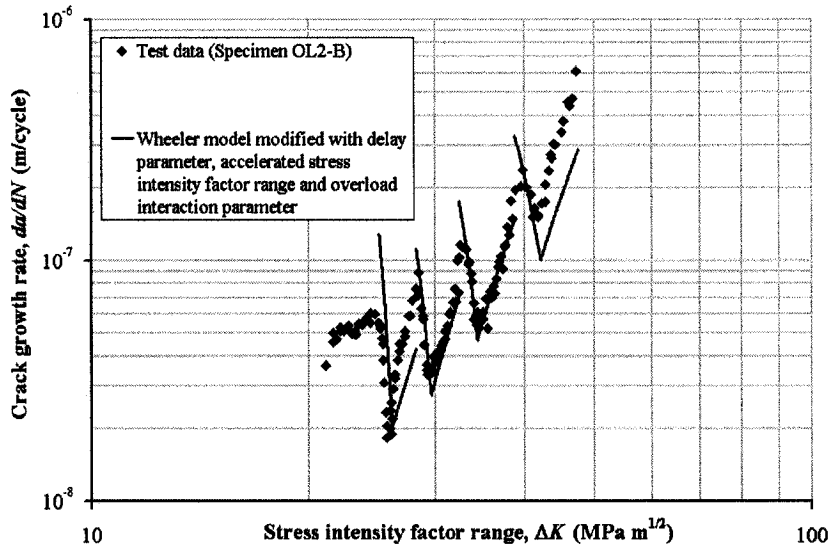

(b)

Figure 7-7 Fatigue rate curve of Specimen OL2-B and the Wheeler model prediction: (a) Modified with the delay parameter and the accelerated stress intensity factor range; (b) Modified with the delay parameter, the accelerated stress intensity factor range and the overload interaction parameter

7.2.2.4 Net Section Yielding

According to ASTM Standard E647, *Standard Test Method for Measurement of Fatigue Crack Growth Rates* [139], the crack length data in a fatigue test for the middle tension specimen is valid as long as the average stress in the uncracked ligament of the

specimen is less than 80% of the yield strength of the material. In the present fatigue tests, it was observed that when an overload was applied at a crack length close to the aforementioned 80% yield strength limit (a_{lim}), the resulting crack growth retardation was reduced. This observation can be seen from Figure 7-8(a), where Figure 7-7(b) is re-plotted to illustrate the occurrence of the reduced crack growth retardation.

In this test, the crack growth retardation from the last overload ended prematurely for the crack growth rate to return to its constant amplitude value at a_{lim}. The figure also shows that without consideration of the net section yielding effect, the modified Wheeler model over predicts the amount of crack growth retardation from the last overload. In addition, it appeared that net section yielding effect reduced the crack growth retardation in such a way that during the reduced retardation process, the crack growth rates were higher than the that predicted, as if the overload was applied earlier, at $a_{OL,lim}$, as shown in Figure 7-8(a). Furthermore, an overload that is applied at $a_{OL,lim}$ would have its total retardation crack length ended at a_{lim}. In conclusion, it appears that the crack growth retardation from an overload is reduced if its total retardation crack length exceeds a_{lim}.

In order to account for the net section yielding effect on the crack growth retardation, the following procedure is adopted in the modified Wheeler model:

1) Calculate the crack length at which the net section stress is 80% of the yield strength of the material, a_{lim}. For the middle tension specimen:

$$a_{lim} = (W - \frac{P_{max}}{0.8\sigma_{yld}B})/2, \tag{7-11}$$

where W and B are the width and the thickness of the specimen respectively and P_{max} is the maximum load at a_{lim}.

2) Calculate the effective plastic zone size at a_{lim}, $r_{p,lim}$, by using Equation 7-3.

3) For each overload, using Equation 7-3, calculate the effective plastic zone size, $r_{p,OL}$.

4) For each overload, determine if $a_{OL} + r_{p,OL} > a_{lim} + r_{p,\lim}$, thus determining whether the overload affected zone exceeds a_{lim}; if so, then calculate (by iteration) the crack length, $a_{OL,lim}$, at which $a_{OL,lim} + r_{p,OL,lim} = a_{lim} + r_{p,lim}$.

5) Calculate the crack growth rate, da/dN, by using Equation 7-5 with each actual a_{OL}. This is the retarded crack growth rate in the absence of the net section yielding effect.
6) For each overload that satisfies Step 4, also calculate da/dN by using Equation 7-5 with the corresponding $a_{OL,lim}$. This is the retarded crack growth rate if the overload were applied at the corresponding $a_{OL,lim}$.
7) If the value determined from Step 6 is greater than the value in Step 5, then da/dN is equal to the value determined in Step 6. This represents the higher crack growth rate and the reduced crack growth retardation caused by the net section yielding effect.

It should be noticed that the above procedure and calculations could be easily, and has been, formulated into a spreadsheet.

The above procedure to account for the net section yielding effect was applied into the prediction in Figure 7-8(a), with the results shown in Figure 7-8(b). By comparing Figure 7-8(a) to Figure 7-8(b), it can be seen how incorporating the above procedure into the modified Wheeler model provided a better prediction of the reduced crack growth retardation near the a_{lim}.

7.2.2.5 Summary of the Modifications

A number of modifications were proposed to the Wheeler retardation model to account for the delay crack growth retardation, the initial crack growth acceleration following an overload, and the overload interaction and the net section yielding effect observed in the tests conducted in our laboratory. In effect, the Wheeler model has been extended such that it could account for the fatigue life in multiple overloading fatigue tests at the expense of an additional constant, the effective delay zone size constant, β. However, it should be noted that the crack growth behavior after overload is dependent on both the stress ratio, R, of the baseline and the applied overload level [167]. The original Wheeler model does not consider the effects of the R ratio and no attempts were made in the present work to account for the R ratio effects in the modified model. Therefore, as in the original model, the values of the effective plastic zone size constant, α, the shaping exponent, m, and β have to be experimentally determined for each combination of R ratio and overload level from single overloading fatigue tests.

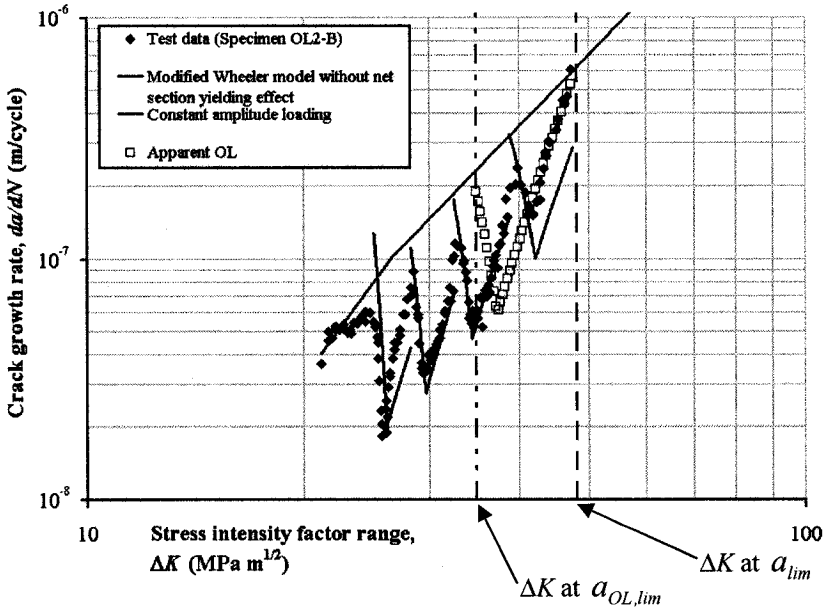

(a)

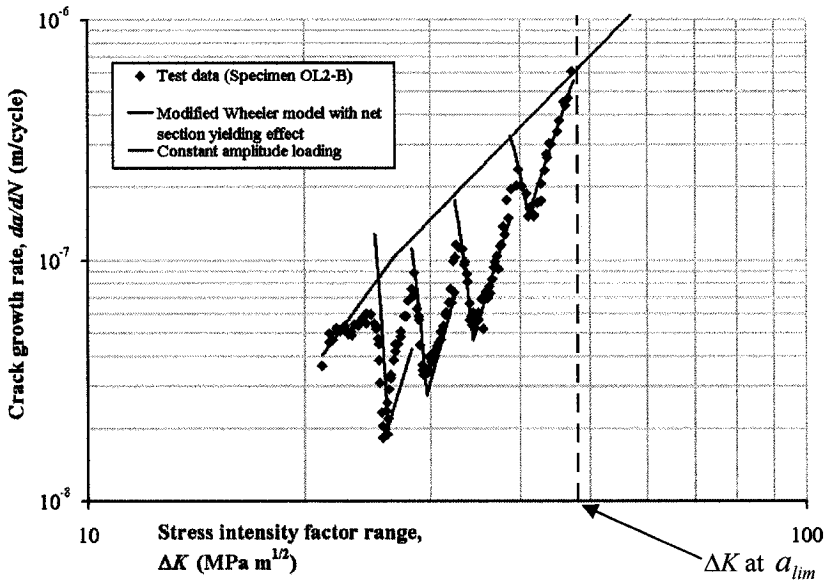

(b)

Figure 7-8 Fatigue rate curve of Specimen OL2-B and the modified Wheeler model prediction: (a) Without the net section yielding effect incorporated; (b) With the net section yielding effect incorporated

To compare the accuracy of the modified model to the original model, fatigue life predictions were made to a number of multiple overloading fatigue crack propagation tests conducted in the present work. The following sections provide details of the experimental investigation.

7.3 Experimental Procedure

7.3.1 Overview

The experimental fatigue crack propagation testing consisted of subjecting centre-cracked specimens of 350WT steel to either single or multiple overloading within constant amplitude fatigue loading. The fatigue crack growth tests were conducted in accordance with ASTM Standard E647, *Standard Test Method for Measurement of Fatigue Crack growth Rates* [139]. The test material, test specimens and test apparatus have been described in Section 6.3.

7.3.2 Test Procedure

All the fatigue tests were performed under load control in accordance with ASTM E647. The fatigue loading on the specimens comprised of axial tension in a sinusoidal wave form at room temperature in air. The baseline constant amplitude loading consisted of cycles at maximum load of 60 kN and stress ratio, R, of 0.1 at a load frequency of 20 Hz. Three overload levels (P_{OL}) of 80, 90 and 100 kN, as defined in Figure 7-9, were employed to be applied within the constant amplitude loading for both single and multiple overloads tests. A single overloading test was performed for each P_{OL} for the calibration of the model constants, namely, the effective plastic zone size constant, α, the effective delay zone size constant, β, and the shaping exponent, m_{org} or m_{mod}.

The multiple overloading tests for each P_{OL} were conducted with constant crack growth between each overload application, Δa, within each test. Four multiple overloading tests were conducted for each P_{OL} with Δa between 0.013 and 0.160. In the present work, Δa is defined to be the ratio of the actual crack growth interval between overloads to the effective overload plastic zone size given by Equation 7-3. In each test, the crack length at which first overload was applied, a_o, was approximately 15 mm. The multiple overloading fatigue tests details are summarized in Table 7-1, where a_f is the final recorded valid crack length, n_{OL} is the total number of overloads applied, N_{exp} is the number of cycles to propagate the crack from a_o to a_f observed in the experiments

and N_{org} and N_{mod} are the corresponding number of cycles predicted by the original and the modified Wheeler models, respectively.

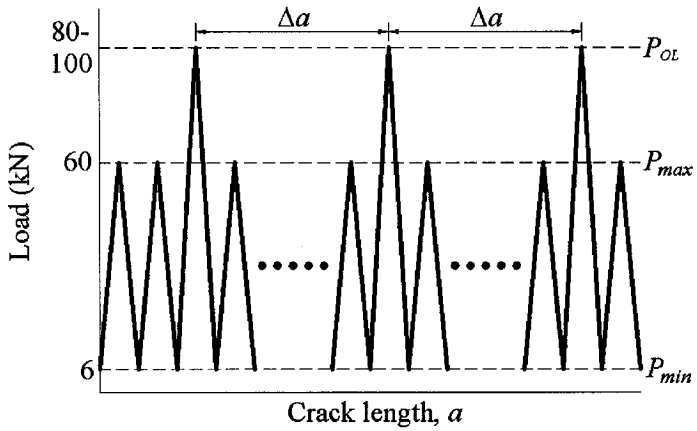

Figure 7-9 Schematic representation of the loading terms

Table 7-1 Multiple overloading fatigue tests details and retardation results

Specimen	P_{OL} (kN)	a_o (mm)	a_f (mm)	Δa	n_{OL}	N_{exp} (cycles)	N_{org} (cycles)	$\frac{N_{org}-N_{exp}}{N_{exp}}$ (%)	N_{mod} (cycles)	$\frac{N_{mod}-N_{exp}}{N_{exp}}$ (%)
OL1-A	80	14.95	32.20	0.081	4	145,000	125,700	-13.31	121,000	-16.55
OL1-B	80	14.94	32.25	0.054	5	155,000	134,500	-13.23	126,900	-18.13
OL1-C	80	14.99	32.33	0.027	9	161,000	139,800	-13.17	114,641	-28.79
OL1-D	80	15.06	32.53	0.013	17	134,000	145,100	8.28	98,800	-26.27
OL2-A	90	14.99	32.35	0.153	3	230,500	255,800	10.98	238,800	3.60
OL2-B	90	14.97	32.08	0.102	4	242,500	273,400	12.74	253,300	4.45
OL2-C	90	14.99	32.48	0.051	7	236,500	316,000	33.62	258,700	9.39
OL2-D	90	15.06	32.41	0.026	12	210,250	336,000	59.81	176,600	-16.00
OL3-A	100	15.06	32.44	0.160	2	297,250	374,800	26.09	367,700	23.70
OL3-B	100	14.97	31.88	0.106	3	275,250	417,600	51.72	367,400	33.48
OL3-C	100	15.04	32.32	0.053	5	353,000	492,600	39.55	352,900	-0.03
OL3-D	100	15.05	32.42	0.027	9	282,000	548,000	94.33	203,700	-27.77

Before the tests, each of the specimens was precracked to a minimum length of 1.0 mm on both sides of the starter notch as required by the Standard before valid crack length data was recorded. This procedure removed the effect of the blunt starter notch and provided a sharpened fatigue crack of adequate size and straightness. The crack length was then measured periodically with the help of the traveling microscope until failure. The crack length data was calculated by the average of the left and right cracks,

and then reduced to fatigue crack growth rate data by both the secant and the incremental methods as recommended by ASTM E647.

7.4 Experimental Results and Discussion

7.4.1 Single Overloading Fatigue Tests Results

For each of the overload levels (P_{OL} = 80 kN, 90 kN and 100 kN) employed in the present work, the model's constants α, β and m were calibrated from a single overloading test using a procedure similar to the one given in [18]. In each case, a single overload was applied at a crack length of a_o = 15 mm and the total retardation crack length, a_r, where the crack growth rate had returned to the steady state value, and the delay retardation crack length, a_d, where the crack growth rate had reached its local minimum value, were estimated from the crack length data of the test. The constants α and β were then computed from a_r and a_d, respectively, from the procedures described in Sections 7.2.1 and 7.2.2.1. After α and β were determined, the number of cycles to propagate the crack from a_o to a_r could then be predicted from either the original model (Equation 7-1) or the modified model (Equation 7-5) for a given shaping exponent, m. The desired value of m for each model was then chosen such that the predicted number of cycles from the respective model was comparable to the experimental value, N_r.

Table 7-2 summarizes the model constants for both models determined from single overloading fatigue tests for each of the overload levels, which were used for the fatigue life prediction of the multiple overloading fatigue tests in the present work for the corresponding P_{OL}. As expected, the value of m increased with the overload level since a higher overload creates more crack growth retardation. In addition, the value of m was higher in the modified model (m_{mod}) than the original model (m_{org}) to compensate for the delay crack growth retardation and the initial crack growth acceleration immediately following the overload simulated in the modified model. Furthermore, it can be seen that the values of α and β were similar for P_{OL} of 90 and 100 kN, while they were higher for

P_{OL} = = 80 kN. These values were, however, sensitive to the values of a_r and a_d estimated from the crack length data.

Table 7-2 Single overloading fatigue tests details and model constants

Specimen	P_{OL} (kN)	a_o (mm)	a_d (mm)	a_r (mm)	N_r (cycles)	α	β	m_{org}	m_{mod}
OL1-S	80	15.13	16.47	20.85	66500	5.91	0.49	0.90	1.46
OL2-S	90	15.00	16.03	22.10	138500	3.11	0.21	1.77	2.25
OL3-S	100	14.94	16.45	24.43	244500	2.99	0.22	1.93	2.52

The fatigue rate curve for a typical single overloading fatigue test in the present work is plotted in Figure 7-10 along with both the original and the modified Wheeler models fitted curves. It can be seen that the modified model provides a closer correlation to the experimental data than the original model by accounting for the observed delay retardation and the initial crack growth acceleration.

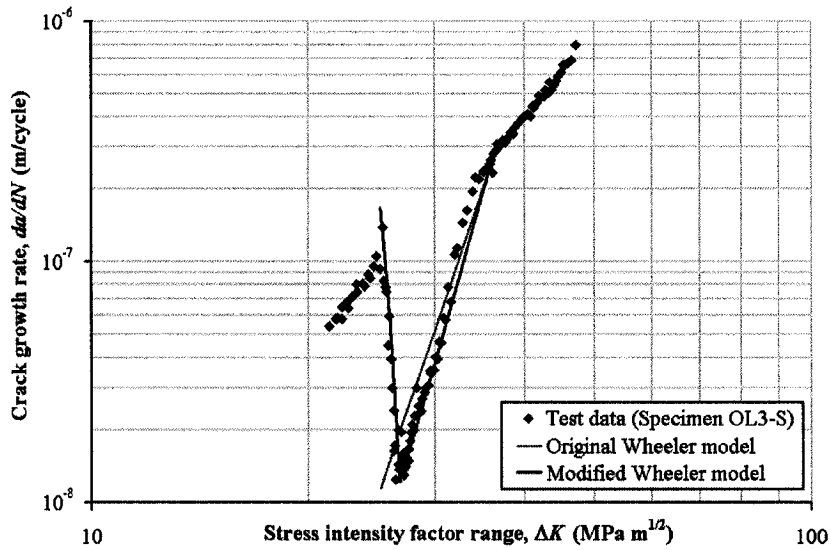

Figure 7-10 Fatigue rate curve of Specimen OL3-S with both the original and modified Wheeler model predictions

7.4.2 Multiple Overloading Fatigue Tests Results

The results for the multiple overloading fatigue tests are summarized in Table 7-1, where N_{exp} is the number of cycles to propagate the crack from a_o to a_f observed in the

experiments and N_{org} and N_{mod} are the corresponding number of cycles predicted by the original and the modified Wheeler models, respectively. The fatigue rate curve for a typical multiple overloading fatigue test in the present work is plotted in Figure 7-11 along with both models' predictions. It can be seen from the experimental data that the fatigue life increased with the increase in overload level, P_{OL}, as expected, since a higher overload created more crack growth retardation. In addition, up to a point, the fatigue life generally increased as the distance between overload application, Δa, decreased. However, from that point on (at $\Delta a \approx 0.05$), a decrease in the fatigue rate was observed as Δa was further decreased. This can be explained by the fact that as the overloads were applied more frequently, the increase in the total crack growth acceleration immediately following the overloads began to outweigh the increase in the total crack growth retardation.

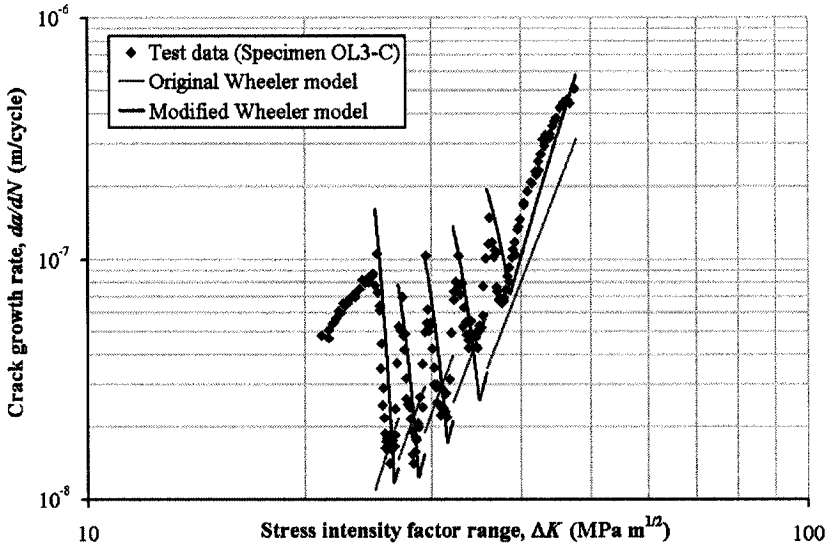

Figure 7-11 Fatigue rate curve of Specimen OL3-C with both the original and modified Wheeler model predictions

As stated, the overload interaction effect and the net section yielding correction cannot be considered when using the original Wheeler model, since those phenomena are not accounted for in the model. In other words, any previous crack growth retardation was disregarded in the calculations when a new overload was applied. In addition, the

model predicts the minimum crack growth rate immediately following an overload. Therefore, the predicted fatigue life from the original Wheeler model would increase monotonically as Δa decreases for all P_{OL} as shown in Table 7-1. In contrary, the experimental fatigue life decreased as Δa decreased beyond a certain point as described in detail in above (*i.e.*, at $\Delta a \approx 0.05$). Thus, the original Wheeler predictions in general became more and more un-conservative as Δa decreased beyond the above point, as indicated by the general increasing of the percentage error (column 9) in Table 7-1.

In comparison, the modified Wheeler model was able to, more or less, generate the reduced crack growth retardation at small Δa, that was present in the experimental data. This ability makes the modified model predictions in general more conservative and accurate in comparison to the original model predictions, especially as Δa decreases, as noted by the smaller percentage error (column 11) in Table 7-1. Thus, it appears that the modifications to the Wheeler model could predict the fatigue life of the steel subject to multiple overloading more accurately than the original Wheeler model.

7.5 Conclusions

For a number of materials, the fatigue crack growth retardation caused by a tensile overload exhibits an initial crack growth acceleration immediately following the overload, and a subsequent delay in reaching the minimum crack growth rate. In addition, when multiple overloads are applied, they can interact with each other, and as a result they could either accelerate or decelerate the overall crack growth retardation depending on the frequency of the overload. Furthermore, the crack growth retardation is reduced during the latter stage of the fatigue life of a structure when the net section stress approaches the yield strength of the material.

In the present work, a number of modifications to the Wheeler fatigue crack retardation model were proposed to account for the above phenomena. The parameters in both the original Wheeler model and the modified model were then calibrated from a number of single overloading fatigue tests conducted on 350WT steel, middle tension specimens. In addition, initial crack growth acceleration and delay retardation were observed following the overload application in these tests.

Multiple overloading tests were then performed on the same type of steel specimens and the results showed that crack growth retardation was enhanced, as the frequency of overload applications increased, up to a point. As the frequency was increased further, this beneficial effect began to be outweighed by the cumulative crack growth acceleration that occurred immediately following each overload application, causing a decreasing trend in fatigue life. It was also demonstrated that in comparison to the original Wheeler model, the proposed modified model could more accurately predict the fatigue life of 350WT steel subjected to the imposed multiple-overloading in the current experimental investigation. Specifically, the modified Wheeler model was able to predict the reduced crack growth retardation at small overload spacing, while the original model predicted the fatigue life inaccurately (in fact, the resulting fatigue life was erroneously increased as the overload spacing decreased). To summarize, it is believed that the proposed modifications would be applicable to any types of steels since the modifications were based on general observations on the fatigue retardation behaviour caused by tensile overloading. Furthermore, the required parameters could be obtained from a single overloading fatigue test.

Chapter 8 Investigation into the "Prying" Effect due to Crack Surface Roughness

8.1 Introduction

The crack closure concept was proposed by Elber [60] to account for the effects of load interaction as well as stress ratio and to estimate the fatigue crack growth rates under variable amplitude loading. Crack closure refers to the fact that during the initial part of a fatigue cycle, the crack tip is found to remain closed while the crack behind the tip region is already open. As the crack cannot propagate while it is closed at the crack tip, the crack closure phenomenon reduces the load amplitude that is actually experienced by the crack tip and leaves the initial part of the fatigue cycle ineffective in propagating the crack. Thus, only a portion of a fatigue cycle is responsible for the extension of fatigue cracks as a result of crack closure. In addition, the crack opening level can be altered by the load interaction effects in variable amplitude loading to cause deviations in the fatigue crack growth rates.

One of the most studied crack closure mechanisms, the roughness-induced crack closure, was first identified by Walker and Beevers [62]. In many materials, the fatigue crack surface is not flat since the crack advance is influenced by crystallographic slip or encounters with microstructural barriers and the crack follows the weakest path in the material to propagate. This results in a serrated or zig-zag fracture path as illustrated in Figures 8-1. Roughness-induced crack closure is attributed to this deflection of crack path as the asperities (roughness) on opposite crack faces come into early contact and interlock, resulting in compressive residual stress that reduces the crack-tip driving force.

Crack surface roughness is found to significantly alter both fracture loads and the direction of crack propagation. In addition, the rougher crack surface resulted in the higher crack opening stress. A number of studies have shown that roughness-induced crack closure level is increased with increasing the degree and variation of the angle of crack path deflection and increasing the asperity height and density [64-74]. Furthermore, asperities nearest to the crack tip were found to have the largest contributions to crack closure while the influence of crack surface roughness was smaller

as the distance from the crack tip increased [65, 70, 75-76]. Finally, although studies on the contribution of crack surface friction have been limited, it was found that part of the input energy to the crack was consumed in resisting the friction along the crack contact surfaces. In other words, friction tended to shield the crack tip from applied load, and thus retarded the development of plasticity, increased crack closure and decreased the crack tip stress intensity factor [72, 77-82].

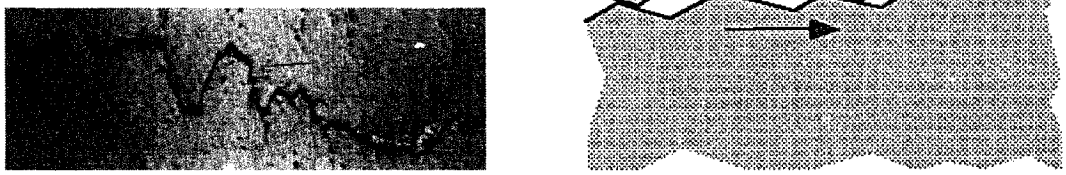

(a) (b)

Figure 8-1 (a) Typical fatigue crack profile [63]; (b) Schematic illustration of roughness-induced crack closure [61]

A compressive underload in fatigue loading is known to cause crack growth acceleration in the subsequent loading cycles by creating a zone of tensile residual stress ahead of the crack tip and flattening the crack tip asperities as the crack closes under the compressive stress. As a result, the contribution from crack closure is reduced and the effectiveness of the stress intensity factor at the crack tip is increased [76, 83, 95-106]. The crack growth rates in the subsequent fatigue cycles immediately following the underload are then accelerated and the rates gradually return to the steady-state level as the crack grows and crack surface roughness again develops until the influence of the underload is eliminated. In addition, the amount of crack growth acceleration generally increases with the underload ratio (*ULR*). In the present work, the underload ratio was defined as $ULR = UL/\Delta P$, where ΔP is the range of the subsequent fatigue loading as shown in Figure 8-2.

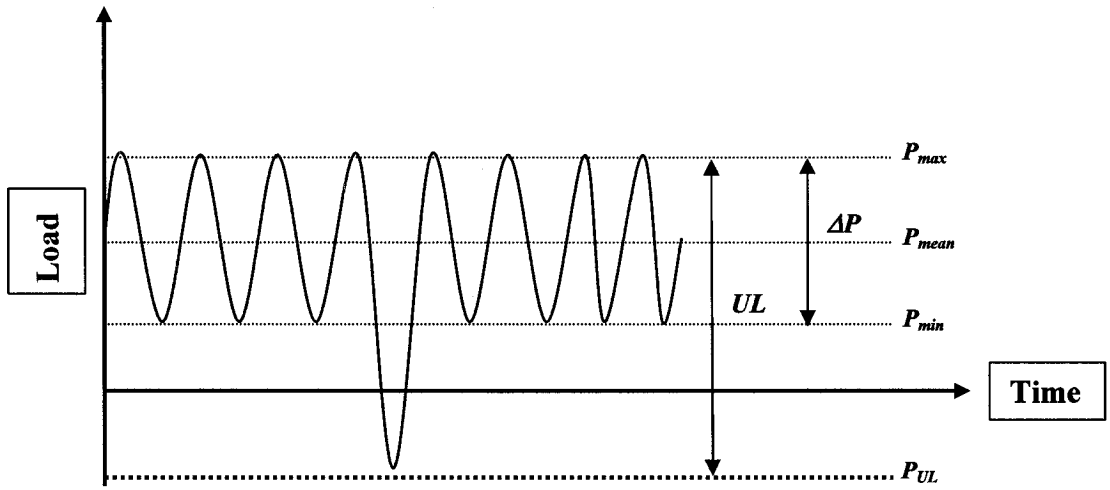

Figure 8-2 Schematic illustration of the various loading terminologies

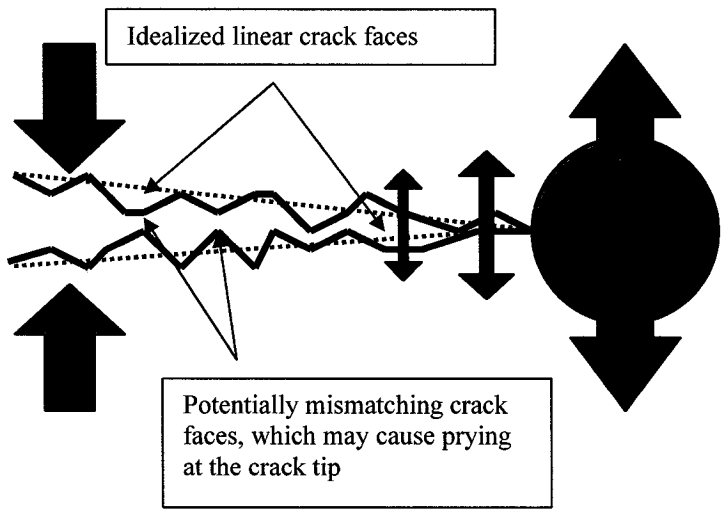

Figure 8-3 Schematic illustration of potential crack tip prying under compressive underloads due to mismatched crack faces [2]

In the investigation by Rushton [2], it was hypothesized that when a compressive underload is applied, instead of the crack tip asperities being flattened as the crack closes, the crack tip might instead be "pried" open as some of the more rigid asperities on the opposite mismatched crack surfaces make contact, as illustrated in Figure 8-3. This "prying" effect could possibly enhance the tensile plastic zone at the crack tip, reduce crack closure and cause additional fatigue crack growth acceleration following the compressive underload. In order to investigate this possibility, a parametric study by the finite element method was performed in the present work on centre-cracked steel plates

to examine the effects of crack inclination angle, compressive underload, crack surface roughness and friction on the *J*-integral following the underload. It was assumed that the *J*-integral could be regarded as the driving force behind fatigue crack growth. The finite element models incorporated contact elements between the crack surfaces to simulate the "prying" and frictional forces at the crack tip. The model development and the results of this investigation are presented in the next two sections.

8.2 Development of the Finite Element Models

8.2.1 Model Overview

In the present investigation, the general purpose commercial finite element code NISA was employed to model the centre-cracked plate specimens used for fatigue testing. The finite element model layout and plate's dimensions are shown in Figure 8-4. The models had a length L = 210 mm, width W = 100 mm, thickness B = 5 mm and crack length $2a$ = 30 mm. The crack inclination angle θ considered in the present work were 0°, 22.5°, 45° and 67.5°. The crack face separation at the middle of the crack was 0.254 mm, which was equal to the width of the EDM notch, and was assumed to decrease linearly to zero towards the crack tips in the models. The plate had fixed displacement boundary conditions imposed at one end, while it was loaded with a uniform axial stress in either tension or compression at the opposite end. For the 0° crack inclination angle, the plate was considered symmetrical about its centre. Thus, only one half of the plate was idealized in the present finite element models to provide a complete picture of the crack tip plastic zone, while the full plate was modeled for the other crack inclination angles.

The mechanical properties of the plate were as follows: modulus of elasticity E = 200 GPa, Poisson's ratio ν = 0.3 and yield strength σ_{yld} = 365 MPa, which were chosen to be analogous to the properties of 350WT Category 5 steel. In addition, the material in the models was assumed to be elastic-perfectly plastic with the plastic deformation of the material assumed to obey the von Mises yield criterion and the associated flow rule, which is most commonly used criterion for isotropic ductile metals [168].

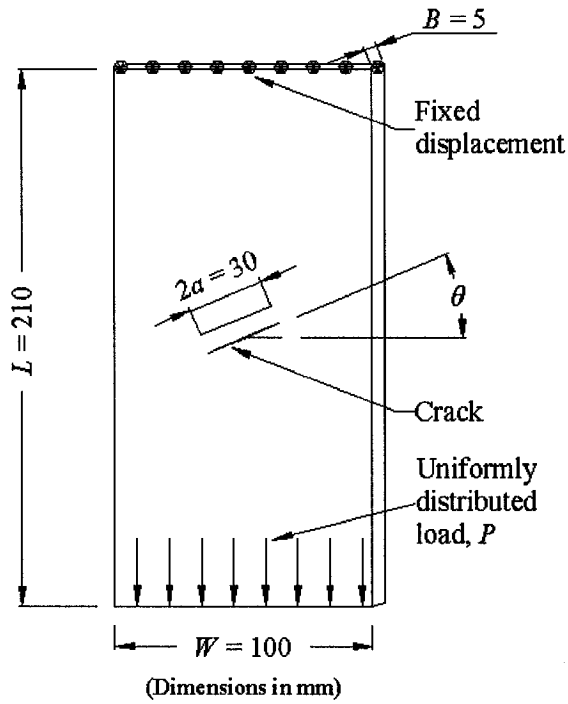

Figure 8-4 Finite element model layout and dimensions

8.2.2 Element Descriptions

The finite element models were constructed using both 4- and 8-node quadrilateral plane stress elements (NKTP = 1 in NISA), with the 8-node elements used to discretize the region near the crack tip. In addition, the singularity of the crack-tip stress field was simulated by moving the mid-side nodes of the 8-node elements surrounding the crack tip to the quarter point near the crack tip, as shown in Figure 8-5. Depending on the analyzed case, the dimensions of the crack tip elements ranged between 0.13 mm and 0.32 mm. Furthermore, the 2-D gap/friction elements (NKTP = 49) were inserted across the crack surfaces as shown in Figure 8-5 to prevent the overlapping of the crack surfaces when the plate was subjected to compressive loading. Finally, depending on the analyzed case, the number of elements in the models ranged between 1,128 and 2,255.

The 2-D gap/friction element in NISA is a 2-node interface element that may be used to model contact at discrete points between two bodies with or without friction. The element has two translational degrees of freedom at each node. The element is

represented by a pair of coupled nonlinear springs in both the normal and tangential directions to the interface as shown in Figures 8-6. The element has a specified initial gap width g_0 associated with it. The element is said to be closed when it is compressed in the normal direction beyond g_0; otherwise the element is said to be open (no contact).

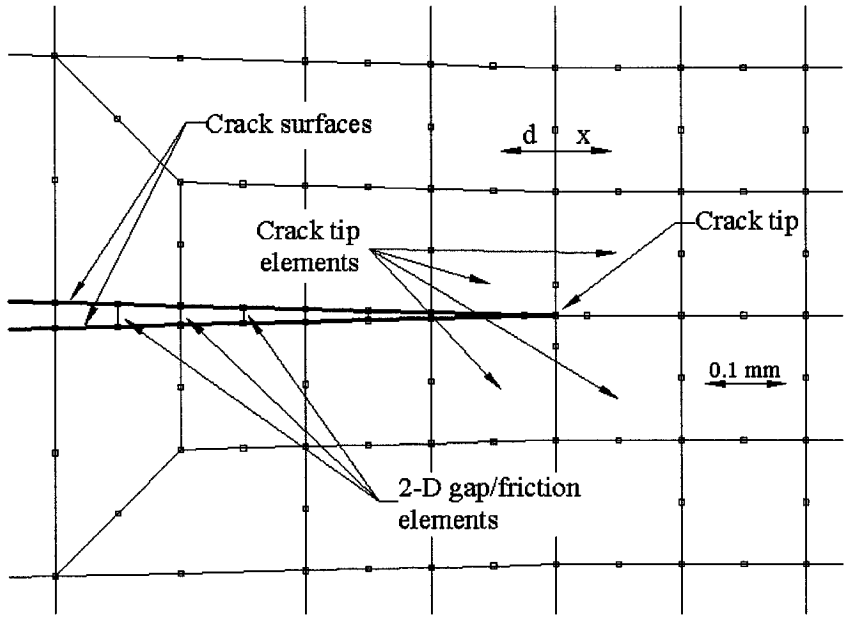

Figure 8-5 Finite element mesh around crack tip showing element types

In order to resist the normal compressive (contact) force, in the normal direction (Figure 8-6(a)), when the gap/friction element is closed, the element is very stiff (K_n) relative to the bodies it is attached to. When the element is open, the element is much softer ($S_n << K_n$). The purpose of the small stiffness is to prevent the rigid body motion that may occur initially, upon break in contact or during sliding motion.

Similarly, in the tangential direction (Figure 8-6 (b)), the gap/friction element is stiff (K_t) when it is closed. In addition, Coulomb friction between the contact points can be introduced to the model by specifying the coefficient of friction, μ, for the element. The friction limit, f_L, is defined as $f_L = \mu|f_n|$, where f_n is the normal compressive force in the element. When the element is in contact and the shear force in the element, f_t, is below the friction limit, the element is said to be in a sticking mode. In this case, the

increment in the relative tangential displacement represents recoverable (elastic) deformation. If the predicted elastic shear force in the element exceeds the friction limit, the shear force is set to the friction limit and the element is said to be in a sliding mode. In this case, the increment includes irrecoverable part (sliding displacement, similar to plastic deformation, as shown by v_s in Figure 8-6 (b)). Finally, the element is again much softer ($S_t << K_t$) when the gap is open [169].

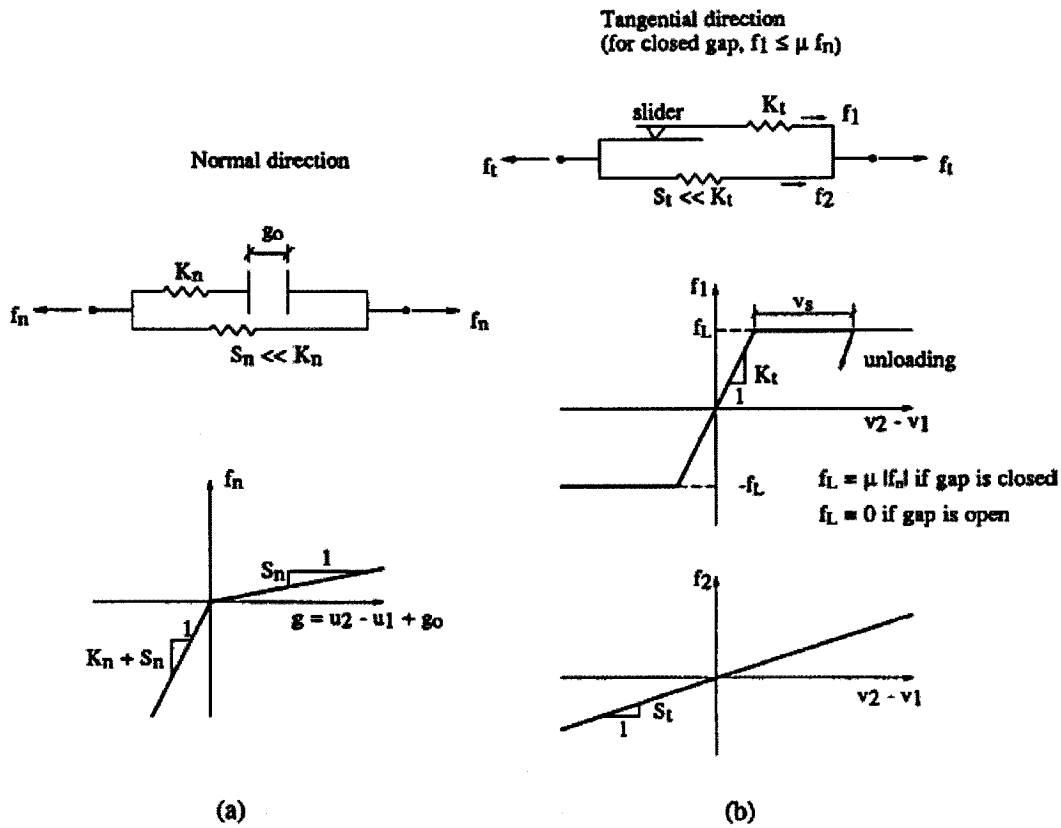

Figure 8-6 Force-deflection relationships of the 2-D gap/friction element: (a) Normal direction; (b) Tangential direction [169]

8.2.3 Model Parameters

In the present work, a parametric study by finite element analyses was performed to investigate the possible "prying" effect of the mismatched crack surface when the crack is subjected to a compressive underload. Each of the finite element models was subjected to a compressive underload followed by a baseline load with the crack surface roughness modeled by the aforementioned gap/friction elements. The parameters in the

study were the crack inclination angle, underload ratio, asperity location and coefficient of friction on the crack surfaces. The "prying" effect was quantified by comparing the *J*-integral in the baseline loading cycle following the underload. The *J*-integral was calculated using NISA in a two-steps process. In the present work, a nonlinear static analysis was first performed by NISA for each of the finite element models. The resulting stress and displacement solution in the output file was then read by ENDURE, a fracture mechanics module, to calculate the *J*-integral. For each of the models, the *J*-integral was calculated from the average of three closed contours around the crack tip.

Four crack inclination angles, $\theta = 0°$, $22.5°$, $45°$ and $67.5°$, were considered in the parametric study. The loading condition of the models consisted of a compressive underload cycle followed by one cycle of baseline constant amplitude loading as shown in Figure 8-7. The underload level P_{UL} ranged from -15 kN to -105 kN while the baseline constant amplitude loading was a cycle between P_{min} = 6 kN and P_{max} = 60 kN, which was the baseline loading employed in the fatigue testing previously in Chapters 6 and 7. In other words, the underload ratio (*ULR*) in the present work ranged from 1.39 to 3.06. In addition, Figure 8-7 shows where the *J*-integral range, ΔJ, of each model was calculated for the loading part of the baseline load cycle, that is, between points A and B of the load history in Figure 8-7, to quantify the "prying" effect of mismatched crack surfaces.

In order to simulate the "prying" effect that may occur due to the contact between asperities on the mismatched crack surfaces, in the majority of the finite element models, one of the gap/friction elements between the crack surfaces was specified to have the initial gap width equal to zero (0-gap element). By having an initial gap width of zero, the 0-gap element was closed and the two points on the crack surfaces connected to the element were in effect initially in contact with each other. It is believed that such contact was analogous to the contact between two rigid crack surface asperities, as schematically shown in Figure 8-8, and thus creating the possible "prying" effect at the crack tip when the crack was under compressive loading. In order to study the effect of the asperity location, a 0-gap element was inserted at one of the six nodal positions in the models behind crack tip, as shown in Figure 8-8. In the present work, the location of the asperity was specified by the distance between the asperity and the crack tip, *d*, in the direction of

the crack that is normalized by the half-crack length, a = 15 mm. In other words, the normalized asperity location (d/a) considered in the present parametric study ranged from 0 to 0.0625. Finally, friction between the crack surfaces was simulated by specifying the coefficient of friction (μ) in the gap/friction elements. Four values of μ, *i.e.* 0, 0.5, 1.0 and 1.5, were considered in the present study.

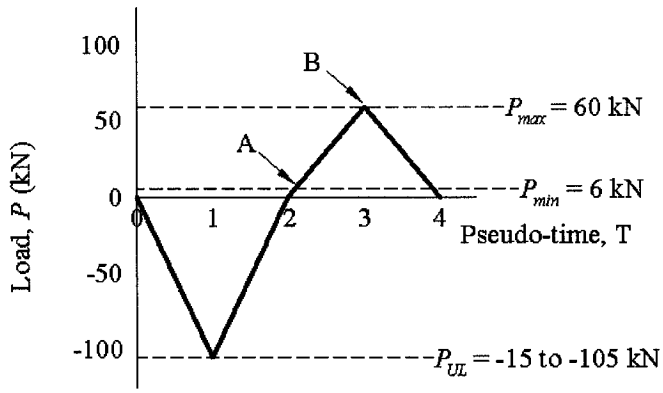

Figure 8-7 Schematic illustration of loading applied to finite element models

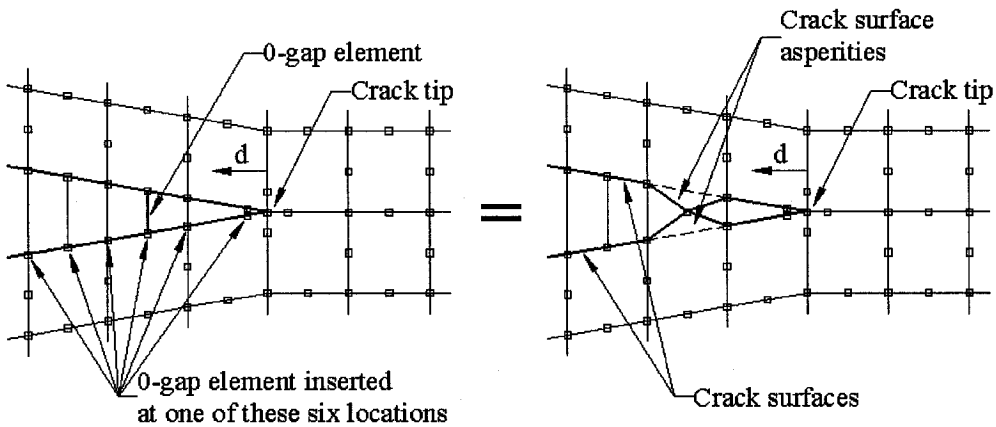

Figure 8-8 Simulation of the contact between crack surface asperities by 0-gap element

In summary, each of the finite element models in the present parametric study can be specified by its crack inclination angle (θ), underload ratio (ULR), asperity location (d/a) and coefficient of crack surface friction (μ). As a result, each of the models in the present work can be identified by a 4-digit code. A complete listing of all the models their J-integral results is given in Appendix A, where the names of the models are shown

in parentheses. For example, Model 1231 has a 22.5° crack inclination angle, an underload of ULR = 1.67 applied, a crack surface asperity located at d/a = 0.0155 and a crack surface coefficient of friction of μ = 0.5. Using combinations of the four parameters, a total of approximately 800 models were analyzed in the present work and the results are discussed below.

8.3 Results and Discussion

8.3.1 Crack Tip Stress Observations

8.3.1.1 Effects of Underload

As mentioned before, a compressive underload in fatigue loading results in crack growth acceleration in the subsequent loading cycles. One of the possible causes of this phenomenon is the creation of residual tensile stresses ahead of the crack tip following the underload. The formation of this tensile plastic zone is demonstrated by the finite element models in the present work, as illustrated by the following figures. The figures show the axial stress distributions, σ_y, around the crack tip of several finite element models at the major loading points of interest in the load history: maximum compressive underload (T = 1 in Figure 8-7), zero load following the underload (T = 2) and maximum baseline load (T = 3). The models selected for the illustration has a 0° crack inclination angle ($\theta = 0$) and no crack surface asperity (d/a = 0) and friction ($\mu = 0$). In addition, the stress distributions are shown for three underload ratios (ULR): 2.50 (Model 0500), 2.78 (Model 0600) and 3.06 (Model 0700).

Figure 8-9(a) shows the distribution of the normalized crack tip axial stress (σ_y/σ_{yld}) of Model 0600 at the maximum compressive underload of ULR = 2.78 (T = 1) while Figure 8-9(b) plots the value of the normalized axial stress ahead of the crack tip along the crack line (x/a) at the same point in the load history for the three ULRs. It can be seen from Figure 8-9(a) that a compressive plastic zone was formed ahead of the crack tip due to the underload. In addition, it can be seen from Figure 8-9(b) that the extent of the stress ahead of the crack tip exceeding the yield strength ($|\sigma_y/\sigma_{yld}| > 1$), and hence the approximate extent of the compressive plastic zone, increased with ULR.

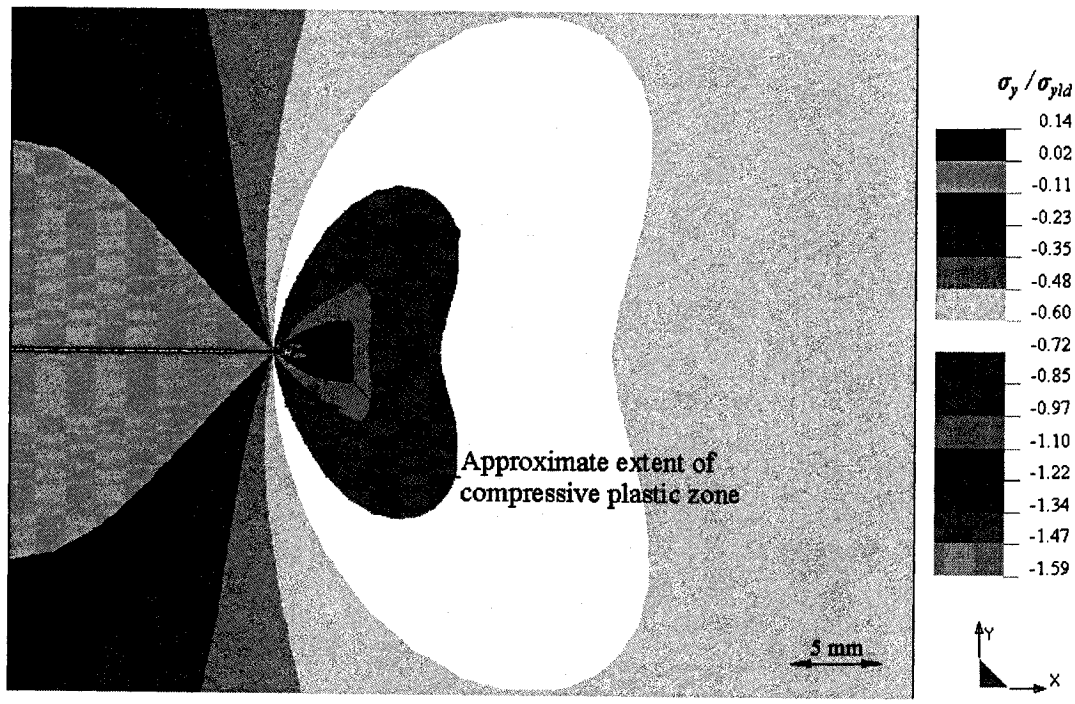

(a)

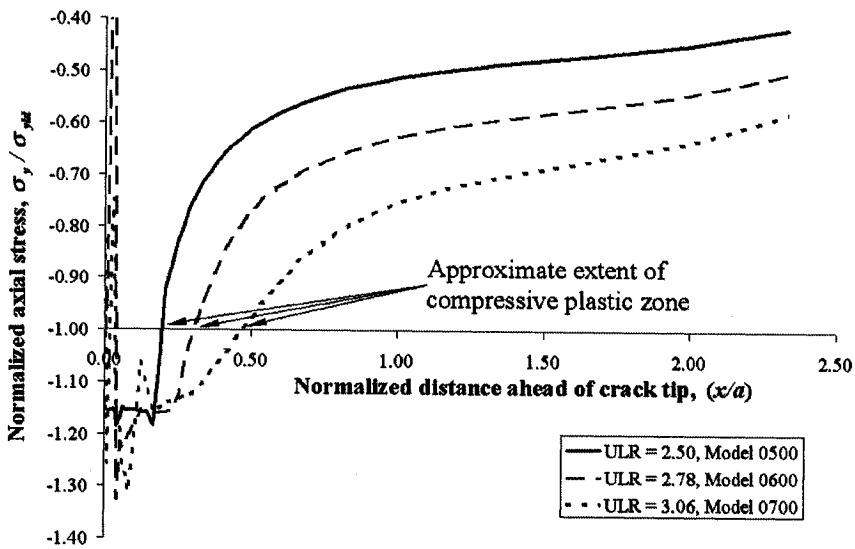

(b)

Figure 8-9 Illustrating effects of underload: (a) Axial stress around crack tip at T = 1, Model 0600; (b) Axial stress ahead of crack tip at T = 1

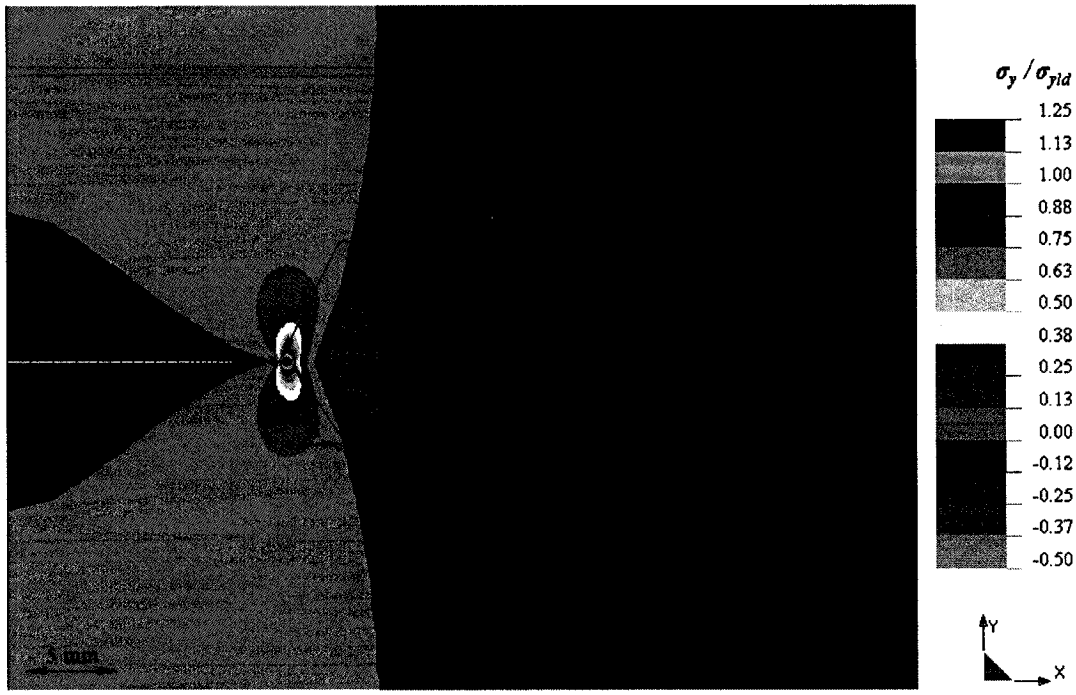

(a)

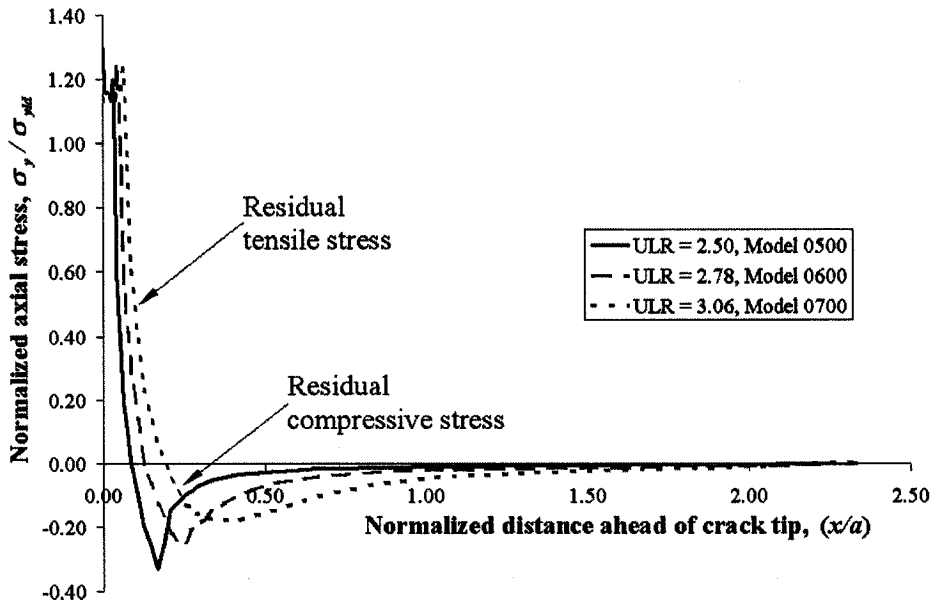

(b)

Figure 8-10 Illustrating effects of underload: (a) Axial stress around crack tip at T = 2, Model 0600; (b) Axial stress ahead of crack tip at T = 2

Figure 8-10(a) shows the distribution of the normalized crack tip axial stress of Model 0600 at the zero load following the underload of *ULR* = 2.78 (T = 2) while Figure

8-10(b) plots the value of the normalized axial stress ahead of the crack tip along the crack line at the same point in the load history for the three *ULR*s. Figure 8-10(a) illustrates the formation of the crack tip residual tensile plastic zone following a compressive underload that could possibly be responsible for crack growth acceleration in the following fatigue cycles. In addition, it can be seen from Figure 8-10(b) that the extent of the residual tensile stress increased with *ULR* due possibly to the greater extent of compressive plastic zone during the underload. Furthermore, a zone of residual compressive stress was formed ahead of the tensile plastic zone that functions to equilibrate the net section stress. The magnitude and the extent of this residual compressive stress were greater for higher *ULR* as shown in Figure 8-10(b).

Finally, Figure 8-11(a) shows the distribution of the normalized crack tip axial stress of Model 0600 at the maximum baseline load following the underload of *ULR* = 2.78 (T = 3) while Figure 8-11(b) plots the value of the normalized axial stress ahead of the crack tip along the crack line at the same point in the load history for the three *ULR*s. It can be seen from Figure 8-11(b) that the size of the crack tip tensile plastic zone at the maximum baseline load increased with the *ULR*, possibly due to the additional tensile residual stresses following the underload as discussed above. Since the size of the plastic zone is a function of the stress intensity factor, it appeared that the underload effect on the subsequent fatigue cycle was similar to an increase in the effective stress intensity factor, which would increase the crack growth rate.

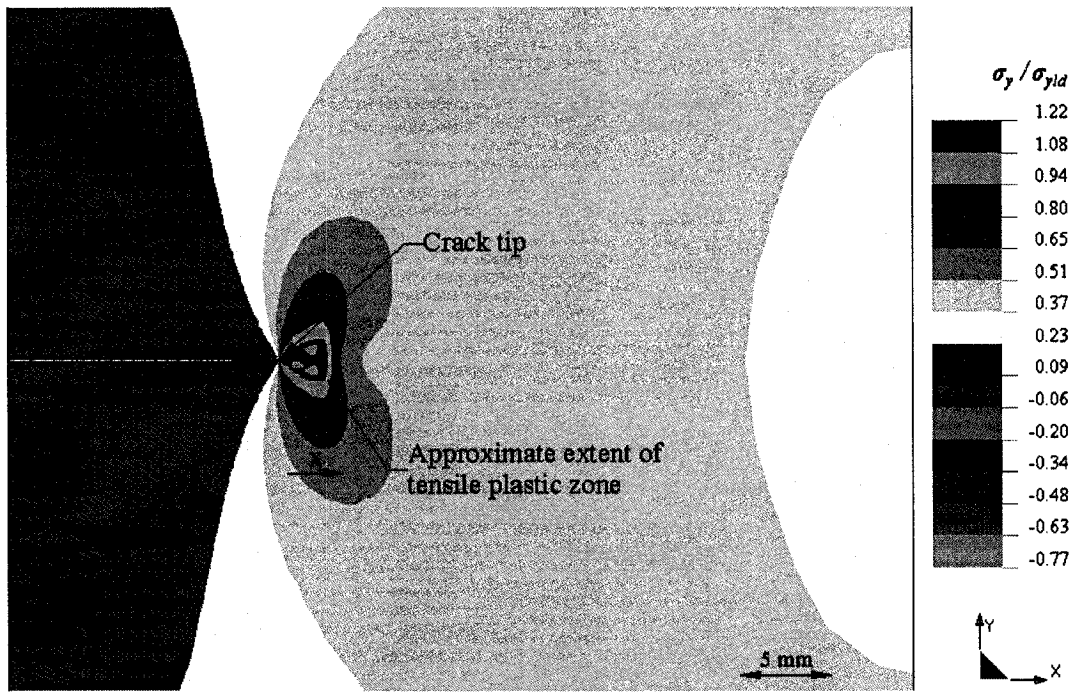

(a)

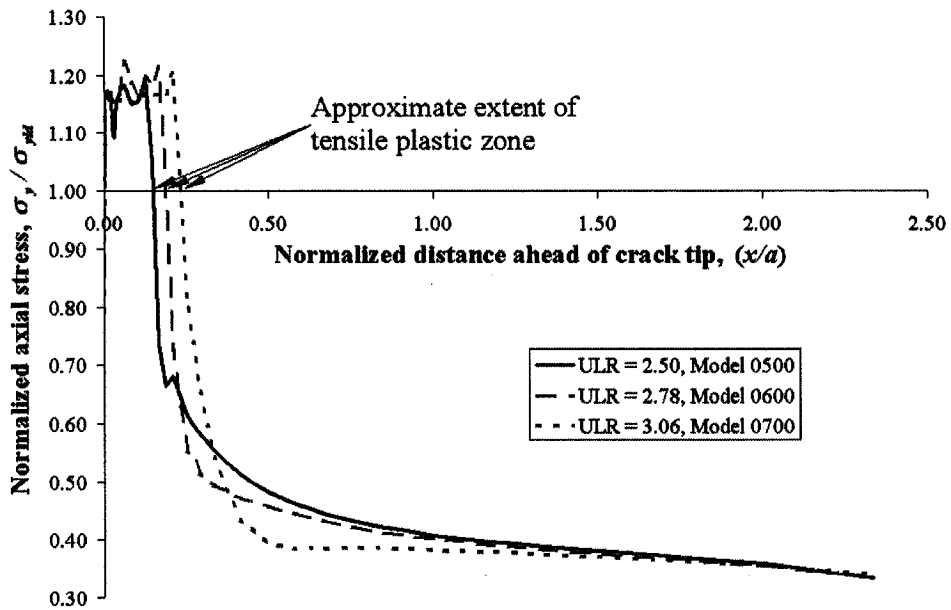

(b)

Figure 8-11 Illustrating effects of underload: (a) Axial stress around crack tip at T = 3, Model 0600; (b) Axial stress ahead of crack tip at T = 3

8.3.1.2 Effects of Crack Surface Roughness

In the present investigation, the crack surface roughness was modeled using a 0-gap element between the crack surfaces. The 0-gap element was introduced to create initial contact between two points on the crack surface, thus simulating a "prying" effect at the crack tip when a compressive underload was applied. An evidence of the "prying effect" was the change in the crack tip stress distribution for a number of finite element models in the present work, due to the introduction of the crack surface roughness, as illustrated by Figure 8-12. The model selected for the illustration (Model 0640) has a 0° crack inclination angle ($\theta = 0.0$), an underload ratio of $ULR = 2.78$, an asperity location of 0.0208 ($d/a = 0.0208$) and no crack surface friction ($\mu = 0.0$).

Figure 8-12 shows the distribution of the crack tip axial stress of Model 0640 at the maximum baseline load following the underload (T = 3). Compared to Figure 8-11(a), where Model 0600 had no crack surface roughness, it can be seen from Figure 8-12 that in addition to the formation of a crack tip tensile plastic zone due to the baseline load, residual stresses were produced near the crack surfaces where the crack was "pried" open by the crack surface asperity (0-gap element). The appearance of the residual stresses near the crack surface asperity could be seen as an evidence of the "prying" effect due to the crack surface roughness during an applied compressive underload. In the present investigation, this "prying" effect was further quantified by the *J*-integral and the results are discussed in the next section.

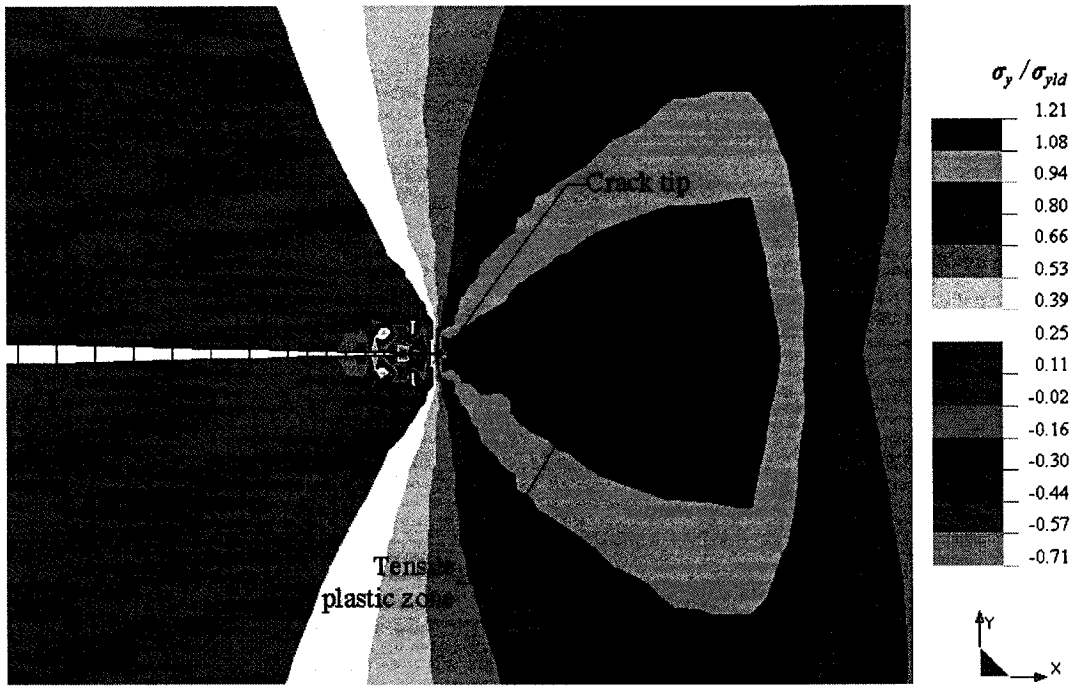

Figure 8-12 Axial stress around crack tip at T = 3 for Model 0640 to illustrate effects of crack surface roughness

8.3.2 *J*-Integral Results

The *J*-integral is a measure of the amount of strain energy released by crack extension and an indication of the severity of the crack tip stresses in a body. It can also be regarded as the driving force behind fatigue crack growth. In the present investigation, the normalized *J*-integral range (ΔJ_n) of the baseline load cycle that was preceded by a compressive underload was used to assess the possible "prying" effect of the crack surface roughness on fatigue crack growth due to the compressive underload on the body. The parameters in the present investigation were the crack inclination angle (θ), underload ratio (*ULR*), asperity location (*d/a*) and coefficient of crack surface friction (μ). The *J*-integral results from the finite element analyses are summarized in Appendix A while the effects of the parameters on the *J*-integral calculations are discussed in the following sections.

8.3.2.1 Effects of Crack Inclination Angle, θ

As seen from Tables A-1, for any given values of underload ratio, asperity location and coefficient of friction of the crack surface, the magnitude of the *J*-integral

decreased as the crack inclination angle increased. This was expected as the axial loading made less contribution to the mixed opening mode of the crack as the crack inclination angle increased. In addition, as demonstrated below, the effects of the other three parameters on the *J*-integral in general also diminished as the crack inclination angle increased.

8.3.2.2 Effects of Underload Ratio, ULR

To illustrate the effects of the underload ratio (*ULR*), Figure 8-13 plots the normalized *J*-integral range (ΔJ_n) of the models without any crack surface roughness or friction (d/a = 0.0 and μ = 0.0) against the *ULR* for the four crack inclination angles (θ) considered in the present work. To highlight the effect of *ULR*, ΔJ_n was normalized with respect to the value with no underload applied (*ULR* = 1.0) for their respective θ. However, it should be noted the trend in the graph was essentially the same for the models with crack surface roughness and friction included.

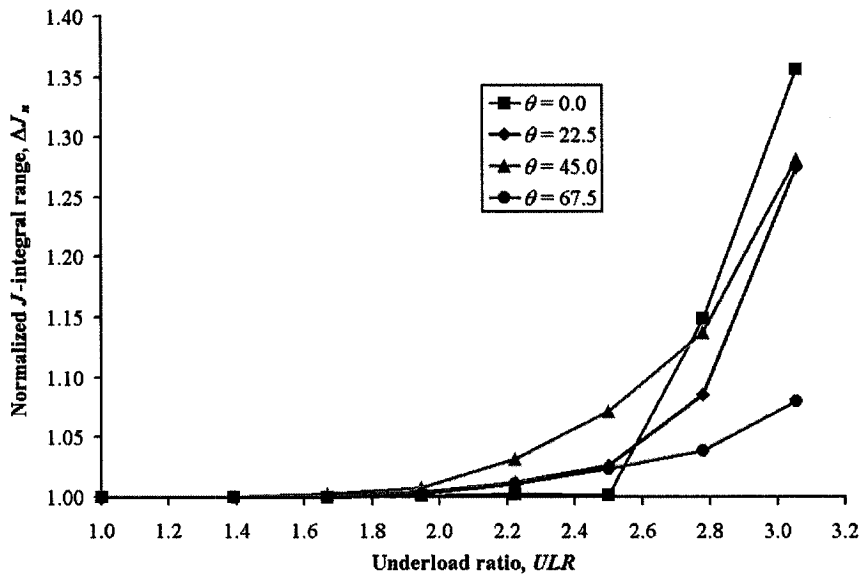

Figure 8-13 Plot of ΔJ_n against *ULR* without crack surface roughness for each θ

As seen from Figure 8-13, in general, a compressive underload raised the ΔJ_n of the following load cycle, which increased with the *ULR*. In addition, the underload appeared to initially have the most effect for $\theta = 45°$ while at the highest *ULR*s

considered, the underload caused the greatest increase in ΔJ_n for $\theta = 0°$ and the least increase for $\theta = 67.5°$. Furthermore, as demonstrated below, the effects of crack surface roughness and friction on the *J*-integral in general were more significant at higher *ULR*. To summarize, the results from the present finite element analyses suggested that a compressive underload increases the size of the tensile plastic zone and the effective *J*-integral range, or the effective stress intensity factor range, in the following fatigue cycles, which leads to crack growth acceleration.

8.3.2.3 Effects of Crack Surface Roughness

To illustrate the effects of the underload ratio on the possible "prying" effect of the crack surface roughness, that is, when a 0-gap element was inserted in the finite element model, Figure 8-14(a) plots the normalized *J*-integral range (ΔJ_n) of the models at $\theta = 0°$ and $\mu = 0$ for the range of asperity location (*d/a*) considered in the present work against the underload ratio (*ULR*). To highlight the effect of crack surface roughness, ΔJ_n was normalized with respect to the values from models with no crack surface roughness (*d/a* = 0) for their respective *ULR*. In addition, the trend in the data is indicated in the figure by plotting the average value at each *ULR*. Furthermore, the data for the models at the other three crack inclination angles are similarly plotted in Figures 8-14(b) to (d) respectively. Finally, the average trends in Figures 8-14(a) to (d) are plotted together in Figure 8-14(e) for comparison.

As seen from the Figures 8-14, the introduction crack surface roughness to the models produced additional changes to the *J*-integral results when compared to the no-roughness (*d/a* = 0) models and provided evidence to the possible "prying" effect. However, the changes produced were less substantial than previously seen from the compressive underloading effects alone. Nonetheless, it appears that the "prying" effect was more pronounced and the *J*-integral results became more scattered as *ULR* increased. In addition, as seen from Figure 8-14(e), it appeared that the "prying" effect lowered ΔJ_n when *ULR* was low, while ΔJ_n increased when *ULR* was high for $\theta = 0°$, 22.5° and 67.5°. In other words, the present results suggested that for these crack inclination angles, the "prying" effect would enhance the effects of a compressive underload and

increase crack growth acceleration if *ULR* is high enough. However, at low *ULR*, the "prying" effect would generally diminish the underload effects. Finally, it appears that the "prying" effect is the most significant and produces the most increase in ΔJ_n when the crack is in the horizontal direction ($\theta = 0°$).

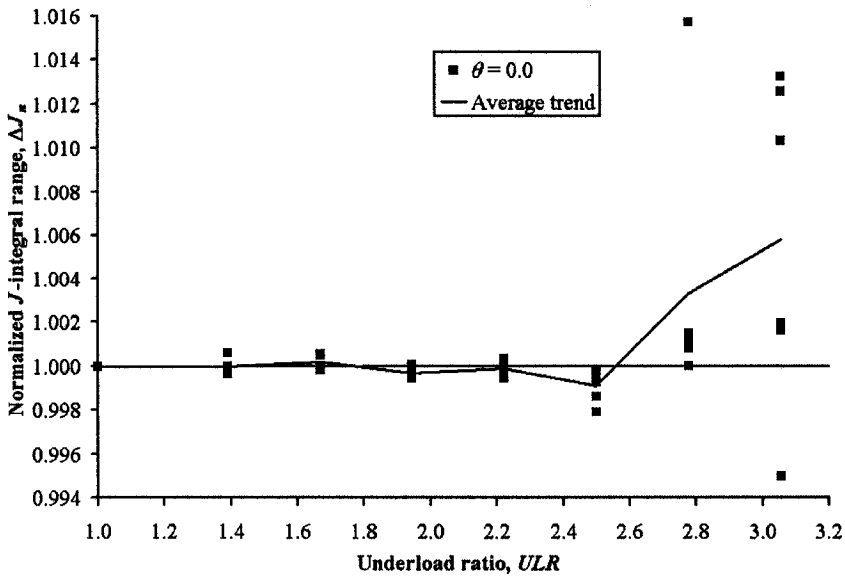

Figure 8-14(a) Plot of ΔJ_n and average trend against *ULR* with crack surface roughness for $\theta = 0.0°$

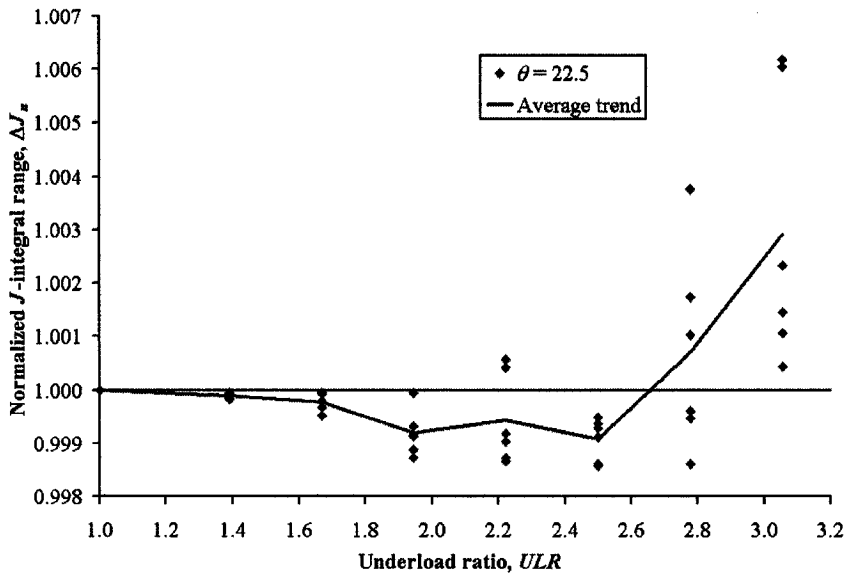

Figure 8-14(b) Plot of ΔJ_n and average trend against *ULR* with crack surface roughness for $\theta = 22.5°$

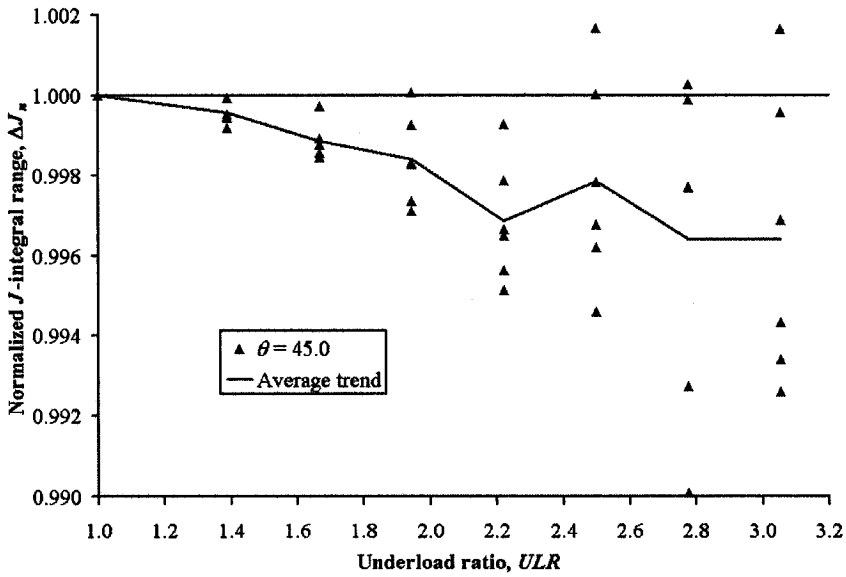

Figure 8-14(c) Plot of ΔJ_n and average trend against *ULR* with crack surface roughness for $\theta = 45.0°$

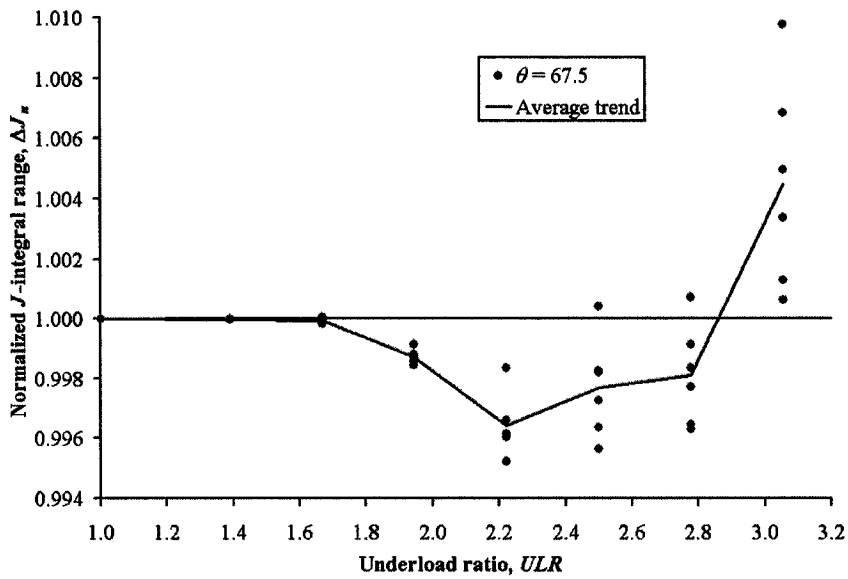

Figure 8-14(d) Plot of ΔJ_n and average trend against *ULR* with crack surface roughness for $\theta = 67.5°$

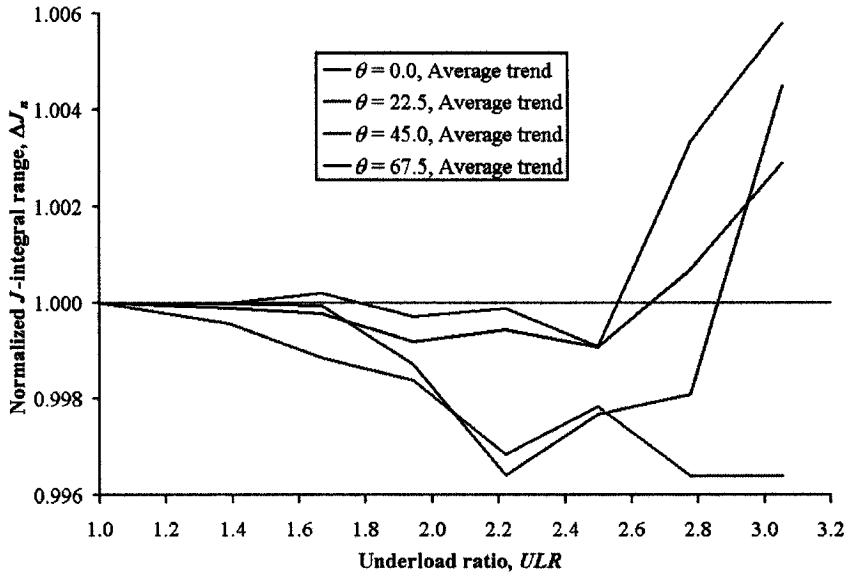

Figure 8-14(e) Plot of average trend against *ULR* with crack surface roughness for all four θ

Figure 8-14 Plot of ΔJ_n and average trend against *ULR* with crack surface roughness for each θ: (a) 0.0°; (b) 22.5°; (c) 45.0°; (d) 67.5°; (e) Average trend for all four θ

8.3.2.4 Effects of Asperity Location, d/a

It was established in the previous section that the "prying" effect of the crack surface roughness was more significant at high underload ratio. Therefore, to illustrate the effects of the asperity location on the "prying" effect, Figures 8-15(a) and (b) re-plot the data (ΔJ_n) from Figures 8-14(a) to (d) for the two highest underload ratio considered in the present work, *i.e.* *ULR* = 2.78 and 3.06 respectively, against the asperity location (*d/a*). To highlight the effect of *d/a*, ΔJ_n was again normalized with respect to the values from models with no crack surface roughness (*d/a* = 0) for their respective *ULR*.

By comparing Figure 8-15(a) to (b), it was once again shown that, in general, the "prying" effect produced greater changes to ΔJ_n at higher *ULR*. The figures also confirmed the fact that the "prying" effect was the most significant and produced the most increase in ΔJ_n, on average, at $\theta = 0°$. Unfortunately, the present investigation did not appear to yield a conclusive relationship between the asperity location and the "prying" effect, at least viewing through the *J*-integral perspective. Nonetheless, a few noteworthy observations could still be made from Figures 8-15.

- At ULR = 2.78 (Figure 8-15(a)), the crack surface asperity appeared to have the most significant effect at approximately d/a = 0.02, particularly for $\theta = 0°$ and $22.5°$.
- There also appeared to be a less significant peak at approximately d/a = 0.0025 for $\theta = 0°$.
- At ULR = 3.06 (Figure 8-15(b)), the peak in the "prying" effect at approximately d/a = 0.0025 became noticeable for $\theta = 22.5°$ and $45°$, while the peak at this location became more significant for $\theta = 0°$.
- In addition, while the second peak remained more or less at approximately d/a = 0.02 for $\theta = 22.5°$ and $45°$, such a peak had shifted to approximately d/a = 0.025 for $\theta = 0°$.
- Furthermore, for $\theta = 45°$ the "prying" effect appeared to increase at approximately d/a = 0.030. Finally, for $\theta = 67.5°$, a peak had emerged at approximately d/a = 0.030.

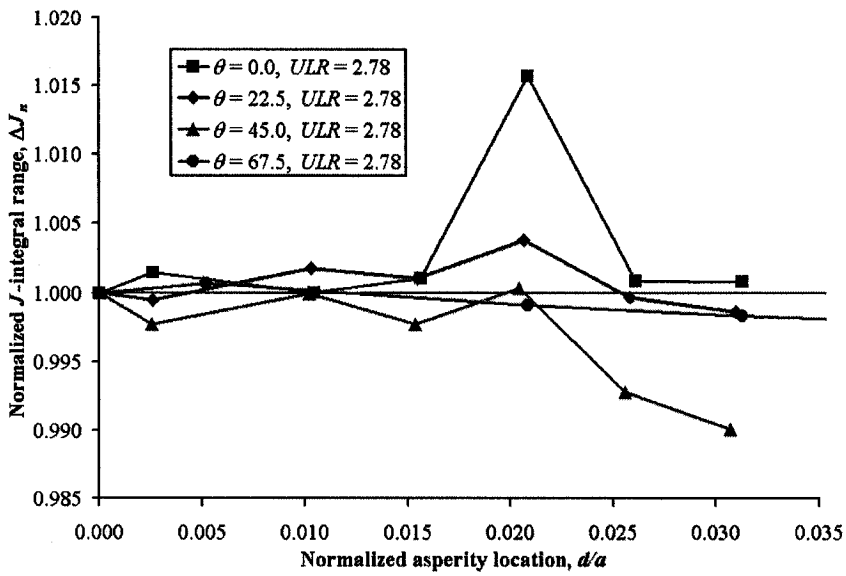

Figure 8-15(a) Plot of ΔJ_n against d/a for each θ at ULR = 2.78

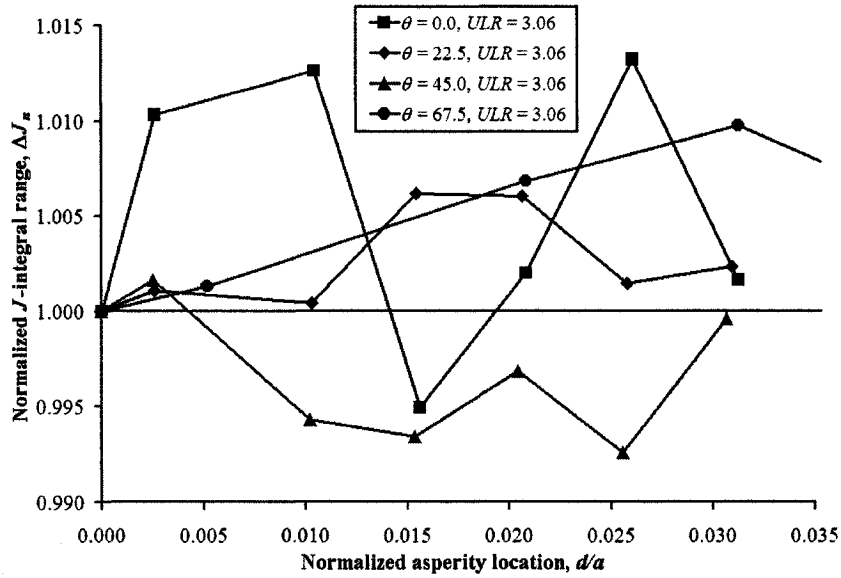

Figure 8-15(b) Plot of ΔJ_n against d/a for each θ at $ULR = 3.06$

Figure 8-15 Plot of ΔJ_n against d/a for each θ: (a) At $ULR = 2.78$; (b) At $ULR = 3.06$

To summarize, the above observations from the plot of the normalized J-integral range against the asperity location suggested that the "prying" effect was noticeable when the crack surface asperity was located either at very close to the crack tip, where it would provide the greatest "prying" force at the crack tip, or at a location that was farther away from the crack tip. In addition, the distance between the second location and the crack tip appeared to increase as the underload ratio increased. Finally, it should be noted that these observations were the most pronounced at $\theta = 0°$.

8.3.2.5 Effects of Crack Surface Friction, μ

In the present investigation, the crack surface friction was simulated by specifying the coefficient of friction for the gap/friction elements that were inserted across the crack surfaces in the finite element models. In addition, it was established from the previous sections that the "prying" effect of the crack surface roughness was more significant at high underload ratio (ULR) and when the crack surface asperity was located either at very close to the crack tip or at a second location that appeared to be ULR-dependent. Therefore, to illustrate the effects of the crack surface friction on the "prying" effect, Figures 8-16(a) and (b) show the plot of the normalized J-integral range (ΔJ_n) versus the

coefficient of crack surface friction (μ). The J-integral values are for the two asperity locations (d/a) where the "prying" effect was significant at ULR = 3.06 and for the four crack inclination angles (θ) considered in the study. To highlight the effect of μ, ΔJ_n was normalized with respect to the values from models with no crack surface friction (μ = 0) for each crack inclination angle, underload ratio and asperity location considered.

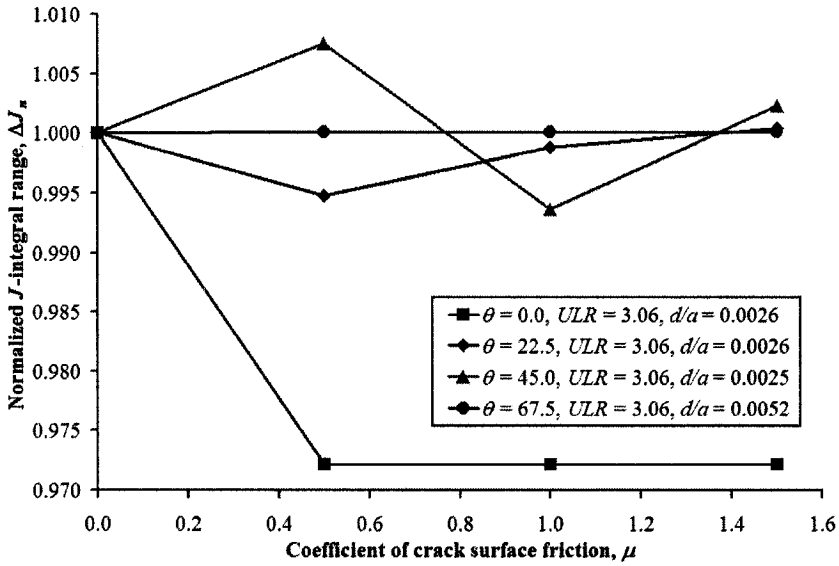

(a)

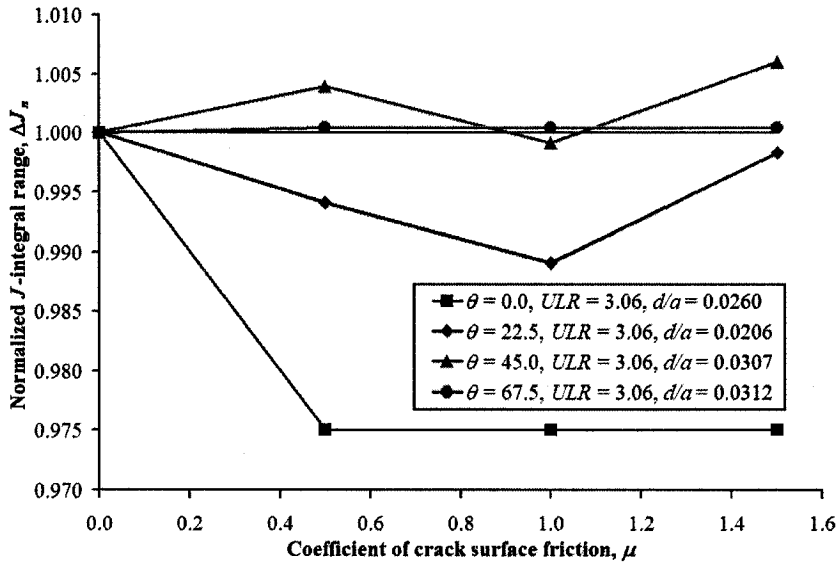

(b)

Figure 8-16 Plot of ΔJ_n against μ at ULR = 3.06 for each θ: (a) At d/a = 0.0025-0.0052; (b) At d/a = 0.0206-0.0312

As seen from Figures 8-16, there does not appear to be a conclusive relationship between the coefficient of crack surface friction and the "prying" effect from the *J*-integral perspective. For example, while the effects of the crack surface friction appeared to be constant for any value of $\mu > 0$ for $\theta = 0°$ and $67.5°$, it was not apparent how the value of μ influenced the "prying" effect for $\theta = 22.5°$ and $45°$. Nonetheless, it appeared that crack surface friction in general diminished the "prying" effect for $\theta = 0°$ and $22.5°$ at both asperity locations while the "prying" effect was enhanced by crack surface friction, at certain values of μ, for $\theta = 45°$ and $67.5°$. The results, particularly for $\theta = 0°$ and $22.5°$, appeared to confirm the aforementioned finding that part of the input energy to the crack was consumed in resisting the friction along the crack contact surfaces, and thus reduced the "prying" effect in the present investigation. In addition, the crack surface friction appeared to have the most effect for $\theta = 0°$ and the least effect for $\theta = 67.5°$, although the friction effects were again less substantial than shown previously from the compressive underloading effects alone.

8.4 Conclusions

Crack closure was a concept proposed to account for the effects of load interaction and to estimate the fatigue crack growth rates under variable amplitude loading. Due to crack closure, only a portion of a fatigue cycle is effective for the crack propagation. The roughness-induced crack closure is one of the crack closure mechanisms and is attributed to the contact between the asperities on the opposite crack surfaces. However, during a compressive underload in fatigue loading, it is possible that the crack tip might be "pried" open by the contact of these asperities and cause additional fatigue crack growth acceleration following the underload.

The present work investigated the possibility of the "prying" effect by performing finite element analyses on centre-cracked steel plates to examine the effects of crack inclination angle, compressive underload ratio, crack surface roughness and friction on the *J*-integral following the underload. The finite element models incorporated gap/friction elements between the crack surfaces to simulate the "prying" and frictional forces at the crack tip. The following conclusions were drawn from the analyses:

1) The magnitude of the J-integral decreased as the crack inclination angle, θ, increased. In addition, the effects of the underload ratio, asperity locations and coefficient of crack surface friction on the J-integral in general also diminished as the crack inclination angle increased.
2) A compressive underload increased the size of the tensile plastic zone and the effective J-integral range in the following fatigue cycles that leads to crack growth acceleration. In addition, the effects of crack surface roughness and friction on the J-integral in general were enhanced as the underload ratio increased. Furthermore, the underload effects on the J-integral were more significant than either the crack surface roughness or friction effects.
3) For the crack inclination angle of 0°, 22.5° and 67.5°, the "prying" effect of crack surface roughness enhanced the effects of a compressive underload if the underload ratio was high enough. However, at low underload ratio, the "prying" effect generally diminished the effects from underload.
4) The "prying" effect was more significant when the crack surface asperity was located either very close to the crack tip or at a location that was farther away from the crack tip. The distance between the second location and the crack tip appeared to increase as the underload ratio increased.
5) The crack surface friction in general diminished the "prying" effect for the crack inclination angle of 0° and 22.5°. The "prying" effect was enhanced by the crack surface friction, at certain values of coefficient of friction, for crack inclination angle of 45° and 67.5°.

Chapter 9 Simulation of Reduced Ductility in Steel by using PMMA for Fatigue Testing

9.1 Introduction

It is well-known in steel that due to load interaction effects, the fatigue crack growth is retarded after an application of tensile overload and is accelerated to a lesser degree after a compressive underload, as described in Chapter 3. This phenomenon is attributed to the formation of a relatively large zone of residual compressive or tensile stress in front of the crack tip after the application of the overload or underload respectively. Since the amount of crack growth retardation and acceleration is influenced by the amount of crack tip plastic deformation, it is then conceivable that the reduction in the ductility of steel caused by low temperature, high strain rate, high constraint and/or welding, as described in Chapter 4, would decrease the overload and underload effects as well. In order to investigate this possibility, overloading and underloading fatigue tests were performed on centre-cracked polymethyl methacrylate (PMMA) specimens in the present work. PMMA is a semi-brittle glassy polymer which shows little reduction in cross-section area and elongation at fracture. In the present work, the effects of loading frequency, tensile overload and compressive underload on the fatigue crack propagation of PMMA were examined.

9.2 Experimental Procedure

9.2.1 Overview

The experimental fatigue crack propagation testing program consisted of subjecting centre-cracked specimens of PMMA to repeated cycles of axial loading. The first stage of the experimental program involved constant amplitude testing at various load frequencies. The second stage investigated the amount of fatigue crack growth retardation after applying a single tensile overload (*OL*) within an otherwise constant amplitude loading sequence. The final stage examined the amount of fatigue crack growth acceleration by applying a single compressive underload (*UL*) as in stage two.

The loading terms are defined in Figure 9-1. The fatigue crack growth tests were conducted in accordance with ASTM Standard E647, *Standard Test Method for Measurement of Fatigue Crack growth Rates* [139].

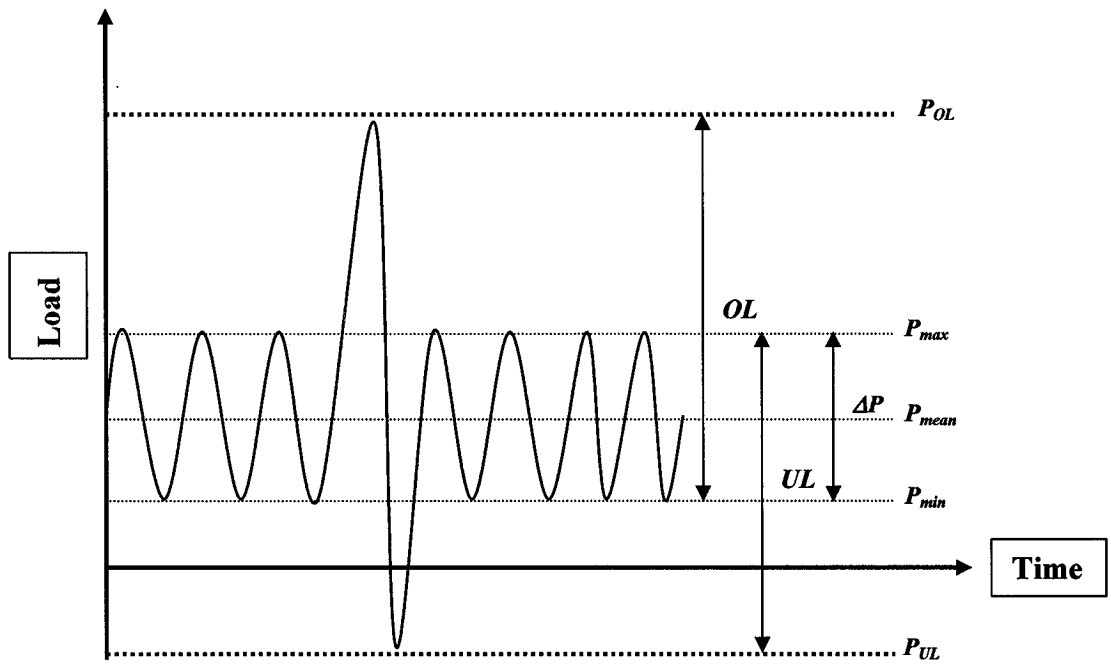

Figure 9-1 Schematic representation of overload and underload terms [2]

9.2.2 Test Material

In the present work, PMMA was used to simulate the reduced ductility experienced by steel when it is subjected to the conditions described in Chapter 4. PMMA is a semi-brittle glassy polymer used in a variety of applications in place of glass. The PMMA used in the present work comes from commercial sheets of 5.75 mm thick manufactured by CYRO Industries and ATOFINA Chemicals, Inc. The material properties for the PMMA obtained from standard tension tests are shown in Table 9-1. In this table, yield strength is the 0.2% offset yield strength.

9.2.3 Test Specimen

The PMMA test specimens were similar to the 350WT steel specimens as described in Section 6.3. However, the starter notch for the PMMA specimens was done by a hand saw with a blade thickness of 0.25 mm to a length of approximately 5 mm

from each side of the centre hole. The overall specimen dimensions were approximately 300 mm long x 100 mm wide x 5.75 mm thick, with a starter notch length (2a) of approximately 14 mm.

Table 9-1 Material properties of PMMA

Material Property	Value
2% Offset Yield Strength, σ_{yld}	42 MPa
Ultimate Strength, σ_{ult}	56 MPa
Modulus of Elasticity, E	2,870 MPa
Reduction in Area, RA	1.04%
Elongation at Fracture, EL	2.54%

9.2.4 Test Procedure

The test apparatus has been described previously in Section 6.3.4. All fatigue tests were performed in accordance with ASTM Standard No. E647. The fatigue loading on the specimens comprised of axial tension in a sinusoidal wave form at room temperature in air. In all cases, the baseline constant amplitude loading consisted of cycles at maximum load of P_{max} = 2 kN and stress ratio, R, of 0.1. Specimens in the first stage of the experimental program were tested with the baseline constant amplitude loading at frequencies ranging from 1 to 30 Hz. In the second stage, tensile overloading (OL) of either 2.3 kN or 2.8 kN was applied to each specimen at crack length, a, of either approximately 10 mm or 12 mm. In the third and final stage, compressive underloading (UL) of 2.3 kN, 2.8 kN, 3.3 kN or 3.8 kN was applied to each specimen at crack length of approximately 14 mm. All specimens in the second and final stage were tested at load frequency of 30 Hz. The detailed loading scenario for each specimen is presented in the next sections.

Before the tests, each of the specimens was precracked to a minimum length of 1.0 mm on both sides of the starter notch as required by the standard before valid crack length data was recorded. This procedure removed the effect of the blunt starter notch and provided a sharpened fatigue crack of adequate size and straightness. The crack length was then measured periodically with the help of the traveling microscope until failure. The crack length data was calculated by the average of the left and right cracks,

and then reduced to fatigue crack growth rate data by both the secant and the incremental methods as recommended by ASTM E647.

9.3 Results and Discussion

9.3.1 First Stage Tests Results

The purpose of this stage of testing was to determine the effect of load frequency on the fatigue response of PMMA. Therefore, the first stage of the experimental program involved testing specimens with the baseline constant amplitude loading at loading frequencies of 1 Hz (series CAL 1), 5 Hz (series CAL 5), 10 Hz (series CAL 10), 20 Hz (series CAL 20) and 30 Hz (series CAL 30). The fatigue rate curves of each specimen as well as the fitted average fatigue rate curve for all the first stage specimens are plotted in Figures 9-2.

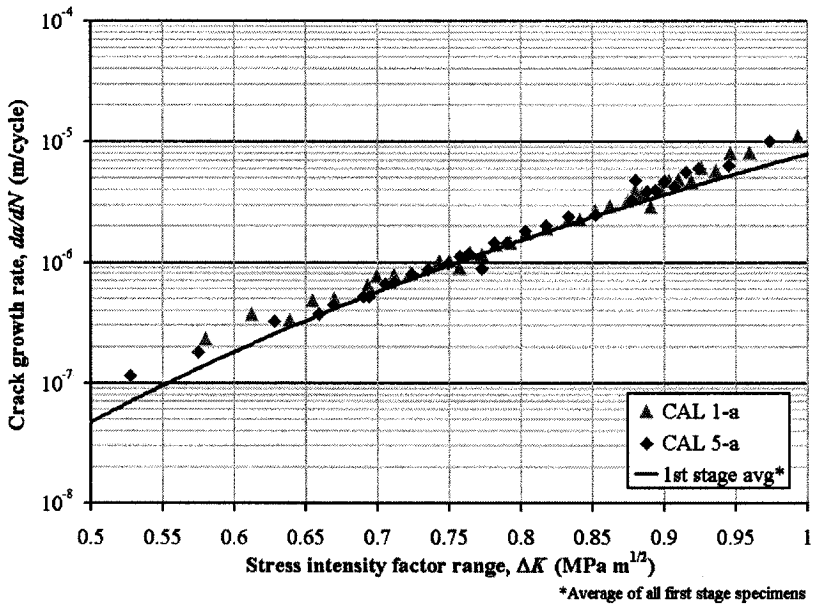

Figure 9-2(a) Fatigue rate curves of the first stage specimens, Series CAL 1 and CAL5

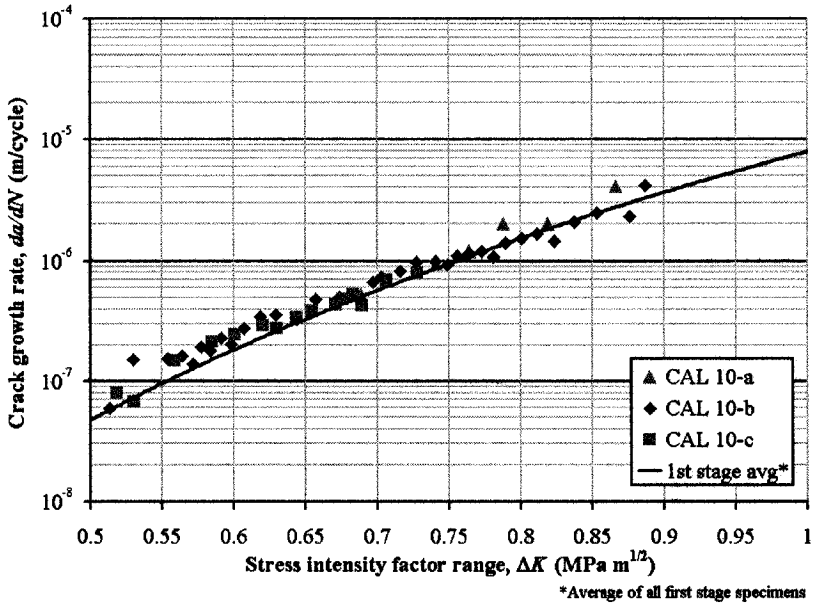

Figure 9-2(b) Fatigue rate curves of the first stage specimens, Series CAL 10

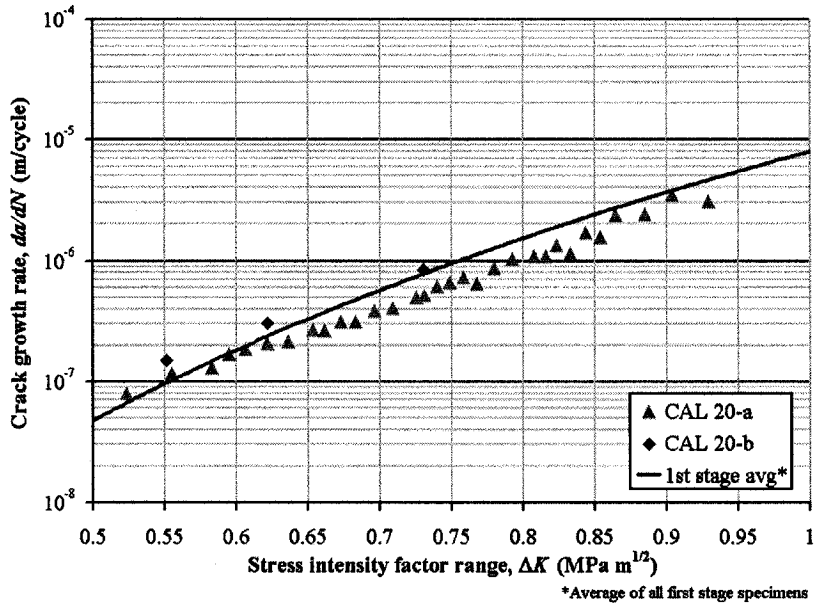

Figure 9-2(c) Fatigue rate curves of the first stage specimens, Series CAL 20

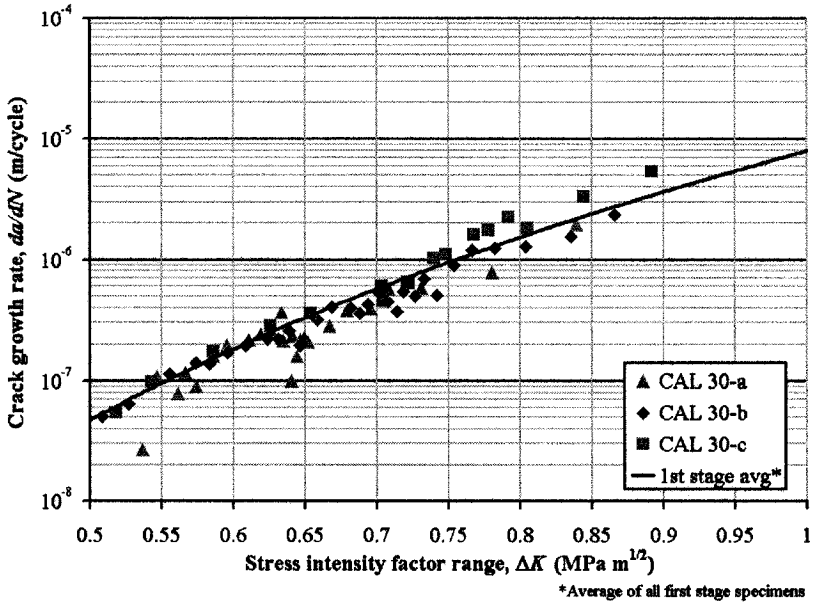

Figure 9-2(d) Fatigue rate curves of the first stage specimens, Series CAL 30

Figure 9-2 Fatigue rate curves of the first stage specimens: (a) Series CAL 1 and CAL5; (b) Series CAL 10; (c) Series CAL 20; (d) Series CAL 30

Fatigue crack growth data for PMMA at loading frequencies that range from 1 to 30 Hz were similar as demonstrated by the fact that the average fatigue rate curve fitted the combined fatigue crack growth rate data with a coefficient of determination (R^2) of 0.949. Therefore, it appears that the loading frequency has little or no effect on the fatigue crack growth rate of PMMA in an inert environment. In addition, the average fatigue rate curve has Paris constants of $C = 7.99\times10^{-6}$ and $n = 7.39$. Thus, the value of n for PMMA was not as high as that reported for highly brittle materials such as ceramics (*i.e.* 15-50).

9.3.2 Second Stage Tests Results

The second stage of the experimental program involved testing specimens with the baseline constant amplitude loading with a single tensile overload (*OL*) of 2.3 kN at a crack length of approximately 10 mm (series OL A), followed by a single *OL* of 2.3 kN applied at approximately 12 mm (series OL B), a single *OL* of 2.8 kN applied at crack length of approximately 10 mm (series OL C), and subjecting the specimens of Series OL

D to load of P_{max} = 3 kN and R = 0.1 up to a crack length of approximately 12 mm (multiple overloading). The purpose of this stage of testing was to determine the amount of fatigue crack growth retardation (if any) after the application of a tensile overload for PMMA tested in air.

The amount of fatigue crack growth retardation can be measured by the number of retarded or delay cycles, N_d. In this report, the number of delay cycles for each specimen was defined as the difference between the number of elapsed cycles measured between the overload and the last recorded crack length in the overload test (N_{OL}) and the corresponding number of cycles in a constant amplitude load test (N_{CAL}), that is $N_d = N_{OL} - N_{CAL}$. Since the amount of retardation has been shown to be affected by constant amplitude fatigue crack growth of the specimen (that is, the higher the constant amplitude fatigue crack growth, the lower the number of delay cycles and vice versa), the ratio of N_d to N_{CAL}, $R_d = N_d/N_{CAL}$, was calculated for each specimen to provide a normalized comparison of the amount of fatigue crack growth retardation between different specimens. Table 9-2 shows the overload level (OL), the actual crack length at which the overload was applied, a_{OL}, and the values of N_{CAL}, N_{OL}, N_d and R_d for each specimen in this stage. The value of R_d has also been averaged for each series of specimens. The fatigue rate curve of each specimen and the average fatigue rate curve obtained from the first stage specimens are plotted in Figures 9-3.

Overall, the specimens in the second stage of testing showed below average fatigue crack growth rate in comparison to the results obtained at the first stage. The crack extension occurring during tensile overload as reported in [129, 170] was only observed in specimen OL C-3 out of all the specimens. A crack extension of 0.94 mm was measured in specimen OL C-3 during the tensile overload. In addition, the overload stress intensity factor for that specimen was the highest among the series' specimens subjected to a single overload. Thus it appears that the reoccurrence of crack extension during overload requires a certain level of overload stress intensity factor. For all the above second stage specimens, the fatigue rate data became more scattered right after the application of the overload as the crack lengths were recorded at closer intervals of elapsed cycles. This produces difficulty in determining whether fatigue crack growth

retardation had occurred. Nevertheless, there was relatively little scatter in the rest of the fatigue rate data after the application of overload and the Paris equation could fit well to the data.

Table 9-2 Summary of delay cycles for second stage test specimens

Specimen ID	*OL* (kN)	a_{OL} (mm)	N_{CAL}	N_{OL}	N_d	R_d (%)
OL A-1	2.3	9.96	16,213	16,800	587	3.62
OL A-2	2.3	10.02	31,625	33,500	1,875	5.93
OL A-3	2.3	9.99	35,891	39,750	3,859	10.8
					Average	6.77
OL B-1	2.3	12.25	20,957	21,250	293	1.40
OL B-2	2.3	12.03	28,609	30,850	2,241	7.83
OL B-3	2.3	11.93	16,253	16,650	397	2.44
					Average	3.89
OL C-1	2.8	9.97	45,107	48,250	3,143	6.97
OL C-2	2.8	9.92	52,916	42,550	-10,366	-19.6
OL C-3	2.8	10.16	20,336	21,100	764	3.76
					Average	-2.95
OL D-1	2.8	11.36	22,471	21,500	-971	-4.32
OL D-2	2.8	11.96	17,432	18,500	1,068	6.13
OL D-3	2.8	11.85	17,193	18,350	1,157	6.73
					Average	2.85

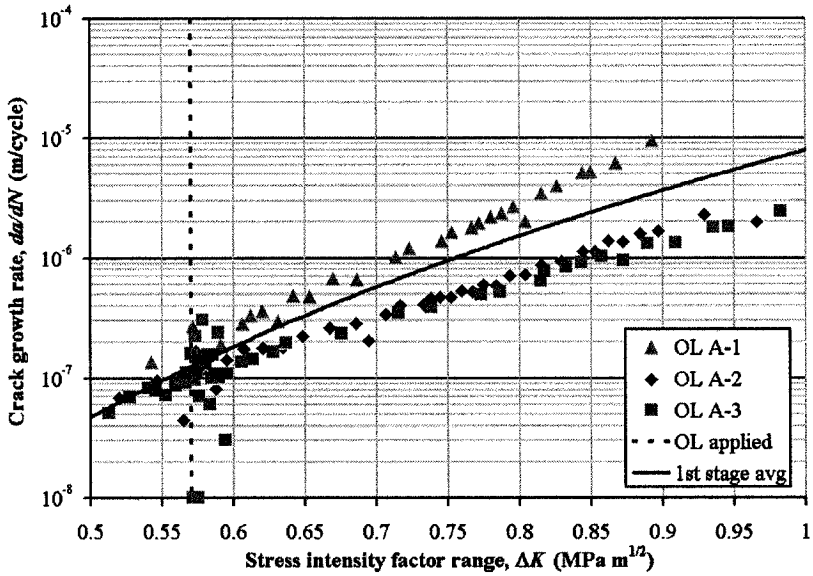

Figure 9-3(a) Fatigue rate curves of the second stage specimens, Series OL A

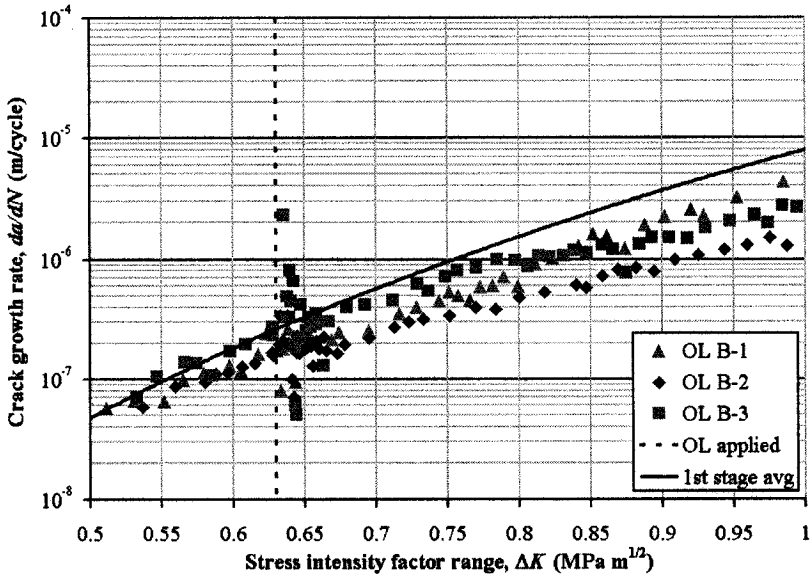

Figure 9-3(b) Fatigue rate curves of the second stage specimens, Series OL B

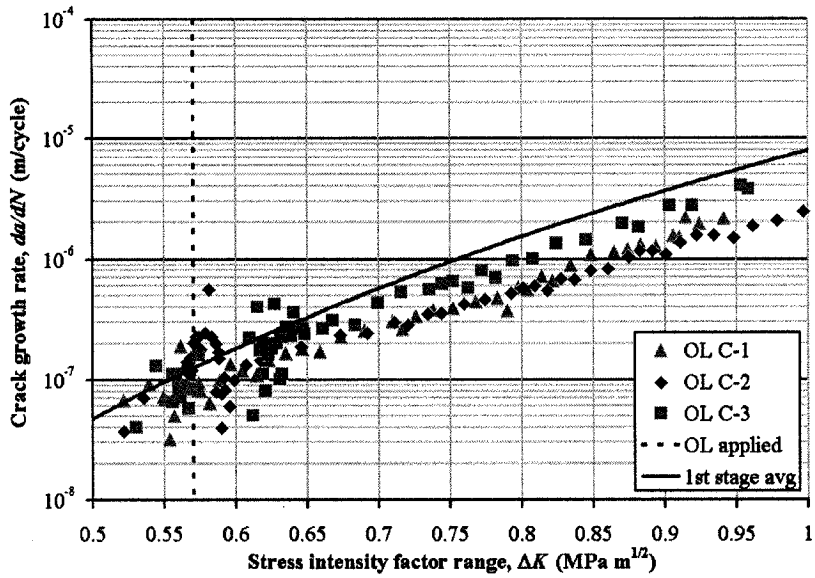

Figure 9-3(c) Fatigue rate curves of the second stage specimens, Series OL C

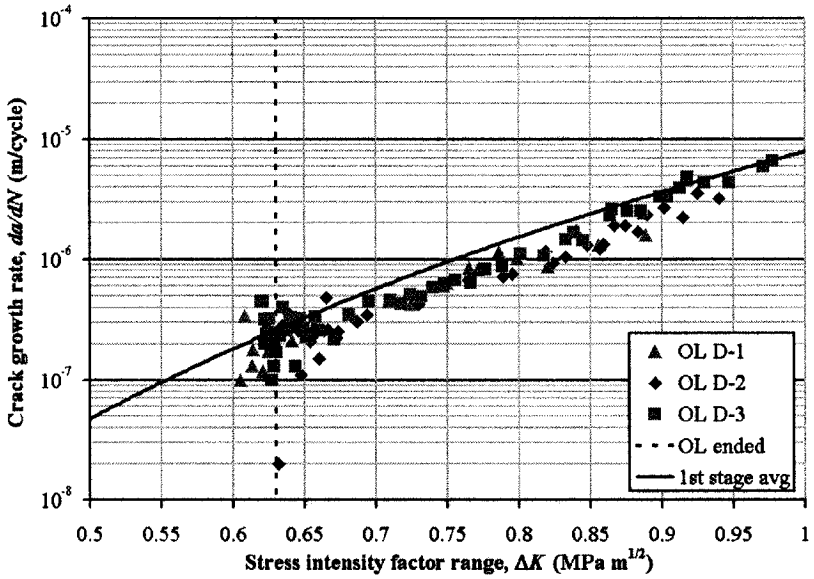

Figure 9-3(d) Fatigue rate curves of the second stage specimens, Series OL D

Figure 9-3 Fatigue rate curves of the second stage specimens: (a) Series OL A; (b) Series OL B; (c) Series OL C; (d) Series OL D

Most of the test results in this stage showed a small number of delay cycles following a tensile overload in an otherwise constant amplitude loading scenario. The only exceptions were two of the specimens having an overload level of 2.8 kN, specimens OL C-2 and OL D-1. In addition, by comparing the average R_d values in series OL A and OL B, it can be seen that an overload applied at shorter crack length produced more retardation than the one applied at longer crack length. Furthermore, by comparing the average R_d values in series OL A and OL C, it can be seen that the amount of fatigue crack growth retardation in PMMA decreased with higher overload level, which is contrary to the results reported in [129]. These suggested that too high of an overload stress intensity factor (*i.e.*, long crack length or high load) may reduce the amount of crack growth retardation or may even cause crack growth acceleration. Lastly, by comparing the average R_d values in series OL C and OL D, it was observed that retardation would also increase when multiple overloads were applied, compared to a single overload, which is in agreement to the results reported in [128].

9.3.3 Third Stage Tests Results

The purpose of this stage of testing was to determine the amount of fatigue crack growth acceleration (if any) after the application of a compressive underload for PMMA tested in air. Therefore, the third stage of the experimental program involved testing specimens with the baseline constant amplitude loading at which a single compressive underload (*UL*) of 2.3 kN (series UL A), 2.8 kN (series UL B), 3.3 kN (series UL C) and 3.8 kN (series UL D) were applied at a crack length of approximately 14 mm.

The amount of fatigue crack growth acceleration was determined by the number of accelerated cycles, N_a. Similar to the second stage testing, the number of accelerated cycles for each specimen was calculated by $N_a = N_{CAL} - N_{UL}$, where N_{UL} is the number of elapsed cycles measured between the underload and the last recorded crack length in the underload test. Similarly, the ratio of N_a to N_{CAL}, $R_a = N_a / N_{CAL}$ was calculated for each specimen. Table 9-3 shows the underload level (*UL*), the actual crack length at which the underload was applied, a_{UL} and the values of N_{CAL}, N_{UL}, N_a and R_a for each specimen in this stage. The value of R_a is the averaged value for each series of specimens. The fatigue rate curve of each specimen, as well as the average fatigue rate curve obtained from the first stage specimens are plotted in Figures 9-4.

Overall, the specimens in the third stage of testing showed below average fatigue crack growth rate similar to the ones from the second stage of testing. Seven out of the twelve test specimens in this stage experienced crack growth retardation (as indicated by their negative R_a values), rather than the accelerated cycles following a compressive underload as experienced by the other specimens of the series. Nevertheless, the amount of fatigue crack growth retardation following an underload was less than the amount following an overload as demonstrated by the smaller average R_a values in this stage compared to the previous stage. From the test results of the investigation it cannot be conclusively stated whether a compressive underload causes crack growth retardation or acceleration in PMMA. There appears to be no evidence of a relationship between the level of underload and the amount of fatigue crack growth retardation or acceleration.

Table 9-3 Summary of accelerated cycles for third stage test specimens

Specimen ID	*UL* (kN)	a_{UL} (mm)	N_{CAL}	N_{UL}	N_a	R_a (%)
UL A-1	2.3	14.12	3,387	3,600	-213	-6.29
UL A-2	2.3	14.08	14,803	16,100	-1,297	-8.76
UL A-3	2.3	14.08	3,811	3,250	561	14.7
					Average	-0.11
UL B-1	2.8	14.26	2,801	2,500	301	10.7
UL B-2	2.8	14.16	10,332	10,500	-168	-1.63
UL B-3	2.8	13.98	6,927	6,050	877	12.7
					Average	7.26
UL C-1	3.3	14.45	8,064	8,000	64	0.79
UL C-2	3.3	14.16	10,974	11,750	-776	-7.07
UL C-3	3.3	14.14	5,953	6,100	-147	-2.47
					Average	-2.92
UL D-1	3.8	14.05	11,076	11,500	-424	-3.83
UL D-2	3.8	14.01	17,879	18,200	-321	-1.80
UL D-3	3.8	14.09	1,644	1,600	44	2.68
					Average	-0.98

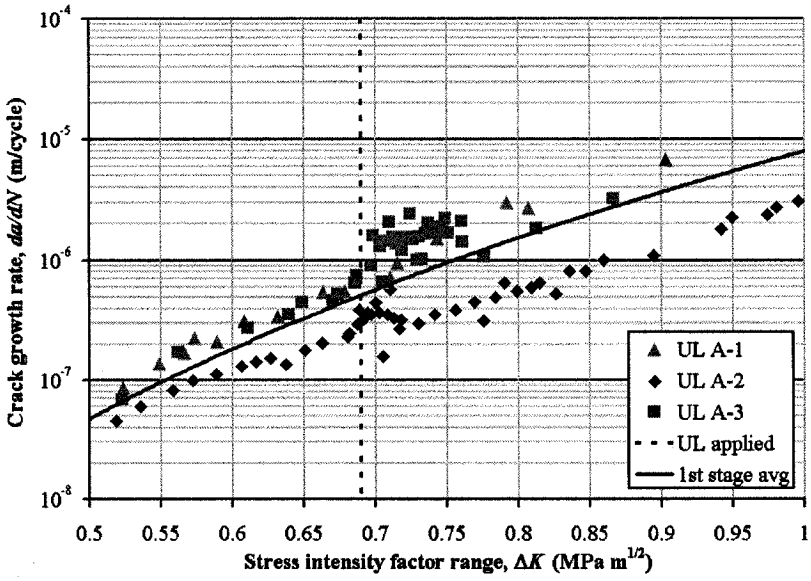

Figure 9-4(a) Fatigue rate curves of the third stage specimens, Series UL A

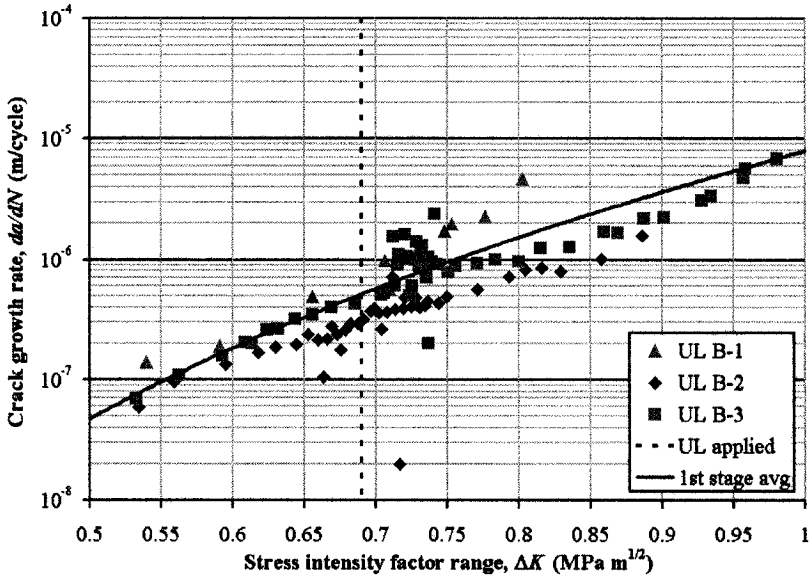

Figure 9-4(b) Fatigue rate curves of the third stage specimens, Series UL B

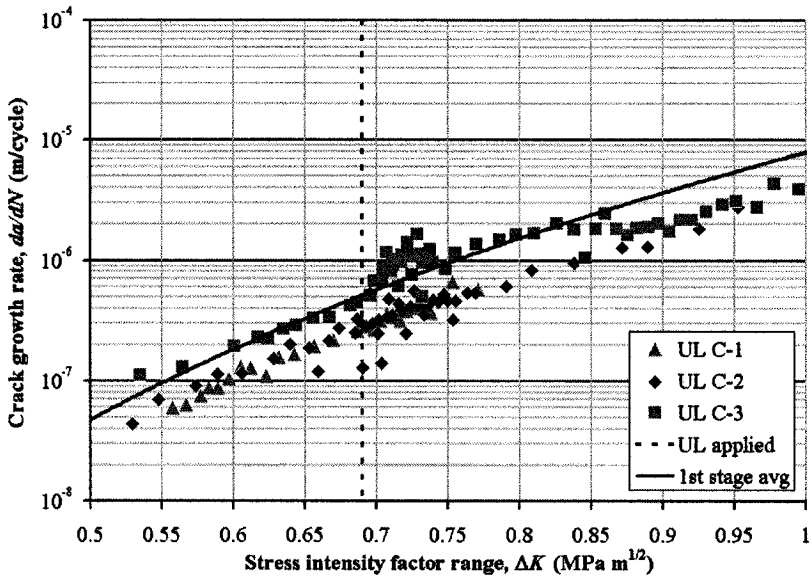

Figure 9-4(c) Fatigue rate curves of the third stage specimens, Series UL C

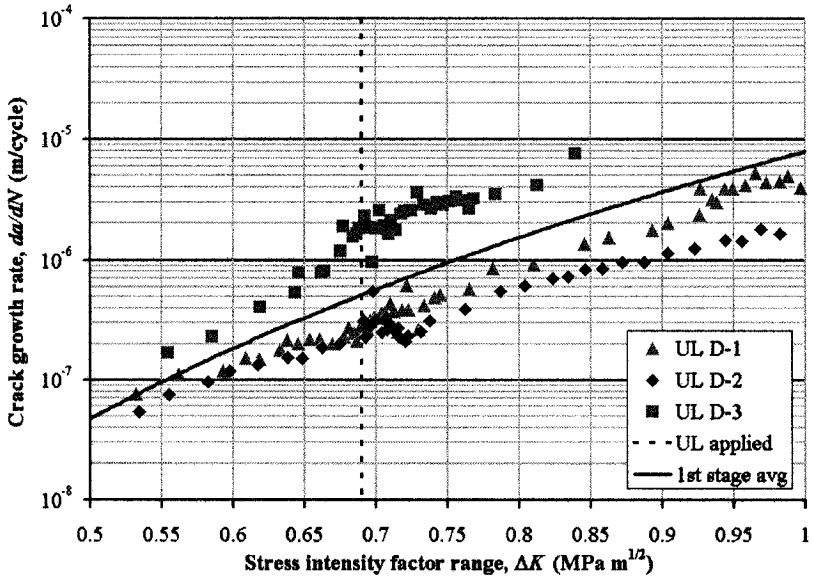

Figure 9-4(d) Fatigue rate curves of the third stage specimens, Series UL D

Figure 9-4 Fatigue rate curves of the third stage specimens: (a) Series UL A; (b) Series UL B; (c) Series UL C; (d) Series UL D

9.4 Conclusions

The load interaction effects in steel cause the fatigue crack growth retardation after an application of tensile overload and acceleration after a compressive underload. An experimental investigation into the fatigue behaviour of polymethyl methacrylate (PMMA), a semi-brittle glassy polymer, was performed to simulate the fatigue crack growth retardation and acceleration of steel when its ductility is reduced due to low temperature, high strain rate, high constraint and/or welding. Through three stages of testing in this investigation the following observations were made:

1) The first stage consisted of constant amplitude loading of specimens at loading frequencies ranging from 1 to 30 Hz. The results showed that loading frequency had insignificant or no effect on the fatigue behaviour of PMMA.
2) The second stage consisted of applying different levels and number of tensile overload to the specimens at different crack lengths in an otherwise constant amplitude loading scenario. The results showed that the amount of fatigue crack growth retardation following a tensile overload in PMMA decreased with both

increased crack length at which the overload was applied and with increased overload level. Retardation was found to increase following multiple overloads compared to a single overload.

3) The third stage consisted of applying different levels of single compressive underload in an otherwise constant amplitude loading scenario. The results did not show any pronounced relationship between the level of compressive underload and the amount of crack growth retardation or acceleration in PMMA.

The results from PMMA demonstrated that the amount of fatigue crack growth retardation and acceleration would likely be reduced for steel under the above embrittling conditions that limit the amount of crack tip plastic deformation. In addition, the beneficial effect of fatigue crack growth retardation after a tensile overload is further limited by the lowered allowable overload level due to the decrease in fracture toughness in steel. An overload could be in fact potentially detrimental by the fact that increase crack extension can occur during the overload.

Chapter 10 Fatigue of Welded Stiffened Steel Plates

10.1 Introduction

Typical stiffened sheet structures are metal sheets reinforced by stiffeners and are widely used in aircraft, ships and chemical industry structures for their light weight and high strength and stiffness. They are mostly found in the airframes, fuselages and wings of aircraft and the deck and side plating on a ship where the amount of fatigue loading is the greatest. Much research has been performed in the past to address fatigue crack growth in aircraft, with the studies made on aluminum panels that have either riveted or adhesive bonded stiffeners. On the other hand, relatively few studies [23-29] have been conducted on welded stiffeners that are often found in ship structures. This type of stiffeners induces complex residual stresses in the structure that are caused by the heating and cooling effects of welding. In general, the fatigue behaviour of welded stiffeners is not well understood and test data of this type are scarce. Nonetheless, the distribution of these residual stresses is recognized to have considerable influence on the fatigue crack growth rates of welded stiffened panel. In addition, experimental techniques for the determination of residual stresses have their disadvantages. Therefore, the motivation of the present research was to investigate whether a finite element approach could provide a comparable alternative for evaluating the residual stresses and their influence on the fatigue of welded stiffened steel plates. Further background information on welded stiffeners can be found in Section 5.6.

In the present investigation, the fatigue behaviour of welded stiffened centre-cracked 350WT steel plates was studied. Using the neutron diffraction method, the residual stress fields near the fatigue crack tips in the steel plates were evaluated. The residual stress intensity factors produced by the measured residual stress fields were then calculated using the Green's function in order to determine the effective stress intensity factors. The residual stress fields were also simulated by the finite element method, which consisted of heat transfer analysis followed by nonlinear static analysis. Following the residual stress simulation, the effective stress intensity factors were computed from fracture mechanics analysis. Finally, the fatigue crack growth rates of the stiffened plates

were predicted using the effective stress intensity factors from both methods and compared to the experimental results from fatigue testing.

10.2 Experimental Procedure

10.2.1 Overview

In the present work, the neutron diffraction technique was used to obtain the residual stress distribution in the welded stiffened 350WT steel specimens. The principle of this technique was presented in Section 5.6.3 and the experimental produce of this technique is presented in this section. In addition, these specimens were also subjected to the fatigue testing procedure that is described in the Section 6.3.

10.2.2 Test Material

The test material, 350WT Category 5 steel, has been described in Section 6.3.2. The mechanical properties of the steel are presented in Table 10-1. Steel has a cubic crystal structure and its stiffness matrix, [C], can be written as:

$$[C]=\begin{bmatrix} C_{11} & C_{12} & C_{12} & 0 & 0 & 0 \\ C_{12} & C_{11} & C_{12} & 0 & 0 & 0 \\ C_{12} & C_{12} & C_{11} & 0 & 0 & 0 \\ 0 & 0 & 0 & C_{44} & 0 & 0 \\ 0 & 0 & 0 & 0 & C_{44} & 0 \\ 0 & 0 & 0 & 0 & 0 & C_{44} \end{bmatrix}. \tag{10-1}$$

It should be noted that the stiffness matrix components, C_{11}, C_{12} and C_{44}, must be transformed by the following equation to the corresponding values, C'_{11}, C'_{12} and C'_{44}, in the coordinate system defined by the diffracting plane:

$$C'_{ijkl} = a_{im}a_{jn}a_{ko}a_{lp}C_{mnop}, \tag{10-2}$$

where a_{ij} are the direction cosines between the original and the transformed coordinate systems. Equation 10-2 is written in tensor notation and in Einstein notation to represent summation over each repeated index.

Table 10-1 Material properties of 350WT steel

Material Property	Value
Yield Strength, σ_{yld}	365 MPa
Ultimate Strength, σ_{ult}	496 MPa
Reduction in Area, RA	68%
Modulus of Elasticity, E	200 GPa
Poisson's Ratio, ν	0.3
Fracture Strength, σ_f	1,063 MPa
Fracture Ductility, ε_f	1.15
C_{11}	237 GPa [171]
C_{12}	141 GPa [171]
C_{44}	116 GPa [171]

10.2.3 Test Specimen

The welded stiffened test specimens used in the present work were of a middle tension type described in Section 6.3.3. In addition, the mid-section of the base plates was reduced to a width of 75 mm with a fillet radius of 12.5 mm. Stiffeners of dimensions 160 mm long by 2.5 mm wide by 5 mm high were fillet welded to 25 mm from the centre line of the base plate by a wire-fed MIG welder at a current of 90 A and a voltage of 18 V using a filler metal of BOC Solidarc 70S-6. During welding the base plate was clamped to the work table and the stiffeners were held in place by tack welds. Finally, the specimens were fatigue-cracked to various crack lengths before undergoing the neutron diffraction experiment. The details of the specimens tested are summarized in Table 10-2. The test specimen layout and dimensions are shown in Figure 10-1. A typical stiffened specimen is shown in Figure 10-2.

Table 10-2 Details of test specimens

Specimen	Fatigue crack length from notch (mm)	Comment
1	------	fatigue test only
2	1.10	short crack, diffraction measurement around crack tip
3	6.79	long crack, diffraction measurement around crack tip
4	0.00	no crack, diffraction measurement along whole uncracked section

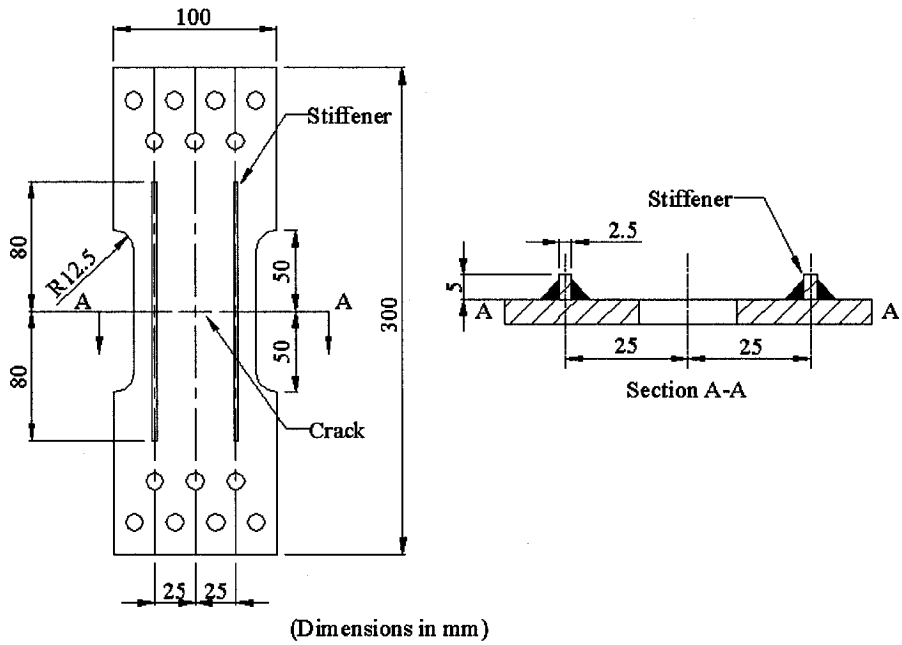

Figure 10-1 Stiffened specimen layout and dimensions

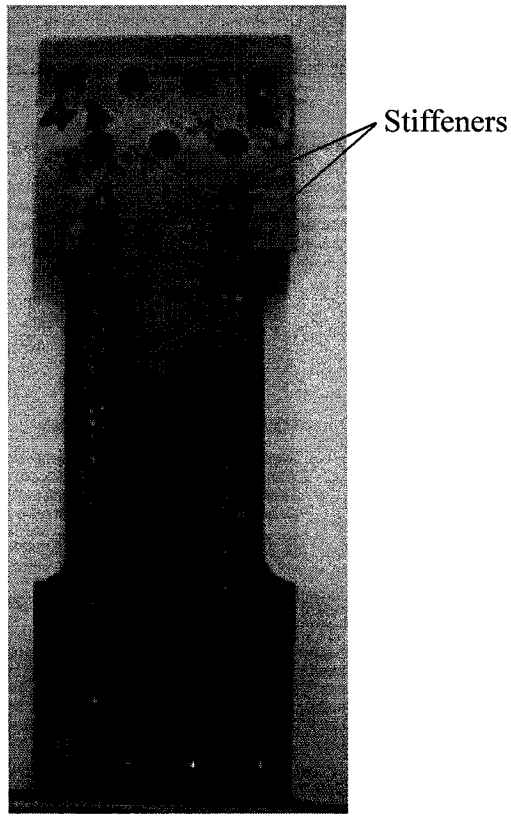

Figure 10-2 Typical stiffened specimen

10.2.4 Test Apparatus

Neutron diffraction measurements were performed using the L3 Strain Scanning Diffractometer at the Canadian Neutron Beam Centre (CNBC). The diffractometer was connected to the NRU nuclear reactor (Figure 10-3(a)), which was the source of the neutrons. Neutrons having the desired wavelength (1.5 Å) were extracted from the white beam exiting the reactor using a squeezed single crystal germanium monochromator. The beam then came out from the incident beam slit (Figure 10-3(b)) and impinged on the specimen that was mounted on the specimen table, which had a computer-controlled three-dimensional translation stage that allowed the specimen to be properly oriented and positioned for strain measurements in the desired directions. From the diffracted beam off the specimen, the neutrons were counted by a 32-wire multi-detector – spanning an angle of approximately 2.5° – for the selected scattering angle. The true diffraction angle was then determined by fitting a Gauss function to the measured neutron counts distribution as shown in Figure 10-4. The intersection of the incident and diffracted

beams defined the sampled volume in the specimen, as shown in Figure 5-23, in which the average strain was measured.

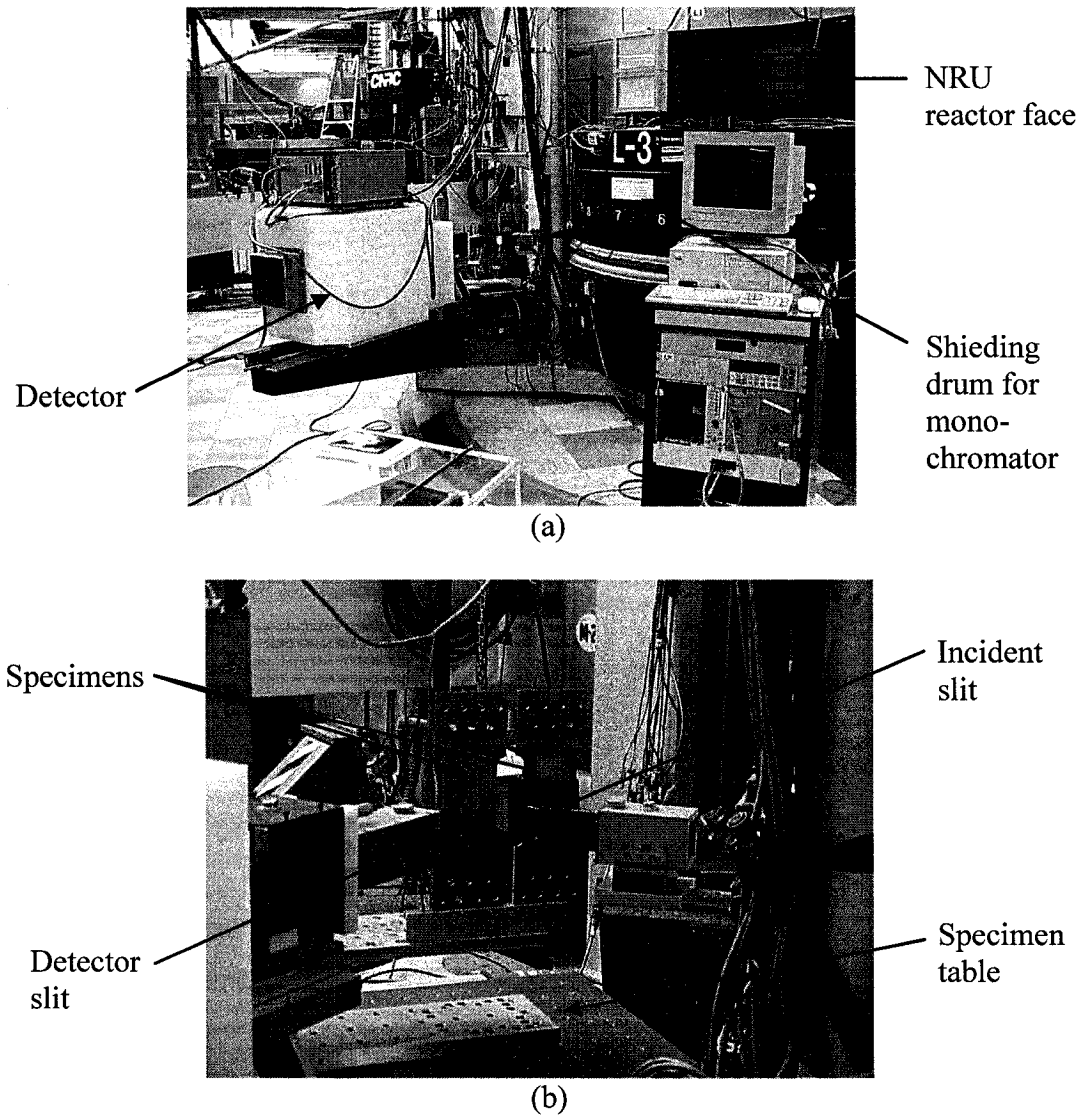

Figure 10-3 L3 Diffractometer: (a) Overall view; (b) Close up view

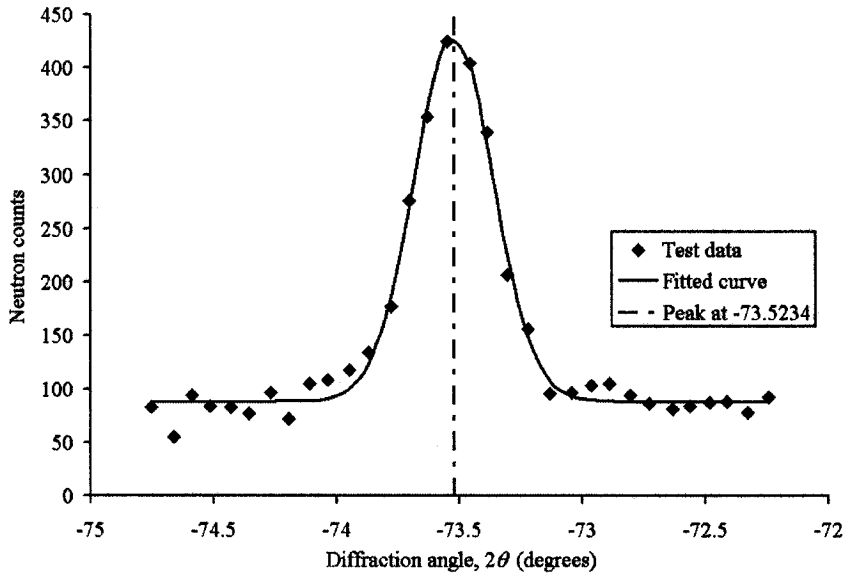

Figure 10-4 Typical diffraction peak

10.2.5 Test Procedure

The diffractometer was first properly aligned with a pair of telescopes in accordance with CNBC procedure. The wavelength of the neutron beam was chosen to be approximately 1.5 Å by rotating the germanium crystal in the monochromator to the (115) diffraction plane. The detector was then driven to the appropriate angle 2θ such that strains were measured normal to the (211) plane of the specimen, which is the recommended diffraction plane for ferritic steel [42-43]. In the present investigation, the principal strain directions were assumed to follow the symmetry axes of the specimen: transverse (x), longitudinal (y) and normal (z) as shown in Figure 10-5. Each specimen was properly oriented using a three-dimensional translation stage such that each principal strain was measured in the plane of the crack at incremental steps of 0.125 to 0.5 mm. Finally, neutron-absorbing cadmium masks were employed to define the sampling volume in the present work, which had dimensions of 0.5 mm in width by 3 mm in height such that the sampled volume was a rhomboid with dimensions 0.5 x 0.5 x 3 mm.

As mentioned before, in order to calculate the residual stresses, the stiffness matrix must be transformed to a coordinate system defined by the diffraction plane, which is the (211) plane in the present case. Therefore, in the present case the longitudinal axis was assigned to the [211] direction since it was assumed that the

longitudinal residual stress had the most influence on the fatigue behaviour of the stiffened plates. The transverse and normal axes were assigned, respectively, to the $[\bar{1}11]$ and $[0\bar{1}1]$ directions such that they were perpendicular to [211]. Shear strains were not measured and were assumed to be zero in computing the residual stresses.

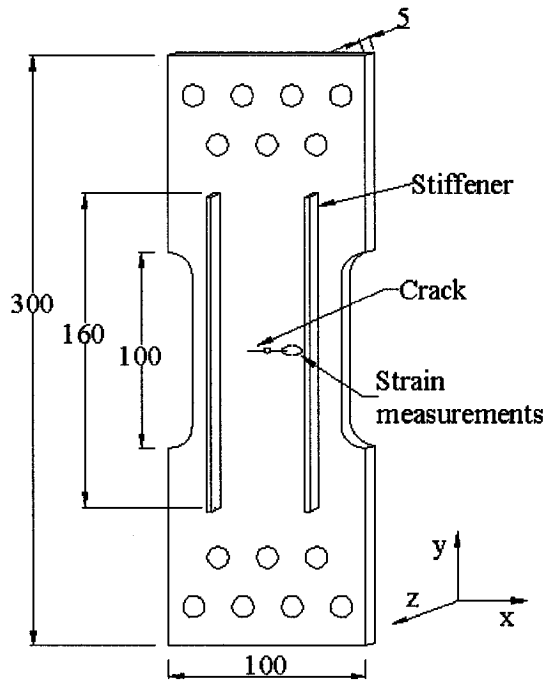

(Dimensions in mm)

Figure 10-5 Principal strains directions

To summarize, the determination of residual stresses by neutron diffraction involved the following steps:

1) Diffraction angles of deformed and undeformed specimens were measured.
2) The spacing of the diffracting planes of atoms was calculated from the deformed and undeformed diffracted angle using Bragg's law (Equation 5-16).
3) Residual strains were computed from the deformed and undeformed atomic plane spacing using Equation 5-17.
4) Residual stresses were determined from the residual strains and the transformed stiffness matrix using Equation 5-18.

10.3 Finite Element Simulation of Residual Stresses

10.3.1 Heat Transfer Analysis

In the present work, the general purpose commercial finite element code NISA was employed to simulate the residual stresses in the welded stiffened plate by first performing a heat transfer analysis to the model to obtain the temperature distribution generated from the welding process. The resulting temperature distribution then became the thermal loading in the subsequent nonlinear static analysis to give the residual stress pattern. As shown in Figure 10-6(a), only one-quarter of the stiffened plate was modeled to take advantage of symmetry. For the heat transfer analysis, a total of 5,696 second-order 3-D solid elements (NKTP = 4, Figure 10-6(b)) was used. The dimensions of the elements along the crack plane were approximately 0.5 mm x 0.5 mm x 2.5 mm.

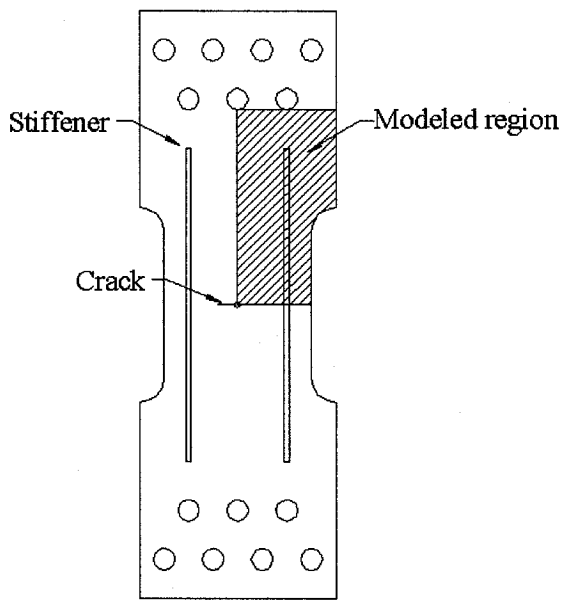

(a)

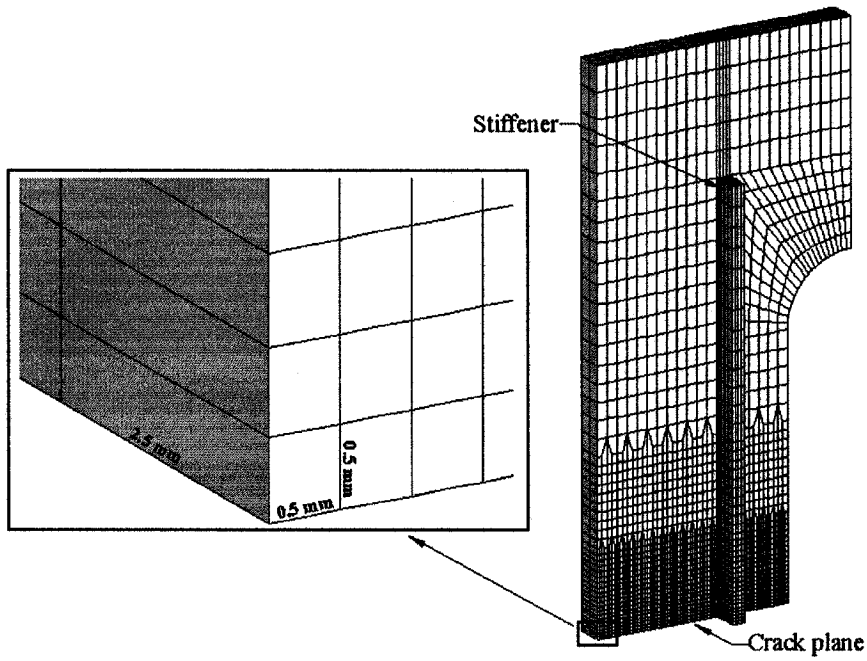

(b)

Figure 10-6 (a) Model layout; (b) Finite element mesh of the heat transfer analysis

The purpose of the heat transfer analysis, performed by the HEAT module in NISA, was to obtain the temperature distribution generated from the heat of the welding process to be applied as thermal loading in the subsequent nonlinear static analysis. The parameters, or thermal properties, governing the change in temperature within a material are the density, ρ, heat capacity, C, and thermal conductivity, k [172].

Heat capacity is the material's ability to absorb heat and is defined as the amount of energy required to produce a unit rise in temperature in the material:

$$C = \frac{dQ}{dT}, \tag{10-3}$$

where dQ is the energy required to produce a dT temperature change. Specific heat, c, is used in HEAT analysis, which is the heat capacity per unit mass of the material.

Thermal conductivity is the material's ability to transfer heat. It relates the heat flux to the temperature gradient in the material by the following equation:

$$q = -k\frac{dT}{dn}, \tag{10-4}$$

where q is the heat flux, or the rate of energy flowing through a unit area that is perpendicular to the flow direction and dT/dn is the temperature gradient through the material in the flow direction.

The material in the finite element model, 350WT steel, was assumed to be homogenous and isotropic and its thermal properties are summarized in Table 10-3.

Table 10-3 Material properties for finite element model

Material Property	**Value**
Density, ρ	7,850 x 10^{-9} kg/mm^3 [172]
Specific Heat, c	490 J/kg·°C [138]
Thermal Conductivity, k	42 x 10^{-3} W/mm·°C [172]
Convective Heat Transfer Coefficient between plate and air, h_1	12 x 10^{-6} W/mm^2·°C [45]
Heat Transfer Coefficient between plate and work table, h_2	300 x 10^{-6} W/mm^2·°C [45]
Modulus of Elasticity, E	200 GPa
Poisson's Ratio, ν	0.3
Yield Strength, σ_{yld}	365 MPa
Work Hardening Parameter, H	13 GPa
Hardening Control Parameter, β	0.5
Coefficient of Thermal Expansion, α	12 x 10^{-6} /°C [172]

The heat from the welding process was simulated by applying specified nodal temperature, T, at the root of the weld as shown in Figures 10-7(a) and (b). The temperature T was assumed to linearly increase from the ambient temperature of 20 °C to T_{max} in 150 s, where 150 s was the approximate amount of time it took for a complete weld around a stiffener. In the present work, two cases of T_{max} were considered: 1,500 °C (Model 1), which is the typical melting temperature of steel, and 1,000 °C (Model 2). The plate was then cooled back to the ambient temperature by convection at the boundaries of the plate. The temperature distribution within the plate resulting from this heating and cooling was governed by both the aforementioned thermal properties of the material and by the convective boundary conditions. It should be noted that although

heat loss also occurred through radiation, preliminary finite element models had shown that radiation had an insignificant effect on both the temperature and residual stress distribution in the present case. In addition, the inclusion of radiation would increase the complexity and the number of iterations of analysis and was therefore not incorporated in the final models.

The convective heat loss at the boundary of the plate to the surrounding was calculated by the convective heat transfer (film) coefficient, h, which relates the convective heat flux, q, to the temperature difference between the boundary of the plate, T_s, and the surrounding, T_∞:

$$q = h(T_s - T_\infty) \tag{10-5}$$

The convective heat transfer coefficient was assigned zero at the planes of symmetry and had the value h_1 between the plate and air as shown in Table 10-3 and Figures 10-7(a) and (b). The heat loss from the bottom of the plate was practically heat conduction from the plate to the work table. "However, the complicated unknown contact resistance between the plate and the work table presents difficulty in modeling" [50]. Therefore, to simplify the analysis, this heat loss was approximately modeled using the heat flux loss by convection and the heat transfer coefficient between the bottom of the plate and work table was assigned the value h_2 (obtained from [50]) as shown in Table 10-3 and Figures 10-7(a) and (b). Furthermore, two additional cases of convective heat transfer coefficients were considered for Model 1: 20% above (Model 1b) and 20% below (Model 1c) the values of h_1 and h_2 shown in Table 10-3. Finally, Figure 10-8 shows the temperature distribution of Model 1 at the end of the welding process while Figure 10-9 shows the heating and cooling history of a typical node at the intersection of the stiffener and the base plate of Model 1, Model 1b and Model 1c. It can be seen from Figure 10-9 that increasing the convective heat transfer coefficient (Model 1b) increased the rate of cooling of the plate, and vice versa.

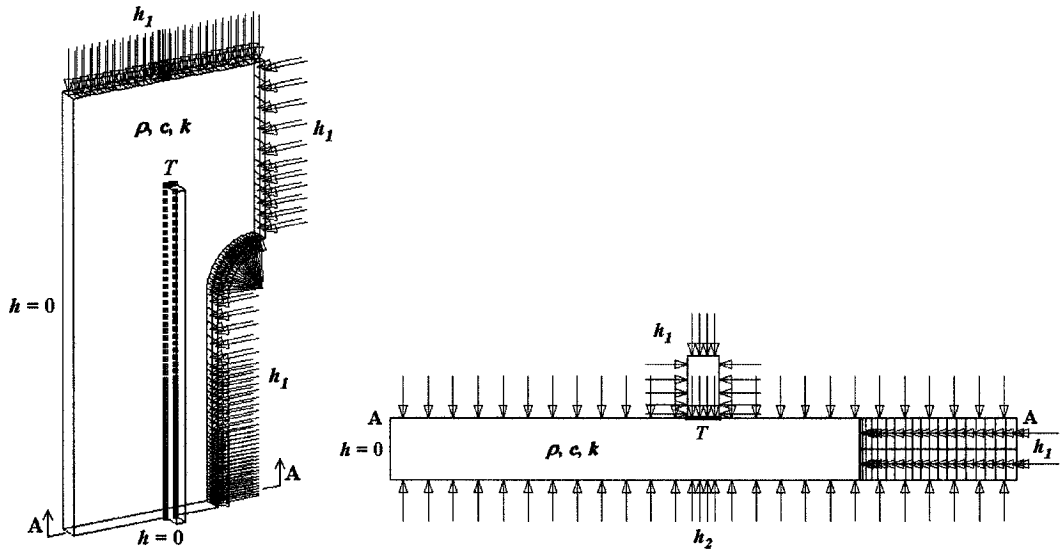

Figure 10-7 Heat transfer analysis boundary conditions of finite element model: (a) Overall view; (b) Cross-section view

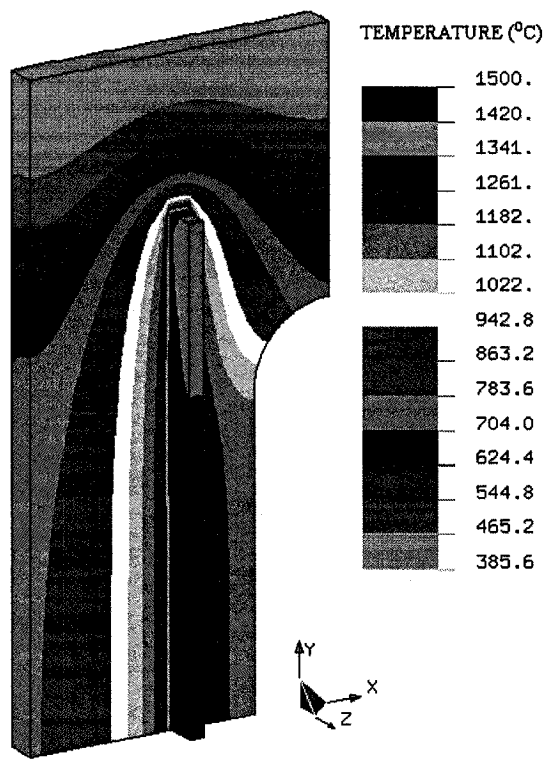

Figure 10-8 Contours of the temperature distribution of Model 1 at the end of the welding process

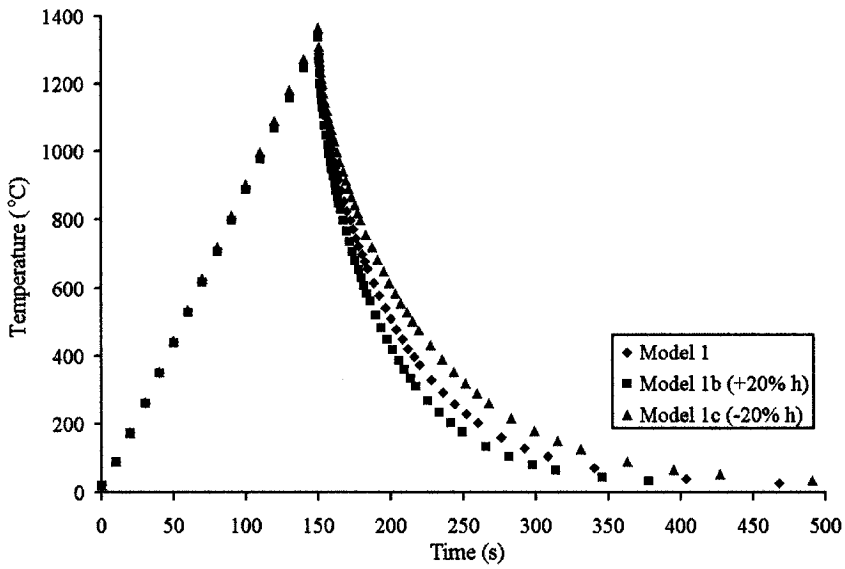

Figure 10-9 Heating and cooling history of a typical node at the intersection of stiffener and base plate of Model 1, Model 1b and Model 1c

10.3.2 Nonlinear Static Analysis

The temperature distribution during the heating and cooling of the plate obtained from the heat transfer analysis was then applied as thermal loading in the subsequent nonlinear static analysis. The residual stresses in the plate were the result of thermal expansion and volumetric changes of the material, which is governed by the coefficient of thermal expansion, α. The coefficient of thermal expansion relates the change in stress, σ, to the change in temperature of the material, ΔT, in the following way:

$$\sigma = E\alpha\Delta T \tag{10-6}$$

In the nonlinear static model, the material was assumed to be bilinear and obey the von Mises yield criterion with yield strength of 365 MPa and a work hardening parameter of 13 GPa. In addition, the hardening control parameter was set at 0.5, which resulted in a mixed kinematic and isotropic hardening for the material and "usually gives results that are closer to experimental data" [169]. The values of the coefficient of thermal expansion, modulus of elasticity and Poisson's ratio specified in the model are summarized in Table 10-3.

In order to calculate the effective stress intensity factor, the model for the nonlinear static analysis was constructed using a total of 2,709 8-node quadrilateral 2-D

general shell elements (NKTP = 20) since NISA was unable to calculate the J-integral of 3-D elements. The nonlinear static model had the same mesh configuration as the mid-plane of the heat transfer model. The thickness of the base plate was 5 mm, while the thickness of the stiffener was 4.3 mm to approximately account for both the actual width of the stiffener and the weldment. In addition, a total of 153 3-D gap/friction elements (NKTP = 50) were inserted between the crack face and a row of dummy shell elements to prevent the overlapping of the crack face into the bottom half of the plate, as shown in Figure 10-10. The dummy elements, which had all their degrees of freedom set to zero, were created solely to accommodate the gap elements. Proper displacement boundary conditions were also applied at both the crack plane and the plane of symmetry of the model.

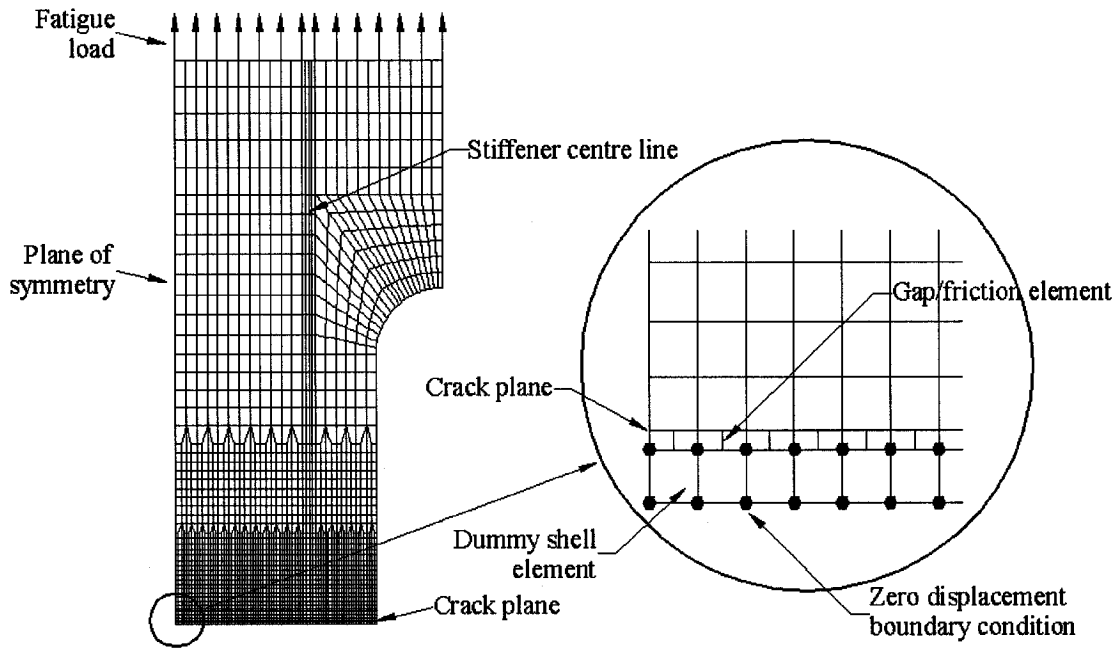

Figure 10-10 Overall finite element mesh of the nonlinear analysis and showing the elements along the crack plane

The nonlinear static analysis was carried out in two sessions. First, the temperature distribution from the heat transfer analysis, representing the heating and cooling of the welding process, was applied to the model as specified nodal temperatures to generate the welding residual stresses. A tensile loading, which went from 6 kN to 60 kN, representing one half of a baseline fatigue cycle, was then applied to the end of the

model. After the nonlinear static analysis, the effective stress intensity factor, or more precisely, the *J*-integral, during the fatigue loading was calculated using the ENDURE module within the NISA suite of programs. This process was repeated for several crack lengths. However, since the fatigue models employed in the present work were based on linear elastic fracture mechanics, the *J*-integral results from the nonlinear analyses were scaled to obtain the corresponding linear elastic values. This was accomplished by performing both a linear and a nonlinear static analysis of the model at each crack length of interest, by applying the fatigue loading only. The scaling factor was then taken as the ratio of the *J*-integral from the linear analysis to that of the nonlinear analysis. Finally, it should be noted that since the welding was done at the initial notch length of 10 mm, in the nonlinear analysis, the thermal loading was always applied at 10 mm, while the fatigue loading was applied at the crack length of interest. This was accomplished by applying reaction forces to the crack faces between 10 mm and the crack length of interest during the thermal loading to prevent crack opening. The reaction forces were then removed before the fatigue loading was applied. This procedure is illustrated in Figure 10-11.

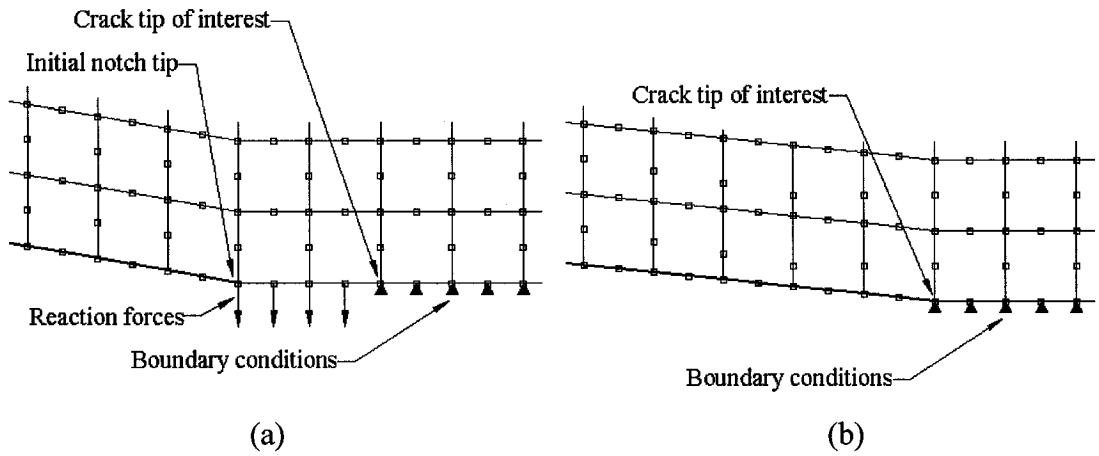

Figure 10-11 Finite element mesh of the nonlinear analysis around the crack tip: (a) Reaction forces applied during thermal loading; (b) Reaction forces removed during fatigue loading

10.4 Results and Discussion

10.4.1 Residual Stresses Results and Simulations

In the present work, residual stresses of three stiffened specimens were measured using the neutron diffraction method. Specimens 2 and 3 had fatigue crack lengths of 1.10 and 6.79 mm, respectively, measured from the starter notch, while Specimen 4 had a starter notch only and no fatigue crack. Residual stresses were measured in one half of each specimen along the plane of the crack, at the mid thickness of the base plate. The measurements were taken for a few milimetres ahead of the crack tip for Specimens 2 and 3, while they were taken along the whole uncracked section of Specimen 4. Reference specimens were cut from unstiffened plates by EDM. The residual stresses were also simulated by the finite element method, which consisted of a heat transfer analysis followed by a nonlinear static analysis. Two cases of T_{max} were considered in the analyses: 1,500 °C (Model 1) and 1,000 °C (Model 2). Furthermore, two additional cases of convective heat transfer coefficients were considered for Model 1: 20% above (Model 1b) and 20% below (Model 1c) the values of h_1 and h_2 shown in Table 10-3.

10.4.1.1 Transverse Residual Stress

Figure 10-12 plots both the measured (by neutron diffraction) and simulated transverse residual stress in the plane of the crack ahead of the starter notch tip. The measurements from Specimen 2 showed that the transverse residual stress was compressive near the notch tip, while the measurements from Specimen 3 showed that the residual stress was tensile near the stiffener. Measurements from Specimen 4 showed a similar pattern of transverse residual stress, but with a much lower magnitude of compressive stress near the notch tip.

Meanwhile, the finite element simulations overestimated the magnitude of the compressive stress near the notch tip. The simulated residual stress then became tensile as one approaches the stiffener, more so for the case of T_{max} = 1,000 °C, but neither case reached the same magnitude of tensile residual stress as shown by the experimental measurements. In addition, higher magnitude of T_{max} appeared to produce more severe

compressive residual stress. Figure 10-13 plots the simulated transverse residual stresses for the three different cases of convective heat transfer coefficients, which controlled the rate of cooling of the plate. It appeared that increasing the cooling rate (Model 1b) lowered the overall transverse residual stress, and vice versa. However, the effects of the cooling rate on the residual stress appeared to be much less significant than the aforementioned effects of T_{max}. Finally, Figure 10-14 shows the contours of the simulated transverse residual stress for the case of T_{max} = 1,500 °C (Model 1). The finite element simulation showed that the transverse residual stress was low throughout the plate except for the areas around the starter notch tip.

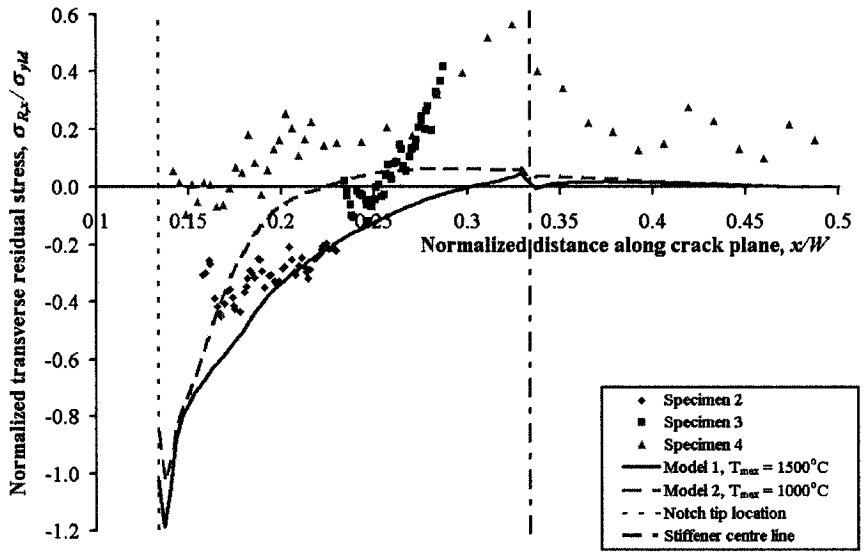

Figure 10-12 Comparison of the measured (Specimens 2, 3 and 4) and calculated (Models 1 and 2) transverse residual stresses

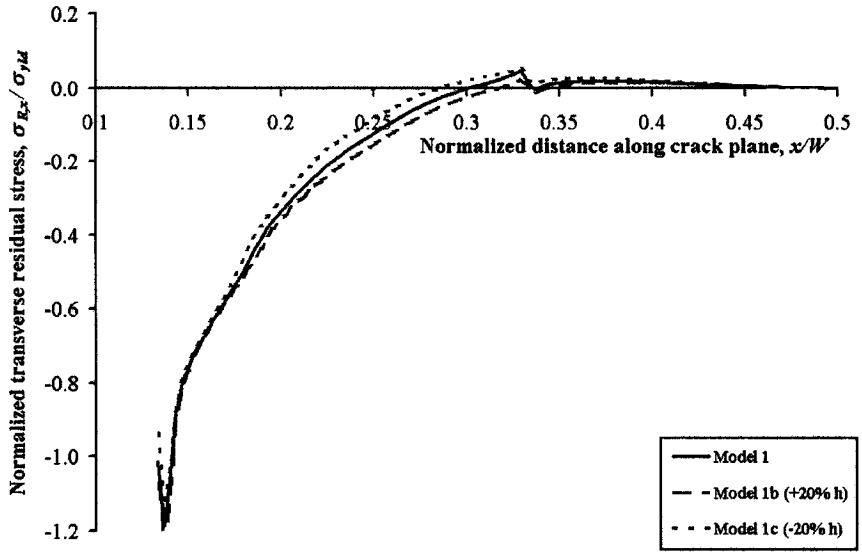

Figure 10-13 Comparison of the calculated transverse residual stresses of Model 1, Model 1b and Model 1c

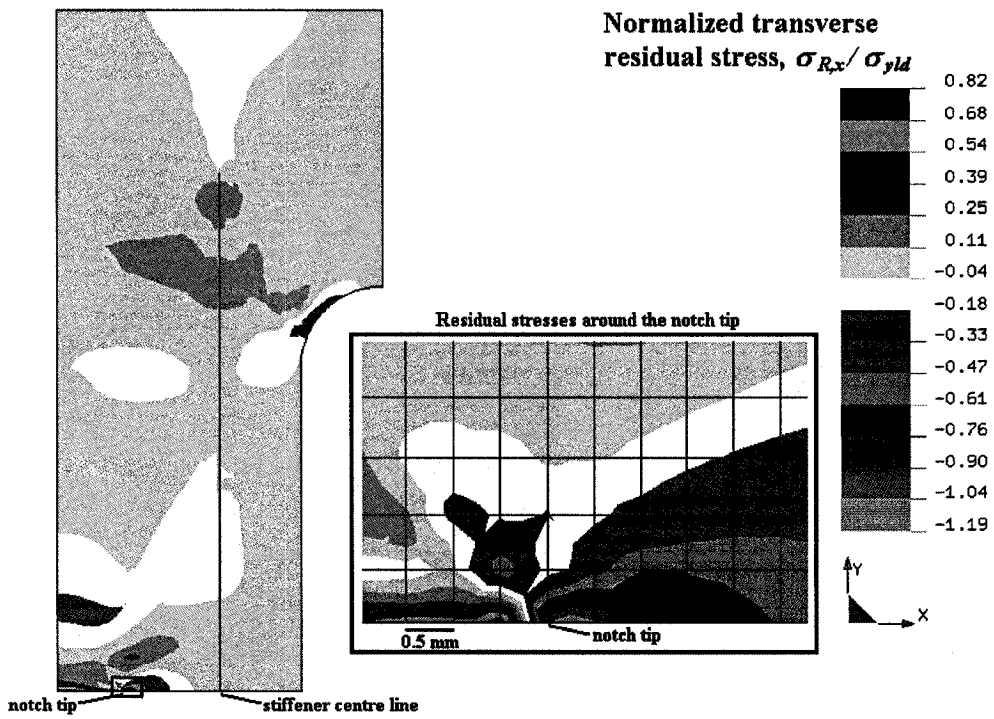

Figure 10-14 Contours of the calculated transverse residual stresses of Model 1

10.4.1.2 Longitudinal Residual Stress

The longitudinal component of the residual stress conceivably had the most influence on the fatigue life of the stiffened plate as it was in the direction of the fatigue loading. Figure 10-15 plots both the measured and simulated longitudinal residual stress

in the plane of the crack ahead of the starter notch tip. The measurements from Specimen 2 again showed that the longitudinal residual stress was compressive near the notch tip while the measurements from Specimen 3 showed that the residual stress was tensile near the stiffener. Measurements from Specimen 4 showed a similar pattern of longitudinal residual stress, but again with a lower magnitude of compressive stress near the notch tip.

Meanwhile, the finite element simulations overestimated the magnitude of the compressive stress near the notch tip. The simulated residual stress again became tensile as one approaches the stiffener, but again neither case reached the same magnitude of tensile residual stress as shown by the experimental measurements. In addition, while the measured tensile residual stress reached its peak at approximately the centre line of the stiffener, the simulated tensile residual stress reach its peak at an earlier location before the stiffener, although there was a second peak at the stiffener centre line for the case of T_{max} = 1,500°C. Furthermore, higher magnitude of T_{max} appeared to produce greater extent of compressive residual stress, but also shifted the peak of the tensile residual stress towards the stiffener. Figure 10-16 plots the simulated longitudinal residual stresses for the three different cases of convective heat transfer coefficients. It appeared that increasing the cooling rate (Model 1b) produced both lower compressive residual stress near the notch tip and higher tensile residual stress near the stiffener, and vice versa. However, the effects of the cooling rate on the residual stress again appeared to be much less significant than the effects of T_{max}. Finally, Figure 10-17 shows the contours of the simulated transverse residual stress for the case of T_{max} = 1,500°C (Model 1). The finite element simulation showed that the longitudinal residual stress was tensile near the stiffener and compressive between the stiffeners, a pattern that is consistent with that reported in literature.

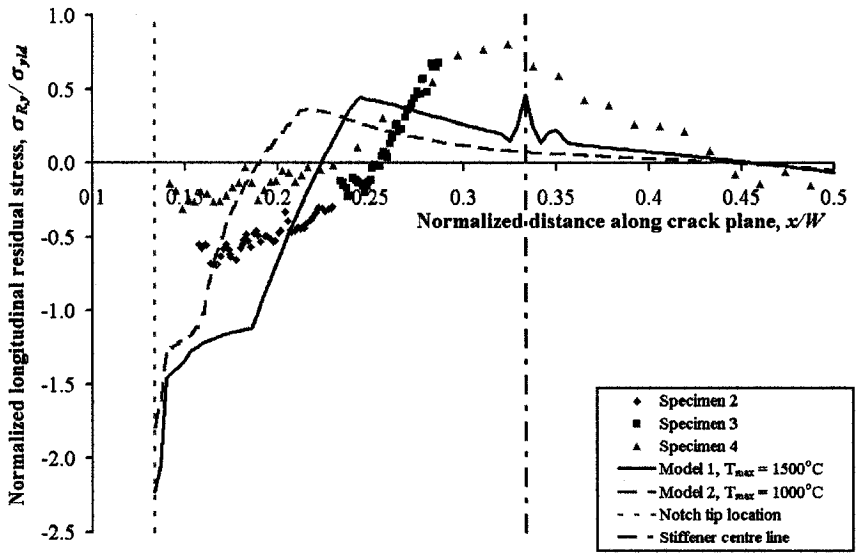

Figure 10-15 Comparison of the measured (Specimens 2, 3 and 4) and calculated (Models 1 and 2) longitudinal residual stresses

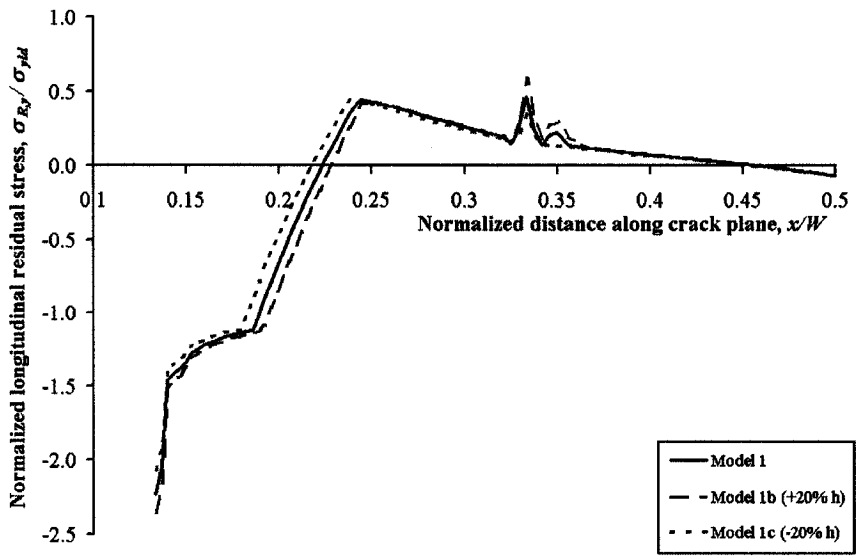

Figure 10-16 Comparison of the calculated longitudinal residual stresses of Model 1, Model 1b and Model 1c

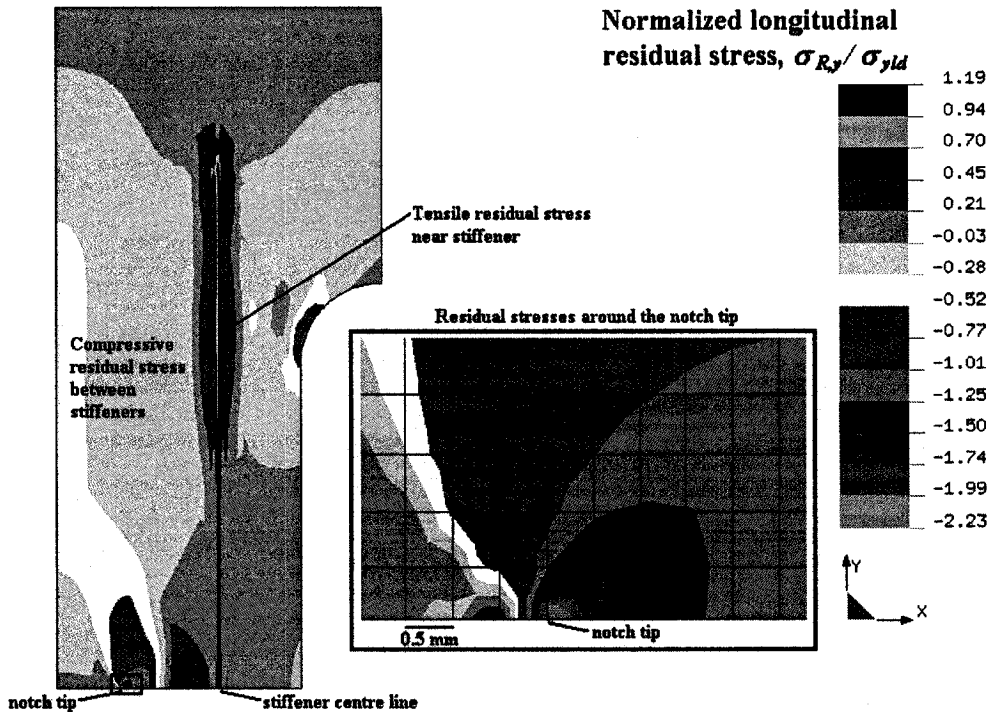

Figure 10-17 Contours of the calculated longitudinal residual stresses of Model 1

In reality, the heat from welding causes phase changes and properties changes in the material that are beyond the scope of the present finite element model. In addition, it can be seen from the experimental measurements that there were significant variations in the magnitude of the residual stresses between these specimens, even though they were fabricated in the same fashion. This is perhaps caused by other factors that would be too complex to be accounted for in a finite element analysis. Nonetheless, the present finite element simulation appeared to be able to capture the principal trend in the residual stress of a welded stiffened plate; that is, tensile stress near the stiffeners and compressive between stiffeners.

10.4.2 Fatigue Tests Results and Predictions

In the present work, constant amplitude fatigue tests (at P_{max} = 60 kN and R = 0.1) were performed on four welded stiffened centre-cracked steel plates. The results (Figure 10-18) showed that for the same crack length, a, the fatigue crack growth rate, da/dN, in general, was lower in the stiffened plates than in an unstiffened plate, especially in the beginning where both neutron diffraction measurements and finite

element simulations indicated high degree of compressive residual stresses near the starter notch tip. The literature review in Chapter 5 suggested that the lower crack growth rate was the effect of a combination of factors: the load transfer from the crack tip to the stiffeners, the constraining of the crack opening displacement by the stiffeners and the compressive residual stresses between the stiffeners caused by welding. However, as the crack propagated away from the notch tip residual stress zone, the fatigue rate curves for the specimens appeared to converge to a single line, until the onset of net section yielding caused crack growth acceleration that was most noticeably shown in Specimen 4.

It should be noted that fatigue testing of Specimen 2 ended prematurely when the base plate fractured at one end of a stiffener. It is also interesting to note that the crack growth rates in Specimen 2 and 3 were in general lower than those in Specimen 4 while more severe compressive residual stresses were measured in those two specimens. Thus, this provided evidence that the magnitude of the compressive residual stress plays a significant role on reducing the fatigue crack growth rates in welded structures. Nonetheless, it can be seen that there were significant variations in the fatigue crack growth rates between these specimens, even though they were fabricated in the same fashion. Therefore, it should be appreciated that predicting the fatigue behaviour of welded structures is a challenging engineering problem.

In the present work, two methods were employed to predict the fatigue crack propagation rates of the welded stiffened steel plates. First, a finite element model of the stiffened plate was constructed to calculate the effective stress intensity factor after the residual stresses were simulated. Second, the Green's function was used to calculate the residual stress intensity factor from the neutron diffraction measurements.

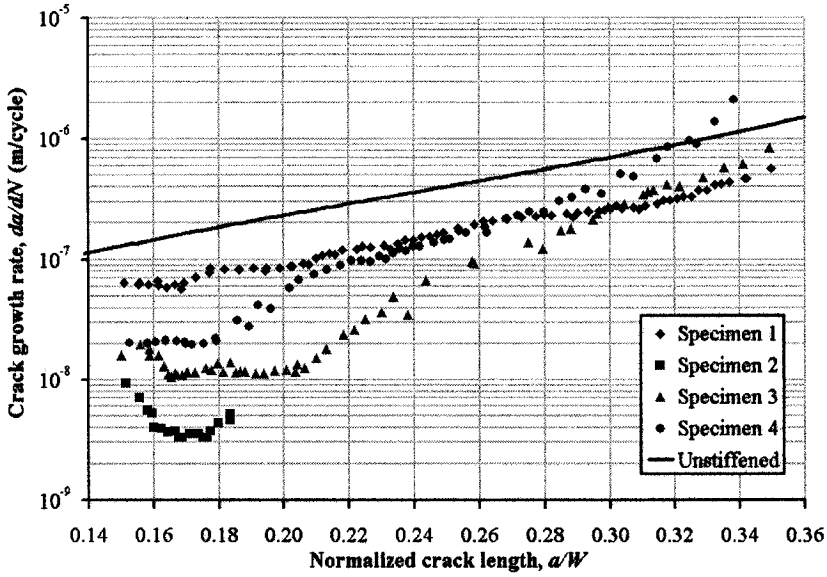

Figure 10-18 Fatigue rate curves of stiffened and unstiffened specimens

10.4.2.1 Fatigue Prediction by Finite Element Analyses

After the residual stresses were simulated in the finite element model, a tensile load was applied as one half of a fatigue load cycle. The *J*-integral during the fatigue load was calculated in a fracture mechanics analysis. The *J*-integral was then converted to an effective stress intensity factor range available for crack propagation by replacing *G* with *J* in Equation 2-5. At the same time, the effective stress ratio was also determined as the ratio of the effective stress intensity factor at the minimum fatigue load to the effective stress intensity factor at the maximum fatigue load. This process was repeated for several crack lengths. Two cases of residual stresses were considered, which were produced by T_{max} = 1,500 °C (Model 1) and 1,000 °C (Model 2), respectively. In addition, as mentioned before, the effective stress ratio of the fatigue load changes as the crack propagates through a residual stress field. In the present work, the Walker model was chosen to describe the stress ratio effect on crack propagation rates. According to Trask [168], who has performed fatigue testing on 350WT steel at several stress ratios, the Walker model for the steel can be represented by:

$$da/dN = \begin{cases} \dfrac{1.51\times10^{-13}}{(1-R)^{0.91}}(\Delta K)^{4.06} & \text{, when} \quad \Delta K < 26.5\ \text{MPa}\cdot\text{m}^{1/2} \\ \dfrac{4.04\times10^{-12}}{(1-R)^{0.91}}(\Delta K)^{3.06} & \text{, when} \quad \Delta K \geq 26.5\ \text{MPa}\cdot\text{m}^{1/2} \end{cases}, \qquad (10\text{-}7)$$

where da/dN is in m/cycle and ΔK is in MPa $\text{m}^{1/2}$. The fatigue crack growth rates of the stiffened plates were then predicted from Equation 10-7 using the effective stress intensity factor range and effective stress ratio determined from the finite element analyses.

Figure 10-19 plots both the experimental fatigue crack growth rates and the crack growth rates predicted based on the finite element analyses. The predictions were shown for the two cases of residual stresses as well as for the case of a stiffened plate model with no residual stresses (Model 3). As mentioned before, higher magnitude of T_{max} appeared to produce more severe compressive residual stresses. This in turn led to lower predicted fatigue crack growth rates in Model 1 than in Model 2 as shown in Figure 10-19. This agrees with the relationship experimentally observed between Specimen 3 and 4, where Specimen 3 had both higher magnitudes of compressive residual stresses and lower fatigue crack growth rates than Specimen 4. As a result, Model 1's prediction appeared to be better correlated to Specimen 3's crack growth rates while the same was true between Model 2 and Specimen 4. Meanwhile, in general, Model 3, which had no residual stresses, overestimated the fatigue crack growth rates, especially in the beginning near the starter notch tip where the most severe compressive residual stresses existed. On the other hand, both Model 1 and 2 predicted reduced crack growth rates near the notch tip residual stress zone. However, crack arrest was predicted for a number of crack lengths within the zone while no crack arrest was detected in the experiments. On the other hand, given the wide range of crack growth rates observed near the notch tip in the experiments, it is understandable that the factors affecting the fatigue crack growth rates within the compressive residual stress zone might be beyond the scope of the current finite element analyses and hence the predictions within the zone were not as reliable. Nonetheless, the accuracy of the finite element predictions in general improved at longer crack lengths. However, since the predictions were based on linear elastic fracture

mechanics, at the onset of net section yielding, the crack growth rates began to accelerate and deviated from the predictions.

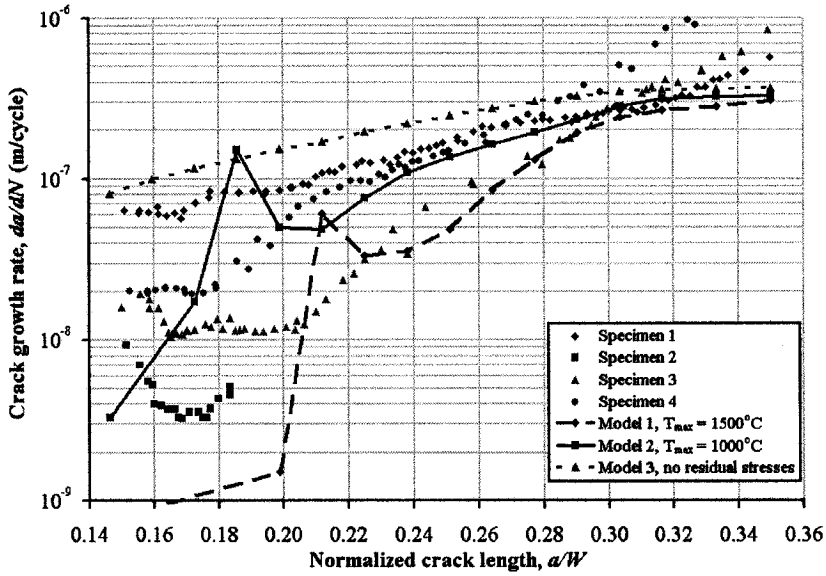

Figure 10-19 Experimental fatigue rate curves (Specimens 1, 2, 3 and 4) and the predictions of finite element analysis (Models 1, 2 and 3)

10.4.2.2 Fatigue Prediction by Green's Function

In the present work, a second approach to predicting the fatigue crack growth rates in the welded stiffened steel plates was through the use of the Green's function (Equation 5-15). The Green's function was used to calculate the residual stress intensity factor produced by the residual stresses acting on the crack faces. Meanwhile, the minimum and maximum stress intensity factors of the fatigue load were obtained from the previous finite element analysis of a stiffened plate model with no residual stresses (Model 3). The effective stress intensity factor range and the effective stress ratio were then determined from Equations 5-13 and 5-14. This process was repeated for several crack lengths. Two cases of longitudinal residual stresses were considered, which were the combination of Specimens 2 and 3 neutron diffraction measurements and the Specimen 5's measurements. Finally, the fatigue crack growth rates of the stiffened plates were predicted by the Walker Model (Equation 10-7), using the effective stress intensity factor range and effective stress ratio determined from the Green's function.

Figure 10-20(a) plots both the experimental fatigue crack growth rates of Specimens 2 and 3 and the crack growth rates predicted based on the Green's function with the combination of residual stress measurements from the two specimens. It can be seen that the Green's function significantly underestimated the crack growth rates of the two specimens. Meanwhile, Figure 10-20(b) plots both the experimental fatigue crack growth rates of Specimen 4 and the crack growth rates predicted based on the Green's function with the residual stress measurements from the specimen. In this case, it can be seen that the prediction was much more accurate. As noted before, the compressive residual stresses in Specimen 4 were less severe. Therefore, it appeared that the prediction by the Green's function was quite sensitive to the magnitude of the residual stresses. In addition, it is possible that Equations 5-13 and 5-14 might not be adequate in describing the fatigue behaviour within a compressive residual stress field. Nonetheless, the Green's function appeared to be able to provide reasonable fatigue prediction when the magnitude of the residual stress in the structure is small.

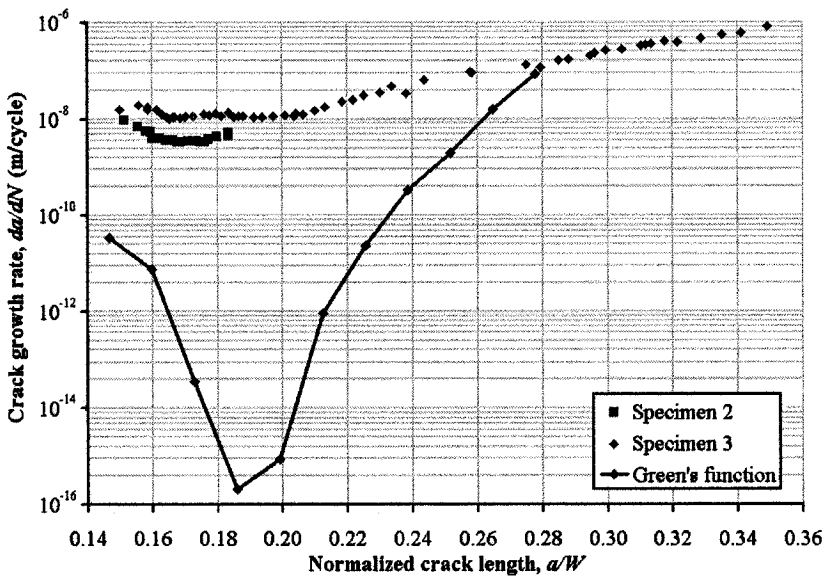

Figure 10-20(a) Experimental fatigue rate curves (Specimens 2 and 3) and the prediction by Green's function

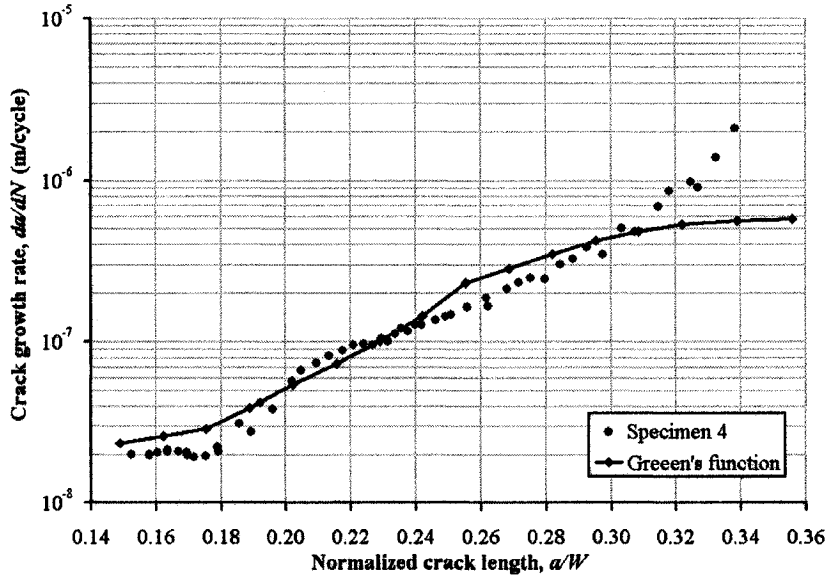

Figure 10-20(b) Experimental fatigue rate curves (Specimen 4) and the prediction by Green's function

Figure 10-20 Experimental fatigue rate curves and the predictions by Green's function: (a) Specimens 2 and 3; (b) Specimen 4

10.5 Conclusions

In a stiffened structure, the crack tip stress intensity factor and the strain energy release rate in the base plate is lowered at the vicinity of a stiffener as the stiffener provide a secondary structure for the load to bypass the cracked panel. The strain energy release rate can drop below the crack resistance of the structure to the point that crack arrest is possible. At the same time the residual strength of the structure increases as the crack approaches the stiffener. In the case of welded stiffeners, the welding creates residual stresses in the base plate that have additional influence on fatigue crack growth. In general, tensile residual stresses are found near the stiffeners, which tend to accelerate the fatigue crack growth rates in the base plate, and compressive residual stresses are found between stiffeners, which tend to retard the fatigue crack growth rates.

The present work consisted of the investigation of the fatigue behaviour of welded stiffened centre-cracked 350WT steel plates. The residual stresses in the plates were first measured by the neutron diffraction method, which is a versatile and nondestructive method for determining these residual stresses. The measurements showed that in

general the residual stresses in a welded stiffened plate were tensile near the welded stiffeners and compressive between the stiffeners and ahead of the starter notch tip. The residual stresses were also simulated by a series of uncoupled finite element analyses, which consisted of a heat transfer analysis to obtain the temperature distribution from welding, followed by a nonlinear static analysis that applied the nodal temperature from the heat transfer analysis as thermal loading. The simulation appeared to be able to capture the principal trend in the residual stresses; that is, tensile stress near the stiffeners and compressive between stiffeners. In addition, it appeared that higher magnitude of temperature and higher convective heat transfer coefficients in the heat transfer analysis produced more severe residual stresses. However, the effects of the convective heat transfer coefficients on the residual stress simulations appeared to be insignificant by comparison.

After the neutron diffraction measurements, the plates underwent constant amplitude fatigue testing. The results showed that the fatigue crack growth rate of a welded stiffened plate was lower than that of a corresponding unstiffened plate. The rates were especially low near the starter notch tip where a high degree of compressive residual stresses existed. It also appeared that higher magnitude of compressive residual stresses causes lower fatigue crack growth rates in the plate. The fatigue crack growth rates were then predicted by both finite element analysis and by the use of the Green's function. In the finite element analysis, the effective stress intensity factor range was determined from a fracture mechanics analysis. The analysis results showed agreement with the experimental observation that higher magnitude of compressive residual stresses causes lower fatigue crack growth rates in the plate. Reduced crack growth rates near the starter notch tip were predicted, albeit with questionable reliability. Nonetheless, the accuracy of the finite element predictions in general improved at longer crack lengths. Meanwhile, the Green's function calculated the residual stress intensity factor caused by the residual stresses acting on the crack faces using the neutron diffraction measurements. The Green's function significantly underestimated the fatigue crack growth rates of the specimens with more severe compressive residual stresses. The predictions also appeared to be quite sensitive to the magnitude of the residual stresses. Nonetheless, the Green's

function appeared to be able to provide reasonable fatigue prediction when the magnitude of the residual stress in the structure is small.

To summarize, the following procedure was used to predict the fatigue crack growth rates of a welded stiffened plate using the finite element method:

1) A heat transfer analysis was performed to obtain the temperature distribution generated from the heat of the welding process.
2) A nonlinear static analysis was performed to establish the residual stresses from the welding process. A fatigue (tensile) load was also applied. This step was repeated for several crack lengths of interest.
3) For each crack length in Step 2, the effective stress intensity factor range and the effective stress ratio were calculated from the fatigue load by a fracture mechanics analysis.
4) The effective stress intensity factor range and the effective stress ratio were used to calculate the fatigue crack growth rate of the welded stiffened plate by the Walker model.

Alternatively, the fatigue crack growth rates of the welded stiffened plate were also predicted from the residual stress measurements using the following procedure:

1) The residual stresses were evaluated using the neutron diffraction technique.
2) The residual stress intensity factors produced by the measured residual stress fields were then calculated using the Green's function for several crack lengths of interest.
3) The effective stress intensity factor range and the effective stress ratio were calculated from the applied stress intensity factor range.
4) The effective stress intensity factor range and the effective stress ratio were used to calculate the fatigue crack growth rate of the welded stiffened plate by the Walker model.

Chapter 11 Conclusions and Recommendations

11.1 Summary and Conclusions

In engineering, fatigue is defined as the decrease in strength of a material under repeated cycles of stress or strain, ultimately leading to fracture. The cause of this failure is a result of the formation and propagation of micro-cracks, then coalescing into a visible crack, at the stress concentrations of a member, where the localized cyclic stresses are much greater than the average value acting over the cross section. Nowadays, fatigue is an issue for bridges, cranes, towers, ships and airplanes.

The objective of this thesis was to investigate the fatigue behaviour of stiffened and untiffened 350WT Category 5 steel plates, a typical material used in bridges, offshore structures and the hulls of the Canadian City class frigates, when subjected to a number of different loading scenarios. The following conclusions are drawn from the experimental and numerical investigations into the fatigue crack propagation of stiffened and unstiffened 350WT steel plates and polymethyl methacrylate plates subjected to variable amplitude loading:

11.1.1 Proposed Modification to a Constant Amplitude Fatigue Model

The Zheng and Hirt constant amplitude fatigue model describes the fatigue behaviour of metals based on the tensile properties, thus eliminating the need for extensive fatigue crack propagation tests as required by other fatigue models. The model uses the fracture strength of the material based on a relationship. A modification was proposed to the model, using the measured fracture strength of the metal instead of the calculated strength. Standard tension tests were performed to determine the tensile properties, in particular the true stress at fracture of 350WT category 5 steel. In addition, fatigue crack growth threshold tests were performed to determine the necessary model parameter. Finally, constant amplitude loading fatigue tests were performed on the steel to evaluate the modifications to the model. Based on the analysis of tests results, it is

concluded that the proposed modified Zheng and Hirt model using the measured fracture strength of the metal provides a better estimate of its fatigue crack propagation rates.

11.1.2 Proposed Modifications to a Fatigue Retardation Model

For a number of materials, the fatigue crack growth retardation caused by a tensile overload exhibits an initial crack growth acceleration immediately following the overload, and a subsequent delay in reaching the minimum crack growth rate. In addition, when multiple overloads are applied, they can interact with each other, and as a result they could either accelerate or decelerate the overall crack growth retardation depending on the frequency of the overload. Furthermore, the crack growth retardation is reduced during the latter stage of the fatigue life of a structure when the net section stress approaches the yield strength of the material.

In the present work, a number of modifications to the Wheeler fatigue crack retardation model were proposed to account for the above phenomena. The parameters in both the original Wheeler model and the modified model were then calibrated from a number of single overloading fatigue tests conducted on 350WT steel, middle tension specimens. In addition, initial crack growth acceleration and delay retardation were observed following the overload application in these tests.

Multiple overloading tests were then performed on the same type of steel specimens and the results showed that crack growth retardation was enhanced, as the frequency of overload applications increased, up to a point. As the frequency was increased further, this beneficial effect began to be outweighed by the cumulative crack growth acceleration that occurred immediately following each overload application, causing a decreasing trend in fatigue life. It was also demonstrated that in comparison to the original Wheeler model, the proposed modified model could more accurately predict the fatigue life of 350WT steel subjected to the imposed multiple-overloading in the current experimental investigation. Specifically, the modified Wheeler model was able to predict the reduced crack growth retardation at small overload spacing, while the original model predicted the fatigue life inaccurately (in fact, the resulting fatigue life was erroneously increased as the overload spacing decreased). To summarize, it is believed that the proposed modifications would be applicable to any types of steels since the

modifications were based on general observations on the fatigue retardation behaviour caused by tensile overloading. Furthermore, the required parameters could be obtained from a single overloading fatigue test.

11.1.3 Investigation into the "Prying" Effect due to Crack Surface Roughness

Crack closure was a concept proposed to account for the effects of load interaction and to estimate the fatigue crack growth rates under variable amplitude loading. Due to crack closure, only a portion of a fatigue cycle is effective for the crack propagation. The roughness-induced crack closure is one of the crack closure mechanisms and is attributed to the contact between the asperities on the opposite crack surfaces. However, during a compressive underload in fatigue loading, it is possible that the crack tip might be "pried" open by the contact of these asperities and cause additional fatigue crack growth acceleration following the underload.

The present work investigated the possibility of the "prying" effect by performing finite element analyses on centre-cracked steel plates to examine the effects of crack inclination angle, compressive underload ratio, crack surface roughness and friction on the *J*-integral following the underload. The finite element models incorporated gap/friction elements between the crack surfaces to simulate the "prying" and frictional forces at the crack tip. The following conclusions were drawn from the analyses:

1) The magnitude of the *J*-integral decreased as the crack inclination angle, θ, increased. In addition, the effects of the underload ratio, asperity locations and coefficient of crack surface friction on the *J*-integral in general also diminished as the crack inclination angle increased.
2) A compressive underload increased the size of the tensile plastic zone and the effective *J*-integral range in the following fatigue cycles that led to crack growth acceleration. In addition, the effects of crack surface roughness and friction on the *J*-integral in general were enhanced as the underload ratio increased. Furthermore, the underload effects on the *J*-integral were more significant than either the crack surface roughness or friction effects.

3) For the crack inclination angle of 0°, 22.5° and 67.5°, the "prying" effect of crack surface roughness enhanced the effects of a compressive underload if the underload ratio was high enough. However, at low underload ratio, the "prying" effect generally diminished the effects from underload.
4) The "prying" effect was more significant when the crack surface asperity was located either at very close to the crack tip or at a location that was farther away from the crack tip. The distance between the second location and the crack tip appeared to increase as the underload ratio increased.
5) The crack surface friction in general diminished the "prying" effect for the crack inclination angle of 0° and 22.5°. The "prying" effect was enhanced by the crack surface friction, at certain values of coefficient of friction, for crack inclination angle of 45° and 67.5°.

11.1.4 Simulation of the Reduced Ductility in Steel using PMMA

Brittle fracture takes place at stresses below the net section yield with very little observable plastic deformation and minimal absorption of energy. It has been responsible for numerous sudden and unexpected structural failures since the industrial revolution. Rupture is the dominant fracture mechanism for ductile materials. It is the formation and coalescence of voids caused by plastic deformation around brittle particles in a material. Cleavage is the most brittle form of fracture. It is the dominant fatigue crack propagation and fracture mechanism in brittle materials. Cleavage is a direct separation along crystallographic planes due to a breaking of atomic bonds. It requires no plastic deformation and absorbs little energy. Steel, a normally ductile material, behaves in a brittle manner when subjected to low temperature, high strain rate, high constraint and/or welding. Under these conditions, the yield strength of steel is increased and the fracture toughness is decreased, thus promoting cleavage fracture. Brittle fracture can be prevented by specifying a certain fracture toughness of the material at the lowest operating temperature of the structure, avoiding high constraint at areas of stress concentration of the structure and improving the welding process.

The load interaction effects in steel cause the fatigue crack growth retardation after an application of tensile overload and acceleration after a compressive underload.

An experimental investigation into the fatigue behaviour of polymethyl methacrylate (PMMA), a semi-brittle glassy polymer, was performed to simulate the fatigue crack growth retardation and acceleration of steel when its ductility is reduced due to the above embrittling conditions. Through three stages of testing in this investigation the following observations were made:

1) The first stage consisted of constant amplitude loading of specimens at loading frequencies ranging from 1 to 30 Hz. The results showed that loading frequency had insignificant or no effect on the fatigue behaviour of PMMA.
2) The second stage consisted of applying different levels and number of tensile overload to the specimens at different crack lengths in an otherwise constant amplitude loading scenario. The results showed that the amount of fatigue crack growth retardation following a tensile overload in PMMA decreased with both increased crack length at which the overload was applied and with increased overload level. Retardation was found to increase following multiple overloads compared to a single overload.
3) The third stage consisted of applying different levels of single compressive underload in an otherwise constant amplitude loading scenario. The results did not show any pronounced relationship between the level of compressive underload and the amount of crack growth retardation or acceleration in PMMA.

Base on the results from PMMA, which is a semi-brittle material, it is postulated that the amount of fatigue crack growth retardation and acceleration would likely be reduced for steel under the above embrittling conditions that limit the amount of crack tip plastic deformation. In addition, the beneficial effect of fatigue crack growth retardation after a tensile overload is further limited by the lowered allowable overload level due to the decrease in fracture toughness in steel. An overload could be in fact potentially detrimental by the fact that increase crack extension can occur during the overload.

11.1.5 Fatigue of Welded Stiffened Steel Plates

In a stiffened structure, the crack tip stress intensity factor and the strain energy release rate in the base plate is lowered at the vicinity of a stiffener as the stiffener provide a secondary structure for the load to bypass the cracked panel. The strain energy

release rate can drop below the crack resistance of the structure to the point that crack arrest is possible. At the same time the residual strength of the structure increases as the crack approaches the stiffener. In the case of welded stiffeners, the welding creates residual stresses in the base plate that have additional influence on fatigue crack growth. In general, tensile residual stresses are found near the stiffeners, which tend to accelerate the fatigue crack growth rates in the base plate, and compressive residual stresses are found between stiffeners, which tend to retard the fatigue crack growth rates.

The present work consisted of the investigation of the fatigue behaviour of welded stiffened centre-cracked 350WT steel plates. The residual stresses in the plates were first measured by the neutron diffraction method, which is a versatile and nondestructive method for determining these residual stresses. The measurements showed that in general the residual stresses in a welded stiffened plate were tensile near the welded stiffeners and compressive between the stiffeners and ahead of the starter notch tip. The residual stresses were also simulated by a series of finite element analyses, which consisted of a heat transfer analysis to obtain the temperature distribution from welding, followed by a nonlinear static analysis that applied the nodal temperature from the heat transfer analysis as thermal loading. Although there was only a moderate agreement between the simulated and the measured the residual stresses, which themselves showed significant variations between the plates, the finite element simulation appeared to be able to capture the principal trend; that is, tensile stress near the stiffeners and compressive between stiffeners. Therefore, the finite element approach appeared to provide an adequate alternative to the experimental techniques for evaluating the residual stresses in the welded stiffened steel plates. In addition, it appeared that higher magnitude of temperature and higher convective heat transfer coefficients in the heat transfer analysis produced more severe residual stresses in the simulation. However, the effects of the convective heat transfer coefficients on the residual stress simulation appeared to be insignificant by comparison.

After the neutron diffraction measurements, the plates then underwent constant amplitude fatigue testing. The results showed that the fatigue crack growth rate of a welded stiffened plate was lower than that of a corresponding unstiffened plate. The rates were especially low near the starter notch tip where a high degree of compressive

residual stresses existed. It also appeared that higher magnitude of compressive residual stresses causes lower fatigue crack growth rates in the plate. The fatigue crack growth rates were then predicted by both finite element analysis and by the use of the Green's function. In the finite element analysis, the effective stress intensity factor range was determined from a fracture mechanics analysis. The analysis agreed with the experimental observation that higher magnitude of compressive residual stresses causes lower fatigue crack growth rates in the plate. Reduced crack growth rates near the starter notch tip were predicted, albeit with questionable reliability. Nonetheless, the accuracy of the finite element predictions in general improved at longer crack lengths. Meanwhile, the Green's function calculated the residual stress intensity factor caused by the residual stresses acting on the crack faces using the neutron diffraction measurements. The Green's function significantly underestimated the fatigue crack growth rates of the specimens with more severe compressive residual stresses. The predictions also appeared to be quite sensitive to the magnitude of the residual stresses. Nonetheless, the Green's function appeared to be able to provide reasonable fatigue prediction when the magnitude of the residual stress in the structure is small.

To summarize, the following procedure was used to predict the fatigue crack growth rates of a welded stiffened plate using the finite element method:

1) A heat transfer analysis was performed to obtain the temperature distribution generated from the heat of the welding process.
2) A nonlinear static analysis was performed to establish the residual stresses from the welding process. A fatigue (tensile) load was also applied. This step was repeated for several crack lengths of interest.
3) For each crack length in Step 2, the effective stress intensity factor range and the effective stress ratio were calculated from the fatigue load by a fracture mechanics analysis.
4) The effective stress intensity factor range and the effective stress ratio were used to calculate the fatigue crack growth rate of the welded stiffened plate by the Walker model.

Alternatively, the fatigue crack growth rates of the welded stiffened plate were also predicted from the residual stress measurements using the following procedure:

1) The residual stresses were evaluated using the neutron diffraction method.
2) The residual stress intensity factors produced by the measured residual stress fields were then calculated using the Green's function for several crack lengths of interest.
3) The effective stress intensity factor range and the effective stress ratio were calculated from the applied stress intensity factor range.
4) The effective stress intensity factor range and the effective stress ratio were used to calculate the fatigue crack growth rate of the welded stiffened plate by the Walker model.

11.2 Contributions to Knowledge

The present work had provided valuable data on 350WT steel, both experimental and computational, in a number of fatigue scenarios that are commonly experienced in the life of ship plating, including constant amplitude loading, multiple overloading, compressive underloading with crack surface roughness, fatigue of a brittle material and welded stiffened plates. As a result of the present research:

- The accuracy of two well-known fatigue models, that is, the Zheng and Hirt model and the Wheeler model, were improved. This would allow better fatigue prediction in the threshold region and under multiple tensile overloading.
- A systematic study of crack surface roughness and compressive underloading, which in the past had not been given as much attention as tensile overloading, was developed. There appears to be some merit to the "prying" effect of the crack surface asperities, comparable to the well-known crack closure concept.
- By testing PMMA, evidence was provided for the lack of load interaction effects in brittle materials. In other words, it was discovered that the load interaction effects are largely the result of plastic deformation. This has implications on the fatigue behaviour of steel under certain embrittling conditions.
- A procedure was established to predict the fatigue crack growth rates of welded stiffened steel plates using the finite element method, which involved the simulation of the residual stresses followed by a fracture mechanics analysis. The procedure was shown to offer an adequate alternative to experimental testing in predicting the fatigue behaviour of welded stiffened structures.

To summarize, it is believed that fatigue life prediction of ship plating could be improved based on the results of the present research.

11.3 Recommendations for Future Work

Based on the results of the present work, the following are a few recommendations for future experimental and numerical investigations into the fatigue crack propagation behaviour of 350WT steel:

1) The Zheng and Hirt model uses the material's fracture strength from a conventional tension test in its formulation. Perhaps using the fracture toughness of the material instead would have been more appropriate since it is related to the strength of a cracked body. Since the fracture toughness is a function of the crack length, fracture toughness tests at several crack lengths would have to be performed to investigate this possibility.
2) Overload block, *i.e.* overloads applied successively, produces more crack growth retardation then a single overload. However, it also generates larger crack increments during the block and higher crack growth acceleration immediately after the block. Therefore, above a certain size of the overload block these detrimental effects may outweigh the post-overload retardation. The size of the overload block could be investigated to optimize the retardation.
3) A compressive underload can cause crack growth acceleration in the subsequent fatigue cycles and reduce the amount of crack growth retardation from a tensile overload. The effects of an underload could perhaps be described by an effective tensile plastic zone, similar to the effective plastic zone defined for an overload in the Wheeler retardation model. Investigation could be undertaken to explore this possibility and could perhaps provide further modifications to the Wheeler model for fatigue life prediction from more realistic random loading.
4) In the present finite element analyses, a compressive underload has been shown to affect the J-integral in the subsequent load cycle. Investigation could be carried out to examine the possibility of using the J-integral results from finite element analyses to model the crack growth retardation or acceleration due to reduction or increase in J-integral following an overload or underload, respectively.

5) The stress intensity factor and the crack tip plastic zone of a crack in a welded stiffened structure are influenced by both the constraining effect of the stiffeners and the welding residual stresses. Therefore, the effective plastic zone created by a tensile overload or a compressive underload is also expected to be modified in a welded stiffened structure. Investigation could be performed to determine how the load interaction effects are affected in a welded stiffened structure. An important parameter in this investigation would be the location of the overload/underload application due to the residual stress distribution in the structure.

References

(In order of first appearance in thesis)

[1] Lampman, S.R., Ed., *ASM Handbook, Volume 19: Fatigue and Fracture*, ASM International, USA, 1996.

[2] Rushton, P.A., *An Experimental and Numerical Investigation into Fatigue Crack Propagation in 350WT Steel Subjected to Semi-Random Loading*, M.A.Sc. Thesis, Dalhousie University, Halifax, Nova Scotia, 2000.

[3] Rushton, P.A., Taheri, F. and Stredulinsky, D.C., "Threshold & Variable Amplitude Crack Growth Behavior in 350WT Steel", *Proceedings of the 21st International Conference on Pressure Vessels and Piping, ASME-PVP*, Vol. 441, 2002, pp. 81-89.

[4] Rushton, P.A., Taheri, F., "Prediction of Variable Amplitude Crack Growth in 350WT Steel Using a Modified Wheeler Approach", *Journal of Marine Structure*, Vol. 16, No. 7, 2003, pp. 517-539.

[5] Taheri, F., Trask, D. and Pegg, N., "Experimental and Analytical Investigation of Fatigue Characteristics of 350WT Steel Under Constant and Variable Amplitude Loadings", *Journal of Marine Structures*, Vol. 16, 2003, pp. 69-91.

[6] Trask, D.A., *Experimental and Numerical Investigation into Fatigue Crack Propagation Models for 350WT Steel*, M.A.Sc. Thesis, Dalhousie University, Halifax, Nova Scotia, 1998.

[7] Paris, P.C. and Erdogan, F., "A Critical Analysis of Crack Propagation Laws", *Journal of Basic Engineering Transactions, American Society of Mechanical Engineers, Series D*, Vol. 85, Dec. 1963, pp. 528-534.

[8] Zheng, X.L. and Hirt, M.A., "Fatigue Crack Propagation in Steels", *Engineering Fracture Mechanics*, Vol. 18, No. 5, 1983, pp. 965-973.

[9] Wheeler, O.E., "Spectrum Loading and Crack Growth", *Journal of Basic Engineering, Transaction of the ASME*, Vol. 94, No. 1, 1972, pp. 181-186.

[10] Goel, H.S. and Chand. S., "A Fatigue Crack Growth Model for Single Overload Tests", *Journal of Engineering Materials and Technology, Transaction of the ASME*, Vol. 14, No. 116, 1994, pp. 168-172.

[11] Corbly, D.M. and Packman, P.F., "On the Influence of Single and Multiple Peak Overloads on Fatigue Crack Propagation in 7075-T6511 Aluminum", *Engineering Fracture Mechanics*, Vol. 5, 1973, pp. 479-497.

[12] Kim, K.S., Kim, S.C., Shim, C.S. and Park, J.Y., "A Study on the Effect of Overload Ratio on Fatigue Crack Growth", *Key Engineering Materials*, Vols. 261-263, 2004, pp. 1159-1168.

[13] Kim, K.S., Kim, K.S., Shim, C.S. and Cho, H.M., "A Study on Evaluation of Overload Effects on Fatigue Crack Growth", *Key Engineering Materials*, Vols. 261-263, 2004, pp. 1169-1178.

[14] Finney, J.M., "Modelling for Fatigue Crack Growth Prediction in Aircraft", *Fatigue & Fracture of Engineering Materials & Structures*, Vol. 8, No. 3, 1985, pp. 205-222.

[15] Gray, T.D. and Gallagher, J.P., "Predicting Fatigue Crack Retardation Following a Single Overload Using a Modified Wheeler Model", *Mechanics of Crack Growth, ASTM STP 590*, American Society for Testing and Materials, 1976, pp. 331-344.

[16] Dolinski, K., "Fatigue Crack Growth with Retardation under Stationary Stochastic Loading", *Engineering Fracture Mechanics*, Vol. 27, No. 3, 1987, pp. 279-290.

[17] Alawi, H., "Designing Reliably for Fatigue Crack Growth under Random Loading", *Engineering Fracture Mechanics*, Vol. 37, No. 1, 1990, pp. 75-85.

[18] Sheu, B.C., Song, P.S. and Hwang, S., "Shaping Exponent in Wheeler Model Under a Single Overload", *Engineering Fracture Mechanics*, Vol. 51, No. 1, 1995, pp. 135-143.

[19] Khan, Z., Rauf, A. and Younas, M., "Prediction of Fatigue Crack Propagation Life in Notched Members under Variable Amplitude Loading", *Journal of Materials Engineering and Performance*, Vol. 6, No. 3, 1997, pp. 365-373.

[20] Hawkyard, M., Powell, B.E., Stephenson, J.M. and McElhone, M., "Fatigue Crack Growth from Simulated Flight Cycles Involving Superimposed Vibrations", *International Journal of Fatigue*, Vol. 21, 1999, pp. S59-S68.

[21] Song, P.S., Sheu, B.C. and Chang, L., "A Modified Wheeler Model to Improve Predictions of Crack Growth Following a Single Overload", *JSME International Journal Series A*, Vol. 44, No. 1, 2001, pp. 117-122.

[22] Wahab, M.A., Rohrsheim, G.R. and Park, J.H., "Experimental Study on the Influence of Overload Induced Residual Stress Field on Fatigue Crack Growth in Aluminium Alloy", *Journal of Materials Processing Technology*, Vols. 153-154, 2004, pp. 945-951.

[23] Nussbaumer, A., *Propagation of Long Fatigue Cracks in Multi-Cellular Box Beams*. Ph.D. Thesis, Lehigh University, Bethlehem, Pennsylvania, 1993.

[24] Xu, T. and Bea, R., "Load Shedding of Fatigue Fracture in Ship Structures", *Marine Structures*, Vol. 10, 1997, pp. 49-80.

[25] Nussbaumer, A.C., Fisher, J.W. and Dexter, R.J., "Behavior of Long Fatigue Cracks in Cellular Box Beam", *Journal of Structural Engineering*, Vol. 125, No. 11, 1999, pp. 1232-1238.

[26] Dexter, R.J. and Pilarski, P.J., "Effect of Welded Stiffeners on Fatigue Crack Growth Rate", *SSC-413*, August 2000.

[27] Dexter, R.J. and Pilarski, P.J., "Crack Propagation in Welded Stiffened Panels", *Journal of Constructional Steel Research*, Vol. 58, 2002, pp. 1081-1102.

[28] Dexter, R.J., Pilarski, P.J. and Mahmoud, H.N., "Analysis of Crack Propagation in Welded Stiffened Panels", *International Journal of Fatigue*, Vol. 25, 2003, pp. 1169-1174.

[29] Dexter, R.J. and Mahmoud, H.N., "Predicting Fatigue Crack Propagation in Stiffened Panels", *SSC-444*, March 2004.

[30] Lorentzen, T. and Ibsø, J.B., "Neutron Diffraction Measurements of Residual Strains in Offshore Welds", *Materials Science and Engineering A*, Vol. 197, 1995, pp. 209-214.

[31] Webster, P.J., Mills, G., Wang, X.D., Kang, W.P. and Holden, T.M., "Neutron Strain Scanning of a Small Welded Austenitic Stainless Steel Plate", *Journal of Strain Analysis for Engineering Design*, Vol. 30, No. 1, 1995, pp. 35-43.

[32] Bruno, G., Carrado, A., Dunn, B., Fiori, F., Girardin, E., Pirling, T. and Rustichelli, F., "Neutron Diffraction Measurements for the Determination of Residual Stress in Ti6Al4V Welded Plates", *Materials Science Forum*, Vols. 347-349, 2000, pp. 684-690.

[33] Sutton, M.A., Abdelmajid, I., Zhao, W., Wang, D. and Hubbard, C., "Weld Characterization and Residual Stress Measurements for TC-128B Steel Plate", *Journal of Pressure Vessel Technology*, Vol. 124, 2002, pp. 405-414.

[34] Wimpory, R.C., May, P.S., O'Dowd, N.P., Webster, G.A., Smith, D.J. and Kingston, E., "Measurement of Residual Stresses in T-Plate Weldments", *Journal of Strain Analysis for Engineering Design*, Vol. 38, No. 4, 2003, pp. 349-365.

[35] Park, M.J., Yang, H.N., Jang, D.Y., Kim, J.S. and Jin, T.E., "Residual Stress Measurement on Welded Specimen by Neutron Diffraction", *Journal of Materials Processing Technology*, 2004, pp. 1171-1177.

[36] Itoh, Y.Z., Suruga, S. and Kashiwaya, H., "Prediction of Fatigue Crack Growth Rate in Welding Residual Stress Field", *Engineering Fracture Mechanics*, Vol. 33, No. 3, 1989, pp. 397-407.

[37] Prask, H.J., Gnäupel-Herold, T., Luzin, V., Fisher, J.W., Cheng, X. and Roy, S., "Residual Stress Modification and Fatigue Life Enhancement", *6th International Trends in Welding Research Conference Proceedings*, 2002, pp. 897-901.

[38] Webster, P.J., Wang, X.D., Kang, W.P. and Mills, G., "Experimental Verification of Residual Stress Models Using Neutron Strain Scanning", *Proceedings of the 1995 7th Conference on Modeling of Casting, Welding and Advanced Solidification Processes*, 1995, pp. 311-318.

[39] Dupas, P., Todeschini, P., Yrieix, B. and Waeckel, F., "Evaluation of Residual Stress Measurement Techniques and Finite Element Simulations on Friction Welded Pipes", *ASME Pressure Vessels and Piping Division (Publication) PVP*, Vol. 373, 1998, pp. 439-446.

[40] Mochizuki, M., Hayashi, M. and Hattori, T., "Comparison of Five Evaluation Methods of Residual Stress in a Welded Pipe Joint", *JSME International Journal, Series A, Solid Mechanics and Material Engineering*, Vol. 42, No. 1, 1999, pp. 104-110.

[41] Stone, H.J., Withers, P.J., Holden, T.M., Roberts, S.M. and Reed, R.C., "Comparison of Three Different Techniques for Measuring the Residual Stresses in an Electron Beam-Welded Plate of WASPALOY", *Metallurgical and Materials Transaction A: Physical Metallurgy and Materials Science*, Vol. 30A, No. 7, 1999, pp. 1797-1808.

[42] Hayashi, M., Ishiwata, M., Morii, Y., Minakawa, N. and Root, J.H., "Residual Stress Distribution in Carbon Steel Pipe Welded Joint Measured by Neutron Diffraction", *Materials Science Research International*, Vol. 6, No. 4, 2000, pp. 287-294.

[43] Tanaka, K., Akiniwa, Y. and Hayashi, M., "Neutron Diffraction Measurements of Residual Stresses in Engineering Materials and Components", *Materials Science Research International*, Vol. 8, No. 4, 2002, pp. 165-174.

[44] Grünitz, L., "Evaluation of the Welding Residual Stress State in a Thick NY-80 Steep Plate", *Proceedings of the Thirteenth (2003) International Offshore and Polar Engineering Conference*, 2003, pp. 141-146.

[45] Wikander, L., Karlsson, L., Mäsström, M. and Webster, P., "Finite Element Simulation and Measurement of Welding Residual Stresses", *Modelling and Simulation in Materials Science and Engineering*, Vol. 2, No. 4, 1994, pp. 845-864.

[46] Feng, Z., Wang, X.L., Spooner, S., Goodwin, G.W., Maziasz, P.J., Hubbard, C.R. and Zacharia, T., "A Finite Element Model for Residual Stress in Repair Welds", *ASME Pressure Vessels and Piping Division (Publication) PVP*, Vol. 327, 1996, pp. 119-125.

[47] Youtsos, A.G., Robin, V. and Bhandari, S., "Residual Stress Evaluation in a RPV Bimetallic Weld for Evaluating the Crack Behaviour", *ASME Pressure Vessels and Piping Division (Publication) PVP*, Vol. 404, 2000, pp. 173-184.

[48] Webster, P.J., Ananthaviravakumar, N., Hughes, D.J., Mills, G., Preston, R.V., Shercliff, H.R. and Withers, P.J., "Measurement and Modelling of Residual Stresses in a TIG Weld", *Applied Physics A: Materials Science and Processing*, Vol. 74, No. SII, 2002, pp. S1421-S1423.

[49] O'Dowd, N.P., Nikbin, K.M., Lee, H.Y., Wimpory, R.C. and Biglari, F.R., "Stress Intensity Factors Due to Residual Stresses in T-Plate Welds", *ASME Pressure Vessels and Piping Division (Publication) PVP*, Vol. 479, 2004, pp. 139-146.

[50] Zhu, X.K. and Chao, Y.J., "Numerical Simulation of Transient Temperature and Residual Stresses in Friction Stir Welding of 304L Stainless Steel", *Journal of Materials Processing Technology*, Vol. 146, 2004, pp. 263-272.

[51] Broek, D., *Elementary Engineering Fracture Mechanics*, Martinus Nijhoff Publishers, The Hague, 1983.

[52] Griffith, A.A., "The Phenomena of Rupture and Flow in Solids", *Philosophical Transactions*, Series A, Vol. 221, 1920, pp. 163-198.

[53] Westergaard, H.M., "Bearing Pressures and Cracks", *Journal of Applied Mechanics*, Vol. 6, 1939, pp. 49-53.

[54] Rice, J.R., "A Path Independent Integral and the Approximate Analysis of Strain Concentration by Notches and Cracks", *Journal of Applied Mechanics*, Vol. 35, 1968, pp. 379-386.

[55] *Endure User's Manual*, Engineering Mechanics Research Corporation, Version 6.0, Michigan, 1995.

[56] Feddersen, C.E., "Evaluation and Prediction of the Residual Strength of Center Cracked Tension Panels", *Damage Tolerance in Aircraft Structures, STP 486*, American Society for Testing and Materials, 1971, pp. 50-78.

[57] Irwin, G.R., "Plastic Zone Near a Crack and Fracture Toughness", *Sagamore Research Conference Proceedings*, Vol. 4, 1961.

[58] Dowling, N.E., *Mechanical Behaviour of Materials: Engineering Methods for Deformation, Fracture, and Fatigue*, Prentice Hall, Englewood Cliffs, New Jersey, 1993.

[59] Broek, D., *The Practical Use of Fracture Mechanics*, Kluwer Academic Publishers, The Netherlands, 1989.

[60] Elber, W., "The Significance of Fatigue Crack Closure", *Damage Tolerance in Aircraft Structures, ASTM STP 486*, American Society for Testing and Materials, 1971, pp. 230-242.

[61] Suresh, S. and Ritchie, R.O., "Propagation of Short Fatigue Cracks", *International Metallurgical Reviews*, Vol. 29, No. 6, 1984, pp. 445-476.

[62] Walker, N. and Beevers, C.J., "Fatigue Crack Closure Mechanism in Titanium", *Fatigue of Engineering Materials and Structures*, Vol. 1, No. 1, 1979, pp. 135-148.

[63] Suresh, S., *Fatigue of Materials*, Second Edition, Cambridge University Press, UK, 1998.

[64] Llorca, J., "Roughness-Induced Fatigue Crack Closure: A Numerical Study", *Fatigue & Fracture of Engineering Materials & Structures*, Vol. 15, No. 7, 1992, pp. 655-669.

[65] Garcia, A.M. and Sehitoglu, H., "Contact of Crack Surfaces during Fatigue: Part 1. Formulation of the Model", *Metallurgical and Materials Transactions A, Physical Metallurgy and Materials Science*, Vol. 28A, 1997, pp. 2263-2275.

[66] Sehitoglu, H. and Garcia, A.M., "Contact of Crack Surfaces during Fatigue: Part 2. Simulations", *Metallurgical and Materials Transactions A, Physical Metallurgy and Materials Science*, Vol. 28A, 1997, pp. 2277-2289.

[67] Wang, S.H. and Müller, C., "Fracture Surface Roughness and Roughness-Induced Fatigue Crack Closure in Ti-2.5 wt% Cu", *Materials Science & Engineering A: Structural Materials: Properties, Microstructure and Processing*, Vol. A255, No. 1-2, 1998, pp. 7-15.

[68] Wang, S.H., Müller, C. and Exner, H.E., "A Model for Roughness-Induced Fatigue Crack Closure", *Metallurgical and Materials Transactions A, Physical Metallurgy and Materials Science*, Vol. 29A, 1998, pp. 1933-1939.

[69] Sehitoglu, H. and Garcia, A.M., "Contact of Nonflat Crack Surfaces During Fatigue", *Advances in Fatigue crack Closure Measurement and Analysis: Second Volume, ASTM STP 1343*, R.C. McClung and J.C. Newman, Jr., Eds., American Society for Testing and Materials, West Conshohocken, PA, 1999, pp. 367-378.

[70] Parry, M.R., Syngellakis, S. and Sinclair, I., "Investigation of Roughness Induced Crack Closure Effects in Fatigue", *Damage and Fracture Mechanics VI: Computer Aided Assessment and Control*, 2000, pp. 313-322.

[71] Parry, M.R., Syngellakis, S. and Sinclair, I., "Numerical Modelling of Roughness and Plasticity Induced Crack Closure Effects in Fatigue", *Materials Science Forum*, Vols. 331-337, 2000, pp. 1473-1478.

[72] Wei, L.W. and James, M.N., "Fatigue Crack Closure for Inclined and Kinked Cracks", *International Journal of Fracture*, Vol. 116, 2002, pp. 25-50.

[73] Zhang, X.P., Li, J.C., Wang, C.H., Ye, L. and Mai, Y.W., "Prediction of Short Fatigue Crack Propagation Behaviour by Characterization of Both Plasticity and Roughness Induced Crack Closures", *International Journal of Fatigue*, Vol. 24, No. 5, 2002, pp. 529-536.

[74] Kamp, N., Parry, M.R., Singh, K.D. and Sinclair, I., "Analytical and Finite Element Modelling of Roughness Induced Crack Closure", *Acta Materialia*, Vol. 52, 2004, pp. 343-353.

[75] Li, S.X., Sun, L.Z., Zang, Q.S. and Wang, Z.G., "A Geometric Model for Fatigue Crack Closure Induced by Fracture Surface Roughness under Mode I Displacements", *Materials Science and Engineering*, Vol. A150, 1992, pp. 209-212.

[76] Shuter, D.M. and Geary, W., "Some Aspects of Fatigue Crack Growth Retardation Behaviour Following Tensile Overloads in a Structural Steel", *Fatigue & Fracture of Engineering Materials & Structures*, Vol. 19, No. 2/3, 1996, pp. 185-199.

[77] Hammouda, M.M.I. and El-Sehily, B.M., "A Two-Dimensional Elastic-Plastic Finite Element Analysis of Friction Effects on Sliding Crack Surfaces in Full or Partial Contact", *Fatigue & Fracture of Engineering Materials & Structures*, Vol. 22, 1999, pp. 101-110.

[78] Noda, N., Yagishita, M. and Kihara, T., "Effect of Crack Shape, Inclination Angle, and Friction Coefficient in Crack Surface Contact Problems", *International Journal of Fracture*, Vol. 105, 2000, pp. 367-389.

[79] Hammouda, M.M.I., Fayed, A.S. and Sallam, H.E.M., "Mode II Stress Intensity Factors for Central Slant Cracks with Frictional Surfaces in Uniaxially Compressed Plates", *International Journal of Fatigue*, Vol. 24, 2002, pp. 1213-1222.

[80] Hammouda, M.M.I., Fayed, A.S. and Sallam, H.E.M., "Stress Intensity Factors of a Shortly Kinked Slant Central Crack with Frictional Surfaces in Uniaxially Loaded Plates", *International Journal of Fatigue*, Vol. 25, 2003, pp. 283-298.

[81] Hammouda, M.M.I., Fayed, A.S. and Sallam, H.E.M., "Simulation of Mixed Mode I/II Cyclic Deformation at the Tip of a Short Kinked Inclined Crack with Frictional Surfaces", *International Journal of Fatigue*, Vol. 25, 2003, pp. 743-753.

[82] Hammouda, M.M.I., Fayed, A.S. and Sallam, H.E.M., "Stress Intensity Factors of a Central Slant Crack with Frictional Surfaces in Plates with Biaxial Loading", *International Journal of Fracture*, Vol. 129, 2004, pp. 141-148.

[83] Geary, W., "A Review of Some Aspects of Fatigue Crack Growth Under Variable Amplitude Loading", *International Journal of Fatigue*, Vol. 14, No. 6, 1992, pp. 377-386.

[84] Kumar, R. Kumar, A. and Kumar, S., "Delay Effects in Fatigue Crack Propagation", *International Journal of Pressure Vessels & Piping*, Vol. 67, 1996, pp. 1-5.

[85] Borrego, L.P., Ferreira, J.M., Pinho da Cruz, J.M. and Costa, J.M., "Evaluation of Overload Effects on Fatigue Crack Growth and Closure", *Engineering Fracture Mechanics*, Vol. 70, 2003, pp. 1379-1397.

[86] Mills, W.J. and Hertzberg, R.W., "Load Interaction Effects on Fatigue Crack Propagation in 2024-T3 Aluminum Alloy", *Engineering Fracture Mechanics*, Vol. 8, 1976, pp. 657-667.

[87] Cheng, X., Okuhara, Y., Yamada, K. and Kondo, A., "Fatigue Crack Growth Rate Measurement of Structural Steel Under Overload Conditions", *Proceedings of JSCE, Structural Engineering/Earthquake Engineering*, Vol. 11, No. 1, 1994, pp. 45s-52s.

[88] Hammouda, M.M.I., Ahmad, S.S.E., Seleem, M.H. and Sallam, H.E.M., "Fatigue Crack Growth Due to Two Successive Single Overloads", *Fatigue & Fracture of Engineering Materials & Structures*, Vol. 21, 1998, pp. 1537-1547.

[89] Lang, M. and Marci, G., "The Influence of Single and Multiple Overloads on Fatigue Crack Propagation", *Fatigue & Fracture of Engineering Materials & Structures*, Vol. 22, 1999, pp. 257-271.

[90] Vardar, Ö. and Yildirim, N., "Crack Growth Retardation Due to Intermittent Overloads", *International Journal of Fatigue*, Vol. 12, No. 4, 1990, pp. 283-287.

[91] Yildirim, N. and Vardar, Ö., "Study of Periodic Overloads at a Fixed Overload-Ratio", *Engineering Fracture Mechanics*, Vol. 36, No. 1, 1990, pp. 71-76.

[92] Tür, Y.K. and Vardar, Ö., "Periodic Tensile Overloads in 2024-T3 Al-Alloy", *Engineering Fracture Mechanics*, Vol. 53, No. 1, 1996, pp. 69-77.

[93] Skorupa, M., Schijve, J. Skorupa, A. and Zachwieja, A., "Experimental Results and Predictions on Crack Growth in a Structural Steel Under Periodically Applied Single and Multiple Overloads", *Proceedings of the 1998 17th International Conference on Offshore Mechanics and Arctic Engineering*, OMAE98-2453, 1998.

[94] Yamada, K., Cao, Q., Okuhara, Y. and Cheng, X., "Fatigue Crack Growth Behavior of Various Structural Steel After Single and Periodic Overloads", *Proceedings of JSCE, Structural Engineering/Earthquake Engineering*, Vol. 15, No. 2, 1998, pp. 191s-200s.

[95] Marissen, R., Trautmann, K.H. and Nowack, H., "The Influence of Compression Loads and of dK/da on the Crack Propagation under Variable Amplitude Loading", *Engineering Fracture Mechanics*, Vol. 19, No. 5, 1984, pp. 863-879.

[96] Yu, M.T., Topper, T.H. and Au, P., "The Effects of Stress Ratio, Compressive Load and Underload on the Threshold Behaviour of a 2024-T351 Aluminum Alloy", *Engineering Materials Advisory Services Ltd*, Vol. 1, 1984, pp. 179-190.

[97] Dexter, R.J., Hudak, S.J., Jr. and Davidson, D.L., "Modelling and Measurement of Crack Closure and Crack Growth Following Overloads and Underloads", *Engineering Fracture Mechanics*, Vol. 33, No. 6, 1989, pp. 855-870.

[98] Pompetzki, M.A., Topper, T.H., DuQuesnay, D.L., and Yu, M.T., "Effect of Compressive Underloads and Tensile Overloads on Fatigue Damage Accumulation in 2024-T351 Aluminum", *Journal of Testing & Evaluation*, Vol. 18, No. 1, 1990, pp. 53-61.

[99] Zhang, X., Chan, A.S.L. and Davies, G.A.O., "Numerical Simulation of Fatigue Crack Growth under Complex Loading Sequences", *Engineering Fracture Mechanics*, Vol. 42, No. 2, 1992, pp. 305-321.

[100] Dabayeh, A.A. and Topper, T.H., "Changes in Crack-Opening Stress after Underloads and Overloads in 2024-T351 Aluminium Alloy", *International Journal of Fatigue*, Vol. 17, No. 4, 1995, pp. 261-269.

[101] Lang, M. and Huang, X., "The Influence of Compressive Loads on Fatigue Crack Propagation in Metals", *Fatigue & Fracture of Engineering Materials & Structures*, Vol. 21, 1998, pp. 65-83.

[102] Lang, M., "Description of Load Interaction Effects by the ΔK_{eff} Concept", *Advances in Fatigue Crack Closure Measurement and Analysis: Second Volume, ASTM STP 1343*, R.C. McClung and J.C. Newman, Jr., Eds., American Society for Testing and Materials, West Conshohocken, PA, 1999, pp. 207-223.

[103] Jono, M., Sugeta, A. and Uematsu, Y., "Fatigue Crack Growth and Crack Closure Behavior of Ti-6Al-4V Alloy under Variable Amplitude Loadings", *Advances in Fatigue Crack Closure Measurement and Analysis: Second Volume, ASTM STP 1343*, R.C. McClung and J.C. Newman, Jr., Eds., American Society for Testing and Materials, West Conshohocken, PA, 1999, pp. 265-284.

[104] Varvani-Farahani, A. and Topper, T.H., "Effect of Periodic Compressive Overstrain Excursions on Crack Closure and Crack Growth Rates of Short Fatigue Cracks–Measurements and Modeling", *Advances in Fatigue and Crack Closure Measurement and Analysis: Second Volume, ASTM STP 1343*, R.C. McClung and J.C. Newman, Jr. Eds., American Society for Testing and Materials, West Conshohocken, PA, 1999, pp. 304-320.

[105] Stephens, R.I., Stephens, R.R. and Schoenefeld, D.A., "Effect of Transient Loads on Fatigue Crack Growth in Mill Annealed Ti-62222 at -54, 25, and 175°C", *Fatigue and Fracture Mechanics: 33rd Volume, ASTM STP 1417*, W.G. Reuter and R.S. Piascik, Eds., ASTM International, West Conshohocken, PA, 2002, pp. 557- 572.

[106] Makabe, C., Purnowidodo, A. and McEvily, A.J., "Effects of Surface Deformation and Crack Closure on Fatigue Crack Propagation after Overloading and Underloading", *International Journal of Fatigue*, Vol. 26, 2004, pp. 1341-1348.

[107] Liu, A.F., *Structural Life Assessment Methods*, ASM International, USA, 1998.

[108] Walker, K., "Effects of Environment and Complex Load History on Fatigue Life", *ASTM STP 462*, American Society for Testing and Materials, 1970, pp. 1-14.

[109] Lal, D.N. and Weiss, V., "A Notch Analysis of Fracture Approach to Fatigue Crack Propagation," *Metallurgical Transactions*, Vol. 9A, March 1978, pp. 413-425.

[110] Zheng, X., "Local Strain Range and Fatigue Crack Initiation Life", *IABSE Proc. Fatigue Colloquium*, 1982, pp. 169-178.

[111] Liu, S.C., Hashida, T., Takahashi, H., Kuwano, H. and Hamaguchi, Y., "A Study on Fractography in the Low-Temperature Brittle Fracture of an 18Cr-18Mn-0.7N Austenitic Steel", *Metallurgical and Materials Transactions A*, Vol. 29A, 1998, pp. 791-798.

[112] *Standard Test Method for Notch Bar Impact Testing of Metallic Materials*, Standard E23-05, ASTM, West Conshohocken, Pa, 2005.

[113] Shank, M.E., Ed. *Control of Steel Construction to Avoid Brittle Failure*, Welding Research Council, New York, NY, 1957.

[114] Barsom, J.M. and Rolfe, S.T., *Fracture and Fatigue Control in Structures: Applications of Fracture Mechanics*, Third Edition, American Society for Testing and Materials, USA, 1999.

[115] Fuchs, H.O. and Stephens, R.I., *Metal Fatigue in Engineering*, John Wiley & Sons, USA, 1980.

[116] Fang, H. and Duan, M., "Fatigue Crack Propagation Behaviour of Steel A537 at Different Temperatures", *International Symposium on Fatigue and Fracture in Steel and Concrete Structures*, 1991, pp. 235-242.

[117] Gan, P. and Guo, H., "The Characteristics of the Fatigue Crack Growth at Low Temperatures in Medium Strength Steel (16Mn)", *Microstructure and Mechanical Behaviour of Materials: Volume II*, 1986, pp. 861-866.

[118] Le Pautremat, E. and Vallet, C., "Low Temperature Fatigue Behaviour of E355 grade RAD Steel Welded Joints", *Welding International 1997*, Vol. 11(4), 1997, pp. 17-28.

[119] Liu, C.T. and Duan, M.L., "Experimental Investigation on Low-Temperature Fatigue Crack Propagation in Offshore Structural Steel A131 Under Random Sea Ice Loading", *Engineering Fracture Mechanics*, Vol. 53, No. 2, 1996, pp. 231-237.

[120] Lu, B. and Zheng, X., "An Approach for Predicting Fatigue Crack Initiation Life of a Low Alloy Steel Below Room Temperature", *Engineering Fracture Mechanics*, Vol. 46, No. 2, 1993, pp. 339-346.

[121] Arimochi, K., Konda, N., Toyosada, M., Fujii, E. and Nakagomi, T., "Evaluation of Strain Rate Effect on Fracture Behaviour of Steel and its Weldment", *17th International Conference on Offshore Mechanics and Arctic Engineering*, OMAE98-2182, 1998.

[122] Lorentzon, M. and Eriksson, K., "Influence of Intermediate Loading Rates and Temperature on the Fracture Toughness of Ordinary Carbon-Manganese Structural Steels", *Fatigue & Fracture of Engineering Materials & Structures*, Vol. 21, 1998, pp. 805-817.

[123] Shul'ginov, B.S. and Matveyev, V.V., "Impact Fatigue of Low-Alloy Steels and Their Welded Joints at Low Temperature", *International Journal of Fatigue*, Vol. 19, Nos. 8-9, 1997, pp. 621-627.

[124] Yang, P., Liao, X., Zhu, J. and Zhou, H., "High Strain-Rate Low-Cycle Fatigue of a Medium-Carbon Alloy Steel", *International Journal of Fatigue*, Vol. 16, July 1994, pp. 327-330.

[125] Shuter, D.M. and Geary, W., "The Influence of Specimen Thickness on Fatigue Crack Growth Retardation Following an Overload", *International Journal of Fatigue*, Vol. 17, No. 2, 1995, pp. 111-119.

[126] Osorio, A.M.B.A. and Williams, J.G., "Some Results on Fatigue Crack Growth in Polymers", *Fatigue in Polymers*, 1983, pp. 7.1-7.10.

[127] Woo, C.W. and Chow, C.L., "Fatigue Crack Propagation in Aluminium and PMMA", *International Journal of Fracture*, Vol. 26, 1984, pp. R37-R42.

[128] Pitoniak F.J., Grandt A.F., Montulli L.T. and Packman P.F., "Fatigue Crack Retardation and Closure in Polymethylmethacrylate", *Engineering Fracture Mechanics*, Vol. 6, 1974, pp. 663-670.

[129] Shiraishi, T. and Soyama, Y., "Fatigue Crack Acceleration and Retardation in Glassy Polymers due to Single Peak Overload", *Key Engineering Materials, Proceedings of the KSME/JSME Joint Conference*, Vol. 51-52, 1991, pp. 289-294.

[130] Poe, C.C., Jr., *Stress-Intensity Factor for a Cracked Sheet with Riveted and Uniformly Spaced Stringers*, Report TR-R-358, National Aeronautics and Space Administration, Langley Research Center, Hampton, VA, 1971.

[131] Poe, C.C., Jr., "Fatigue Crack Propagation in Stiffened Panels", *Damage Tolerance in Aircraft Structures, ASTM STP 486*, American Society for Testing and Materials, 1971, pp. 79-97.

[132] Bae, D.H., Sohn, I.S. and Hong, J.K., "Assessing the Effects of Residual Stresses on the Fatigue Strength of Spot Welds", *Welding Journal*, Vol. 82, No. 1, 2003, pp. 18S-23S.

[133] Bussu, G. and Irving, P.E., "The Role of Residual Stress and Heat Affected Zone Properties on Fatigue Crack Propagation in Friction Stir Welded 2024-T351 Aluminium Joints", *International Journal of Fatigue*, Vol. 25, 2003, pp. 77-88.

[134] Goo, B.C., Yang, S.Y. and Lee, D.H., "A Study on the Effect of Welding Residual Stress on Fatigue Behavior by Finite Element Analysis", *Key Engineering Materials*, Vol. 270-273, 2004, pp. 2296-2301.

[135] Jang, C.D., Song, H.C. and Jo, Y.C., "Fatigue Life Assessment of Fillet Welded Joint Considering the Relaxation and Redistribution of Residual Stresses", *23rd International Conference on Offshore Mechanics and Arctic Engineering*, Vol. 2, 2004, pp. 319-323.

[136] Park, E.J., Kim, E.J. and Yoo, S.H., "Prediction of the Crack Opening Behaviour for the Fatigue Crack Propagation in Welding Residual Stress Field", *Key Engineering Materials*, Vol. 270-273, 2004, pp. 96-101.

[137] Rooke, D.P. and Cartwright, D.J., *Compendium of Stress Intensity Factors*, Hillington Press, Uxbridge, Middex, UK, 1976.

[138] Callister, W.D., Jr., *Materials Science and Engineering: An Introduction*, John Wiley & Sons, Inc., New York, 2000.

[139] *Standard Test Method for Measurement of Fatigue Crack Growth Rates*, Standard E647-00, ASTM, West Conshohocken, Pa, 2000.

[140] *Standard Test Methods for Tension Testing of Metallic Materials [Metric]*, Standard E8M-01, ASTM, West Conshohocken, Pa, 2001.

[141] Willenborg, J.D., Engle, R.M. and Wood, H.A., "A Crack Growth Retardation Model using an Effective Stress Concept", *Report AFFEL-TM-71-1-FBR*, Air Force Flight Dynamics Laboratory, Wright-Patterson Air Force Base, Dayton, Ohio, 1971.

[142] Rudd, J.L. and Engle, R.M., Jr., "Crack Growth Behavior of Center-Cracked Panels under Random Spectrum Loading", *Methods and Models for Predicting Fatigue Crack Growth under Random Loading, ASTM STP 748*, J.B. Chang and C.M. Hudson, Eds., American Society for Testing and Materials, 1981, pp. 103-114.

[143] Chang, J.B., Szamossi, M. and Liu, K.W., "Random Spectrum Fatigue Crack Life Predictions With or Without Considering Load Interactions", *Methods and Models for Predicting Fatigue Crack Growth under Random Loading, ASTM STP 748*, J.B. Chang and C.M. Hudson, Eds., American Society for Testing and Materials, 1981, pp. 115-132.

[144] Johnson, W.S., "Multi-Parameter Yield Zone Model for Predicting Spectrum Crack Growth", *Methods and Models for Predicting Fatigue Crack Growth under Random Loading, ASTM STP 748*, J.B. Chang and C.M. Hudson, Eds., American Society for Testing and Materials, 1981, pp. 85-102.

[145] Manjunatha, C.M. and Parida, B.K., "A Model for Predicting the Overload Effects on Fatigue Crack Growth Behavior", *Collection of Technical Papers – AIAA/ASME/ASCE/AHS/ASC Structures, Structural Dynamics and Materials Conference*, Vol. 2, 2003, pp. 1129-1138.

[146] Nicholas, T., Haritos, G.K., Hastie R.L., Jr. and Harms, K. "The Effects of Overloads on Sustained-Load Crack Growth in a Nickel-Based Superalloy: Part I—Analysis", *Theoretical and Applied Fracture Mechanics*, Vol. 16, 1991, pp. 35-49.

[147] Kim, J.K. and Shim, D.S., "A Statistical Approach for Predicting the Crack Retardation due to a Single Tensile Overload", *International Journal of Fatigue*, Vol. 25, 2003, pp. 335-342.

[148] Pavlou, D.G., "Prediction of Fatigue Crack Growth under Real Stress Histories", *Engineering Structures*, Vol. 22, 2000, pp. 1707-1713.

[149] Darcis, Ph., Li, J. and Recho, N., "Calculation of the Stress Intensity Factor Variation due to Residual Stress Following an Overload", *Advances in Damage Mechanics, Fatigue Damage of Materials: Experiment and Analysis*, 2003, pp. 99-109.

[150] Kim, C.Y. and Song, J.H., "Fatigue Crack Closure and Growth Behavior under Random Loading", *Engineering Fracture Mechanics*, Vol. 49, No. 1, 1994, pp. 105-120.

[151] Dominguez, J., Zapatero, J. and Moreno, B., "A Statistical Model for Fatigue Crack Growth under Random Loads Including Retardation Effects", *Engineering Fracture Mechanics*, Vol. 62, 1999, pp. 351-369.

[152] Lee, C.F., "EndoFEM Intergrated Methodology of Fatique Crack Propagation with Overloaded Delay Retardation", *The Chinese Journal of Mechanics – Series A*, Vol. 19, No. 2, 2003, pp. 327-335.

[153] Sander, M. and Richard, H.A., "Finite Element Analysis of Fatigue Crack Growth with Interspersed Mode I and Mixed Mode Overloads", *International Journal of Fatigue*, Vol. 27, 2005, pp. 905-913.

[154] Ljustell, P. and Nilsson, F., "Variable Amplitude Crack Growth in Notched Specimens", *Engineering Fracture Mechanics*, Vol.72, 2005, pp. 2703-2720.

[155] de Koning, A.U., "A Simple Crack Closure Model for Prediction of Fatigue Crack Growth Rates Under Variable-Amplitude Loading", *Fracture Mechanics: Thirteenth Conference, ASTM STP 743*, Richard Roberts, Ed., American Society for Testing and Materials, 1981, pp. 63-85.

[156] Skorupa, M., Skorupa, A. and Ladecki, B., "Predicting Overload-Affected Fatigue Crack Growth in Steels", *Proceedings of the 15th International Conference on Offshore Mechanics and Arctic Engineering – OMAE*, Vol. 3, 1996, pp. 359-364.

[157] Newman, J.C., Jr., "A Crack-Closure Model for Predicting Fatigue Crack Growth under Aircraft Spectrum Loading", *Methods and Models for Predicting Fatigue Crack Growth under Random Loading, ASTM STP 748*, J.B. Chang and C.M. Hudson, Eds., American Society for Testing and Materials, 1981, pp. 53-84.

[158] Newman, J.C., Jr., "Prediction of Fatigue Crack Growth under Variable-Amplitude and Spectrum Loading Using a Closure Model", *Design of Fatigue and Fracture Resistant Structures, ASTM STP 761*, P.R. Abelkis and C.M. Hudson, Eds., American Society for Testing and Materials, 1982, pp. 255-277.

[159] Patankar, R., Ray, A. and Lakhtakia, A., "A State-Space Model of Fatigue Crack Growth", *International Journal of Fracture*, Vol. 90, 1998, pp. 235-249.

[160] Ray, A. and Patankar, R., "A Stochastic Model of Fatigue Crack Propagation under Variable-Amplitude Loading", *Engineering Fracture Mechanics*, Vol. 62, 1999, pp. 477-493.

[161] Skorupa, M., Schijve, J., Skorupa, A. and Machniewicz, T., "Fatigue Crack Growth in a Structural Steel under Single and Multiple Periodic Overload Cycles", *Fatigue & Fracture of Engineering Materials & Structures*, Vol. 22, 1999, pp. 879-887.

[162] McMaster, F.J. and Smith, D.J., "Predictions of Fatigue Crack Growth in Aluminium Alloy 2024-T351 using Constraint Factors", *International Journal of Fatigue*, Vol. 23, 2001, pp. S93-S101.

[163] Zapatero, J., Moreno, B., Gonzalez-Herrera, A. and Dominguez, J., "Numerical and Experimental Analysis of Fatigue Crack Growth under Random Loading", *International Journal of Fatigue*, Vol. 27, 2005, pp. 878-890.

[164] Skorupa, M. and Skorupa, A., "Experimental Results and Predictions on Fatigue Crack Growth in Structural Steel", *International Journal of Fatigue*, Vol. 27, 2005, pp. 1016-1028.

[165] Bolotin, V.V. and Lebedev, V.L., "Analytical Model of Fatigue Crack Growth Retardation due to Overloading", *International Journal of Solids and Structures*, Vol. 33, No. 9, 1996, pp. 1229-1242.

[166] Lee, B.L., Kim, K.S. and Nam, K.M., "Fatigue Analysis under Variable Amplitude Loading Using an Energy Parameter", *International Journal of Fatigue*, Vol. 25, 2003, pp. 621-631.

[167] Makabe, C., Purnowidodo, A., Miyazaki, T. and McEvily, A.J. "Deceleration and Acceleration of Crack Propagation After an Overload Under Negative Baseline Stress Ratio", *Journal of Testing and Evaluation*, Vol. 33, No. 3, 2005, pp. 181-187.

[168] Cook, R.D., Malkus, D.S. and Plesha, M.E., *Concepts and Applications of Finite Element Analysis*, Third Edition, John Wiley & Sons, Inc., New York, 1989.

[169] *NISA Users Manual*, Engineering Mechanics Research Corporation, Version 91.0, Michigan, 1991.

[170] Bucknall, C.B. and Dumpleton, P., "Acceleration of FCP in toughened PMMA following a step increase in load amplitude", *International Journal of Fatigue*, Vol. 9, No. 2, 1987, pp. 103-108.

[171] Courtney, T.H., *Mechanical Behavior of Materials*, McGraw-Hill, Boston, 2000.

[172] Chandrupatla, T.R. and Belegundu, A.D., *Introduction to Finite Elements in Engineering*, Prentice Hall, Upper Saddle River, 1997.

(In alphabetical order)

[17] Alawi, H., "Designing Reliably for Fatigue Crack Growth under Random Loading", *Engineering Fracture Mechanics*, Vol. 37, No. 1, 1990, pp. 75-85.

[121] Arimochi, K., Konda, N., Toyosada, M., Fujii, E. and Nakagomi, T., "Evaluation of Strain Rate Effect on Fracture Behaviour of Steel and its Weldment", *17th International Conference on Offshore Mechanics and Arctic Engineering*, OMAE98-2182, 1998.

[132] Bae, D.H., Sohn, I.S. and Hong, J.K., "Assessing the Effects of Residual Stresses on the Fatigue Strength of Spot Welds", *Welding Journal*, Vol. 82, No. 1, 2003, pp. 18S-23S.

[114] Barsom, J.M. and Rolfe, S.T., *Fracture and Fatigue Control in Structures: Applications of Fracture Mechanics*, Third Edition, American Society for Testing and Materials, USA, 1999.

[165] Bolotin, V.V. and Lebedev, V.L., "Analytical Model of Fatigue Crack Growth Retardation due to Overloading", *International Journal of Solids and Structures*, Vol. 33, No. 9, 1996, pp. 1229-1242.

[85] Borrego, L.P., Ferreira, J.M., Pinho da Cruz, J.M. and Costa, J.M., "Evaluation of Overload Effects on Fatigue Crack Growth and Closure", *Engineering Fracture Mechanics*, Vol. 70, 2003, pp. 1379-1397.

[51] Broek, D., *Elementary Engineering Fracture Mechanics*, Martinus Nijhoff Publishers, The Hague, 1983.

[59] Broek, D., *The Practical Use of Fracture Mechanics*, Kluwer Academic Publishers, The Netherlands, 1989.

[32] Bruno, G., Carrado, A., Dunn, B., Fiori, F., Girardin, E., Pirling, T. and Rustichelli, F., "Neutron Diffraction Measurements for the Determination of Residual Stress in Ti6Al4V Welded Plates", *Materials Science Forum*, Vols. 347-349, 2000, pp. 684-690.

[170] Bucknall, C.B. and Dumpleton, P., "Acceleration of FCP in toughened PMMA following a step increase in load amplitude", *International Journal of Fatigue*, Vol. 9, No. 2, 1987, pp. 103-108.

[133] Bussu, G. and Irving, P.E., "The Role of Residual Stress and Heat Affected Zone Properties on Fatigue Crack Propagation in Friction Stir Welded 2024-T351 Aluminium Joints", *International Journal of Fatigue*, Vol. 25, 2003, pp. 77-88.

[138] Callister, W.D., Jr., *Materials Science and Engineering: An Introduction*, John Wiley & Sons, Inc., New York, 2000.

[172] Chandrupatla, T.R. and Belegundu, A.D., *Introduction to Finite Elements in Engineering*, Prentice Hall, Upper Saddle River, 1997.

[143] Chang, J.B., Szamossi, M. and Liu, K.W., "Random Spectrum Fatigue Crack Life Predictions With or Without Considering Load Interactions", *Methods and Models for Predicting Fatigue Crack Growth under Random Loading, ASTM STP 748*, J.B. Chang and C.M. Hudson, Eds., American Society for Testing and Materials, 1981, pp. 115-132.

[87] Cheng, X., Okuhara, Y., Yamada, K. and Kondo, A., "Fatigue Crack Growth Rate Measurement of Structural Steel Under Overload Conditions", *Proceedings of JSCE, Structural Engineering/Earthquake Engineering*, Vol. 11, No. 1, 1994, pp. 45s-52s.

[168] Cook, R.D., Malkus, D.S. and Plesha, M.E., *Concepts and Applications of Finite Element Analysis*, Third Edition, John Wiley & Sons, Inc., New York, 1989.

[11] Corbly, D.M. and Packman, P.F., "On the Influence of Single and Multiple Peak Overloads on Fatigue Crack Propagation in 7075-T6511 Aluminum", *Engineering Fracture Mechanics*, Vol. 5, 1973, pp. 479-497.

[171] Courtney, T.H., *Mechanical Behavior of Materials*, McGraw-Hill, Boston, 2000.

[100] Dabayeh, A.A. and Topper, T.H., "Changes in Crack-Opening Stress after Underloads and Overloads in 2024-T351 Aluminium Alloy", *International Journal of Fatigue*, Vol. 17, No. 4, 1995, pp. 261-269.

[149] Darcis, Ph., Li, J. and Recho, N., "Calculation of the Stress Intensity Factor Variation due to Residual Stress Following an Overload", *Advances in Damage Mechanics, Fatigue Damage of Materials: Experiment and Analysis*, 2003, pp. 99-109.

[155] de Koning, A.U., "A Simple Crack Closure Model for Prediction of Fatigue Crack Growth Rates Under Variable-Amplitude Loading", *Fracture Mechanics: Thirteenth Conference, ASTM STP 743*, Richard Roberts, Ed., American Society for Testing and Materials, 1981, pp. 63-85.

[97] Dexter, R.J., Hudak, S.J., Jr. and Davidson, D.L., "Modelling and Measurement of Crack Closure and Crack Growth Following Overloads and Underloads", *Engineering Fracture Mechanics*, Vol. 33, No. 6, 1989, pp. 855-870.

[26] Dexter, R.J. and Pilarski, P.J., "Effect of Welded Stiffeners on Fatigue Crack Growth Rate", *SSC-413*, August 2000.

[27] Dexter, R.J. and Pilarski, P.J., "Crack Propagation in Welded Stiffened Panels", *Journal of Constructional Steel Research*, Vol. 58, 2002, pp. 1081-1102.

[28] Dexter, R.J., Pilarski, P.J. and Mahmoud, H.N., "Analysis of Crack Propagation in Welded Stiffened Panels", *International Journal of Fatigue*, Vol. 25, 2003, pp. 1169-1174.

[29] Dexter, R.J. and Mahmoud, H.N., "Predicting Fatigue Crack Propagation in Stiffened Panels", *SSC-444*, March 2004.

[16] Dolinski, K., "Fatigue Crack Growth with Retardation under Stationary Stochastic Loading", *Engineering Fracture Mechanics*, Vol. 27, No. 3, 1987, pp. 279-290.

[151] Dominguez, J., Zapatero, J. and Moreno, B., "A Statistical Model for Fatigue Crack Growth under Random Loads Including Retardation Effects", *Engineering Fracture Mechanics*, Vol. 62, 1999, pp. 351-369.

[58] Dowling, N.E., *Mechanical Behaviour of Materials: Engineering Methods for Deformation, Fracture, and Fatigue*, Prentice Hall, Englewood Cliffs, New Jersey, 1993.

[39] Dupas, P., Todeschini, P., Yrieix, B. and Waeckel, F., "Evaluation of Residual Stress Measurement Techniques and Finite Element Simulations on Friction Welded Pipes", *ASME Pressure Vessels and Piping Division (Publication) PVP*, Vol. 373, 1998, pp. 439-446.

[60] Elber, W., "The Significance of Fatigue Crack Closure", *Damage Tolerance in Aircraft Structures*, *ASTM STP 486*, American Society for Testing and Materials, 1971, pp. 230-242.

[55] *Endure User's Manual*, Engineering Mechanics Research Corporation, Version 6.0, Michigan, 1995.

[116] Fang, H. and Duan, M., "Fatigue Crack Propagation Behaviour of Steel A537 at Different Temperatures", *International Symposium on Fatigue and Fracture in Steel and Concrete Structures*, 1991, pp. 235-242.

[56] Feddersen, C.E., "Evaluation and Prediction of the Residual Strength of Center Cracked Tension Panels", *Damage Tolerance in Aircraft Structures*, *STP 486*, American Society for Testing and Materials, 1971, pp. 50-78.

[46] Feng, Z., Wang, X.L., Spooner, S., Goodwin, G.W., Maziasz, P.J., Hubbard, C.R. and Zacharia, T., "A Finite Element Model for Residual Stress in Repair Welds", *ASME Pressure Vessels and Piping Division (Publication) PVP*, Vol. 327, 1996, pp. 119-125.

[14] Finney, J.M., "Modelling for Fatigue Crack Growth Prediction in Aircraft", *Fatigue & Fracture of Engineering Materials & Structures*, Vol. 8, No. 3, 1985, pp. 205-222.

[115] Fuchs, H.O. and Stephens, R.I., *Metal Fatigue in Engineering*, John Wiley & Sons, USA, 1980.

[117] Gan, P. and Guo, H., "The Characteristics of the Fatigue Crack Growth at Low Temperatures in Medium Strength Steel (16Mn)", *Microstructure and Mechanical Behaviour of Materials: Volume II*, 1986, pp. 861-866.

[65] Garcia, A.M. and Sehitoglu, H., "Contact of Crack Surfaces during Fatigue: Part 1. Formulation of the Model", *Metallurgical and Materials Transactions A, Physical Metallurgy and Materials Science*, Vol. 28A, 1997, pp. 2263-2275.

[83] Geary, W., "A Review of Some Aspects of Fatigue Crack Growth Under Variable Amplitude Loading", *International Journal of Fatigue*, Vol. 14, No. 6, 1992, pp. 377-386.

[10] Goel, H.S. and Chand. S., "A Fatigue Crack Growth Model for Single Overload Tests", *Journal of Engineering Materials and Technology, Transaction of the ASME*, Vol. 14, No. 116, 1994, pp. 168-172.

[134] Goo, B.C., Yang, S.Y. and Lee, D.H., "A Study on the Effect of Welding Residual Stress on Fatigue Behavior by Finite Element Analysis", *Key Engineering Materials*, Vol. 270-273, 2004, pp. 2296-2301.

[15] Gray, T.D. and Gallagher, J.P., "Predicting Fatigue Crack Retardation Following a Single Overload Using a Modified Wheeler Model", *Mechanics of Crack Growth, ASTM STP 590*, American Society for Testing and Materials, 1976, pp. 331-344.

[52] Griffith, A.A., "The Phenomena of Rupture and Flow in Solids", *Philosophical Transactions*, Series A, Vol. 221, 1920, pp. 163-198.

[44] Grünitz, L., "Evaluation of the Welding Residual Stress State in a Thick NY-80 Steep Plate", *Proceedings of the Thirteenth (2003) International Offshore and Polar Engineering Conference*, 2003, pp. 141-146.

[88] Hammouda, M.M.I., Ahmad, S.S.E., Seleem, M.H. and Sallam, H.E.M., "Fatigue Crack Growth Due to Two Successive Single Overloads", *Fatigue & Fracture of Engineering Materials & Structures*, Vol. 21, 1998, pp. 1537-1547.

[77] Hammouda, M.M.I. and El-Sehily, B.M., "A Two-Dimensional Elastic-Plastic Finite Element Analysis of Friction Effects on Sliding Crack Surfaces in Full or Partial Contact", *Fatigue & Fracture of Engineering Materials & Structures*, Vol. 22, 1999, pp. 101-110.

[79] Hammouda, M.M.I., Fayed, A.S. and Sallam, H.E.M., "Mode II Stress Intensity Factors for Central Slant Cracks with Frictional Surfaces in Uniaxially Compressed Plates", *International Journal of Fatigue*, Vol. 24, 2002, pp. 1213-1222.

[80] Hammouda, M.M.I., Fayed, A.S. and Sallam, H.E.M., "Stress Intensity Factors of a Shortly Kinked Slant Central Crack with Frictional Surfaces in Uniaxially Loaded Plates", *International Journal of Fatigue*, Vol. 25, 2003, pp. 283-298.

[81] Hammouda, M.M.I., Fayed, A.S. and Sallam, H.E.M., "Simulation of Mixed Mode I/II Cyclic Deformation at the Tip of a Short Kinked Inclined Crack with Frictional Surfaces", *International Journal of Fatigue*, Vol. 25, 2003, pp. 743-753.

[82] Hammouda, M.M.I., Fayed, A.S. and Sallam, H.E.M., "Stress Intensity Factors of a Central Slant Crack with Frictional Surfaces in Plates with Biaxial Loading", *International Journal of Fracture*, Vol. 129, 2004, pp. 141-148.

[20] Hawkyard, M., Powell, B.E., Stephenson, J.M. and McElhone, M., "Fatigue Crack Growth from Simulated Flight Cycles Involving Superimposed Vibrations", *International Journal of Fatigue*, Vol. 21, 1999, pp. S59-S68.

[42] Hayashi, M., Ishiwata, M., Morii, Y., Minakawa, N. and Root, J.H., "Residual Stress Distribution in Carbon Steel Pipe Welded Joint Measured by Neutron Diffraction", *Materials Science Research International*, Vol. 6, No. 4, 2000, pp. 287-294.

[57] Irwin, G.R., "Plastic Zone Near a Crack and Fracture Toughness", *Sagamore Research Conference Proceedings*, Vol. 4, 1961.

[36] Itoh, Y.Z., Suruga, S. and Kashiwaya, H., "Prediction of Fatigue Crack Growth Rate in Welding Residual Stress Field", *Engineering Fracture Mechanics*, Vol. 33, No. 3, 1989, pp. 397-407.

[135] Jang, C.D., Song, H.C. and Jo, Y.C., "Fatigue Life Assessment of Fillet Welded Joint Considering the Relaxation and Redistribution of Residual Stresses", *23rd International Conference on Offshore Mechanics and Arctic Engineering*, Vol. 2, 2004, pp. 319-323.

[144] Johnson, W.S., "Multi-Parameter Yield Zone Model for Predicting Spectrum Crack Growth", *Methods and Models for Predicting Fatigue Crack Growth under Random Loading, ASTM STP 748*, J.B. Chang and C.M. Hudson, Eds., American Society for Testing and Materials, 1981, pp. 85-102.

[103] Jono, M., Sugeta, A. and Uematsu, Y., "Fatigue Crack Growth and Crack Closure Behavior of Ti-6Al-4V Alloy under Variable Amplitude Loadings", *Advances in Fatigue Crack Closure Measurement and Analysis: Second Volume, ASTM STP 1343*, R.C. McClung and J.C. Newman, Jr., Eds., American Society for Testing and Materials, West Conshohocken, PA, 1999, pp. 265-284.

[74] Kamp, N., Parry, M.R., Singh, K.D. and Sinclair, I., "Analytical and Finite Element Modelling of Roughness Induced Crack Closure", *Acta Materialia*, Vol. 52, 2004, pp. 343-353.

[19] Khan, Z., Rauf, A. and Younas, M., "Prediction of Fatigue Crack Propagation Life in Notched Members under Variable Amplitude Loading", *Journal of Materials Engineering and Performance*, Vol. 6, No. 3, 1997, pp. 365-373.

[150] Kim, C.Y. and Song, J.H., "Fatigue Crack Closure and Growth Behavior under Random Loading", *Engineering Fracture Mechanics*, Vol. 49, No. 1, 1994, pp. 105-120.

[147] Kim, J.K. and Shim, D.S., "A Statistical Approach for Predicting the Crack Retardation due to a Single Tensile Overload", *International Journal of Fatigue*, Vol. 25, 2003, pp. 335-342.

[12] Kim, K.S., Kim, S.C., Shim, C.S. and Park, J.Y., "A Study on the Effect of Overload Ratio on Fatigue Crack Growth", *Key Engineering Materials*, Vols. 261-263, 2004, pp. 1159-1168.

[13] Kim, K.S., Kim, K.S., Shim, C.S. and Cho, H.M., "A Study on Evaluation of Overload Effects on Fatigue Crack Growth", *Key Engineering Materials*, Vols. 261-263, 2004, pp. 1169-1178.

[84] Kumar, R. Kumar, A. and Kumar, S., "Delay Effects in Fatigue Crack Propagation", *International Journal of Pressure Vessels & Piping*, Vol. 67, 1996, pp. 1-5.

[109] Lal, D.N. and Weiss, V., "A Notch Analysis of Fracture Approach to Fatigue Crack Propagation," *Metallurgical Transactions*, Vol. 9A, March 1978, pp. 413-425.

[1] Lampman, S.R., Ed., *ASM Handbook, Volume 19: Fatigue and Fracture*, ASM International, USA, 1996.

[101] Lang, M. and Huang, X., "The Influence of Compressive Loads on Fatigue Crack Propagation in Metals", *Fatigue & Fracture of Engineering Materials & Structures*, Vol. 21, 1998, pp. 65-83.

[102] Lang, M., "Description of Load Interaction Effects by the ΔK_{eff} Concept", *Advances in Fatigue Crack Closure Measurement and Analysis: Second Volume, ASTM STP 1343*, R.C. McClung and J.C. Newman, Jr., Eds., American Society for Testing and Materials, West Conshohocken, PA, 1999, pp. 207-223.

[89] Lang, M. and Marci, G., "The Influence of Single and Multiple Overloads on Fatigue Crack Propagation", *Fatigue & Fracture of Engineering Materials & Structures*, Vol. 22, 1999, pp. 257-271.

[118] Le Pautremat, E. and Vallet, C., "Low Temperature Fatigue Behaviour of E355 grade RAD Steel Welded Joints", *Welding International 1997*, Vol. 11(4), 1997, pp. 17-28.

[166] Lee, B.L., Kim, K.S. and Nam, K.M., "Fatigue Analysis under Variable Amplitude Loading Using an Energy Parameter", *International Journal of Fatigue*, Vol. 25, 2003, pp. 621-631.

[152] Lee, C.F., "EndoFEM Intergrated Methodology of Fatique Crack Propagation with Overloaded Delay Retardation", *The Chinese Journal of Mechanics – Series A*, Vol. 19, No. 2, 2003, pp. 327-335.

[75] Li, S.X., Sun, L.Z., Zang, Q.S. and Wang, Z.G., "A Geometric Model for Fatigue Crack Closure Induced by Fracture Surface Roughness under Mode I Displacements", *Materials Science and Engineering*, Vol. A150, 1992, pp. 209-212.

[119] Liu, C.T. and Duan, M.L., "Experimental Investigation on Low-Temperature Fatigue Crack Propagation in Offshore Structural Steel A131 Under Random Sea Ice Loading", *Engineering Fracture Mechanics*, Vol. 53, No. 2, 1996, pp. 231-237.

[107] Liu, A.F., *Structural Life Assessment Methods*, ASM International, USA, 1998.

[111] Liu, S.C., Hashida, T., Takahashi, H., Kuwano, H. and Hamaguchi, Y., "A Study on Fractography in the Low-Temperature Brittle Fracture of an 18Cr-18Mn-0.7N Austenitic Steel", *Metallurgical and Materials Transactions A*, Vol. 29A, 1998, pp. 791-798.

[154] Ljustell, P. and Nilsson, F., "Variable Amplitude Crack Growth in Notched Specimens", Engineering Fracture Mechanics, Vol.72, 2005, pp. 2703-2720.

[64] Llorca, J., "Roughness-Induced Fatigue Crack Closure: A Numerical Study", *Fatigue & Fracture of Engineering Materials & Structures*, Vol. 15, No. 7, 1992, pp. 655-669.

[30] Lorentzen, T. and Ibsø, J.B., "Neutron Diffraction Measurements of Residual Strains in Offshore Welds", *Materials Science and Engineering A*, Vol. 197, 1995, pp. 209-214.

[122] Lorentzon, M. and Eriksson, K., "Influence of Intermediate Loading Rates and Temperature on the Fracture Toughness of Ordinary Carbon-Manganese Structural Steels", *Fatigue & Fracture of Engineering Materials & Structures*, Vol. 21, 1998, pp. 805-817.

[120] Lu, B. and Zheng, X., "An Approach for Predicting Fatigue Crack Initiation Life of a Low Alloy Steel Below Room Temperature", *Engineering Fracture Mechanics*, Vol. 46, No. 2, 1993, pp. 339-346.

[106] Makabe, C., Purnowidodo, A. and McEvily, A.J., "Effects of Surface Deformation and Crack Closure on Fatigue Crack Propagation after Overloading and Underloading", *International Journal of Fatigue*, Vol. 26, 2004, pp. 1341-1348.

[167] Makabe, C., Purnowidodo, A., Miyazaki, T. and McEvily, A.J. "Deceleration and Acceleration of Crack Propagation After an Overload Under Negative Baseline Stress Ratio", *Journal of Testing and Evaluation*, Vol. 33, No. 3, 2005, pp. 181-187.

[145] Manjunatha, C.M. and Parida, B.K., "A Model for Predicting the Overload Effects on Fatigue Crack Growth Behavior", *Collection of Technical Papers – AIAA/ASME/ASCE/AHS/ASC Structures, Structural Dynamics and Materials Conference*, Vol. 2, 2003, pp. 1129-1138.

[95] Marissen, R., Trautmann, K.H. and Nowack, H., "The Influence of Compression Loads and of dK/da on the Crack Propagation under Variable Amplitude Loading", *Engineering Fracture Mechanics*, Vol. 19, No. 5, 1984, pp. 863-879.

[162] McMaster, F.J. and Smith, D.J., "Predictions of Fatigue Crack Growth in Aluminium Alloy 2024-T351 using Constraint Factors", *International Journal of Fatigue*, Vol. 23, 2001, pp. S93-S101.

[86] Mills, W.J. and Hertzberg, R.W., "Load Interaction Effects on Fatigue Crack Propagation in 2024-T3 Aluminum Alloy", *Engineering Fracture Mechanics*, Vol. 8, 1976, pp. 657-667.

[40] Mochizuki, M., Hayashi, M. and Hattori, T., "Comparison of Five Evaluation Methods of Residual Stress in a Welded Pipe Joint", *JSME International Journal, Series A, Solid Mechanics and Material Engineering*, Vol. 42, No. 1, 1999, pp. 104-110.

[157] Newman, J.C., Jr., "A Crack-Closure Model for Predicting Fatigue Crack Growth under Aircraft Spectrum Loading", *Methods and Models for Predicting Fatigue Crack Growth under Random Loading, ASTM STP 748*, J.B. Chang and C.M. Hudson, Eds., American Society for Testing and Materials, 1981, pp. 53-84.

[158] Newman, J.C., Jr., "Prediction of Fatigue Crack Growth under Variable-Amplitude and Spectrum Loading Using a Closure Model", *Design of Fatigue and Fracture Resistant Structures, ASTM STP 761*, P.R. Abelkis and C.M. Hudson, Eds., American Society for Testing and Materials, 1982, pp. 255-277.

[146] Nicholas, T., Haritos, G.K., Hastie R.L., Jr. and Harms, K. "The Effects of Overloads on Sustained-Load Crack Growth in a Nickel-Based Superalloy: Part I—Analysis", *Theoretical and Applied Fracture Mechanics*, Vol. 16, 1991, pp. 35-49.

[169] *NISA Users Manual*, Engineering Mechanics Research Corporation, Version 91.0, Michigan, 1991.

[78] Noda, N., Yagishita, M. and Kihara, T., "Effect of Crack Shape, Inclination Angle, and Friction Coefficient in Crack Surface Contact Problems", *International Journal of Fracture*, Vol. 105, 2000, pp. 367-389.

[23] Nussbaumer, A., *Propagation of Long Fatigue Cracks in Multi-Cellular Box Beams*. Ph.D. Thesis, Lehigh University, Bethlehem, Pennsylvania, 1993.

[25] Nussbaumer, A.C., Fisher, J.W. and Dexter, R.J., "Behavior of Long Fatigue Cracks in Cellular Box Beam", *Journal of Structural Engineering*, Vol. 125, No. 11, 1999, pp. 1232-1238.

[49] O'Dowd, N.P., Nikbin, K.M., Lee, H.Y., Wimpory, R.C. and Biglari, F.R., "Stress Intensity Factors Due to Residual Stresses in T-Plate Welds", *ASME Pressure Vessels and Piping Division (Publication) PVP*, Vol. 479, 2004, pp. 139-146.

[126] Osorio, A.M.B.A. and Williams, J.G., "Some Results on Fatigue Crack Growth in Polymers", *Fatigue in Polymers*, 1983, pp. 7.1-7.10.

[7] Paris, P.C. and Erdogan, F., "A Critical Analysis of Crack Propagation Laws", *Journal of Basic Engineering Transactions, American Society of Mechanical Engineers, Series D*, Vol. 85, Dec. 1963, pp. 528-534.

[136] Park, E.J., Kim, E.J. and Yoo, S.H., "Prediction of the Crack Opening Behaviour for the Fatigue Crack Propagation in Welding Residual Stress Field", *Key Engineering Materials*, Vol. 270-273, 2004, pp. 96-101.

[35] Park, M.J., Yang, H.N., Jang, D.Y., Kim, J.S. and Jin, T.E., "Residual Stress Measurement on Welded Specimen by Neutron Diffraction", *Journal of Materials Processing Technology*, 2004, pp. 1171-1177.

[70] Parry, M.R., Syngellakis, S. and Sinclair, I., "Investigation of Roughness Induced Crack Closure Effects in Fatigue", *Damage and Fracture Mechanics VI: Computer Aided Assessment and Control*, 2000, pp. 313-322.

[71] Parry, M.R., Syngellakis, S. and Sinclair, I., "Numerical Modelling of Roughness and Plasticity Induced Crack Closure Effects in Fatigue", *Materials Science Forum*, Vols. 331-337, 2000, pp. 1473-1478.

[159] Patankar, R., Ray, A. and Lakhtakia, A., "A State-Space Model of Fatigue Crack Growth", *International Journal of Fracture*, Vol. 90, 1998, pp. 235-249.

[148] Pavlou, D.G., "Prediction of Fatigue Crack Growth under Real Stress Histories", *Engineering Structures*, Vol. 22, 2000, pp. 1707-1713.

[128] Pitoniak F.J., Grandt A.F., Montulli L.T. and Packman P.F., "Fatigue Crack Retardation and Closure in Polymethylmethacrylate", *Engineering Fracture Mechanics*, Vol. 6, 1974, pp. 663-670.

[130] Poe, C.C., Jr., *Stress-Intensity Factor for a Cracked Sheet with Riveted and Uniformly Spaced Stringers*, Report TR-R-358, National Aeronautics and Space Administration, Langley Research Center, Hampton, VA, 1971.

[131] Poe, C.C., Jr., "Fatigue Crack Propagation in Stiffened Panels", Damage Tolerance in Aircraft Structures, *ASTM STP 486*, American Society for Testing and Materials, 1971, pp. 79-97.

[98] Pompetzki, M.A., Topper, T.H., DuQuesnay, D.L., and Yu, M.T., "Effect of Compressive Underloads and Tensile Overloads on Fatigue Damage Accumulation in 2024-T351 Aluminum", *Journal of Testing & Evaluation*, Vol. 18, No. 1, 1990, pp. 53-61.

[37] Prask, H.J., Gnäupel-Herold, T., Luzin, V., Fisher, J.W., Cheng, X. and Roy, S., "Residual Stress Modification and Fatigue Life Enhancement", *6th International Trends in Welding Research Conference Proceedings*, 2002, pp. 897-901.

[160] Ray, A. and Patankar, R., "A Stochastic Model of Fatigue Crack Propagation under Variable-Amplitude Loading", *Engineering Fracture Mechanics*, Vol. 62, 1999, pp. 477-493.

[54] Rice, J.R., "A Path Independent Integral and the Approximate Analysis of Strain Concentration by Notches and Cracks", *Journal of Applied Mechanics*, Vol. 35, 1968, pp. 379-386.

[137] Rooke, D.P. and Cartwright, D.J., *Compendium of Stress Intensity Factors*, Hillington Press, Uxbridge, Middex, UK, 1976.

[142] Rudd, J.L. and Engle, R.M., Jr., "Crack Growth Behavior of Center-Cracked Panels under Random Spectrum Loading", *Methods and Models for Predicting Fatigue Crack Growth under Random Loading, ASTM STP 748*, J.B. Chang and C.M. Hudson, Eds., American Society for Testing and Materials, 1981, pp. 103-114.

[2] Rushton, P.A., *An Experimental and Numerical Investigation into Fatigue Crack Propagation in 350WT Steel Subjected to Semi-Random Loading*, M.A.Sc. Thesis, Dalhousie University, Halifax, Nova Scotia, 2000.

[3] Rushton, P.A., Taheri, F. and Stredulinsky, D.C., "Threshold & Variable Amplitude Crack Growth Behavior in 350WT Steel", *Proceedings of the 21st International Conference on Pressure Vessels and Piping, ASME-PVP*, Vol. 441, 2002, pp. 81-89.

[4] Rushton, P.A., Taheri, F., "Prediction of Variable Amplitude Crack Growth in 350WT Steel Using a Modified Wheeler Approach", *Journal of Marine Structure*, Vol. 16, No. 7, 2003, pp. 517-539.

[153] Sander, M. and Richard, H.A., "Finite Element Analysis of Fatigue Crack Growth with Interspersed Mode I and Mixed Mode Overloads", *International Journal of Fatigue*, Vol. 27, 2005, pp. 905-913.

[66] Sehitoglu, H. and Garcia, A.M., "Contact of Crack Surfaces during Fatigue: Part 2. Simulations", *Metallurgical and Materials Transactions A, Physical Metallurgy and Materials Science*, Vol. 28A, 1997, pp. 2277-2289.

[69] Sehitoglu, H. and Garcia, A.M., "Contact of Nonflat Crack Surfaces During Fatigue", *Advances in Fatigue crack Closure Measurement and Analysis: Second Volume, ASTM STP 1343*, R.C. McClung and J.C. Newman, Jr., Eds., American Society for Testing and Materials, West Conshohocken, PA, 1999, pp. 367-378.

[113] Shank, M.E., Ed. *Control of Steel Construction to Avoid Brittle Failure*, Welding Research Council, New York, NY, 1957.

[18] Sheu, B.C., Song, P.S. and Hwang, S., "Shaping Exponent in Wheeler Model Under a Single Overload", *Engineering Fracture Mechanics*, Vol. 51, No. 1, 1995, pp. 135-143.

[129] Shiraishi, T. and Soyama, Y., "Fatigue Crack Acceleration and Retardation in Glassy Polymers due to Single Peak Overload", *Key Engineering Materials, Proceedings of the KSME/JSME Joint Conference*, Vol. 51-52, 1991, pp. 289-294.

[123] Shul'ginov, B.S. and Matveyev, V.V., "Impact Fatigue of Low-Alloy Steels and Their Welded Joints at Low Temperature", *International Journal of Fatigue*, Vol. 19, Nos. 8-9, 1997, pp. 621-627.

[125] Shuter, D.M. and Geary, W., "The Influence of Specimen Thickness on Fatigue Crack Growth Retardation Following an Overload", *International Journal of Fatigue*, Vol. 17, No. 2, 1995, pp. 111-119.

[76] Shuter, D.M. and Geary, W., "Some Aspects of Fatigue Crack Growth Retardation Behaviour Following Tensile Overloads in a Structural Steel", *Fatigue & Fracture of Engineering Materials & Structures*, Vol. 19, No. 2/3, 1996, pp. 185-199.

[156] Skorupa, M., Skorupa, A. and Ladecki, B., "Predicting Overload-Affected Fatigue Crack Growth in Steels", *Proceedings of the 15th International Conference on Offshore Mechanics and Arctic Engineering – OMAE*, Vol. 3, 1996, pp. 359-364.

[93] Skorupa, M., Schijve, J. Skorupa, A. and Zachwieja, A., "Experimental Results and Predictions on Crack Growth in a Structural Steel Under Periodically Applied Single and Multiple Overloads", *Proceedings of the 1998 17th International Conference on Offshore Mechanics and Arctic Engineering*, OMAE98-2453, 1998.

[161] Skorupa, M., Schijve, J., Skorupa, A. and Machniewicz, T., "Fatigue Crack Growth in a Structural Steel under Single and Multiple Periodic Overload Cycles", *Fatigue & Fracture of Engineering Materials & Structures*, Vol. 22, 1999, pp. 879-887.

[164] Skorupa, M. and Skorupa, A., "Experimental Results and Predictions on Fatigue Crack Growth in Structural Steel", *International Journal of Fatigue*, Vol. 27, 2005, pp. 1016-1028.

[21] Song, P.S., Sheu, B.C. and Chang, L., "A Modified Wheeler Model to Improve Predictions of Crack Growth Following a Single Overload", *JSME International Journal Series A*, Vol. 44, No. 1, 2001, pp. 117-122.

[139] *Standard Test Method for Measurement of Fatigue Crack Growth Rates*, Standard E647-00, ASTM, West Conshohocken, Pa, 2000.

[140] *Standard Test Methods for Tension Testing of Metallic Materials [Metric]*, Standard E8M-01, ASTM, West Conshohocken, Pa, 2001.

[112] *Standard Test Method for Notch Bar Impact Testing of Metallic Materials*, Standard E23-05, ASTM, West Conshohocken, Pa, 2005.

[105] Stephens, R.I., Stephens, R.R. and Schoenefeld, D.A., "Effect of Transient Loads on Fatigue Crack Growth in Mill Annealed Ti-62222 at -54, 25, and 175°C", *Fatigue and Fracture Mechanics: 33rd Volume, ASTM STP 1417*, W.G. Reuter and R.S. Piascik, Eds., ASTM International, West Conshohocken, PA, 2002, pp. 557- 572.

[41] Stone, H.J., Withers, P.J., Holden, T.M., Roberts, S.M. and Reed, R.C., "Comparison of Three Different Techniques for Measuring the Residual Stresses in an Electron Beam-Welded Plate of WASPALOY", *Metallurgical and Materials Transaction A: Physical Metallurgy and Materials Science*, Vol. 30A, No. 7, 1999, pp. 1797-1808.

[61] Suresh, S. and Ritchie, R.O., "Propagation of Short Fatigue Cracks", *International Metallurgical Reviews*, Vol. 29, No. 6, 1984, pp. 445-476.

[63] Suresh, S., *Fatigue of Materials*, Second Edition, Cambridge University Press, UK, 1998.

[33] Sutton, M.A., Abdelmajid, I., Zhao, W., Wang, D. and Hubbard, C., "Weld Characterization and Residual Stress Measurements for TC-128B Steel Plate", *Journal of Pressure Vessel Technology*, Vol. 124, 2002, pp. 405-414.

[5] Taheri, F., Trask, D. and Pegg, N., "Experimental and Analytical Investigation of Fatigue Characteristics of 350WT Steel Under Constant and Variable Amplitude Loadings", *Journal of Marine Structures*, Vol. 16, 2003, pp. 69-91.

[43] Tanaka, K., Akiniwa, Y. and Hayashi, M., "Neutron Diffraction Measurements of Residual Stresses in Engineering Materials and Components", *Materials Science Research International*, Vol. 8, No. 4, 2002, pp. 165-174.

[6] Trask, D.A., *Experimental and Numerical Investigation into Fatigue Crack Propagation Models for 350WT Steel*, M.A.Sc. Thesis, Dalhousie University, Halifax, Nova Scotia, 1998.

[92] Tür, Y.K. and Vardar, Ö., "Periodic Tensile Overloads in 2024-T3 Al-Alloy", *Engineering Fracture Mechanics*, Vol. 53, No. 1, 1996, pp. 69-77.

[90] Vardar, Ö. and Yildirim, N., "Crack Growth Retardation Due to Intermittent Overloads", *International Journal of Fatigue*, Vol. 12, No. 4, 1990, pp. 283-287.

[104] Varvani-Farahani, A. and Topper, T.H., "Effect of Periodic Compressive Overstrain Excursions on Crack Closure and Crack Growth Rates of Short Fatigue Cracks–Measurements and Modeling", *Advances in Fatigue and Crack Closure Measurement and Analysis: Second Volume, ASTM STP 1343*, R.C. McClung and J.C. Newman, Jr. Eds., American Society for Testing and Materials, West Conshohocken, PA, 1999, pp. 304-320.

[22] Wahab, M.A., Rohrsheim, G.R. and Park, J.H., "Experimental Study on the Influence of Overload Induced Residual Stress Field on Fatigue Crack Growth in Aluminium Alloy", *Journal of Materials Processing Technology*, Vols. 153-154, 2004, pp. 945-951.

[108] Walker, K., "Effects of Environment and Complex Load History on Fatigue Life", *ASTM STP 462*, American Society for Testing and Materials, 1970, pp. 1-14.

[62] Walker, N. and Beevers, C.J., "Fatigue Crack Closure Mechanism in Titanium", *Fatigue of Engineering Materials and Structures*, Vol. 1, No. 1, 1979, pp. 135-148.

[67] Wang, S.H. and Müller, C., "Fracture Surface Roughness and Roughness-Induced Fatigue Crack Closure in Ti-2.5 wt% Cu", *Materials Science & Engineering A: Structural Materials: Properties, Microstructure and Processing*, Vol. A255, No. 1-2, 1998, pp. 7-15.

[68] Wang, S.H., Müller, C. and Exner, H.E., "A Model for Roughness-Induced Fatigue Crack Closure", *Metallurgical and Materials Transactions A, Physical Metallurgy and Materials Science*, Vol. 29A, 1998, pp. 1933-1939.

[31] Webster, P.J., Mills, G., Wang, X.D., Kang, W.P. and Holden, T.M., "Neutron Strain Scanning of a Small Welded Austenitic Stainless Steel Plate", *Journal of Strain Analysis for Engineering Design*, Vol. 30, No. 1, 1995, pp. 35-43.

[38] Webster, P.J., Wang, X.D., Kang, W.P. and Mills, G., "Experimental Verification of Residual Stress Models Using Neutron Strain Scanning", *Proceedings of the 1995 7th Conference on Modeling of Casting, Welding and Advanced Solidification Processes*, 1995, pp. 311-318.

[48] Webster, P.J., Ananthaviravakumar, N., Hughes, D.J., Mills, G., Preston, R.V., Shercliff, H.R. and Withers, P.J., "Measurement and Modelling of Residual Stresses in a TIG Weld", *Applied Physics A: Materials Science and Processing*, Vol. 74, No. SII, 2002, pp. S1421-S1423.

[72] Wei, L.W. and James, M.N., "Fatigue Crack Closure for Inclined and Kinked Cracks", *International Journal of Fracture*, Vol. 116, 2002, pp. 25-50.

[53] Westergaard, H.M., "Bearing Pressures and Cracks", *Journal of Applied Mechanics*, Vol. 6, 1939, pp. 49-53.

[9] Wheeler, O.E., "Spectrum Loading and Crack Growth", *Journal of Basic Engineering, Transaction of the ASME*, Vol. 94, No. 1, 1972, pp. 181-186.

[45] Wikander, L., Karlsson, L., Mäsström, M. and Webster, P., "Finite Element Simulation and Measurement of Welding Residual Stresses", *Modelling and Simulation in Materials Science and Engineering*, Vol. 2, No. 4, 1994, pp. 845-864.

[141] Willenborg, J.D., Engle, R.M. and Wood, H.A., "A Crack Growth Retardation Model using an Effective Stress Concept", *Report AFFEL-TM-71-1-FBR*, Air Force Flight Dynamics Laboratory, Wright-Patterson Air Force Base, Dayton, Ohio, 1971.

[34] Wimpory, R.C., May, P.S., O'Dowd, N.P., Webster, G.A., Smith, D.J. and Kingston, E., "Measurement of Residual Stresses in T-Plate Weldments", *Journal of Strain Analysis for Engineering Design*, Vol. 38, No. 4, 2003, pp. 349-365.

[127] Woo, C.W. and Chow, C.L., "Fatigue Crack Propagation in Aluminium and PMMA", *International Journal of Fracture*, Vol. 26, 1984, pp. R37-R42.

[24] Xu, T. and Bea, R., "Load Shedding of Fatigue Fracture in Ship Structures", *Marine Structures*, Vol. 10, 1997, pp. 49-80.

[94] Yamada, K., Cao, Q., Okuhara, Y. and Cheng, X., "Fatigue Crack Growth Behavior of Various Structural Steel After Single and Periodic Overloads", *Proceedings of JSCE, Structural Engineering/Earthquake Engineering*, Vol. 15, No. 2, 1998, pp. 191s-200s.

[124] Yang, P., Liao, X., Zhu, J. and Zhou, H., "High Strain-Rate Low-Cycle Fatigue of a Medium-Carbon Alloy Steel", *International Journal of Fatigue*, Vol. 16, July 1994, pp. 327-330.

[91] Yildirim, N. and Vardar, Ö., "Study of Periodic Overloads at a Fixed Overload-Ratio", *Engineering Fracture Mechanics*, Vol. 36, No. 1, 1990, pp. 71-76.

[47] Youtsos, A.G., Robin, V. and Bhandari, S., "Residual Stress Evaluation in a RPV Bimetallic Weld for Evaluating the Crack Behaviour", *ASME Pressure Vessels and Piping Division (Publication) PVP*, Vol. 404, 2000, pp. 173-184.

[96] Yu, M.T., Topper, T.H. and Au, P., "The Effects of Stress Ratio, Compressive Load and Underload on the Threshold Behaviour of a 2024-T351 Aluminum Alloy", *Engineering Materials Advisory Services Ltd*, Vol. 1, 1984, pp. 179-190.

[163] Zapatero, J., Moreno, B., Gonzalez-Herrera, A. and Dominguez, J., "Numerical and Experimental Analysis of Fatigue Crack Growth under Random Loading", *International Journal of Fatigue*, Vol. 27, 2005, pp. 878-890.

[99] Zhang, X., Chan, A.S.L. and Davies, G.A.O., "Numerical Simulation of Fatigue Crack Growth under Complex Loading Sequences", *Engineering Fracture Mechanics*, Vol. 42, No. 2, 1992, pp. 305-321.

[73] Zhang, X.P., Li, J.C., Wang, C.H., Ye, L. and Mai, Y.W., "Prediction of Short Fatigue Crack Propagation Behaviour by Characterization of Both Plasticity and Roughness Induced Crack Closures", *International Journal of Fatigue*, Vol. 24, No. 5, 2002, pp. 529-536.

[110] Zheng, X., "Local Strain Range and Fatigue Crack Initiation Life", *IABSE Proc. Fatigue Colloquium*, 1982, pp. 169-178.

[8] Zheng, X.L. and Hirt, M.A., "Fatigue Crack Propagation in Steels", *Engineering Fracture Mechanics*, Vol. 18, No. 5, 1983, pp. 965-973.

[50] Zhu, X.K. and Chao, Y.J., "Numerical Simulation of Transient Temperature and Residual Stresses in Friction Stir Welding of 304L Stainless Steel", *Journal of Materials Processing Technology*, Vol. 146, 2004, pp. 263-272.

Appendix A *J*-Integral Results from the Investigation into the "Prying" Effect due to Crack Surface Roughness

Table A-1 *J*-integral results ($JE/\sigma^2\pi a$) for $\theta = 0.0°$, $\sigma = 120$ MPa

$\theta = 0.0$

μ	d/a	ULR = 1.00	ULR = 1.39	ULR = 1.67	ULR = 1.94	ULR = 2.22	ULR = 2.50	ULR = 2.78	ULR = 3.06
0.0	0	1.1617 (0000)	1.1617 (0100)	1.1620 (0200)	1.1636 (0300)	1.1649 (0400)	1.1640 (0500)	1.1040 (0600)	1.5761 (0700)
	0.0026	1.1617 (0000)	1.1617 (0110)	1.1626 (0210)	1.1636 (0310)	1.1647 (0410)	1.1637 (0510)	1.1368 (0610)	1.5924 (0710)
	0.0104	1.1616 (0000)	1.1616 (0120)	1.1625 (0220)	1.1629 (0320)	1.1653 (0420)	1.1631 (0520)	1.1348 (0620)	1.5959 (0720)
	0.0156	1.1624 (0000)	1.1624 (0130)	1.1618 (0230)	1.1631 (0330)	1.1643 (0430)	1.1632 (0530)	1.1363 (0630)	1.5982 (0730)
	0.0208	1.1616 (0000)	1.1616 (0140)	1.1619 (0240)	1.1633 (0340)	1.1651 (0440)	1.1635 (0540)	1.1358 (0640)	1.5792 (0740)
	0.0260	1.1613 (0000)	1.1613 (0150)	1.1619 (0250)	1.1633 (0350)	1.1643 (0450)	1.1615 (0550)	1.1360 (0650)	1.5969 (0750)
	0.0313	1.1616 (0000)	1.1616 (0160)	1.1626 (0260)	1.1631 (0360)	1.1651 (0460)	1.1624 (0560)	1.1359 (0660)	1.5787 (0760)
0.5	0	1.1617 (0000)	1.1617 (0101)	1.1620 (0201)	1.1636 (0301)	1.1651 (0401)	1.1640 (0501)	1.1370 (0601)	1.5983 (0701)
	0.0026	1.1617 (0000)	1.1617 (0111)	1.1626 (0211)	1.1636 (0311)	1.1653 (0411)	1.1637 (0511)	1.1378 (0611)	1.5998 (0711)
	0.0104	1.1616 (0000)	1.1616 (0121)	1.1625 (0221)	1.1629 (0321)	1.1653 (0421)	1.1633 (0521)	1.1372 (0621)	1.5952 (0721)
	0.0156	1.1624 (0000)	1.1624 (0131)	1.1618 (0231)	1.1631 (0331)	1.1650 (0431)	1.1637 (0531)	1.1363 (0631)	1.5958 (0731)
	0.0208	1.1616 (0000)	1.1616 (0141)	1.1619 (0241)	1.1633 (0341)	1.1652 (0441)	1.1636 (0541)	1.1540 (0641)	1.5713 (0741)
	0.0260	1.1613 (0000)	1.1613 (0151)	1.1619 (0251)	1.1633 (0351)	1.1643 (0451)	1.1623 (0551)	1.1360 (0651)	1.5791 (0751)
	0.0313	1.1616 (0000)	1.1616 (0161)	1.1626 (0261)	1.1631 (0361)	1.1651 (0461)	1.1624 (0561)	1.1359 (0661)	1.5800 (0761)
1.0	0	1.1617 (0000)	1.1617 (0102)	1.1620 (0202)	1.1636 (0302)	1.1651 (0402)	1.1640 (0502)	1.1370 (0602)	1.5983 (0702)
	0.0026	1.1617 (0000)	1.1617 (0112)	1.1626 (0212)	1.1636 (0312)	1.1653 (0412)	1.1637 (0512)	1.1378 (0612)	1.5998 (0712)
	0.0104	1.1616 (0000)	1.1616 (0122)	1.1625 (0222)	1.1629 (0322)	1.1653 (0422)	1.1633 (0522)	1.1372 (0622)	1.5952 (0722)
	0.0156	1.1624 (0000)	1.1624 (0132)	1.1618 (0232)	1.1631 (0332)	1.1650 (0432)	1.1637 (0532)	1.1363 (0632)	1.5958 (0732)
	0.0208	1.1616 (0000)	1.1616 (0142)	1.1619 (0242)	1.1633 (0342)	1.1652 (0442)	1.1636 (0542)	1.1540 (0642)	1.5713 (0742)
	0.0260	1.1613 (0000)	1.1613 (0152)	1.1619 (0252)	1.1633 (0352)	1.1643 (0452)	1.1623 (0552)	1.1360 (0652)	1.5791 (0752)
	0.0313	1.1616 (0000)	1.1616 (0162)	1.1626 (0262)	1.1631 (0362)	1.1651 (0462)	1.1624 (0562)	1.1359 (0662)	1.5800 (0762)
1.5	0	1.1617 (0000)	1.1617 (0103)	1.1620 (0203)	1.1636 (0303)	1.1651 (0403)	1.1640 (0503)	1.1370 (0603)	1.5983 (0703)
	0.0026	1.1617 (0000)	1.1617 (0113)	1.1626 (0213)	1.1636 (0313)	1.1653 (0413)	1.1637 (0513)	1.1378 (0613)	1.5998 (0713)
	0.0104	1.1616 (0000)	1.1616 (0123)	1.1625 (0223)	1.1629 (0323)	1.1653 (0423)	1.1633 (0523)	1.1372 (0623)	1.5952 (0723)
	0.0156	1.1624 (0000)	1.1624 (0133)	1.1618 (0233)	1.1631 (0333)	1.1650 (0433)	1.1637 (0533)	1.1363 (0633)	1.5958 (0733)
	0.0208	1.1616 (0000)	1.1616 (0143)	1.1619 (0243)	1.1633 (0343)	1.1652 (0443)	1.1636 (0543)	1.1540 (0643)	1.5713 (0743)
	0.0260	1.1613 (0000)	1.1613 (0153)	1.1619 (0253)	1.1633 (0353)	1.1643 (0453)	1.1623 (0553)	1.1360 (0653)	1.5791 (0753)
	0.0313	1.1616 (0000)	1.1616 (0163)	1.1626 (0263)	1.1631 (0363)	1.1651 (0463)	1.1624 (0563)	1.1359 (0663)	1.5800 (0763)

Note on model name:

(1 1 2 3 d/a 1)

Code	θ	ULR	(θ = 0.0°, 22.5°, 45.0°)	(θ = 67.5°)	μ
0	0.0°	1.00	0	0	0.0
1	22.5°	1.39	≈ 0.0025	≈ 0.005	0.5
2	45.0°	1.67	≈ 0.01	≈ 0.02	1.0
3	67.5°	1.94	≈ 0.015	≈ 0.03	1.5
4	----------	2.22	≈ 0.02	≈ 0.04	----------
5	----------	2.50	≈ 0.025	≈ 0.05	----------
6	----------	2.78	≈ 0.03	≈ 0.06	----------
7	----------	3.06	----------	----------	----------

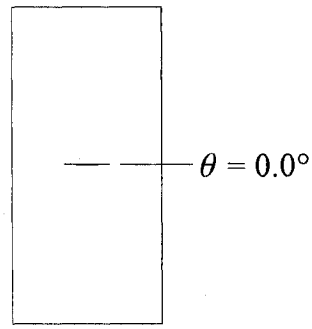

Table A-2 *J*-integral results ($JE/\sigma^2\pi a$) for $\theta = 22.5°$, $\sigma = 120$ MPa

$\theta = 22.5°$

μ	d/a	ULR	1.39	1.67	1.94	2.22	2.50	2.78	3.06
0.0	0	1.00	1.0122 (1100)	1.0120 (1200)	1.0150 (1300)	1.0246 (1400)	1.0307 (1500)	1.0906 (1600)	1.2097 (1700)
	0.0026	1.39	1.0121 (1110)	1.0126 (1210)	1.0158 (1310)	1.0252 (1410)	1.0380 (1510)	1.0980 (1610)	1.2911 (1710)
	0.0103	1.67	1.0120 (1120)	1.0125 (1220)	1.0150 (1320)	1.0250 (1420)	1.0380 (1520)	1.1005 (1620)	1.2903 (1720)
	0.0155	1.94	1.0121 (1130)	1.0123 (1230)	1.0145 (1330)	1.0236 (1430)	1.0378 (1530)	1.0998 (1630)	1.2977 (1730)
	0.0206	2.22	1.0121 (1140)	1.0127 (1240)	1.0150 (1340)	1.0237 (1440)	1.0382 (1540)	1.1027 (1640)	1.2975 (1740)
	0.0258	2.50	1.0120 (1150)	1.0126 (1250)	1.0147 (1350)	1.0232 (1450)	1.0372 (1550)	1.0982 (1650)	1.2916 (1750)
	0.0309	2.78	1.0121 (1160)	1.0127 (1260)	1.0151 (1360)	1.0233 (1460)	1.0373 (1560)	1.0971 (1660)	1.2928 (1760)
0.5	0	1.00	1.0122 (1101)	1.0128 (1201)	1.0159 (1301)	1.0252 (1401)	1.0378 (1501)	1.0997 (1601)	1.2897 (1701)
	0.0026	1.39	1.0122 (1111)	1.0127 (1211)	1.0158 (1311)	1.0250 (1411)	1.0381 (1511)	1.0997 (1611)	1.2844 (1711)
	0.0103	1.67	1.0121 (1121)	1.0125 (1221)	1.0150 (1321)	1.0245 (1421)	1.0387 (1521)	1.0993 (1621)	1.2920 (1721)
	0.0155	1.94	1.0121 (1131)	1.0125 (1231)	1.0147 (1331)	1.0236 (1431)	1.0383 (1531)	1.0992 (1631)	1.2900 (1731)
	0.0206	2.22	1.0121 (1141)	1.0127 (1241)	1.0152 (1341)	1.0237 (1441)	1.0376 (1541)	1.1011 (1641)	1.2898 (1741)
	0.0258	2.50	1.0120 (1151)	1.0125 (1251)	1.0148 (1351)	1.0231 (1451)	1.0375 (1551)	1.0989 (1651)	1.2879 (1751)
	0.0309	2.78	1.0121 (1161)	1.0128 (1261)	1.0151 (1361)	1.0234 (1461)	1.0374 (1561)	1.0940 (1661)	1.2882 (1761)
1.0	0	1.00	1.0122 (1102)	1.0129 (1202)	1.0160 (1302)	1.0250 (1402)	1.0380 (1502)	1.0996 (1602)	1.2969 (1702)
	0.0026	1.39	1.0122 (1112)	1.0127 (1212)	1.0158 (1312)	1.0248 (1412)	1.0380 (1512)	1.0995 (1612)	1.2967 (1712)
	0.0103	1.67	1.0121 (1122)	1.0125 (1222)	1.0150 (1322)	1.0245 (1422)	1.0386 (1522)	1.0989 (1622)	1.2955 (1722)
	0.0155	1.94	1.0121 (1132)	1.0125 (1232)	1.0147 (1332)	1.0236 (1432)	1.0381 (1532)	1.0991 (1632)	1.2982 (1732)
	0.0206	2.22	1.0121 (1142)	1.0127 (1242)	1.0152 (1342)	1.0237 (1442)	1.0372 (1542)	1.1017 (1642)	1.2905 (1742)
	0.0258	2.50	1.0120 (1152)	1.0125 (1252)	1.0146 (1352)	1.0231 (1452)	1.0375 (1552)	1.0987 (1652)	1.2940 (1752)
	0.0309	2.78	1.0121 (1162)	1.0128 (1262)	1.0150 (1362)	1.0234 (1462)	1.0374 (1562)	1.0940 (1662)	1.2875 (1762)
1.5	0	1.00	1.0122 (1103)	1.0129 (1203)	1.0160 (1303)	1.0250 (1403)	1.0380 (1503)	1.0994 (1603)	1.2862 (1703)
	0.0026	1.39	1.0122 (1113)	1.0127 (1213)	1.0156 (1313)	1.0246 (1413)	1.0382 (1513)	1.0990 (1613)	1.2880 (1713)
	0.0103	1.67	1.0121 (1123)	1.0125 (1223)	1.0150 (1323)	1.0245 (1423)	1.0384 (1523)	1.0995 (1623)	1.2893 (1723)
	0.0155	1.94	1.0121 (1133)	1.0125 (1233)	1.0147 (1333)	1.0236 (1433)	1.0381 (1533)	1.0992 (1633)	1.2895 (1733)
	0.0206	2.22	1.0121 (1143)	1.0127 (1243)	1.0152 (1343)	1.0237 (1443)	1.0372 (1543)	1.1017 (1643)	1.2918 (1743)
	0.0258	2.50	1.0120 (1153)	1.0125 (1253)	1.0148 (1353)	1.0231 (1453)	1.0375 (1553)	1.0987 (1653)	1.2919 (1753)
	0.0309	2.78	1.0121 (1163)	1.0128 (1263)	1.0150 (1363)	1.0234 (1463)	1.0374 (1563)	1.0940 (1663)	1.2885 (1763)
ULR = 1.00			1.0121 (1000)						

Note on model name:

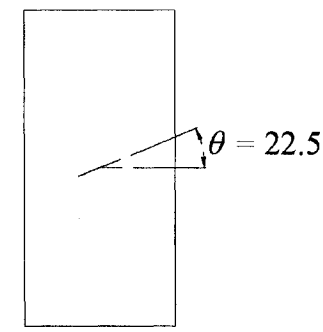

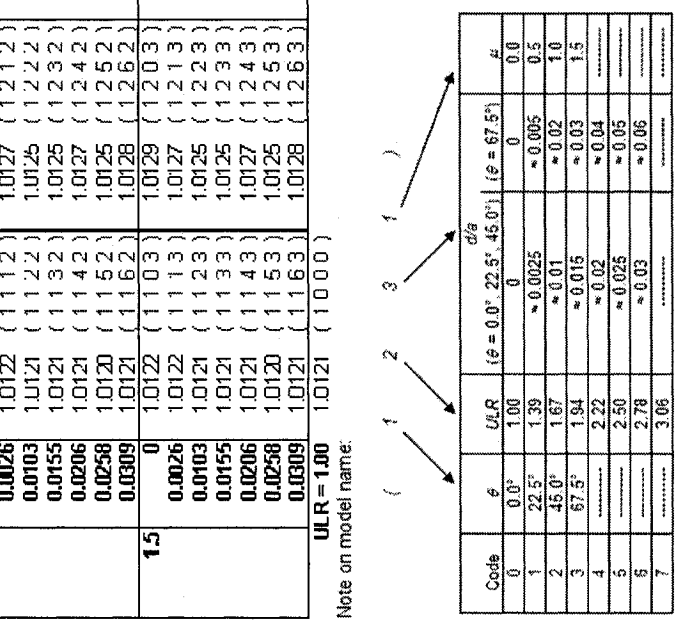

Code	θ	ULR	(θ = 0.0°, 22.5°, 45.0°)	(θ = 67.5°)	μ
0	0.0°	1.00	0	0	0.0
1	22.5°	1.39	≈ 0.0025	≈ 0.005	0.5
2	45.0°	1.67	≈ 0.01	≈ 0.02	1.0
3	67.5°	1.94	≈ 0.015	≈ 0.03	1.5
4	----------	2.22	≈ 0.02	≈ 0.04	----------
5	----------	2.50	≈ 0.025	≈ 0.05	----------
6	----------	2.78	≈ 0.03	≈ 0.06	----------
7	----------	3.06	----------	----------	----------

Table A-3 *J*-integral results ($JE/\sigma^2\pi a$) for $\theta = 45.0°$, $\sigma = 120$ MPa

$\theta = 45.0$

μ	d/a	ULR	1.39	1.67	1.94	2.22	2.50	2.78	3.06
0.0	0	0.5995 (2100)	0.6006 (2200)	0.6042 (2300)	0.6105 (2400)	0.6420 (2500)	0.6017 (2600)	0.7600 (2700)
	0.0025	0.5992 (2110)	0.6004 (2210)	0.6042 (2310)	0.6180 (2410)	0.6423 (2510)	0.6801 (2610)	0.7692 (2710)
	0.0102	0.5995 (2120)	0.5997 (2220)	0.6037 (2320)	0.6171 (2420)	0.6433 (2520)	0.6816 (2620)	0.7636 (2720)
	0.0153	0.5992 (2130)	0.5999 (2230)	0.6026 (2330)	0.6158 (2430)	0.6408 (2530)	0.6801 (2630)	0.7629 (2730)
	0.0204	0.5992 (2140)	0.5999 (2240)	0.6032 (2340)	0.6164 (2440)	0.6402 (2540)	0.6818 (2640)	0.7656 (2740)
	0.0256	0.5995 (2150)	0.5997 (2250)	0.6024 (2350)	0.6154 (2450)	0.6388 (2550)	0.6767 (2650)	0.7623 (2750)
	0.0307	0.5990 (2160)	0.6000 (2260)	0.6031 (2360)	0.6163 (2460)	0.6398 (2560)	0.6749 (2660)	0.7676 (2760)
0.5	0	0.5995 (2101)	0.6006 (2201)	0.6046 (2301)	0.6182 (2401)	0.6415 (2501)	0.6804 (2601)	0.7618 (2701)
	0.0025	0.5992 (2111)	0.6001 (2211)	0.6045 (2311)	0.6176 (2411)	0.6414 (2511)	0.6785 (2611)	0.7688 (2711)
	0.0102	0.5995 (2121)	0.5997 (2221)	0.6047 (2321)	0.6172 (2421)	0.6436 (2521)	0.6808 (2621)	0.7632 (2721)
	0.0153	0.5995 (2131)	0.5993 (2231)	0.6027 (2331)	0.6168 (2431)	0.6408 (2531)	0.6795 (2631)	0.7620 (2731)
	0.0204	0.5992 (2141)	0.6001 (2241)	0.6034 (2341)	0.6164 (2441)	0.6401 (2541)	0.6790 (2641)	0.7648 (2741)
	0.0256	0.5995 (2151)	0.5998 (2251)	0.6024 (2351)	0.6150 (2451)	0.6389 (2551)	0.6741 (2651)	0.7640 (2751)
	0.0307	0.5991 (2161)	0.6000 (2261)	0.6030 (2361)	0.6162 (2461)	0.6407 (2561)	0.6753 (2661)	0.7645 (2761)
1.0	0	0.5995 (2102)	0.6006 (2202)	0.6046 (2302)	0.6180 (2402)	0.6413 (2502)	0.6804 (2602)	0.7655 (2702)
	0.0025	0.5992 (2112)	0.6001 (2212)	0.6045 (2312)	0.6176 (2412)	0.6414 (2512)	0.6801 (2612)	0.7618 (2712)
	0.0102	0.5995 (2122)	0.5997 (2222)	0.6046 (2322)	0.6174 (2422)	0.6427 (2522)	0.6796 (2622)	0.7689 (2722)
	0.0153	0.5995 (2132)	0.5993 (2232)	0.6029 (2332)	0.6169 (2432)	0.6411 (2532)	0.6806 (2632)	0.7650 (2732)
	0.0204	0.5992 (2142)	0.6001 (2242)	0.6034 (2342)	0.6164 (2442)	0.6401 (2542)	0.6790 (2642)	0.7669 (2742)
	0.0256	0.5995 (2152)	0.5998 (2252)	0.6024 (2352)	0.6150 (2452)	0.6389 (2552)	0.6747 (2652)	0.7625 (2752)
	0.0307	0.5990 (2162)	0.6000 (2262)	0.6030 (2362)	0.6162 (2462)	0.6407 (2562)	0.6757 (2662)	0.7645 (2762)
1.5	0	0.5995 (2103)	0.6006 (2203)	0.6046 (2303)	0.6180 (2403)	0.6413 (2503)	0.6804 (2603)	0.7602 (2703)
	0.0025	0.5992 (2113)	0.6001 (2213)	0.6045 (2313)	0.6176 (2413)	0.6414 (2513)	0.6799 (2613)	0.7632 (2713)
	0.0102	0.5995 (2123)	0.5997 (2223)	0.6047 (2323)	0.6175 (2423)	0.6433 (2523)	0.6796 (2623)	0.7612 (2723)
	0.0153	0.5995 (2133)	0.5993 (2233)	0.6029 (2333)	0.6169 (2433)	0.6411 (2533)	0.6806 (2633)	0.7651 (2733)
	0.0204	0.5992 (2143)	0.6001 (2243)	0.6034 (2343)	0.6164 (2443)	0.6401 (2543)	0.6790 (2643)	0.7671 (2743)
	0.0256	0.5995 (2153)	0.5998 (2253)	0.6024 (2353)	0.6150 (2453)	0.6389 (2553)	0.6747 (2653)	0.7621 (2753)
	0.0307	0.5990 (2163)	0.6000 (2263)	0.6030 (2363)	0.6162 (2463)	0.6407 (2563)	0.6757 (2663)	0.7645 (2763)
	ULR = 1.00	0.5995 (2000)						

Note on model name:

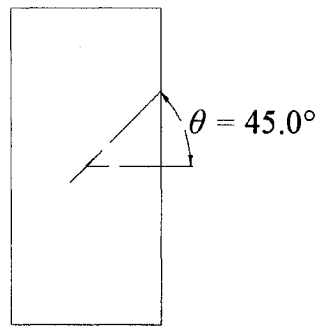

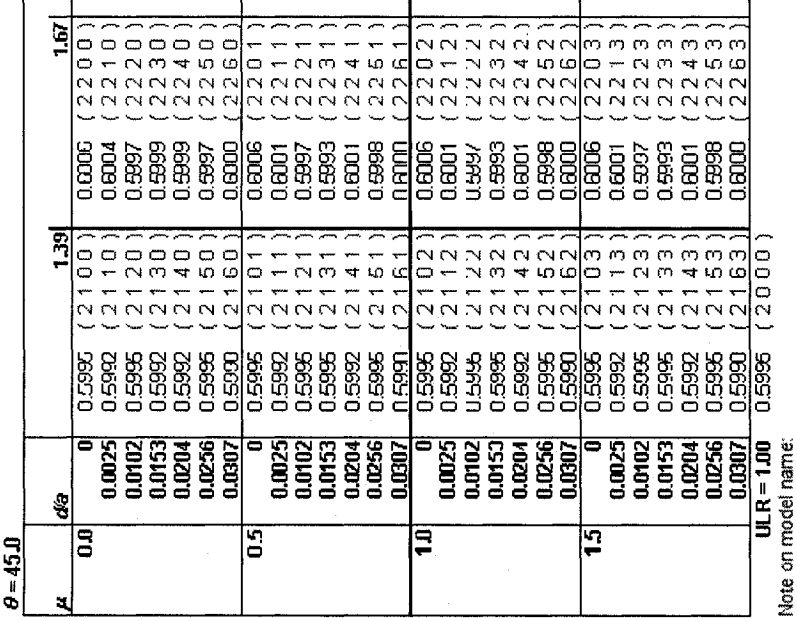

Code	ϕ	ULR	$(\phi = 0.0°, 22.5°, 45.0°)$	$(\phi = 67.5°)$	α
0	0.0°	1.00	0	0	0.0
1	22.5°	1.39	≈ 0.0025	≈ 0.005	0.5
2	45.0°	1.67	≈ 0.01	≈ 0.02	1.0
3	67.5°	1.94	≈ 0.015	≈ 0.03	1.5
4	.....	2.22	≈ 0.02	≈ 0.04	.....
5	.....	2.50	≈ 0.025	≈ 0.05	.....
6	.....	2.78	≈ 0.03	≈ 0.06	.....
7	.....	3.06	.....	.....	.....

Table A-4 *J*-integral results ($JE/\sigma^2\pi a$) for $\theta = 67.5°$, $\sigma = 120$ MPa

$\theta = 67.5$

μ	d/a	ULR 1.39	1.67	1.94	2.22	2.50	2.78	3.06
0.0	0	0.3290 (3100)	0.3299 (3200)	0.3307 (3300)	0.3304 (3400)	0.3377 (3500)	0.3427 (3600)	0.3561 (3700)
	0.0052	0.3298 (3110)	0.3298 (3210)	0.3304 (3310)	0.3329 (3410)	0.3378 (3510)	0.3430 (3610)	0.3566 (3710)
	0.0208	0.3298 (3120)	0.3299 (3220)	0.3302 (3320)	0.3323 (3420)	0.3371 (3520)	0.3424 (3620)	0.3686 (3720)
	0.0312	0.3298 (3130)	0.3299 (3230)	0.3302 (3330)	0.3321 (3430)	0.3371 (3530)	0.3421 (3630)	0.3696 (3730)
	0.0416	0.3298 (3140)	0.3298 (3240)	0.3303 (3340)	0.3321 (3440)	0.3368 (3540)	0.3419 (3640)	0.3679 (3740)
	0.0521	0.3298 (3150)	0.3298 (3250)	0.3302 (3350)	0.3318 (3450)	0.3362 (3550)	0.3414 (3650)	0.3673 (3750)
	0.0625	0.3298 (3160)	0.3298 (3260)	0.3303 (3360)	0.3321 (3460)	0.3365 (3560)	0.3415 (3660)	0.3663 (3760)
0.5	0	0.3298 (3101)	0.3299 (3201)	0.3307 (3301)	0.3334 (3401)	0.3377 (3501)	0.3428 (3601)	0.3560 (3701)
	0.0052	0.3298 (3111)	0.3298 (3211)	0.3304 (3311)	0.3328 (3411)	0.3378 (3511)	0.3432 (3611)	0.3664 (3711)
	0.0208	0.3298 (3121)	0.3299 (3221)	0.3302 (3321)	0.3322 (3421)	0.3370 (3521)	0.3426 (3621)	0.3689 (3721)
	0.0312	0.3298 (3131)	0.3299 (3231)	0.3302 (3331)	0.3321 (3431)	0.3370 (3531)	0.3422 (3631)	0.3696 (3731)
	0.0416	0.3298 (3141)	0.3298 (3241)	0.3303 (3341)	0.3321 (3441)	0.3367 (3541)	0.3418 (3641)	0.3673 (3741)
	0.0521	0.3298 (3151)	0.3298 (3251)	0.3302 (3351)	0.3318 (3451)	0.3362 (3551)	0.3413 (3651)	0.3668 (3751)
	0.0625	0.3298 (3161)	0.3298 (3261)	0.3303 (3361)	0.3321 (3461)	0.3365 (3561)	0.3415 (3661)	0.3662 (3761)
1.0	0	0.3298 (3102)	0.3299 (3202)	0.3307 (3302)	0.3334 (3402)	0.3377 (3502)	0.3428 (3602)	0.3560 (3702)
	0.0052	0.3298 (3112)	0.3298 (3212)	0.3304 (3312)	0.3328 (3412)	0.3378 (3512)	0.3432 (3612)	0.3664 (3712)
	0.0208	0.3298 (3122)	0.3299 (3222)	0.3302 (3322)	0.3322 (3422)	0.3370 (3522)	0.3426 (3622)	0.3689 (3722)
	0.0312	0.3298 (3132)	0.3299 (3232)	0.3302 (3332)	0.3321 (3432)	0.3370 (3532)	0.3422 (3632)	0.3696 (3732)
	0.0416	0.3298 (3142)	0.3298 (3242)	0.3303 (3342)	0.3321 (3442)	0.3367 (3542)	0.3418 (3642)	0.3673 (3742)
	0.0521	0.3298 (3152)	0.3298 (3252)	0.3302 (3352)	0.3318 (3452)	0.3362 (3552)	0.3413 (3652)	0.3668 (3752)
	0.0625	0.3298 (3162)	0.3298 (3262)	0.3303 (3362)	0.3321 (3462)	0.3365 (3562)	0.3415 (3662)	0.3662 (3762)
1.5	0	0.3298 (3103)	0.3299 (3203)	0.3307 (3303)	0.3334 (3403)	0.3377 (3503)	0.3428 (3603)	0.3560 (3703)
	0.0052	0.3298 (3113)	0.3298 (3213)	0.3304 (3313)	0.3328 (3413)	0.3378 (3513)	0.3432 (3613)	0.3664 (3713)
	0.0208	0.3298 (3123)	0.3299 (3223)	0.3302 (3323)	0.3322 (3423)	0.3370 (3523)	0.3426 (3623)	0.3680 (3723)
	0.0312	0.3298 (3133)	0.3299 (3233)	0.3302 (3333)	0.3321 (3433)	0.3370 (3533)	0.3422 (3633)	0.3696 (3733)
	0.0416	0.3298 (3143)	0.3298 (3243)	0.3303 (3343)	0.3321 (3443)	0.3367 (3543)	0.3418 (3643)	0.3673 (3743)
	0.0521	0.3298 (3153)	0.3298 (3253)	0.3302 (3353)	0.3318 (3453)	0.3362 (3553)	0.3413 (3653)	0.3668 (3753)
	0.0625	0.3298 (3163)	0.3298 (3263)	0.3303 (3363)	0.3321 (3463)	0.3365 (3563)	0.3415 (3663)	0.3662 (3763)
ULR = 1.00		0.3298 (3000)						

Note on model name:

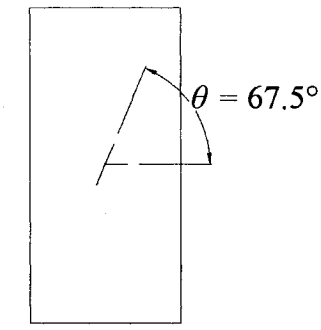

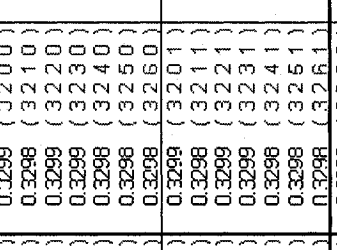

Code	θ	ULR	(θ = 0.0° 22.5° 45.0°) d/a	(θ = 67.5°) d/a	μ
0	0.0°	1.00	0	0	0.0
1	22.5°	1.39	≈ 0.0025	≈ 0.005	0.5
2	45.0°	1.67	≈ 0.01	≈ 0.02	1.0
3	67.5°	1.94	≈ 0.015	≈ 0.03	1.5
4	.....	2.22	≈ 0.02	≈ 0.04	.....
5	.....	2.50	≈ 0.025	≈ 0.05	.....
6	.....	2.78	≈ 0.03	≈ 0.06	.....
7	.....	3.06	.....	.....	.....